Integrated photonic systems for single photon generation and quantum applications: Assembly of fluorescent diamond nanocrystals by novel nano-manipulation techniques

D i s s e r t a t i o n

zur Erlangung des akademischen Grades
d o c t o r r e r u m n a t u r a l i u m
(Dr. rer. nat.)
im Fach Physik

eingereicht an der
Mathematisch-Naturwissenschaftlichen Fakultät I
der Humboldt-Universität zu Berlin

von
Dipl.-Phys. Tim Schröder

Präsident der Humboldt-Universität zu Berlin:
Prof. Dr. Jan-Hendrik Olbertz

Dekan der Mathematisch-Naturwissenschaftlichen Fakultät I:
Prof. Stefan Hecht, PhD

Gutachter/innen:
1. Prof. Dr. Oliver Benson
2. Prof. Dr. Saskia F. Fischer
3. Prof. Dr. Christoph Becher

Tag der mündlichen Prüfung: 30.08.2012

Abstract

The presented thesis covers the development and investigation of novel integrated single photon sources and their application for quantum information schemes. Single photon generation was based on single defect centers in diamond nanocrystals. Such defect centers offer unique optical properties as they are room temperature stable, non-blinking, and do not photo-bleach over time. The fluorescent nanocrystals are mechanically stable, their size down to 20 nm enabled the development of novel nano-manipulation pick-and-place techniques. One of these techniques features an atomic force microscope and allows nanometer precise deposition of pre-selected diamond crystals in complex photonic structures.

Two different approaches were pursued to realize novel single photon sources. The first one is the bottom-up integration of fluorescent diamond nanocrystals into nano- and micrometer scaled fiber devices and resonant structures. Generated single photons couple evanescently to these structures, enabling efficient coupling without additional optical components, making them ultra-stable and maintenance free. The second approach is the application of a solid immersion microscope. Its solid immersion lens acts as a dielectric antenna for the emission of defect centers, enabling the highest photon rates of up to 2.4 Mcts/s and collection efficiencies of up to 4.2 % from nitrogen vacancy defect centers achieved to date.

Furthermore, the microscope can be applied at cryogenic temperatures enabling novel applications and fundamental investigations not possible before due to insufficient photon rates. Such an application was the determination of the spectral diffusion time of a single nitrogen vacancy defect center in diamond nanocrystals to be about $\tau_D = 2.2\,\mu s$, giving new insights into the mechanism causing spectral diffusion. Spectral diffusion is a limiting property for quantum information applications, e.g. to realize two-photon interference.

The table-top solid immersion microscope was integrated into a compact mobile single photon system with dimension of only 7 x 19 x 23 cm^3 while still maintaining record-high stable photon rates. This makes it interesting for various single photon applications. Two of such applications were realized. First, a quantum key distribution scheme based on the BB84 protocol was implemented, for the first time also with silicon vacancy defect centers. Secondly, a conceptually novel scheme for the generation of infrared single photons was introduced and realized. It is based on a photonic crystal fiber which acts as a conversion device for single pump photons provided by the compact mobile system.

Zusammenfassung

Im Rahmen der vorliegenden Dissertation wurden neuartige integrierte Einzelphotonenquellen und ihre Anwendung für die Quanteninformationsverarbeitung entwickelt und untersucht. Die Erzeugung von Einzelphotonen basiert auf einzelnen Defektzentren in nanometergroßen Diamantkristallen. Solche Defektzentren haben einzigartige optische Eigenschaften, sie sind stabil bei Zimmertemperatur, blinken nicht und behalten ihre Eigenschaften für lange Zeiträume. Die Diamantkristalle sind mechanisch stabil, ihre Größe bis unter 20 nm ermöglichte die Entwicklung von neuartigen *pick-and-place* Techniken. Bei einer dieser Techniken wird ein Atomkraftmikroskop benutzt, um vorselektierte Diamantkristalle mit Nanometer-Präzision in komplexe photonische Strukturen zu integrieren.

Zwei unterschiedliche Ansätze für die Realisierung der neuartigen Einzelphotonenquellen wurden verfolgt. Beim ersten werden fluoreszierende Diamantkristalle in nano- und mikrometergroße Faser-basierte oder resonante Strukturen in einem *bottom-up* Ansatz integriert. Die erzeugten Einzelphotonen koppeln evaneszent an diese Strukturen, dadurch werden zusätzliche optische Komponenten überflüssig und das Gesamtsystem ultra-stabil und wartungsfrei. Der zweite Ansatz beruht auf einem Festkörperimmersionsmikroskop. Seine Festkörperimmersionslinse wirkt wie eine dielektrische Antenne für die Emission der Defektzentren. Es ermöglicht die höchsten bisher erreichten Photonenzählraten von Stickstoff-Fehlstellen von bis zu 2.4 Mcts/s und Einsammeleffizienzen von bis zu 4.2 %.

Des Weiteren kann das Mikroskop bei cryogenen Temperaturen benutzt werden. Dadurch werden neuartige Anwendungen und fundamentale Untersuchungen möglich, die vorher auf Grund von nicht ausreichenden Photonenraten nicht realisiert werden konnten. Eine solche Anwendung war die Bestimmung der spektralen Diffusionszeit eines einzelnen Defektzentrums in einem Diamantkristall zu $\tau_D = 2.2\,\mu s$. Dadurch wurden neue Erkenntnisse über die Ursachen von spektraler Diffusion gewonnen. Spektrale Diffusion ist eine limitierende Eigenschaft in Bezug auf die Realisierung von z. B. 2-Photonen-Interferenz.

Das Tisch-basierte Festkörperimmersionsmikroskop wurde außerdem als kompaktes mobiles Einzelphotonensystem mit Ausmaßen von nur 7 x 19 x 23 cm^3 realisiert. Dadurch wird es interessant für verschiedene Einzelphotonenanwen-dungen. Zwei solcher Anwendungen wurden realisiert. Zuerst wurde ein Quantenkryptographie-Experiment aufgebaut, das auf dem BB84 Protokoll basiert. Zum ersten Mal wurden dafür Siliziumdefektzentren benutzt. Zum Zweiten wurde ein neues Konzept für die Erzeugung von infraroten Einzelphotonen entwickelt und realisiert. Es basiert auf einer photonischen Kristallfaser, die einzelne Pumpphotonen zu höheren Wellenlängen konvertiert.

Contents

1 Introduction

Science and technology have always been driven by the ambition to make devices smaller and more potent. Probably one of the best examples for this socially driven desire is the computer. Today, computers are much more compact and faster than ever before. In the future, their miniaturization will proceed and their calculation power will increase. However, already today, electronic systems reach the borders of processes allowed by classical physics. Such limitations could be overcome with the help of quantum physics. It was proven theoretically, that certain mathematical problems can be solved much more efficiently with quantum algorithms [1]. Furthermore, for a deeper understanding of fundamental principles of complex quantum systems, a quantum simulator could be applied. Very recently, first realizations of such a quantum simulator [2] and a quantum network have been presented [3]. However, these experiments have been realized with ultra-cold atoms in an optical lattice and atom-cavity systems, respectively. Such atomic implementations are very complex, bulky, and challenging to control. To overcome these drawbacks, solid state based atom like systems have been introduced, and are expected to enable similar systems in less complex configurations. Currently, such systems still lack efficient and small scale integration.

At the same time as technical devices have become more and more miniaturized, data communication, the external exchange of information from physical point A to physical point B, has sped up by orders of magnitude. The secure exchange of information is a crucial part of our society. However, with increasing computational powers, the vulnerability of classical encryption schemes has increased. New concepts of transferring encrypted data have to be applied. It was shown at the end of the last century, that new concepts of encryption based on quantum physics permit intrinsically secure data transfer [4]. Such quantum encryption schemes will be of major importance for future communication. For long distance quantum key distribution, quantum light sources are essential which generate single photon states. A particularly suited process for their on demand generation is the fluorescent decay of a single two level quantum system, e.g., an atomic transition. However, atoms are challenging to control. Atomic like,

solid state based quantum systems like quantum dots or organic dye molecules on the other hand, are experimentally easy to control but have limited optical properties or demand cryogenic operation. A reliable room temperature quantum light source that has life cycles of up to years and emits with a stable intensity was only realized for the first time in 2000 [5]. It is based on single nitrogen vacancy (NV) defect centers in diamond. Besides its optical properties, also its spin properties make it an interesting candidate for the implementation of quantum technologies. Since its discovery, the system has been object of many studies [6, 7], proving its capability for a wide range of optical and spin based applications. Its stable room temperature emission allows the integration into devices that could be used in everyday environments. One of the most promising examples is the application of quantum key distribution (QKD), i.e. the secure exchange of information via single photons [4]. However, further miniaturization away from standard table-top setups towards fiber based implementations as well as enhancement of photon rates is necessary. To realize this challenging task, two approaches can be pursued: Either the miniaturized device is processed around a single photon emitter or the single emitter is integrated via a bottom-up assembly into the pre-fabricated structure [7].

In the course of this thesis, the latter approach was conducted via the controlled deposition of diamond nanocrystals containing single NV defect centers. Such a bottom-up approach is very promising for the realization of scalable quantum technology with atom-like solid state systems. Various deterministic deposition and integration techniques were developed and applied. They are introduced in **Chapter 3**. The most potent method is a pick-and-place technique via an atomic force microscope. It allows pre-selection and nanometer precise position control of only 20 nm sized crystals.

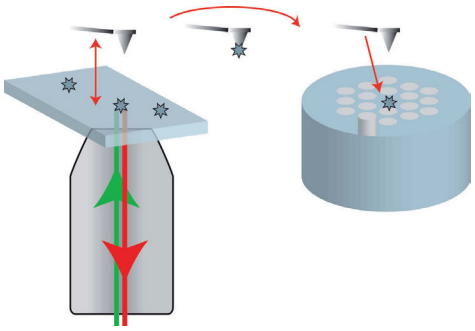

For optical analysis of fluorescent quantum systems, a confocal microscope setup was applied featuring spectral and time resolved measurement devices. Via an inverted microscope, simultaneous manipulation and optical investigation of nano- and microparticles was possible. For low temperature experiments, an efficient cryostat setup was developed. Experimental configurations and technical devices are presented in **Chapter 4**.

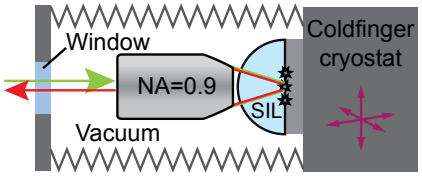

The developed deposition techniques were applied to realize fiber-integrated single photon generation systems as discussed above. Three conceptually different systems were developed. They are introduced in the **first part of Chapter 5** and are based on newly developed concepts that had not been realized before. They have different degrees of fiber integration ranging from millimeter to nanometer sized devices. For the first time, direct near-field coupling of a single quantum emitter to the optical mode of a fiber was achieved. This near-field coupling makes lenses redundant, is ultra-stable and provides efficient photon fiber coupling.

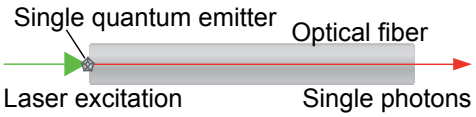

However, single photon rates achieved with these integrated devices are still limited. There are two main reasons. The first one is the limited spontaneous emission rate of the NV defect center in a standard dielectric environment. This spontaneous emission rate can be increased via the Purcell effect by e.g. coupling the quantum emitter to resonant structures [8]. Exploiting this phenomenon will allow ultra-high photon rates. In the course of this thesis, first steps towards such regimes of high Purcell enhancement have been made. For the first time, single quantum emitters were coupled to the modes of optical resonators in a controlled manner. These experiments will be presented in the **second part of Chapter 5**.

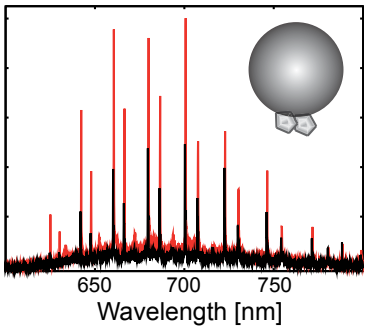

The second reason for limited photon rates is their limited collection efficiency by integrated devices and standard microscopy techniques. The integrated structures as discussed before already offer high collection efficiencies for micro- and nanometer sized devices. However, the achieved photon rates are still too small to realize certain applications with a reasonable efficiency. Therefore, to increase photon collection efficiencies of standard microscopy a solid immersion microscope was developed. It is introduced in **Chapter 6**. This microscope favorably modifies the emission pattern of an optical dipole and achieves the highest collection efficiencies for NV defect centers reported yet.

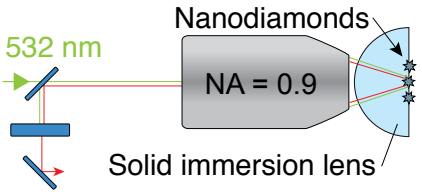

Also at cryogenic temperatures, standard light collection schemes lack high efficiencies. Oil immersion microscopes cannot be applied at cryogenic temperatures. To overcome this limitation and to still achieve highly efficient photon collection, the developed solid immersion microscope was combined with an advanced cryogenic setup. In principle, it allows the efficient collection of indistinguishable single photons only stemming from the zero phonon line of an NV defect center. Such photons could be applied for the implementation of quantum information processing, e.g. for the realization of optical logic circuits. However, to date almost all investigated NV defect centers have shown spectral shifts in their zero phonon emission line over time, prohibiting such schemes. This phenomenon is called spectral diffusion. It is particularly strong for defect centers inside diamond nanocrystals. In this thesis, an important step for the fundamental understanding of the mechanisms causing this problem was achieved. Experiments on the temporal behavior of such spectral drifts are introduced in **Chapter 7**. Their realization gives a deeper insight into the NV^- defect center.

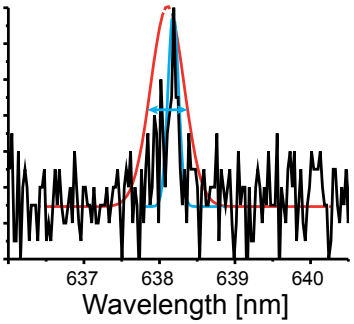

Furthermore, the developed solid immersion microscope was integrated into a compact mobile device with dimensions of only 7 x 19 x 23 cm^3 as shown in the **first part of Chapter 8**. In combination with mobile control and counting instrumentation

and a mobile correlation device it can be operated outside an optical lab. Compared to the only commercially available single photon source [9], it is many times smaller and brighter. The system can be used for various experimental tasks that require a high flux of single photons. Furthermore, the system can be easily modified to be used as a standard confocal microscope. This enables integration and mobile application of other fluorescent and quantum emitters as alternatives to the NV defect center. Very recently, the potential of the silicon vacancy (SiV) defect center was demonstrated [10, 11]. It is an even brighter room temperature single photon source than the NV defect center. It was also integrated into the mobile system and used for new applications.

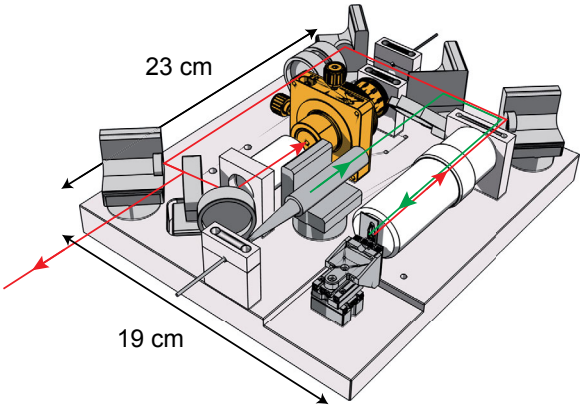

One of such applications of the mobile system is the efficient implementation of QKD schemes. First, the BB84 protocol was realized with NV defect centers. The short lifetimes of 1 to 2 nanoseconds of the SiV defect center, its room temperature emission line width of around 1 nm, and its linearly polarized emission make it a very promising candidate for even higher QKD bit rates. To show the capability of such SiV defect centers in diamond nanocrystals, a proof of principle QKD experiment was realized for the first time with this defect. The experiments are introduced in the **second part of Chapter 8**.

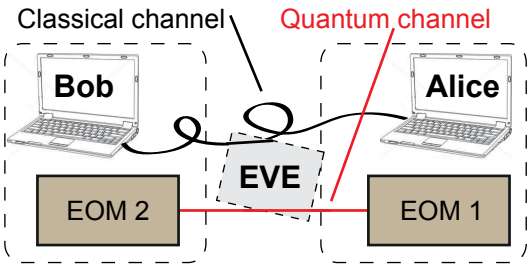

Finally, a conceptually novel scheme for the generation of single photons is introduced. The high rate of single visible photons of the mobile solid immersion microscope can be used to pump an ensemble of infrared quantum emitters for the generation of single

infrared photons. This is complementary to common single photon generation, when a single emitter is pumped by an ensemble of photons. The novel scheme is introduced in the **third part of Chapter 8**. It allows overcoming present limitations of single photon generation in the infrared where single photon emitters have poor performances.

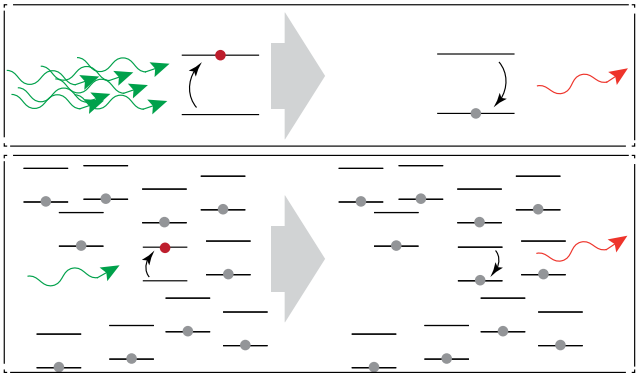

2 Single photon quantum states generated by single defect centers in diamond

Before introducing defect centers in diamond as single photon sources later in this chapter, a more fundamental treatment of a quantized light field, the single photon quantum state, is conducted. The concept of quantization of energy goes back to an idea of Max Planck in the beginnings of the 19^{th} century [12]. Albert Einstein then introduced the concept of the single photon (quantum state) as 'das Lichtquant' (the light quantum) [13].

A short survey on the development of this new revolutionary concept and our present knowledge about the photon is presented. The experimental confirmation of quantum mechanics already took place in the beginning of the last century. However, the direct measurement of single photons was challenging for the scientific community. It was not achieved until much later in the last century, when in the 1970's first photon-correlation measurements were successful, showing a classically prohibited antibunching dip [14].

The generation, detection, and statistical description of such single photons will be discussed. The second order auto-correlation function is introduced as a measure to confirm the existence of single photons. In the end of this chapter, we come back to defect centers in diamond as single photon sources. The nitrogen vacancy and the silicon vacancy defect center will be introduced in detail as they have been used as single photon sources in the course of this thesis.

2.1 A single quanta of light: A single photon

In 1900 Max Planck introduced the quantization of energy, saying that the 'Energieelement ϵ proportional der Schwingungszahl ν sein muss, also: $\epsilon = h\,\nu$' [12] when introducing a new formalism to describe the black body radiation. This new formalism was able to avoid the ultraviolet catastrophe as predicted by the so called Rayleigh-Jeans law. Furthermore, and more thriving for the development of quantum mechanics, Planck had introduced the groundbreaking idea (and with it the Planck constant h),

that energy could only be a multiple of an elementary 'Energieelement' - the light quantum as Einstein then called it later [13]. This was in 1905 when he published his work on the photoelectric effect. He concluded that some form of energy quantization had to be postulated to account for the thermal equilibrium which is observed between matter and electro-magnetic radiation.

Today, we understand a photon as a quantized electro-magnetic field that exhibits the properties of both a wave and a particle. These properties of the photon were experimentally proven (photoelectric effect, Young's double-slit experiment, etc.) in the beginnings of the 20^{th} century. They lead to the concept of wave-particle duality - one of the main motivations why the classical understanding of our world was extended to a more general description - to quantum theory. Presently, quantum physics is well accepted. Its principles have been applied in scientific labs throughout the world and even contribute, most of the times integrated into complex devices, to everyday life in form of atomic clocks, quantum cryptography, random number generators, lasers, and many other applications.

In the next sections the properties of a single photon are introduced which are of importance for the experiments presented in this thesis.

2.1.1 Single photon statistics: Second order auto-correlation function

The direct measurement of a single photon quantum state is a challenging task. How can the experimentalist confirm that he/she has detected a real single photon and not a classical light field? In 1963 Roy Glauber [15] introduced the second order coherence function $G^{(2)}(\tau)$, also referred to as second order auto- or cross-correlation function. This second order correlation function $G^{(2)}(\tau)$ predicts how the photon statistics of a classical light field differ from a quantum light field. The photon statistics describe, how the occurence of a photon is temporally related to earlier or subsequent photon events. Hence, by measuring the unique photon statistics of a quantum light field, the experimentalist could prove its existence. $G^{(2)}(\tau)$ can be normalized with the first order coherence function $G^{(1)}(0) = \langle \hat{\mathrm{E}}^{-}(0)\,\hat{\mathrm{E}}^{+}(0)\rangle$ [15].

The normalized second order auto-correlation function for a stationary, plane parallel light beam is defined in normal order as [16]:

$$g^{(2)}(\tau) = \frac{\langle \hat{\mathrm{E}}^{-}(\mathrm{t})\,\hat{\mathrm{E}}^{-}(\mathrm{t}+\tau)\,\hat{\mathrm{E}}^{+}(\mathrm{t}+\tau)\,\hat{\mathrm{E}}^{+}(\mathrm{t})\rangle}{\langle \hat{\mathrm{E}}^{-}(\mathrm{t})\,\hat{\mathrm{E}}^{+}(\mathrm{t})\rangle}.$$

Here, $\hat{\mathrm{E}}^{-}$ and $\hat{\mathrm{E}}^{+}$ represent electric-field operators. For the intensities of the light fields that are actually measured with the photodetectors, this results in:

$$g^{(2)}(\tau) = \frac{\langle : \hat{\mathrm{I}}(0)\, \hat{\mathrm{I}}(\tau) : \rangle}{\langle \hat{\mathrm{I}}(0) \rangle},$$

with $g^{(2)}(\tau) \to 1$ for $\tau \to \infty$ as random processes loose their correlation at long time scales. Here, : : indicates normal ordering.

In 1976 it was first predicted that a quantum mechanical two level system emitting single photons shows the so called antibunching, i.e., if $g^{(2)}(0) < g^{(2)}(\tau)$ [17]. This can be used to distinguish its photon correlations from a classical field. The following rules can be applied [18]. For classical light fields $g^{(2)}(0) \geq 1$ and $g^{(2)}(0) \geq g^{(2)}(\tau)$. Furthermore, classical thermal light sources have $g^{(2)}(0) > 1$. This so called bunching behavior is caused by strong intensity fluctuations of the emission of a classical source. Furthermore, classical coherent laser light sources emit photons independently. They show a Poissonian statistic and have $g^{(2)}(\tau) = 1$. Finally, for a non-classical light field $g^{(2)}(0) < 1$ with a sub-Poissonian photon statistic. Such a non-classical (or quantum) light field is generated by a quantum light source. A quantum light source is a quantum system that generates single photons. It is therefore, also called single photon emitter. The arrival at a detector of a photon generated by such a source is not independent from an earlier or later detection event. With the detection of a photon, the quantum system is prepared in its ground state. This implies, that it can not emit another photon before it is excited another time. Therefore, photons arrive with a time delay relative to each other. This time delay corresponds to the fluorescent lifetime of the quantum system. Fig. 2.1 illustrates the behavior of the correlation function for the different regimes of thermal light, laser light and non-classical quantum light.

The correlation function can also be derived in the picture of Fock space. This allows the direct treatment in terms of photon numbers [19]. A Fock state is a vector in a Fock space with a well-defined number of, e.g., photons. A Fock state $|\mathrm{n}\rangle$ is an eigenstate of the photon number operator $\hat{\mathrm{n}} = \mathrm{a}^{\dagger}\mathrm{a}$, with the creation operator $\mathrm{a}^{\dagger}$ and the annihilation operator a. It can be shown [20] that

$$g^{(2)}(0) = 1 - \frac{1}{\mathrm{n}}\,.$$

Directly from the value at $g^{(2)}(0)$, knowledge can be gained about the number of contributing single quantum emitters that generate single photon states measured on a

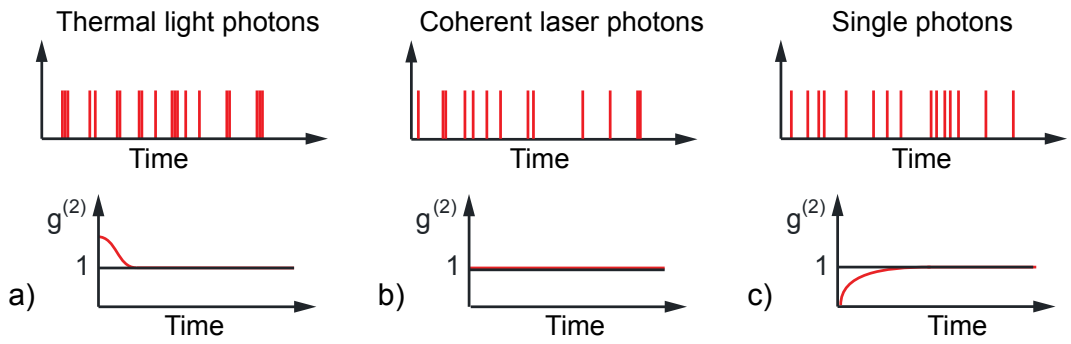

Figure 2.1: Sketch of the photon statistics of different types of light sources. a) A thermal light source generates photons with bunching behavior due to strong intensity fluctuations of its emission. Therefore, the photons occur in pairs or groups and the probability to measure a consecutive photon after detecting a photon is higher than for $\tau \to \infty$. b) A coherent laser light source emits photons randomly distributed over time with a Poissonian statistic. c) A quantum light source only generates one photon after another. With detection of a photon it is prepared in the ground state. Before a next emission (and hence detection) event, the system needs to be excited. Details are explained in the text.

detector. This is an important information for the experimentalist. Therefore, $g^{(2)}(0)$ is a figure of merit for a quantum light source. With this quantity, he/she can evaluate the quantum character of an investigated system. For n = 1, $g^{(2)}(0) = 0$, for n = 2, $g^{(2)}(0) = 1/2$. Therefore, if $g^{(2)}(0) < 1/2$, one can assume that only one single quantum emitter and some background contribute to the fluorescence signal.

2.1.2 Single photon detection

The experimental recording of such photon statistics as predicted in 1976 for a two level quantum system is a challenging task [17]. First, the emission of an optical quantum system has to be collected and directed to a detector. Such a detector has to be sensitive enough to detect the vanishing small amount of energy of a single visible photon of 0.3 aJ for $\lambda = 637$ nm. Furthermore, the detector's dead time must not exceed the fluorescence lifetime of the system in order to resolve single photon arrival events. Therefore, only very fast single photon detectors with ultra-short deadtimes can realize such task. For example, the lifetime of a single photon emitter is typically on a time scale of pico- to a few nanoseconds. Finally, a fast correlation device is necessary to determine the time differences between the measured photon events.

Due to such technical limitations, the first antibunching was only measured in 1977 [14]. However, at that time, the dead times of single photon detectors still exceeded

the lifetimes of the applied atoms by far. Therefore, only a technical trick in form of a Hanbury Brown and Twiss (HBT) interferometer enabled this measurement [21]. Such HBT setup is introduced in the next section.

A direct correlation measurement with very fast superconducting single photon detectors was only presented very recently by our group [22]. However, this measurement was only possible because the single photon system, an NV^- defect center inside a diamond nanocrystal, has a relatively long lifetime of around 25 ns. Therefore, the detector's dead time of a couple nanoseconds is small enough to achieve a time resolution high enough to map the antibunching dip.

Hanbury Brown and Twiss setup

To overcome experimental limitations given by detector deadtimes, a scheme was developed that allows the measurement of single photon events even with slow detectors. The concept goes back to an experimental setup developed to measure the diameter of far away stars [21] by means of photon correlation measurements. This so-called Hanbury Brown and Twiss (HBT) interferometer consists of a 50:50 beam splitter, two photodetectors and a time correlation device as illustrated in Fig. 2.2 a). Today, HBT setups are standard equipment in quantum optics laboratories. With an HBT setup,

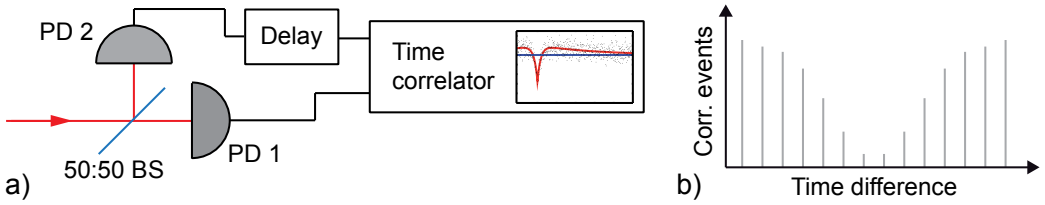

Figure 2.2: a) Sketch of a Hanbury Brown and Twiss setup. BS stands for beam splitter and PD for photodetector. b) Illustration of a time-event histogram derived from correlation measurements with a setup such as in a). The histogram represents a second order auto-correlation function.

the correlation of light intensities (which are measured with the photodetectors) at two space-times points are determined. In 1957 single photon counters were integrated into an HBT setup for the first time to measure such time-resolved intensity correlations [23]. However, these were not yet measurements of the second order auto-correalation function of quantum emitters. Such measurements were carried out for the first time in 1977 [14].

Correlation events are simply created by measuring the time differences between

photon detection events on detector 1 and detector 2 (see Fig. 2.2 a)). These events are binned and written into a time-event histogram as illustrated in Fig. 2.2 b). The recorded correlation events represent the second order auto-correlation function $G^{(2)}(\tau)$. It can be normalized to find $g^{(2)}(\tau)$, see App. A.

A home-built HBT setup was applied to determine the photon statistics of various single photon systems developed in the course of this thesis. Experimental details can be found in Sec. 4.2.4.

2.2 Single photon generation

After discussing the technical and theoretical pre-requisites to investigate single photon statistics, this section gives a short introduction of light generation schemes that create non-classical light and single photons. Fundamentally different concepts have been presented in the literature. In the following, an enumeration of different concepts is presented. To generate single photons, one can use:

I) **Single photon emitters.** A single photon emitter is a quantum system with discrete energy levels which only have a single fluorescent transition at a time in the investigated spectral range. Single photon emitters can be single atoms, ions, molecules, quantum dots and color centers in diamond. A stream of atoms was the first source investigated for non-classical light detection. Generally, single photon emitters are either pumped by an ensemble of photons, most likely a laser source, or they are electrically driven [24, 25] by a small current.

II) **Non-linear processes.** Photon pairs for heralded post selection of single photon events are created in down-converison sources. This idea was first implemented in 1985 [26]. Antibunching without sub-Poissonian statistics was achieved, i.e., a local minimum in the bunching at $g^{(2)}(0)$. In 1986 it was shown for the first time, that single photon sub-Poissonian statistics can be measured by heralding the arrival of a photon[27] . Heralding a single photon arrival event was achieved by creating simultaneously two photons with different frequencies. This photon pair can be separated and one of the photons can be used to gate a detector. By doing so, only single photon events are measured. Furthermore, it was shown in the same experiment that a single photon can interfere with itself.

III) **Photon-pair absorption.** The number of photon pairs, i.e., temporally close photons, in an ensemble of photons is reduced until temporally distant single

photons are left. This idea has not been realized yet due to experimental challenges, but various theoretical proposals have been published [28].

IV) **Single electrons.** Single electrons can be used to resonantly excite atoms in a Franck-Hertz experiment by Coulomb repulsion. Such an experiment was realized in 1985 [29]. Yet, due to a bad signal to noise ratio, only sub-poissonian statistics was shown with $g^{(2)}(0) > 0.5$ not reaching the single photon regime (see Sec. 2.1.1).

V) **Wavelength conversion of single photons by non-linear processes.** In an extended conceptual understanding, also conversion processes can be considered single photon generation schemes. To realize such a scheme, single photons are converted into a different frequency domain in a non-linear material. Either photon up-conversion from low frequencies to higher frequencies [30] or photon down-conversion [31, 32] has been demonstrated.

VI) **An ensemble of single photon emitters pumped by single photons.** This approach is complementing the first idea listed here. Instead of pumping a single emitter with an ensemble of photons, an ensemble of emitters is pumped with single photons. Such a conversion scheme was realized in the course of this thesis for the first time. It is based on efficient single photon generation (see Sec. 6.2) and subsequent conversion by absorption, re-emission and efficient re-collection (see Sec. 8.3). Again, an extended conceptual understanding of single photon generation was assumed.

These concepts and experimental realizations have been more or less successfully improved over the last years. Especially non-linear down-conversion processes to create heralded single photons are widely used and have been adopted to various systems [33]. However, the most variable and promising scheme for future quantum information applications is the generation of single photons via true single photon emitters.

Such single photon emitters were also the first system that was implemented to prove the existence of non-classical light as was already pointed out earlier but not discussed in detail. In 1977, the first observation of antibunching of photon detection events was observed in resonance fluorescence experiments in which sodium atoms were continuously excited by a dye-laser beam. Most remarkably, a relative minimum of $g^{(2)}(\tau)$ for $\tau = 0$ was measured, only occurring for quantum light [14]. However, a sub-poissonian behavior of the probability distribution of the photon number and

hence $g^{(2)}(\tau)<1$ for $\tau = 0$ was not shown. This was achieved finally in 1987, when such a sub-poissonian photon statistic was measured for photons stemming from a single ion inside a Paul-trap [34]. In 1992, single photon emission from a molecule covered in a solid state matrix was detected, starting the integration of single photon emitters in solid state systems for the experimentally convenient implementation of quantum systems in contrast to single ions or atoms. Ions and atoms have to be controlled with a complex experimental system [34].

Today, many different single photon emitters in solid state systems have been implemented, ranging from molecules [35], over quantum dots [36], to color centers in diamond [5]. Such solid state based single photon emitters have attracted a lot of attention in the past years, since they can be implemented into small scale photonic systems. In particular, color centers in diamond have been proven to provide some superior optical and electronic properties as will be discussed in the next section.

2.3 Defect centers in diamond

From the optical point of view, diamond is a remarkable matrial. It has a wide band gap of 5.5 eV at room temperature and an index of refraction of 2.4. The wide band gap makes it optically transparent for wavelengths from the deep ultraviolet to the far infrared. The crystal double face-centered cubic carbon structure can host impurities. Such impurities can be missing carbons and/or additional atoms from other elements. Such defect centers change the electronic structure and can be optically active. More than 500 fluorescent defect centers are known [45]. Only a few of them are presently

Defect center	ZPL	Max. counts	Lifetime	Bandwidth at RT
NV^-	637 nm	2.4 Mcts/s	(11 - 25) ns	$\approx$ 100 nm
SiV [10, 11]	(732 - 748) nm	4.8 Mcts/s	$\approx$ 1 ns	(0.7 - 5) nm
Cr-related [37, 38]	(750 - 770) nm	3 Mcts/s	(1 - 14) ns	(4 - 10) nm
NE8 [39--41]	(793 - 802) nm	70 kcts/s	2.1 ns	several nm
Ni-related [42]	768 nm	200 kcts/s	2 ns	7 nm
unknown [43]	734 nm	1.8 Mcts/s	13.6 ns	4.1 nm
TR12 [44]	470.5 nm	-	3.6 ns	-

Table 2.1: Different types of diamond defect centers to be known as single photon emitters and their optical and electronic structures. Further information can be found in corresponding references. Lifetimes of NV^- defect centers are 11 ns in bulk and up to 25 ns in nanocrystals. ZPL stands for zero phonon line, RT for room temperature, NV for nitrogen vacancy, SiV for silicon vacancy, NE8 represents a nickel nitrogen complex, TR12 represents a carbon related center.

known to be single photon emitters. The following Tab. 2.1 gives a short overview of the properties of some of the known diamond single photon emitters, more have been studied in the literature [6, 46]. All these defect centers in diamond have caught much and increasing attention in the last decade. They are room temperature stable (non bleaching and non blinking [47]) single photon emitters with high single photon count rates. In this thesis only the nitrogen vacancy and the silicon vacancy defect center have been investigated. Their properties are introduced in detail in the following sections.

2.3.1 Classification of diamond

The composition of a diamond matrix has a substantial influence on the electronic and optical properties of the defect centers. Diamond is categorized into different types [48]. More than 98 % of all natural diamond can be attributed to two types with each two sub-categories. The main criterion is the nitrogen concentration which has considerable impact on the optical properties of defect centers.

Type I diamond has a nitrogen content of more than 5 ppm. Type Ia diamond has a nitrogen content of about 0.1 %. The nitrogen atoms are clustered either in a pair of two or in a group of four. More than 90 % of all natural diamond is assigned into this category. In type Ib diamond nitrogen atoms are not clustered but homogeneously distributed over the carbon lattice with a concentration of only 0.05 %. Most type Ib diamond is produced synthetically, while only 0.1 % of all natural diamond belongs to this category.

Type II diamond has a nitrogen content of less than 5 ppm. Type IIa diamond is the category of the purest diamond. Ultra-pure diamond samples that are used for quantum storage implementations [49] belong to this group. Their nitrogen content can be as small as $5 \cdot 10^{-2}$ ppb. Type IIb diamond has a boron content of 0.25 ppm for natural diamond and up to 270 ppm in synthetic diamond. This p-type dopant has been applied in combination with phosphorus dopant to realize electrically driven single nitrogen vacancy defect centers [25].

2.4 The nitrogen vacancy defect center

The nitrogen vacancy (NV) defect center in diamond is composed of a substitutional nitrogen atom (replacing a carbon atom) and an adjacent nearest-neighbour vacancy (missing carbon atom). The defect belongs to the C_{3v} symmetry group [50]. Its atomic

structure is illustrated in Fig. 2.3. The modified lattice structure locally changes the electronic band structure of the diamond. An unmodified diamond carbon lattice has a wide band gap of about 5.5 eV. In the presence of an NV defect center, a level structure is induced in the band gap. Its excited state is energetically located far below the conduction band of the diamond lattice. This creates a stable atom like solid state system.

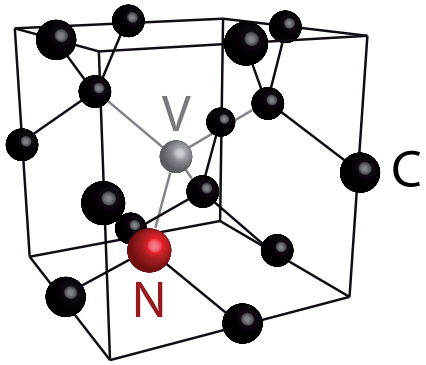

Figure 2.3: Illustration of the atomic structure of a nitrogen vacancy (NV) defect center in the carbon lattice of diamond. The NV defect center is composed of a substitutional nitrogen and nearest-neighbour vacancy [50]. N stands for nitrogen, V for vacancy and C for carbon.

An NV defect center can have different charge states, i.e., additional electrons can be bound or missing. In its neutral state, five electrons are attributed to the defect, due to the nitrogen substituted carbon atom and the vacancy. In a negatively charged NV defect, an additional electron is bound in the defect. A neighboring nitrogen defect center in the diamond lattice is attributed as donor of the electron [51]. Up to today, only the neutral and the negatively charged NV defect have been observed to emit single photons [52]. They are denoted NV^0 and NV^-, respectively. The NV^- will be introduced in detail in the following sections. From a quantum information point of view, it has, compared to the NV^0, more interesting properties besides its single photon emission.

2.4.1 Fluorescent emission from the NV^- defect center

The atom like electronic structures of both the NV^0 and the NV^- system have a radiative transition in the visible spectrum. The phonon free transitions (zero phonon lines) of the NV^0 and NV^- are in the visible light spectrum at 575 nm and 637 nm, respectively. In bulk diamond, a high fraction of single NV defect centers observed,

showed emission at 575 nm as well as around 637 nm as visible in the spectrum of a single NV defect center in Fig. 2.4 b). This is caused by a continuous conversion process between NV^0 and NV^-. It is assumed, that this charge transfer is induced by an electron donor respectively acceptor in the vicinity of the defect [53, 54]. However, in diamond nanocrystals, the contribution from the neutral NV defect can be negligibly small. For the experiments realized in the course of this thesis, mainly defect centers were applied which had an emission dominated by the NV^- attributed transitions, if not stated otherwise. The electronic level structure of the NV^- defect center will be discussed in detail in Sec. 2.4.2.

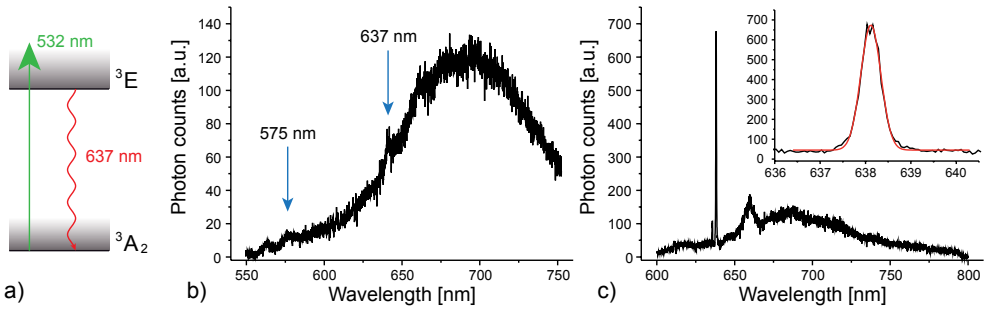

Figure 2.4: a) Simplified illustration of the radiative cycle of an NV^- defect center. A non-resonant green laser excites the electron to the vibronic band of the ^3E state. The radiative electron transition to the ground state generates a photon around 637 nm. However, due to strong coupling to the phonon side bands of the ground state, the emission is very broad as is visible in the spectra. b) Spectrum of an NV^0 defect center at 575 nm and an NV^- defect center at 637 nm under 532 nm excitation at room temperature. c) Spectrum of an NV^- defect center at 5 K. The emission peak is located at 638.1 nm. The inset shows a zoom-in into the ZPL. The FWHM of 0.52 nm was determined with a Gaussian fit.

At room temperature, radiative transitions of both charge states couple strongly to the phonon sidebands of the ground level, causing a wide emission with a FWHM of about 100 nm. These transitions can be excited non-resonantly with laser light in the green to yellow spectrum, from about 480 nm to 570 nm. The electron is excited into the vibronic band of the excited state as illustrated in Fig. 2.4 a) where it relaxes non-radiative into the ^3E state on a picosecond timescale. A spectrum from an exemplary NV^- defect center under continuous wave 532 nm excitation is displayed in Fig. 2.4 b). Clearly visible are the transition line at 637 nm and the wide emission into the phonon side bands.

Phonon coupled emission is reduced at cryogenic temperatures below 10 K. Therefore, the emission into the zero phonon line (ZPL) is more pronounced. For the NV^-

defect center, this is apparent in the spectrum in Fig. 2.4 c). Compared to the room temperature spectrum in Fig. 2.4 b), the emission into the ZPL is much higher than into the phonon side band between 640 nm and 800 nm. However, the coupling of the electron to the phonon sidebands even at cryogenic temperatures is strong, compared to a silicon vacancy defect center (see Sec. 2.5). The NV^- defect has a Debye-Waller factor (DWF) of about 0.05 at T = 5 K, indicating, that only about 5 % of the total emission is phonon free. The DWF is defined as the integrated fluorescence intensity of the ZPL divided by the integrated fluorescence intensity of the defect centre [39]. It depends on various properties of the material matrix surrounding the NV. For example, for diamond nanocrystals (see Sec. 2.4.3), the substrate material on which they are located, has a significant influence [55].

2.4.2 Electronic structure of the NV^- defect center

The electronic structure of the NV^- defect center is not fully understood. For the experiments carried out in the course of this thesis, a simplified, commonly accepted 3-level structure can be assumed. It is sufficiently precise for the determination of the properties of the NV^- defect centers analyzed within this thesis. The 3-level structure is illustrated in Fig. 2.5. An analysis of its electron dynamics is carried out in App. A.

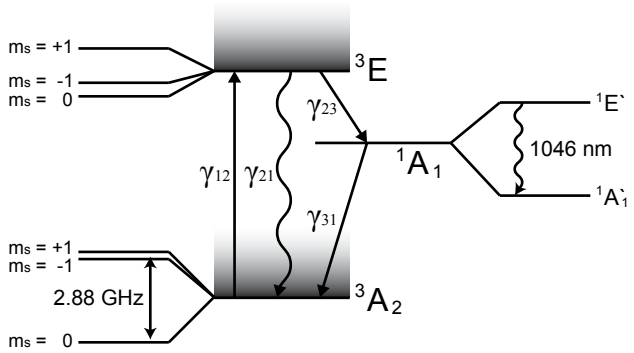

Figure 2.5: Sketch of the electronic level structure of an NV^- defect center in diamond. Waved arrows indicate radiative transitions. Details about the electronic structure are given in the text. The electron dynamics are described in App. A.

However, to reflect the most recent knowledge about the electronic structure of the NV^- defect as illustrated in Fig. 2.5, a short summary of these newest findings is given here [56, 56--61].

The NV^- defect center has a triplet ground state $^3A_2$ with an energetic splitting

of 2.88 GHz of its $^3A_{m=0}$ and degenerate $^3A_{m=\pm1}$ spin sub-levels. This splitting is caused by spin-spin interactions [61, 62]. The excited state ^3E also has a triplet structure. Its energetic splitting is caused by diagonal spin-orbit terms and by spin-spin interactions [57, 61]. As already pointed out earlier, the transition $^3A_2 \leftrightarrow {}^3E$ is radiative. Therefore, it can either emit or resonantly absorb light around 637 nm. Low temperature experiments reveal, that six pronounced ZPL lines can be detected [63]. Transitions into higher vibronic levels of the ground state $^3A_2$ and the excited state ^3E are also allowed with intra-band non-radiative transitions to the vibronic ground level. Very recently an upper bound of 0.7 of fluorescence quantum yield for NV defect centers was determined [64]. Polarization measurements confirm, that a single NV^- defect center has two optically active dipole transitions perpendicular to each other [65]. Therefore, the emission of a single defect shows a limited contrast in its polarization, see Sec. 5.2.5.

The fluorescence lifetime of the excited state ^3E is determined by the dielectric environment of the defect center. For luminescence from a natural type Ib diamond, a lifetime of 12.9 ns was measured, while it was determined to 11.6 ns for synthetic type Ib diamond [66] (see Sec. 2.3.1).

Besides its triplet states, the electronic level structure of the NV^- defect also exhibits two singlet states $^1E'$ and $^1A_1'$ energetically located between the two triplets as indicated in Fig. 2.5. Their existence has been confirmed by detection of infrared emission with a ZPL at 1046 nm [61]. At room temperature it is accompanied by a vibrational band, and at low temperature the ZPL is more pronounced as known already from the visible transition [61]. However, the probability of a radiative decay is three orders of magnitude smaller than the visible radiative decay and the transition to the ground state very fast. Hence, it can be neglected for the description of the electron dynamics of the NV^- carried out in the course of this thesis. Therefore, with the purpose of simplification, these two singlet states are from now on treated as a single state $^1A_1$. This is well according to the present literature.

The singlet state $^1A_1$ can be populated by the electron via a low probability inter-system crossing as indicated in the level structure of Fig. 2.5. This has an important influence on the spin and on the fluorescence properties of the NV^- defect center.

The electronic triplet of the ground state: A single spin state as quantum memory

The polarization of the NV^- defect, i.e., the spin state of the electron, determines the transition rate to the $^1A_1$ state. This has significant consequences as will be discussed

in the following. The transition rate γ_{23} is higher for an excited electron in the $^3E_{m_s=\pm1}$ state. If the electron is in this sub-level $m_s = \pm1$ of the excited state, the transition probability to $^1A_1$ is about 65 % of the transition probability to $^3A_2$ [5]. For $m_s = 0$ this probability is more than three orders of magnitude lower, thus negligible [67]. Furthermore, if the electron had crossed into the intermediate singlet state $^1A_1$, it preferentially decays into the $m_s = 0$ sub-level of the ground state triplet $^3A_2$ [57]. Thus, under constant strong optical excitation, the majority of the population is transferred to the $m_s = 0$ spin state of the ground state $^3A_2$. This causes an optically induced spin polarization of the ground state [68, 69]. This spin state is stable for long times even at room temperature. Its spin-lattice relaxation time is on the order of 10^2-10^4 s. Its spin dephasing time can reach values up to 3 ms at room temperature in synthetic high purity type IIa diamond [49, 70] and is limited by paramagnetic impurities in the diamond, mainly ^{13}C atoms.

Besides optical initialization and long dephasing times, the electronic spin states of the NV^- defect center have another thriving feature. They can directly be red out optically. The photon emission rate of the NV^- is determined by its spin state [67]. For an NV^- defect in its spin state $m_s = 0$, a repeated excitation and emission does not cause a change of the spin state [71]. Therefore, the photon emission rate is stable at a certain level, depending on the setup and the intrinsic properties of the NV^-. This photon emission rate drops, if the spin state is changed by a spin flip to the $m_s = \pm1$ state, for example, induced by a 2.88 GHz continuous microwave (see Fig. 2.5), as is done in optically detected magnetic resonance (ODMR) experiments. The electron now has a higher probability for intersystem crossing into the metastable state $^1A_1$. The metastable singlet state has a temperature dependent lifetime of 460 (371) to 220 (175) ns for temperatures of about 5 to 293 K [72] ([73]), reducing the repetition rate of the excitation and emission cycle and hence resulting in a reduced photon emission rate compared to an NV^- defect in state $m_s = 0$.

The controlled application of such microwave induced spin flips allows the optical control of the electron spin state of the NV^- defect center. This, together with optical state initialization and millisecond dephasing times, makes the NV^- defect center, additionally to its importance as stable and bright room temperature single photon source, a promising candidate for the realization of quantum information technologies. It can serve as a stationary qubit itself or as an interface for stationary and flying qubits which can be controlled optically at room temperature [74, 75]. Furthermore, it has been shown recently, that the electronic spin states can be coupled to nuclear spin

states. Thereby, information can be mapped onto the nuclear spin state and be stored even longer [76, 77].

2.4.3 Properties of the NV^- defect center in diamond nanocrystals

Besides the influence of the intrinsic characteristics of the diamond material on the optical properties of the NV^- defect center as discussed in Sec. 2.3.1, the carbon matrix surrounding a defect center also has a crucial influence. In bulk diamond, this matrix is homogeneously distributed of sp^3 hybridized bond carbon atoms - the typical diamond structure. In such a bulk diamond, lattice strain and sp^2 hybridized bond carbon (graphite) are not present. Furthermore, in high purity synthetic diamond, an almost spin-free carbon ^{12}C matrix is available. This is achieved by reducing the natural ^{13}C fraction of 1.1 % to less than 0.01 %, providing electron spin dephasing times of up to 3 ms [49, 70].

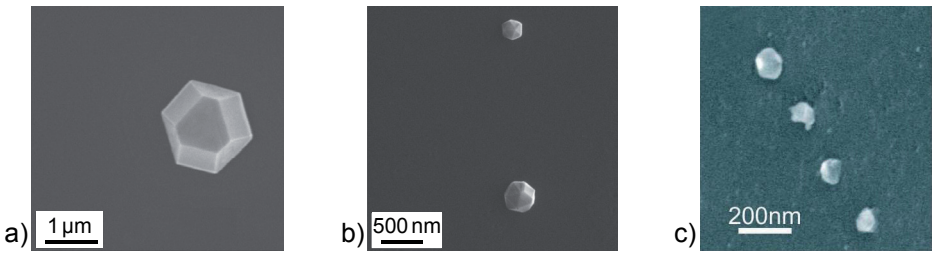

Figure 2.6: Images of diamond nanocrystals taken with a scanning electron microscope (SEM). For most of the experiments conducted, a typical crystal size was around 30 nm according to the smallest crystal in c). The images in a) and b) are taken from [78] and c) from [79].

However, single NV^- defects can also be found in diamond crystals with sizes ranging from micrometers to nanometers (see Fig. 2.6). In 2001, single photon emission of single NV^- defect centers in diamond nanocrystals with a size of roughly 40 nm was measured for the first time. Nanocrystals with sizes of 20 nm to 100 nm were applied for the experiments carried out in the course of this thesis. In most cases, synthetic diamond crystals, and only for some experiments, natural diamond crystals were used (for details please refer to Sec. 3.1). Such nanocrystals have important advantages for certain quantum optical experiments that are only possible due to their compact geometry and size. Most of the experiments conducted in the course of this thesis took advantage of this property. Nanocrystals can be easily deposited on various substrates with, e.g., spin-coating techniques or in a controlled manner via nano-manipulation. Such controlled deposition allows the integration into micro- and nanometer sized

quantum applications.

Furthermore, the photon collection efficiency of fluorescent diamond nanocrystals is generally higher compared to bulk diamond. In bulk diamond, total internal reflection at the air interface takes place for angles larger than 24.6 degrees, inhibiting a large fraction of light to leave the host material into the direction of the observer. This is different for nanocrystals with sizes smaller 100 nm. In a nanocrystal, the matrix of the diamond lattice is to small to cause total internal reflection [80]. Therefore, photons can leave the host material in all directions. However, it was recently shown for bulk diamond, that reduction of excitation intensity and improvement of emission collection of NV centers in bulk diamond can be achieved via etching adequate structures into bulk diamond. Such structures are nanorods [81] or solid immersion lenses either built into bulk diamond [82] or made out of bulk diamond [83]. They facilitate the collection of single photons of up to 500 kcts/s. Unfortunately, the production of these structures out of diamond demands rather sophisticated processes. To overcome the requirement for complex processes, experimental schemes based on diamond nanocrystals can be applied, which do not require diamond processing techniques but nevertheless achieve even higher photon rates.

However, it has also to be pointed out that diamond nanocrystals have altered optical properties compared to bulk. This is partly due to their intrinsic lattice properties, and partly due to material impurities. Diamond nanocrystals containing NV defects are presently only available as type Ib diamond, and not as high purity diamond [84]. While the ZPLs of different NV^- defect centers in bulk diamond have a stable spectral position around 637 nm, the emission of the ZPLs of NV^- in diamond crystals is distributed over more that 5 nm [85, 86]. Furthermore, also the spin properties of NV^- defect centers in nanocrystals are changed, e.g., zero field splitting, and lattice relaxation times. This is attributed to the strain in the diamond matrix induced by lattice inhomogeneities at the surface.

Generally in nanocrystals, due to the reduced diamond matrix, the refractive index $n_{Dia} = 2.4$ around the NV^- defect center is decreased. The NV^- defect perceives an effective refractive index $n_{Eff} < 2.4$, depending on the size of the crystal and the surrounding material. This influences the excited state lifetime [87]. For example, for a 40 nm sized crystal on a silica substrate, 25 ns radiative lifetime was found [88]. Measurements carried out in the course of this thesis confirm this value for a silica substrate. For a 30 nm sized crystal on a material with high refractive index $n = 2.17$, a lifetime of 18 ns was determined, see Sec. 6. These are relatively high values compared

to roughly 13 ns in bulk diamond. Therefore, the overall photon emission is reduced to a factor of 1.5 to 2 for such nanocrystals. However, the experiments presented in Sec. 6 show, that this reduction can be overcompensated by an optical near-field mechanism. The emission pattern of a dipole in the vicinity of an high index material is altered and directed towards the high index material (see Sec. 6.1.5).

2.5 The silicon vacancy defect center

Although NV^- defect centers are promising single photon sources with room temperature stable single photon emission with high photon detection rates of up to 2.4 Mcts/s (see Sec. 6.2), they have certain limitations in their performance. First of all, compared to other solid state based emitters, their lifetime of about 11 ns to 25 ns is relatively high. This limits the theoretically expected maximum emitted photon rate to 40 Mcts/s. Furthermore, the wide spectral emission causes experimental disadvantages in efficiently controlling the whole bandwidth with the same optical elements, such as lenses, wave plates, and electro-optic modulators. Also the polarization properties of the NV^- emission are not ideal, as is discussed in Sec. 5.2.5.

To overcome these limitations, alternative defect centers have been investigated for their application potential. Table 2.1 gives an overview on these efforts. Here, the silicon vacancy (SiV) defect center is introduced in detail [10, 11, 84].

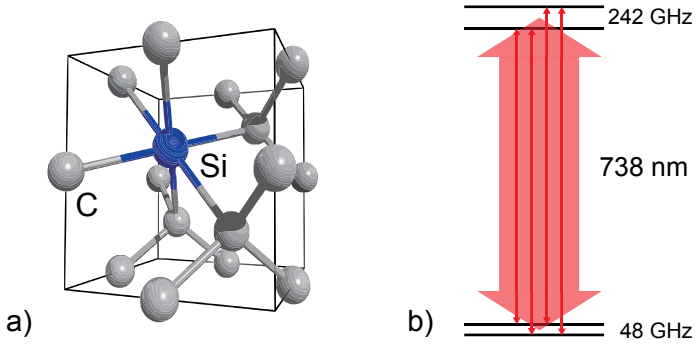

Figure 2.7: a) Sketch of the atomic structure of a silicon vacancy (SiV) defect center. It is composed of a substitutional silicon atom and a vacancy. The figure is taken from [11]. b) Sketch of the electronic level structure of a SiV defect center in diamond. It has a radiative transition at around 738 nm. Not indicated is a metastable third level assumed to be present for correct interpretation of certain experimental data as discussed in the text. The electron can be non-resonantly excited in the vibronic side band with light spectrally ranging from 671 nm to 715 nm from where it decays non-radiatively into the excited state.

The SiV is composed of a silicon atom and a lattice vacancy. They are arranged in a so-called split-vacancy configuration, where the substitutional silicon atom (replacing a carbon atom) relaxes its lattice position towards a neighbouring vacancy [21]. This is illustrated in Fig. 2.7 a). The band gap structure of the diamond lattice is altered due to the presence of the SiV defect and an atom like level structure is formed. A sketch of this level structure is shown in Fig. 2.7 b). The ground state has an energetic distance to the excited state and to the conduction band of 1.65 eV and 2.05 eV, respectively [11, 89]. Both ground state and excited state are split into a doublet by 48 GHz and 242 GHz, respectively [90]. This causes four optically allowed radiative transitions from the excited state to the ground state [11]. These properties were determined for ion implanted SiV defects [10] and for SiV defects created by chemical vapor deposition of diamond [11].

However, measurements of the second order auto-correlation function reveal, that the electron dynamics can only be described with a 3-level model. A pronounced bunching behavior is observed that can be described by considering a metastable non-radiative shelving state. This behavior was already observed for the NV^- defect. Therefore, the same model and the same fitting functions can be applied. Details can be found in App. A. It has to be pointed out, that the nature of the shelving state and the relaxation process is yet unknown.

In the following, only the optical properties of SiV defect centers created by chemical vapor deposition as described in [11] are discussed. The specific values given in the following are either taken from the same manuscript or from the investigations made in the course of this thesis.

The spectral emission lines of different single SiV defect centers are distributed from 730 nm to 750 nm with the majority ranging from 736 nm to 740 nm. All investigated SiV defects have a room temperature line width smaller than 4.9 nm, even down to 0.7 nm. These line width is comparable to the line width of 1.2 nm to 1.5 nm of NE8 defect centers [39, 41]. Furthermore, in contrast to the NV^- defect center, the electron is only weakly coupled to the phonons, resulting in a DWF of 0.75 to 0.88. Radiative lifetimes were measured ranging from 0.2 ns to 2 ns, theoretically determining a maximum photon emission rate of 5 GHz, assuming an intrinsic quantum yield of one. However, estimated quantum yields range from 0.09 to 0.43 [11].

The count rates determined for individual SiV defect centers vary from only a few kcts/s up to 4.8 Mcts/s. This high photon detection rate is the highest yet reported for defect centers in diamond, even exceeding chromium related defect centers with

3.2 Mcts/s [91]. Furthermore, the polarization properties of SiV defect centers are excellent. Only a single dipole is attributed with the optical transitions, resulting in a polarization visibility of 84 % to 91 %. However, it has to be pointed out, that a high fraction of SiV shows pronounced blinking behavior. It was also observed in the experiments introduced in Sec. 8.2, that a high fraction of SiV defects can be bleached with excitation powers even in the range of their saturation intensity.

Nevertheless, these properties make single SiV defect centers to promising candidates as bright and stable room temperature single photon sources. Their first time application for secure data transfer via QKD is presented in Sec. 8.2.

3 Integration of nano particles into macro-, micro- and nano-optical systems

For the preparation of the investigated devices, different deposition techniques have been applied. These deposition techniques range from simple spin-coating techniques over dip-coating to controlled pick-and-place techniques.

First, the preparation of diamond nanocrystal solution is described in Sec. 3.1. In Sec. 3.2, a simple drop-casting method is introduced for deposition of particles in solution with low particle concentration. Spin-coating is described in Sec. 3.3, it allows deposition of particles onto a sample that can be spun itself. For very fragile structures like tapered fibers, a dip-coating technique was developed as introduced in Sec. 3.4. Furthermore, controlled individual particle deposition as described in Sec. 3.5 allows assembly of complex quantum systems from nanoscopic constituents [7]. A pre-selection of these constituents permits to match all their critical properties to each other, e.g., the wavelength of a single emitter to the resonance of a cavity.

Parts of the experimental methods introduced in Sec. 3.3, Sec. 3.4, Sec. 3.5.1, Sec. 3.5.2, and Sec. 3.5.3 were published in Schröder *et al.* 2012b, Schröder *et al.* 2012a, Schietinger *et al.* 2008a, Gregor *et al.* 2009a, and Schröder *et al.* 2011b and Schell *et al.* 2011a, respectively.

3.1 Preparation of diamond nanocrystal solution

Most samples were prepared with commercial diamond particles (Microdiamant, Switzerland). These mono-crystalline diamond nanocrystals are dissolved in an aqueous solution. They were high pressure high temperature (HPHT) synthesized, grinded to nanometer sizes and size-selected by the manufacturer. The crystals are classified type-Ib diamond with up to 300 ppm of nitrogen atoms. They have not been exposed to any kind of extra treatment like surface oxidation, acid cleaning or defect implantation [92, 93].

Different crystal sizes are available. The smallest, 18 nm in average, were not used due to very low defect center content. For most experiments 25 nm sized crystals were applied. They contain a very well suited defect center distribution. Roughly one out of ten nanocrystals contains an NV defect center. Only very few (less than 2 %) contain more than one defect center. This makes them easy to handle as single photon emitters. For some experiments, also 50 nm, 100 nm or 200 nm sized diamond crystals were used. It is indicated in each section which size was applied.

3.1.1 Centrifuge cleaning of diamond nanocrystal solution

The original solution (Microdiamant, Switzerland) contains many dirt particles besides the diamond nanocrystals and is therefore not well suited for further optical experiments. To prepare a clean aqueous diamond solution it was pre-processed. In order to remove these dirt particles for further application as spin-coating or dip-coating, the solution was centrifuged. Therefore 200 µL of the original solution were placed inside a centrifuge (Minispin, Eppendorf, Germany). During the centrifugation process the diamond nanocrystals deposit at the bottom of the solution. These deposited particles are visible as sediment. The remaining solution above this sediment was carefully removed. Ionized water was added to refill the solution to 200 µL. The refilled solution was then placed in an ultrasonic bath to disperse the nanocrystals. This process was repeated ten times until a clean diamond solution was available for the deposition techniques presented in the following sections. For each application only the concentration of diamond nanocrystals had to be adapted by adding ionized water to the solution to thin it out.

For the spin-coating deposition technique, ten parts of this solution were given to one part of 0.1 % polyvinyl alcohol (PVA) to obtain a proportion of 0.01 % PVA. During spin-coating, the crystals are embedded in a PVA matrix. This guarantees a homogenous distribution of the nanocrystals. A process diagram of the cleaning procedure is depicted in Fig. 3.1.

3.2 Drop-casting

For samples and particle solutions that are not suited for spin-coating nor for one of the other methods described in the following sections, a direct drop-casting is the most effective way to deposit particles. A small droplet of 0.5 µL to 5 µL of a prepared particle solution is dropped onto the sample. After the solution has evaporated, the

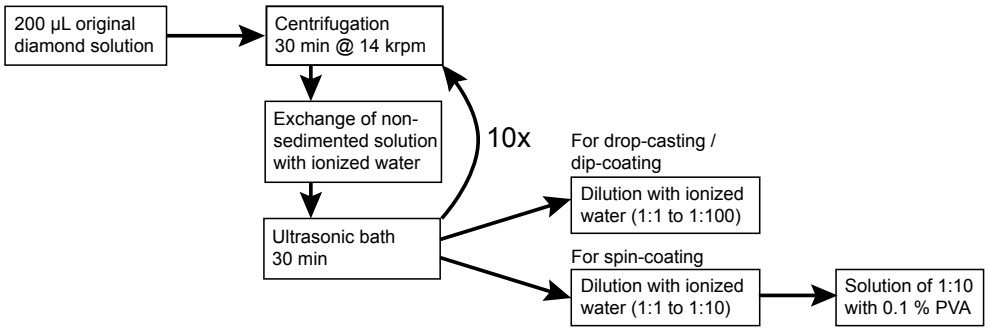

Figure 3.1: Process diagram of centrifugation process and preparation of diamond solution for deposition. Details are given in the text.

sample is ready to be used. The particles can be nano- oder micrometer sized.

This method is best suited for solutions made of solvents. These solvents, e.g. 2-propanol, evaporate fast and therefore allow a rapid sample preparation. To drop-cast polystyrene microspheres (MicroParticles, Germany) with a diameter of roughly 5 µm onto a cover slip (Menzel Gläser, Gerhard Menzel, Germany) that had already been equipped with diamond nanocrystals embedded in a PVA matrix, a solution of 2-propanol and these beads was used. It was experimentally proven that a homogeneous distribution on the cover slip could be attained.

The drop-casting can also be applied to aqueous solutions. This is of particular interest for solutions with a low particle concentration and sample surfaces that are insufficiently hydrophilic for spin-coating like ZrO_2 solid immersion lenses (SILs, see also Sec. 3.3). 300 µL of such a solution were provided by Prof. Wrachtrup's group at the University of Stuttgart. It contains only 0.1 mg/mL of specially treated diamond nanocrystals. Diamond nanocrystals had been milled from high-quality type Ib bulk diamond and have a size smaller than 150 nm. To clean the crystals from non-diamond sp^2 bonded carbon that is expected to have negative influence on the optical properties of the diamond nanocrystals (see Sec. 7.2), their surface was oxidized before they were acid washed. They were also centrifuged in a similar way as described in Sec. 3.1.1. Their low concentration did not allow spin-coating to achieve a density of fluorescent crystals higher than one per 10 μm^2. For some experiments a density of five or more per 10 μm^2 was necessary.

To achieve this high density, a droplet of 0.5 µL of the aqueous solution was drop-casted onto the flat side of a ZrO_2 SIL. The SIL was cleaned and either kept in an aqueous solution of Hellmanex II (Helma, Germany) or in 2-propanol. It turned out

that the 2-propanol makes the ZrO_2 surface more hydrophilic which is advantageous for the drop-casting. Before drop-casting the solution was kept in an ultrasonic bath for 15 min to de-agglomorate the crystals. To allow complete evaporation of the water, the sample was left at rest for about 30 min. Although the distribution of particles is less homogenous than after spin-coating, it was sufficient for the optical experiments carried out. The samples used for the experiments in Sec. 7.2 were prepared in this way.

3.3 Spin-coating

The spin-coating process allows deposition of particles onto a sample that can be spun itself. Examples of such samples are commonly used glass cover slips, but also more customized substrates as the flat side of a ZrO_2 SIL (see Chapter 6) or the facet of a GRIN lens (see Sec. 5.1). Their application in a home-built spin-coating apparatus is sketched in Fig. 3.2 a)-c).

The spin-coated solution can be aqueous or made of solvents, whereas the particles can be nano- or micrometer sized and made of various materials such as solid state, metals or semi-conductors. Most directly, the rotation speed of the substrate and the concentration of particles in the solution determine the density of particles on the surface of the substrate. Yet, substrate and particle surface properties as well as the composition of the solution influence the distribution properties. This high variety makes it impossible to give a general recipe, therefore the recipe given in this section focusses on diamonds with average sizes from 25 nm to 200 nm in an aqueous solution to be deposited on a glass cover slips or ZrO_2 SILs.

3.3.1 Spin-coating on glass cover slips

Commercial glass cover slips (Menzel Gläser, Gerhard Menzel, Germany) where cleaned in an aqueous solution of Hellmanex II (Helma, Germany) following the instructions given on the package. This cleansing solution also makes the glass surface hydrophilic, an important property for controlled spin-coating of particles in aqueous solutions. Diamond nanocrystal solutions were prepared as described in Sec. 3.1.1. The important properties for the spin-coating process are the proportion of PVA as well as the concentration of diamond crystals. The size of the diamond crystals (25 nm, 50 nm, 100 nm, or 200 nm in average, Microdiamant, Germany) did not influence the process. The best suited proportion of PVA was experimentally determined. With 0.01 % PVA

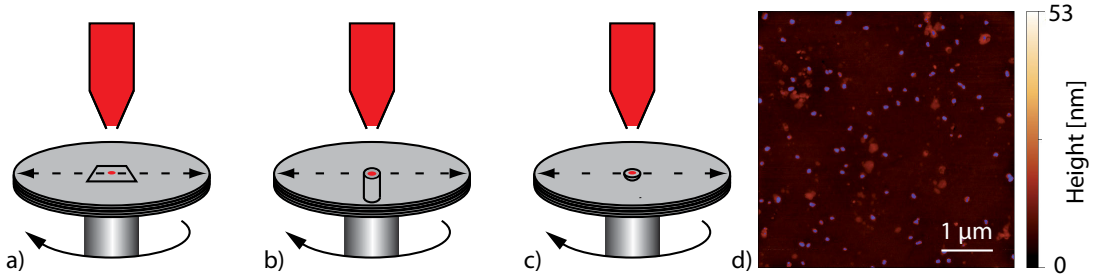

Figure 3.2: Schematic of the spin-coating technique: A sample holder with a flat surface is attached to a rotation table. This attachment is achieved by means of air underpressure to allow for easy sample (holder) exchange. A small droplet of solution can be dropped on the sample holder either before the table is rotated or while the table is already rotating. In this manner particles in the solution are spread out on the surface of the sample holder. Rotation is stopped when the solution is evaporated. This deposition technique can be applied to various samples. In a), b) and c) spin-coating onto a cover slit, onto the facet of a gradient index lens (see Sec. 5.1) and onto the flat surface of a solid immersion lens (see Chapter 6), respectively, is depicted. The influence of rotational speed, acceleration and the properties of sample surface and of the solution on the distribution of particles is further discussed in the text. d) AFM surface scan of spin-coated 25 nm diamond nanocrystals on a cover slip. The blue color mask indicates particles with a height smaller than 20 nm. This image reveals that a homogeneous distribution of the nanocrystals is achieved.

and a rotation speed of 2000 rpm, a homogenous distribution of the nanocrystals was achieved. Their density on the cover slip needs to be adjusted experimentally for each application by modifying the concentration of diamonds in the solution (see process diagram in Fig. 3.1). An example for homogeneously distributed diamonds nanocrystals with an average size of 25 nm is depicted in Fig. 3.2 d) in form of an AFM surface scan. The blue color coding marks particles with a height smaller than 20 nm, indicating that the crystals are well distributed and not clustered. The height represents roughly the size of the particles as they can be considered rather sphere-like than rod-like. The AFM surface scan proves that the parameters of the spin-coating are well understood and allow the controlled preparation of cover slip samples. These samples are either used for experiments on the optical properties of defect centers (see Sec. 7.2) or as reservoir for pick-and-place methods (see Sec. 3.5).

3.3.2 Spin-coating on ZrO_2 solid immersion lenses

For equipment of the flat side of the ZrO_2 SIL with diamonds, two different preparation and deposition processes were developed. The first one is equivalent to the process for glass cover slips. The second one features the drop-casting method (Sec. 3.2).

The spin-coating process turned out to be more difficult and less reproducible when applied to a SIL than for a glass cover slip. The ZrO_2 in the purchased consistency (grinded down from a sphere, Mikrop, Switzerland) is not hydrophilic and can not be made hydrophil with the same process as the glass cover slip (Hellmanex II). Later, it turned out, that dipping the SIL into 2-propanol makes it more hydrophilic. This process step was applied before drop-casting and improved distribution results.

Nevertheless, it was possible to prepare a SIL with well distributed diamond nanocrystals with this process by adjusting the rotation speed and repeating the spin-coating process several times. One of the thereby prepared SILs was used to carry out the experiments described in Chapter 6.

3.4 Dip-coating of tapered fibers

Certain samples cannot be equipped with nanoparticles by drop-casting nor spin-coating. Alternatively, a dip-coating technique can be applied. Therefore, a solution is prepared with nanoparticles, the object to be equipped is dipped into it, and retrieved. The concentration of nanoparticles is chosen in such a way, that the density and distribution on the surface of the object is well suited for the intended experiment.

Such an object can be a tapered fiber. Tapered fibers are very thin fibers with a diameter down to 280 nm. They have very interesting optical properties and can be used for different applications such as sensing [94, 95] or single photon collection. This latter application was developed for diamond nanocrystals in the course of this thesis and is described in detail in Sec.5.3. A dip-coating technique was developed that allows for the controlled deposition of diamond nanocrystals on such tapered fibers.

3.4.1 Production of tapered fibers

Tapered fibers were fabricated from standard single-mode optical fibers (Thorlabs, 630HP). The fiber was heated using a ceramic heater to about 1330 °C where the glass material turns into a viscous phase. At the same time, two linear stages pull the fiber apart. The further the fiber is stretched, the thinner the tapered region will be. The transition from the unprocessed fiber to the tapered region happens adiabatically, power losses of transmitted light only accumulate to a few percent as Tab. 3.1 reveals. In the tapered region the light field is traveling partly outside of the fiber. The thinner the tapered fiber, the bigger the evanescent mode of the light. Details about the light modes of a tapered fiber and its production procedure can be found in [96].

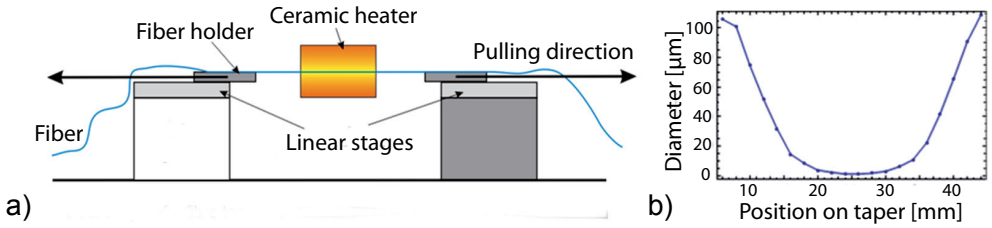

Figure 3.3: a) Schematic showing the tapered fiber production process. A stripped standard fiber is heated with a ceramic heater to approximately 1330 °C and stretched with two linear translation stages. b) Profile of the tapered region for an exemplary fiber with a minimum diameter of 800 nm.

For the experiment presented in Sec. 3.5.2 and 5.4.3, a tapered fiber with a diameter of around 900 nm was produced. For the experiment described in Sec. 5.3, diameters down to 273 nm were made. Such a taper is depicted in Fig. 3.4. Its diameter was measured with a scanning electron microscope (Keyence, VE9800).

During the stretching process the transmission of the fibers is monitored. Only fibers with a transmission higher than 0.9 are used for further experiments. The tapered fibers can be stored in a dust-free environment (class 10 cleanroom) to minimize degradation of their transmittance [97] until taken into use.

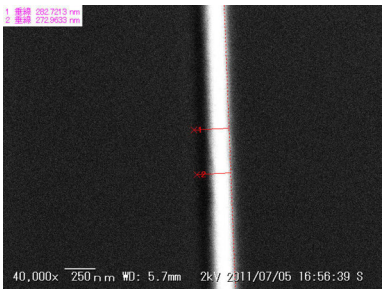

Figure 3.4: Scanning electron microscope picture of a tapered fiber with a diameter of only 273 nm.

3.4.2 Dip-coating procedure

To maximize the control during the dip-coating procedure, only a small droplet of solution is exposed to the tapered fiber. Therefore, a glass rod with a diameter of about 1 mm is used as droplet holder. The concentration of diamond nanocrystals in the aqueous solution is chosen 10 to 1000 times thinner than for spin-coating. By thinning out the concentration the deposition of crystals on the tapered region is well controllable.

For optical control of the deposition a 640 nm laser is coupled into one fiber end. At a power of about 1 mW the scattered laser light is visible at the position of the tapered region, even if no scatterers are present. This is visible in the photographic image in Fig. 3.5 I). The scattering is induced by small inhomogeneities of the glass.

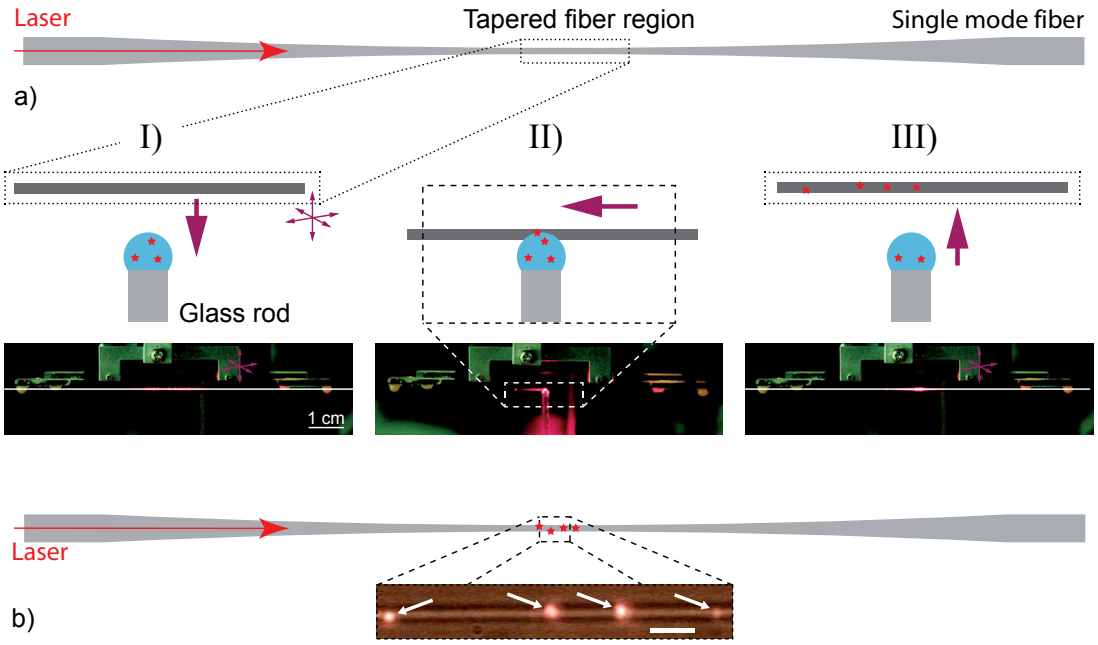

Figure 3.5: a) Schematic of a bare tapered fiber. I) - III) illustrates the dip coating procedure. The tapered fiber is dipped into a small droplet of an aqueous diamond nanocrystal solution. By moving the tapered fiber via a linear stage along the fiber axis through the droplet, diamond nanocrystals are deposited. This deposition can be controlled by the laser scattering signal of the deposited nanoparticles and allows for controlling the deposition of an approximate number of scatterers. The photographic images were taken corresponding to the process step. b) Schematic of a tapered fiber equipped with diamond nanpcrystals. The photographic image is a microscope picture of a tapered fiber section with four scatterers indicated by the white arrows. The laser is guided through the fiber and scattered by the deposited particles. The scale bar is 5 µm.

The dip-coating procedure is described in the following, it is illustrated in Fig. 3.5 I-III).

I) **Immersion of the tapered fiber into the diamond solution**. The fiber holder is installed upside down in a 3d-translation-stage as can be seen in the photographic images. The position of the fiber is indicated with a white dashed line.

II) **Deposition of nanocrystals on the tapered fiber** by translation along its axis when immersed in the diamond solution. The photographic image in II) shows how the laser is scattered into the droplet after passing the scatterers.

III) **Retrieval of the taper from the droplet.** The photographic image shows how the deposited crystals scatter a small part of the laser light.

During the procedure the light scattered off the deposited particles was monitored. In this way it was possible to estimate the number of deposited particles as can be seen in the image taken with a conventional CCD camera in Fig. 3.5 b).

	# of scatterers	Transmission
Bare tapered fiber	-	91%
First deposition cycle	16	87%
Second deposition cycle	9	86%

Table 3.1: Transmission properties of a tapered fiber that was iteratively equipped with diamond nanocrystals with a size range of 10 nm to 100 nm. The fiber was placed inside a microscope and the scatterers were visualized on a CCD camera. At the same time the transmission of a 640 nm laser was measured. About 1 mW laser light was coupled to the fiber. The transmission of the bare tapered fiber was measured relative to the unprocessed fiber transmission.

By in-situ measuring the transmission of the fiber, overall scattering losses were evaluated. An example is given in Table 3.1. For example, controlled deposition of 16 scatterers on a tapered fiber with a diameter of about 360 nm was performed. The fiber transmission loss was only 4 %, a typical value for all examined tapered fibers. In a second deposition run, only 9 additional scatterers were deposited, leading to an additional transmission loss of only 1 %.

These results prove, that the developed deposition technique is well suited for the controlled equipment of ultra-thin tapered fibers with diamond crystals for optical experiments.

3.5 Hybrid bottom-up assembly: Nano- and microparticle pick-and-place techniques

The importance of controlled integration and coupling of pre-selected optical constituents such as single quantum emitters to photonic, resonant and plasmonic structures was discussed in detail in Chapter 1.

Generally speaking, the controlled positioning of a nanoparticle can be realized with any mechanical system that allows the pick-up of such a nanoparticle, the nanometer precise position control and the subsequent deposition of the particle. However, it is obvious that with decreasing particle size such mechanical pick-and-place manipulation gets more challenging.

In the following chapters, three different manipulation techniques will be described. They allow control of the position of functionalized nanoparticles, e.g. fluorescent nanoparticles, and thereby their integration into micro- and nanometer sized structures.

3.5.1 Pick-up by functionalized fiber tip

A scanning near-field optical microscope (SNOM) allows nanometer precise positioning of a micro- to nanometer sized probe [98, 99]. Direct SNOM manipulation of a nanoparticle is difficult due to the fragility of glass fiber tips as probes. Yet, it has been shown, that microparticles like microspheres can be manipulated [100] and picked up with the SNOM probe. This functionalized SNOM probe can thrn be used to pick up nanoparticles, e.g. diamond nanocrystals, by attaching them to the sphere. The sphere - diamond system can then be deposited at a determined position. As is described in the following section, neither the tip, nor the sphere or the diamond nanocrystals have to be surface-functionalized.

The scanning near-field optical microscope

The SNOM setup used for the manipulation of microspheres was home-built in the course of an earlier diploma thesis [101]. For example, it was used to examine and control the backscattering induced coupling between counterpropagating high-Q modes of a microsphere resonator [102].

Tapered optical fiber tips are used as near-field probes. The tips are produced with a micro pipette puller (P-2000, Sutter Instrument, USA). They have a rather strong taper inclinement of a few millimeters (see Fig. 3.6 b)) in contrast to the tapered fibers presented in Sec. 3.4.1. The supporting fibers are inserted into a micropipette and either glued to it or fused with a CO_2 laser. The pipette is inserted into a segmented piezo tube (Staveley Sensors 2, EBL Products Inc., USA) [101]. It is coupled to the piezo with the help of a highly viscous oil (Oppanol B3, BASF, Germany). The piezo consists of three segments, a supporting element, an excitation segment which drives the oscillation and a response element which measures the response of the system. Typical eigenfrequencies of the implemented fiber tips span from 20 kHz to 70 kHz. The oscillation amplitude is set to about 80 % of the maximum at resonance. This allows installation of a feedback loop that is sensitive to the environment in the front of the tip [103]. When approched to a surface the oscillation amplitude is damped due to induced shear forces from van der Waals forces and surface water adsorption. The

position of the fiber tip relative to the sample surface and the focus position in the inverted microscope (see Sec. 4.1.2) is controlled by a 3-d manual translation stage (MDE 260 Series, Elliot Scientific Ltd., England) for coarse adjustment and a 3-d piezo system (MINITRITOR, Piezosystems Jena, Germany) for fine adjustment.

The main purpose of a SNOM, the capture of an optical nearfield signal, is not featured in the manipulation scheme as it is only used for controlled positioning of microspheres. Yet, although its optical functionality is not directly necessary for the manipulation, it can be used for straightforward alignment of the probe relative to the substrate and the focus of the laser. Therefore, light is coupled into the back facet of the fiber. The light exiting the SNOM tip is imaged onto a CCD camera and can be overlapped with the reflection of the laser focus from the cover slip. Its Airy pattern indicates the distance from the tip to the surface. For the final approach of the tip to the surface either the feedback modus is used or the tip is simply moved manually with the z-piezo while monitoring the SNOM signal.

Functionalizing the SNOM tip

In order to pick up nanoparticles with the SNOM, the fiber tip has to be functionalized. Therefore, a single microsphere is attached to it. Such a polystyrene (PS) microsphere (MicroParticles, Germany) has an average diameter of 5 µm. They are prepared in a suitable isopropanol solution and drop-casted on a cover slip that was previously equipped with diamond nanocrystals (see Sec. 3.3).

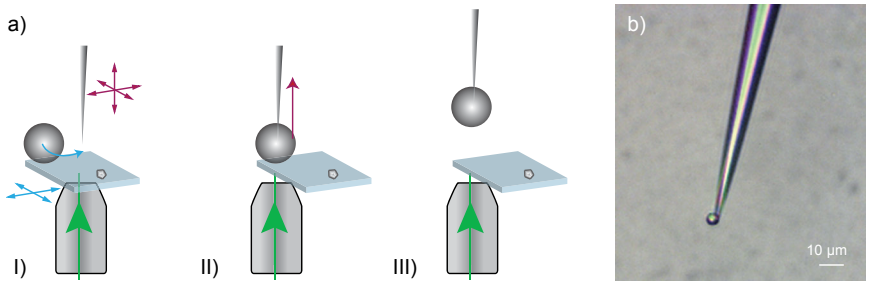

Figure 3.6: a) Procedure of functionalizing a SNOM tip. I) Positioning the tip a few µm above the cover slip and bringing a sphere into contact. II) Retracting the sphere-functionalized tip. III) Elevated sphere-tip position for pre-selection of a quantum emitter. Blue arrows indicate translation of the cover slip. Dark red arrows indicate translation of the SNOM tip. b) Functionalized SNOM tip taken with a scanning electron microscope. The sphere diameter is about 1.8 µm.

The whole functionalization procedure is sketched in Fig. 3.6 a). First, the tip is

moved to a position where it can touch the PS sphere physically. In the case of the 5 µm-spheres used here, the tip - surface distance is 1 µm to 4.5 µm. Then, microspheres in the vicinity of the tip are located on the CCD camera image under white light illumination. The shadows of the spheres as well as the tip can be seen. A selected sphere is then brought into physical contact with the SNOM tip by moving the cover slip manually with the x-y-translation stage. The tip is successfully functionalized if the sphere can be lifted from the cover slip with retraction of the SNOM. In the case of an unsuccessful attempt the procedure needs to be repeated. A successful functionalization is depicted in Fig. 3.6 b) taken with a scanning electron microscope. The forces that attract the PS sphere to the SNOM tip are not theoretically described. The attraction is assumed to stem from van der Waals forces, electro-static forces and adhesion from surface adsorbed water or a combination of those.

Diamond nanocrystal pick-up routine with a functionalized SNOM

After funtionalization of the SNOM tip, the microsphere can be used to pick up diamond nanocrystals in a controlled manner. The whole procedure is done with the same equipment and sample. The sample used for attaching the microsphere to the SNOM tip was also equipped in a prior step with diamond nanocrystals containing single NV centers (25 nm average size, Microdiamant, Germany) via spincoating as described in Sec. 3.3.

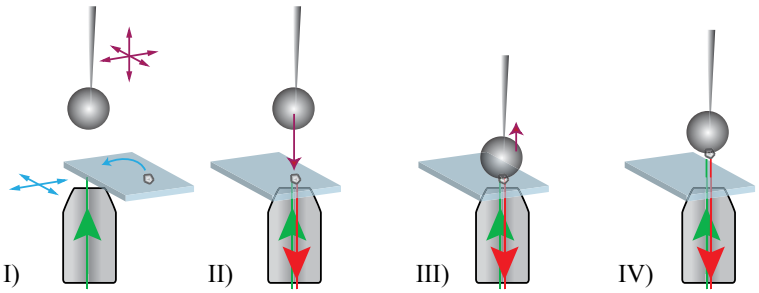

Figure 3.7: Procedure for picking up a diamond nanocrystal with a functionalized SNOM tip. I) A single NV is pre-selected. II) The diamond nanocrystal containing the NV is attached to the sphere. III) The diamond-sphere system is retracted from the surface. IV) Optical analysis of the sphere coupled NV. Blue arrows indicate translation of the cover slip. Dark red arrows indicate translation of the SNOM tip.

The pickup procedure is illustrated in Fig. 3.7 and is executed in the following manner.

I) **Pre-selection of a single NV** inside a diamond nanocrystal by scanning the cover slip manually or software driven. The NV emission is recorded with an EM-CCD camera.

II) **Attachment of a diamond nanocrystal** to the sphere-functionalized SNOM tip by lowering the sphere onto it. The position of the sphere relative to the NV can be tracked via the same EM-CCD camera and white light illumination. The intensity of the white light needs to be adjusted to the NV fluorescence intensity for simultaneous control. The height of the sphere is controlled via the oscillation amplitude of the SNOM which is minimized when a sphere has full contact to the glass surface.

III) **Retraction of the diamond - sphere system** by lifting the SNOM. A reduced optical signal indicates when the diamond - sphere system is lifted because the NV is moved out of the focus. In the case of unsuccessful pickup the procedure needs to be repeated.

IV) **Analysis of the optical properties of the picked-up NV** with the confocal microscope setup.

After a diamond containing a single defect center is attached to the sphere, a second one can be attached as shown in Sec. 5.4.2. This procedure could be repeated for additional diamonds.

Furthermore, the whole system can be deposited on a cover slip by detaching the SNOM tip from the microsphere. This deposition is possible and was realized. However, it has to be pointed out, that this deposition technique is not very precise and as deterministic as the approach presented in Sec. 3.5.3. Detachment of the diamond from the sphere is not practical as the polystyrene generally attracts the diamond more than the cover slip.

3.5.2 Tapered fiber pick-and-place

In 3.4 a dip-coating technique was introduced that allows equipment of tapered fibers with fluorescent diamond nanocrystals. Via this technique, a controlled number of nanocrystals can be deposited. Yet, to localize defect centers, a post-selection of these crystals needs to be performed, resulting in a contamination of the tapered region with unused diamonds.

To overcome this disadvantage a method will be described in this section that allows the pre-selection of a diamond nanocrystal and its subsequent pick-up by a tapered fiber. The single diamond crystal equipped taper is then applied to deposit the crystal on a toroidal microresonator (see Sec. 5.4.3). Besides this resonator, other geometries could also be equipped; such as sphere resonators [104] or fiber integrated resonators [105].

Preparation of equipment

The main element of the envisioned procedure is a tapered fiber with a diameter of about 900 nm that is used to pick up a fluorescent diamond nanocrystal and deposit it again. It is produced the same way as described in Sec. 3.4.1. During the production only the pulling distance was adjusted to confect diameters of about 900 nm that are well suited to perform the pick-and-place.

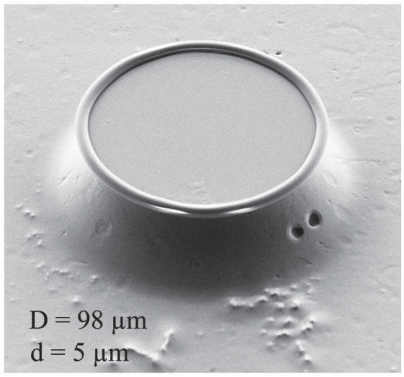

Figure 3.8: Scanning electron microscope picture of a toroidal microresonator. Such resonators were home-fabricated as described in [106]. D and d represent the outer diameter of the toroid and the diameter of the tube of the toroid, respectively.

In contrast to the pick-and-place procedures described in Sec. 3.5.1 and Sec. 3.5.3 not a cover slip but a standard fiber is used as a reservoir for the diamonds. It is easily accessible with the tapered fiber. Therefore, a fiber with a diameter of 125 µm is stripped and cleaned in an ultrasonic bath of alkaline detergent. Then it is dip-coated with diamond nanocrystals with an average size of 100 nm.

The toroidal microresonators were produced as described in [106]. A scanning electron microscope image is depicted in Fig. 3.8. An optical analysis of such a resonator is presented in Sec. 5.4.3.

Pick-and-place procedure

The procedure is illustrated in Fig. 3.9 in form of a sketch as well as corresponding CCD camera images. It is carried out in the following steps.

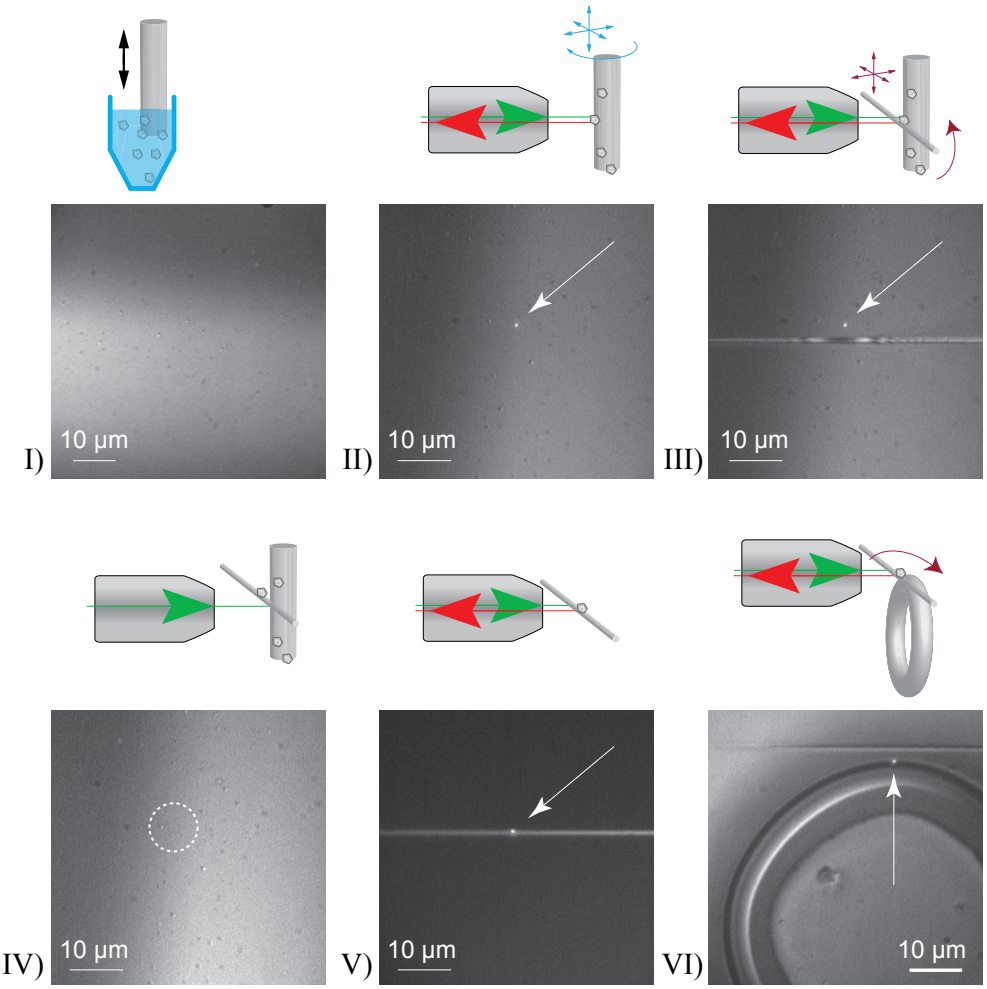

Figure 3.9: Illustration of the fiber pick-and-place procedure. I) Dip-coating of stripped standard fiber in diamond solution. II) Identification of fluorescent nanocrystal. III) Pick-up of crystal with tapered fiber. IV) Former position of the picked-up crystal indicated by the the dashed circle. V) Fluorescent crystal on tapered fiber. VI) Crystal deposited on toroidal resonator. The white arrows illustrate the position of the fluorescent nanocrystal. Details are described in the text.

I) **Equipment of a standard fiber with diamond crystals** by dip-coating it in a diamond solution. The concentration of the solution has to be chosen in such

a way that the density of deposited diamonds is adequate to distinguish them individually.

II) **Pre-selection of a fluorescent nanocrystal** on the surface of the fiber via a confocal microscope (see Sec. 4.1) with 532 nm laser excitation. The dip-coated diamonds can also be visualized on a CCD camera via red LED illumination. The fiber can be translated and rotated. The arrow indicates the position of the diamond.

III) **Pick-up of the pre-selected diamond** by sliding the tapered fiber along its position. The arrow indicates the position of the diamond.

IV) **Control of the pick-up process.** If the diamond was picked up by the tapered fiber, it can not be found at its old position. This can be confirmed either via its diminished fluorescence or a simple CCD camera image check. The dashed circle indicates the missing crystal. If this step is not successful, step III needs to be repeated.

V) **Verification of diamond to taper attachment and transfer to the toroidal resonator.** In case of a successful deposition on the taper, a fluorescence signal from the diamond is measured. The diamond equipped taper can now be transferred to the toroid. The arrow indicates the position of the diamond.

VI) **Deposition of the diamond on the toroidal resonator.** Therefore, the diamond equipped position of the tapered fiber is sled over the equator of the toroid until it can be identified on the toroid. The arrow indicates the position of the diamond.

This deposition technique is expandable to more than one diamond nanocrystal. By repetition of the procedure, an arbitrary number of crystals could be deposited on the toroid, e.g. to couple them to the same optical resonator mode. Such a coupling was realized with micro-sphere resonators in another experiment in the course of this thesis (see Sec. 5.4.2).

The assembled diamond - resonator system was optically analyzed. The results are presented in Sec. 5.4.3.

3.5.3 Pick-and-place with atomic force microscope

The methods presented so far allow integration and coupling of diamond nanocrystals. However, they are limited in their applicability and feasibility. In this section, a more potent pick-and-place technique is introduced that allows pre-selection and nanometer precise pick-and-place on various substrates with complex structures.

Experimental pre-requisite and pre-characterization of diamond nanocrystals

Prior to the pick-and-place procedure, a sample has to be prepared which serves as a reservoir for quantum emitters like defect centers in diamond nanocrystals. A spin-coating process was applied to an aqueous solution with 0.02% polyvinyl alcohol and diamond nanocrystals that were centrifuged cleaned (Microdiamant, Germany) as described in Sec. 3.1. The concentration of the solution is chosen in such a way that the density of nanocrystals on the substrate is sufficiently low to identify a single diamond nanoparticle unambiguously. From such a sample a single fluorescent NV^- center is pre-selected in the inverted microscope with spectrometer and HBT setup (see Sec. 4).

Tip specification

The applied AFM cantilevers should have the following parameters. The cantilever should have a radius of curvature small enough to resolve the surface structure and target particles. Yet, this radius should be as large as possible to decrease the possibility that the nanoparticle sticks to the side of the tip which will make its deposition impossible (see 3.5.3). Furthermore the cantilever material is important. It should not be brittle to avoid breaking of the tip when pressed down with high forces of up to 1 µN. The material also determines the adhesion to the target nanoparticle. For pick-and-place of diamond nanocrystals, metal coated silicon tips (Au or Pt/Ti coated cantilevers, MicroMasch) were suited best. They have a radius of curvature of about 40 nm. It is also possible to deform them without breaking by pressing them on the substrate or on a diamond nanocrystal.

Pick-and-place procedure

The pick-and-place procedure is described in the following enumeration according to the illustration in Fig. 3.10 and was carried out with a commercial AFM (NanoWizard, JPK, Germany).

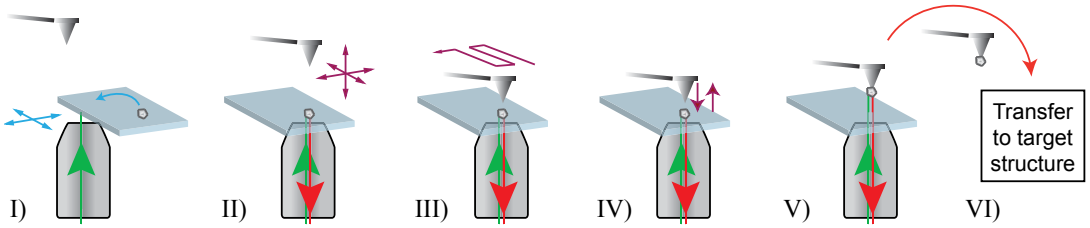

Figure 3.10: Procedure for picking up a diamond nanocrystal with an AFM. A detailed description of the individual steps is given in the text. Sub-process steps of IV) are illustrated in Fig. 3.11 a). Blue arrows indicate translation of the cover slip. Dark red arrows indicate translation of the AFM tip.

I) **Pre-selection of a single NV** inside a diamond nanocrystal by scanning the cover slip relative to the laser focus.

II) **Alignment of the AFM tip** centered over the laser focus with the help of a CCD camera. The pre-selected NV is kept in the focus.

III) **AFM surface scan** in intermittent contact mode to locate the diamond's position relative to the AFM tip. Subsequently, the tip is placed above the diamond crystal.

IV) **Attachment of the diamond** to the tip by pressing the tip onto the center of the nanocrystal. A force of up to 1 μN is used, sufficient to attach the nanocrystal to the tip by surface adhesion. Simultaneously the optical signal is monitored. The optical signal consists of constant fluorescence from the NV and from fluorescence of the AFM tip which depends on the position of the tip relative to the focus. This monitored optical signal will increase when the tip is in contact with the diamond. This is illustrated in 3.11 a). For suppression of the excitation laser a longpass filter ($\lambda = 590$ nm) and for suppression of the infrared AFM laser a shortpass filter ($\lambda = 740$ nm) were used.

V) **Pick-up of the diamond** if the optical signal decreases as sketched in 3.11 a). The signal decreases when the diamond is removed from the laser focus. To double-check that the diamond was truly removed and not only pushed out of the focus, a surface scan in intermittent contact mode can be performed. During this scan the nanocrystal is not removed from the tip if there are no sharp edges on the substrate. If the diamond was not picked up, IV) and V) are repeated.

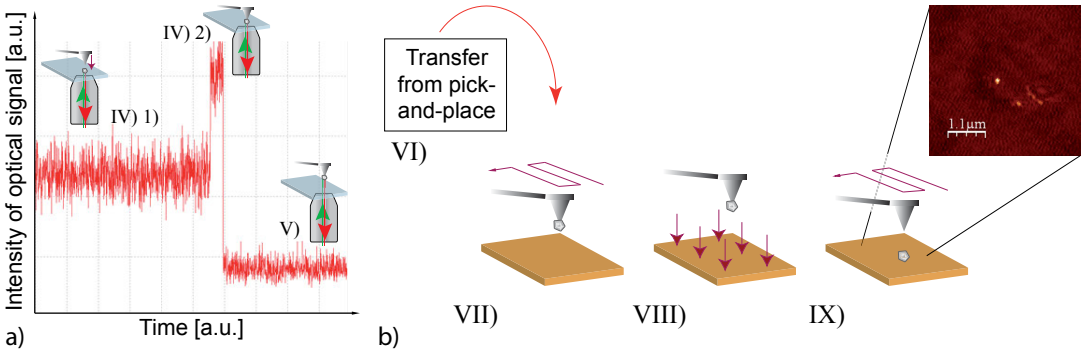

Figure 3.11: a) Monitored optical signal when the AFM tip is pressed onto the diamond. The signal in IV) 1) stems from diamond fluorescence and background light only. If the tip is pressed on the diamond (at the same time it is inserted in the focus) the fluorescence of the tip contributes to the signal in IV) 2). If the diamond is attached to the tip and removed from the focus, the signal intensity will drop to background level as in V). b) Procedure of placing the diamond on a target structure. Details of each step are described in Sec. 3.5.3. Blue arrows indicate translation of the cover slip. Dark red arrows indicate translation of the AFM tip. The inset on the right side is an image of an AFM surface scan of a deposited diamond on the facet of an optical fiber (see Sec. 5.2).

VI) **Transfer of the diamond nanocrystal** to a new sample. Either the AFM head is moved to a second sample holder or the sample is simply exchanged.

The described pick-up procedure for diamond nanocrystals was always successful, but might take many repetitions. Sometimes over 50 iterations were necessary. After successful pick-up and transfer of the diamond, it has to be deposited in the target region. Many targets are not optically transparent and suited to be implemented in the inverted microscope. This inhibits optical control during the deposition procedure which is described in the following.

VII) **Selection of a target area** on the target sample. To be able to unambiguously identify the deposited nanocrystal, a small area on the target of about 100 nm x 100 nm without parasitic nanoparticles has to be scanned in intermittent contact mode. The structure of the target area should not have sharp edges to prevent loosing the nanocrystal. Scanning on a flat surface has shown to be uncritical towards loosing the crystal.

VIII) **Placement of the diamond nanocrystal** by pressing the AFM tip onto the target surface in contact mode. A force of up to 1 µN is applied. Various attempts

can be made on different positions in the pre-scanned target area to increase the deposition success probability before the next step is performed.

IX) **Surface scan** of the target area in intermittent contact mode to verify the successful deposition of the diamond. If the crystal does not appear in the AFM scan, the previous step needs to be repeated.

The deposition of a diamond nanocrystal was only successful in about 30 % of the attempts. During the pick-up or the deposition procedure the nanocrystal can get stuck to the side of the tip from where it can not be removed anymore. If this occurs, the pick-and-place procedure needs to be started again from the first step. To assure that the old particle is not confused with a new diamond the tip needs to be exchanged.

It should be pointed out that the described procedure is a statistical process. If no chemical or physical treatment is applied, a nanoparticle will have a chance to either stick to the tip or to the surface. This accounts for both the pick-up and the deposition process. Therefore this procedure is in principle not limited to diamond nanocrystals.

Two step pick-and-place procedure

In the case of a structured target like a photonic crystal fiber (PCF, see Sec. 5.2), a suspended core fiber (Fig. 3.12 a) and c)) or a photonic crystal cavity [8] an intermediate step before deposition at the final target position has to be performed in order not to loose the diamond crystal at sharp edges. At such edges, it has a high possibility to get lost even for a surface scan in intermittent contact mode. Therefore, the target area, in the case of a PCF, the core region, can not be determined via an AFM scan without risking loss of the diamond.

To avoid this risk, first a position away from the structured area has to be targeted and the crystal has to be temporally stored here. The distance of the storage position to the final position needs to be within the scanning range of the AFM (100 µm for the NanoWizard). In this area the deposition procedure as described in VII) and following has to be performed in order to use a bare tip for scanning. Secondly, after the crystal has been deposited for temporal storage, a joined surface scan of the diamond position and the final target position is carried out with the bare tip to determine the target position precisely without risk. Finally, the entire pick-and-place procedure as described above is repeated for the final position.

The described pick-and-place procedure was applied to a variety of optical fibers

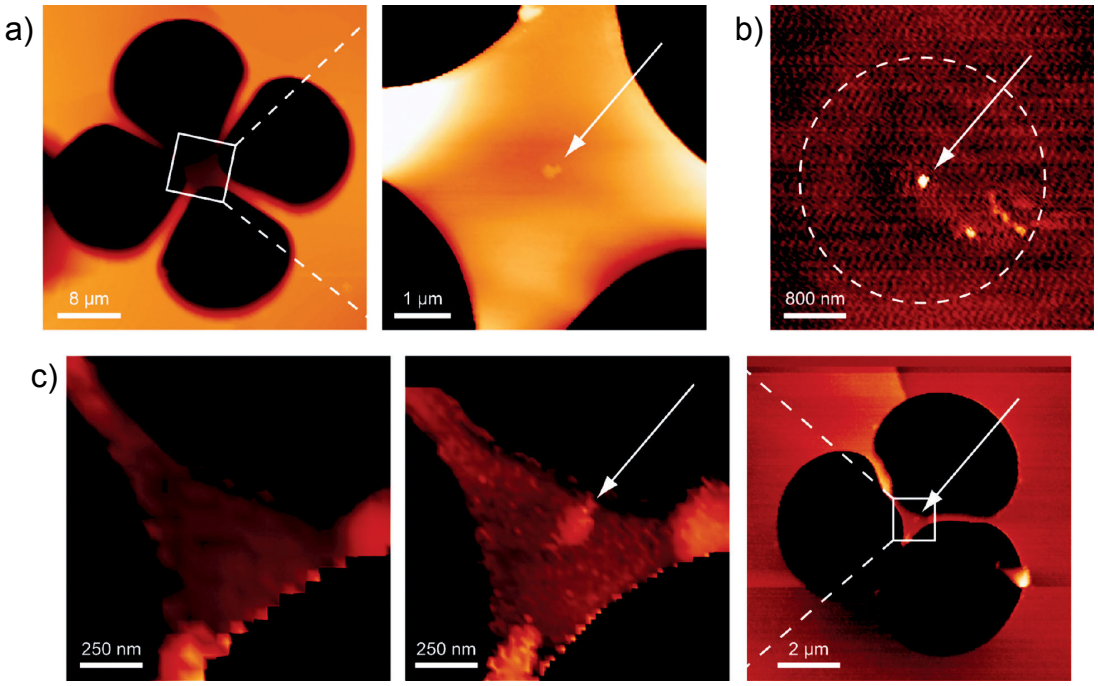

Figure 3.12: A variety of optical fibers was equipped with single diamond nanocrystals placed in the fiber core to show the potential of the pick-and-place technique. The images show atomic force microscope surface scans of these fiber facets. The arrows indicate the position of the diamond. The white boxes indicate a zoom in on details. A cloverleaf shaped suspended core fiber is shown in a) before and after placing of the diamond. In b) a step index fiber is displayed. The dashed circle indicates the core position, which is not clearly visible in the topography image. A suspended core fiber with wagon wheel design is depicted in c), before and after placing of the diamond nanocrystal.

with different glass compositions and designs (Fig. 3.12). Its high positioning precision is a crucial requirement as the cores of these fibers have dimensions down to diameters of 605 nm (Fig. 3.12 c). This proves the broad suitability of the presented manipulation technique which is also not limited to optical fibers but can be applied to photonic crystal cavities [8] and plasmonic structures [107]. Furthermore, it can be carried out at ambient conditions.

Similar manipulation techniques have been published [79, 108] . Although they also allow the nanometer precise positioning of diamond nanocrystals, operation can only be performed inside a scanning electron microscope. This makes their application more complex and limits it to systems that survive vacuum environments and electron beam bombardment. This is not only crucial for biological systems but also particularly for diamond NV^- defect centers as they can be irreversibly destroyed by electron impact.

3.6 Summary

In this chapter, deposition and integration techniques of diamond nanocrystals were introduced. In addition to well established methods, novel nano- and micro-manipulation techniques were developed. They are summarized in the following. Their advantages and disadvantages, limitations and potentials are shown in Table 3.2. For deposition of

Deposition method	Exp. demand	Time consumpt.	Precision	SE	Pre-sel.
Drop-casting	low	1 hour	< 1 mm	-	-
Spin-coating	low	1 hour	> 1 mm	-	-
Dip-coating	low	> 1 hour	100 µm	(✓)	-
SNOM	high	1 day	1 µm	✓	✓
Taper	high	> 1 day	100 nm	✓	✓
AFM	high	> 1 day	1 nm	✓	✓

Table 3.2: Feasibility of different nanoparticle deposition and integration methods. The given values are estimations based on experience. Details are explained in the corresponding section of this chapter. Experimental demand (Exp. demand) represents technical prerequisite and required experience of the investigator. Time consumption (Time consumpt.) estimates the time to perform one deposition cycle. Precision represents the accuracy of deposition. Deposition of single emitters (SE) as well as pre-selection (Pre-sel.) is possible in the case of a check mark.

nanoparticles on tapered fibers with diameters down to 273 nm, a dip-coating technique was developed. The developed deposition technique is well suited for the controlled equipment of ultra-thin tapered fibers with a deterministic number of diamond crystals for optical experiments.

It was shown, that a sphere-functionalized SNOM probe can be used to pick up nanoparticles, e.g. diamond nanocrystals, by attaching them to the sphere. The sphere - diamond system can then be deposited at a determined position.

A method was introduced that allows the pre-selection of a diamond nanocrystal and its subsequent pick-up by a tapered fiber. The single diamond crystal equipped taper can then be used to deposit the diamond crystal, for example on a toroidal microresonator or other geometries, such as sphere resonators or fiber integrated resonators.

A versatile method based on an atomic force microscope to pick-and-place diamond nanocrystals with nanometer precision was introduced. The method enables positioning of pre-selected particles on a variety of structures. It can be used at ambient environments in contrast to manipulation inside a scanning electron microscope.

4 Experimental equipment for optical investigations and analysis of data

The investigated quantum systems emit by definition (as single photon emitters in most cases) very low amounts of energy. For example, for a photon rate of 10^6 photons/s with a wavelength of $\lambda = 637\,\text{nm}$ the energy is only $0.3\,\text{pW}$. Hence, care has to be taken to efficiently *collect* and *detect* these little amounts of energy. For photon collection, new concepts have been developed and standard concepts have been advanced.

In this chapter, the applied detection schemes and devices are introduced. For the detection, highly sensitive, commercially available detectors were used with quantum efficiencies (QE) of up to 0.7. Sections 4.1 and 4.2 give a brief introduction to standard experimental methods that were applied during the coarse of this thesis. The described technical equipment can vary for the different experiments performed, but the conceptual idea of the setup does not change. In Sec. 4.3 transmission and reflection efficiencies of the applied optical components are listed. A standard cryostat system for low temperature experiments was expanded for a highly increased collection efficiency. It is described in Sec. 4.4.

4.1 Confocal microscopy

Confocal microscopy is an experimental method to increase the resolution and the signal to noise ratio for the analysis of optical samples compared to simple microscopy [109]. It is a well established method in all scientific fields where optical microscopes are used [110]. It was applied to single defect centers in diamond for the first time in 1997 [111].

A beam splitter (BS) is used to separate the excitation path from the detection path and superimpose both in such a way that they will share a focal volume. Thereby, the point like laser source is imaged onto the sample and the fluorescence of the sample stemming from this point is imaged onto a pinhole. The confocal setup is illustrated in Fig. 4.1. As indicated in the figure, only light stemming from a small

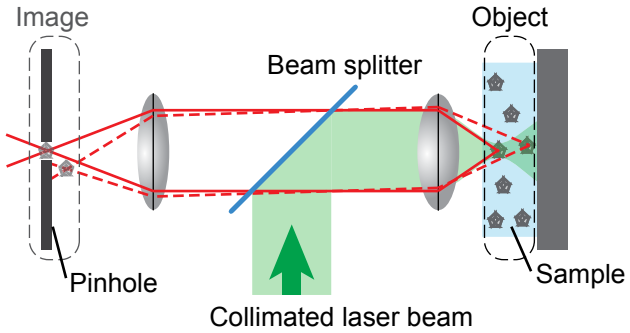

Figure 4.1: Sketch of a confocal microscope. This sketch illustrates how spatial filtering can improve the signal to noise ratio of a quantum emitter. The quantum emitter, e.g. an NV defect center, is excited with a focussed laser beam. Its fluorescence is imaged onto the pinhole. Fluorescence not stemming from within the confocal volume is imaged besides the pinhole and can not pass this spatial barrier.

focus volume can pass the pinhole. Thereby, all residual background light is spatially filtered. Furthermore, also the resolution of the microscope is enhanced. Details can be found in [109]. For the experiments carried out in the course of this thesis, the resulting background reduction is the most important feature of a confocal microscope. It facilitates a high signal to background ratio and hence allows optical analysis of very low single photon rates. For the separation of excitation light and fluorescent signal, different BS were applied. These were either intensity BSs (50:50; 90:10; 92:8) or dichroic BSs adapted to the excitation wavelength. If not stated otherwise, a 90:10 BS was used.

The confocal microscope was integrated into the table-top setup as illustrated in Fig. 4.2. The sketch represents a typical configuration but was also used in a modified arrangement.

4.1.1 Laser scanning technique

To scan a sample and a focussed laser beam relative to each other, either the sample can be moved or the focus of the laser. For some of the experiments, as pointed out in the particular section, the sample was moved with a piezo x-y-translation stage (MIPOS 3, Piezosystems Jena, Germany) that has nanometer resolution and allows faster and wider scanning than focus scanning. However, it cannot be integrated into a cryogenic setup. Therefore, a laser scanner was used that achieves a scanning range of roughly 25 µm x 25 µm. In both cases z-control was realized with an objective translation piezo (MIPOS 100, Piezosystems Jena, Germany).

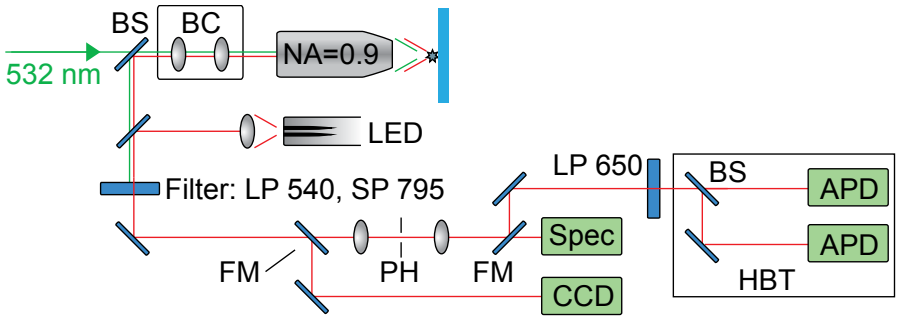

Figure 4.2: Sketch of the experimental setup. BC stands for beam control, FM for flip mirror, PH for pinhole, CCD for charged coupled device camera, Spec for spectrometer, LP for long pass filter, SP for short pass filter, BS for beam splitter, APD for avalanche photo diode and HBT for Hanbury Brown and Twiss setup.

The laser scanner was realized by introducing a pair of bi-convex lenses with a focal length of 150 mm into the optical path towards the sample as illustrated in Fig. 4.2. They are positioned in such a way, that their focal planes superimpose and that the direction of a collimated laser beam is not changed. The focus of the collimated beam of the first lens is imaged onto the sample via the second lens and the objective lens in front of the sample. The lateral position of the focus of the first lens can be controlled with two linear step motors (Mercury, Physik Instrumente, Germany). By shifting the position of the focal spot of the first lens, its image on the sample is also shifted. The ratio of the shift of the focus to the shift of the lens is determined by the ratio of the focal length of the collimating second lens to the objective lens. For an objective with 2 mm focal length it is 75. This high ratio allows nanometer precise control of the lateral position of the focus even with less precise linear translation stages like the applied step motors. Shifting distances of 25 µm on the sample were achieved for an objective with NA = 0.9.

4.1.2 Inverted confocal microscope

The arrangement of the confocal microscope sketched in Fig. 4.2 can also be modified to be used in combination with an atomic force microscope (AFM) or a scanning near-field optical microscope (SNOM). The potentials of such an inverted microscope were already discussed in Chapter 3. It allows investigation or manipulation of nanometer sized particles with an AFM or a SNOM at the same time as optical investigations via the objective are performed. The sketch in Fig. 4.3 of an inverted microscope illustrates how the objective lens is aligned vertically. A sample can therefore be placed horizontally

above it and is accessible with AFM or SNOM.

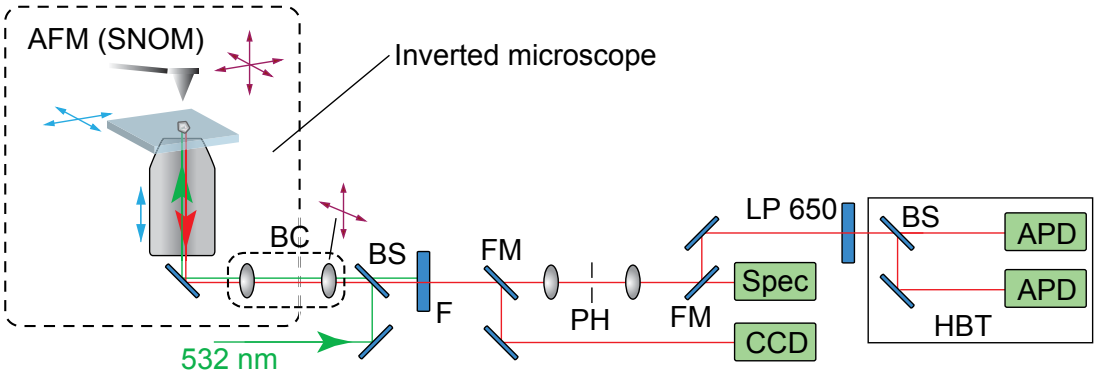

Figure 4.3: Sketch of an inverted microscope (dashed line) and the table-top integration of the detection scheme and devices. Either an atomic force microscope (AFM) or a scanning near-field optical microscope (SNOM) can be integrated into the setup as already introduced in Sec. 3. F stands for filter, FM for flip mirror, PH for pinhole, CCD for charged coupled device camera, Spec for spectrometer, LP for long pass filter, BS for beam splitter, APD for avalanche photo diode and HBT for Hanbury Brown and Twiss setup. The beam control (BC) is realized via two 150 mm lenses. As indicated, one of the lenses can be translated in x-y-direction. For more details refer to text.

4.2 Equipment for analysis of fluorescent systems

The experimental evaluation of the investigated and realized systems was mainly based on their optical analysis. Therefore, a short listing of the most important devices is given in the following. How the devices are integrated into the table-top setup is sketched in Fig. 4.3.

4.2.1 Visual analysis

For imaging sample surfaces and aligning samples, a CCD camera was used. For the sensitive analysis of the fluorescent light of single defect centers, also an electron multiplying CCD (EMCCD) camera (iXon, Andor, USA) was applied. It allows visualization of sample structures at the same time as single emitters are investigated. It is sensitive down photon count rates of a few thousand.

4.2.2 Spectral analysis

For the spectral analysis, single grating spectrometers (Acton 2500i, Princeton Instruments, and SpectraPro 500i, Roper Scientific, USA) were used. Via the grating, the incoming light is diffracted into its different spectral components in a Czerny-Turner layout [112]. The spectral components are imaged onto a CCD camera chip. Its pixels are assigned to calibrated wavelengths. The spectrometer can be operated with three different gratings with 600, 1200, and 1800 grooves per mm (grooves/mm) and blaze wavelengths of 1000 nm, 750 nm, and 500 nm, respectively. For the grating with 1800 grooves/mm a spectral resolution of 0.05 nm can be achieved for a wavelength of 435 nm and an entrance slit opening of 10 µm. Depending on the wavelength blaze of the grating, a spectral range from 330 nm to 1800 nm can be covered. Yet, for wavelengths exceeding 900 nm, an infrared CCD camera needs to be installed. The integration time of the spectra is determined by the integrated CCD camera. Depending on the amount of light sent into the spectrometer, integration times ranging from 30 ms to 600 s were applied.

4.2.3 Single photon detection

For single photon detection, avalanche photodiode (APD) modules were used. Most experiments were realized with SPCM-AQR-14 APDs (PerkinElmer, USA) with dark count rates around 80 cts/s, usually much smaller than signal count rates. These APDs have a maximum quantum efficiency (QE) of about 70 % at 700 nm, dead times smaller than 65 ns and an after-pulsing probability smaller than 1 %. The active region is bigger than 170 µm in diameter.

4.2.4 Time correlation measurements

Time-resolved measurements are an important technique to understand more of the optical and electronic properties of the investigated quantum emitters and systems. To realize such measurements, time resolved event counting and correlation devices were applied (TimeHarp200, and PicoHarp300, PicoQuant, Germany). These time-resolved measurements allow direct determination of various system properties. Furthermore, post-processing schemes can be applied.

To measure the fluorescence lifetime, e.g. of the excited state, of a system, pulsed excitation of the system is applied. The time difference of detected photon events to the laser pulses is determined with a correlation device. These time differences are then

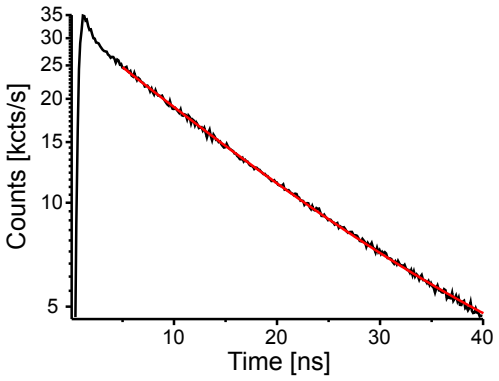

Figure 4.4: Lifetime measurement of a single NV^- defect center on a substrate with a refractive index of n = 2.17. Its fluorescent lifetime was determined to 17.2 ns via a single exponential fit (red line). The plot also indicates a small fraction of fluorescence with much shorter lifetimes of 1 to 2 ns.

written into a time-event histogram and the lifetime can be determined. An example of such a lifetime measurement is shown in Fig. 4.4.

Time-resolved measurements can also be used to record the second order auto-correlation function. This is an important function to determine the quantum nature of the detected light and estimate the number of emitters that contribute photons to the light pulse. For single photon emitters, subsequent events have time differences greater than zero (for more details see Sec. 2.1). The applied photon detectors have dead times (about 50 ns) greater than the lifetime of the investigated emitters of around 20 ns. This prevents detection of subsequent events. One way to overcome this technical limitation is the application of detectors with dead times much smaller than the fluorescent lifetimes of the emitters. This has been shown very recently for the first time [22] via the application of superconducting detectors [113]. A more established scheme was applied for the measurements during this thesis. It is the detection of a pulse train of photons in a Hanbury Brown and Twiss (HBT) setup [21], see Fig. 4.5. The time difference between subsequent photon events can be measured by sending the detection signals of both APDs to a time-correlator. The most direct way to determine the time difference of subsequent events is to use a start (events on APD 1 send to channel 1) and stop (events from APD 2 send to channel 2) scheme. In this scheme, the time difference can be directly measured and written into a time-event histogram. Yet, the second order auto-correlation function is not exactly derived directly. Some considerations about the probability for correlation events with $\tau \to \infty$ need to be made. Details are discussed in App. A.

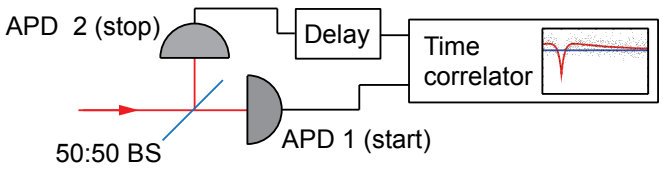

Figure 4.5: Sketch of a HBT setup. The photon pulse is split up into two arms and detected by two APDs. The detection events are sent to a time-correlator or event timer. In case of a start and stop scheme (see text for more details), a time delay device is inserted into the signal channel from APD to time-correlator, in the simplest case an elongated signal cable of about 30 m. BS stands for beam splitter, APD for avalanche photo diode.

To circumvent the dead times of the APDs and to not only measure events with positive time difference to each other but also a negative one, a time delay device can be inserted into the stop channel. Such correlation detection schemes can be used for lifetimes down to the time resolution of about 800 ps of the used APDs and time-correlators.

An example for a post-processing scheme is the post-detection gating of the APDs inside a HBT setup for a pulsed single photon source as described in Sec. 5.2.5. Thereby, detection events not stemming from the quantum emitter but from fluorescent background can be excluded. In this scheme, the events from both APDs as well as the trigger event from the pulsed laser are measured relative to an absolute internal clock of the time-correlator (Time-Tagged Time-Resolved (TTTR) mode, PicoHarp300). This enables, e.g., discarding of events that occurred shortly (up to 3 ns) after the laser pulse and were most likely produced by fast decaying background fluorescence. This scheme was implemented with C++ and applied for the measurements described in Sec. 5.2.5.

4.3 Calculated collection efficiency of the experimental setup

Transmission and reflection efficiencies for a spectral regime around 680 nm of optical components are listed in Fig. 4.6. The data for the reflectivity and transmittance of the optical elements are taken from the specification sheets provided by the manufacturer. From the individual efficiencies, the overall photon collection efficiency of the used experimental setup can be estimated. Knowing this efficiency allows deduction of , e.g., collection efficiencies of assemble devices. For example, it can be used to determine the source collection efficiency of a single photon source system [114]. This was of particular interest for the solid immersion lens microscope as introduced in Sec. 6.2. The source efficiency is the ratio of photons collected by the first optical element in

	Transmission
SIL-air interface	0.86
Objectiv @680	0.85
Silver mirror	0.97
Lambda-viertel	0.90
Lens	0.97
BS 90:10	0.90
Dichroic BS	0.97
LP 532	0.95
LP 532	0.95
SP 795	0.90
BS 50:50	0.99
SP 800	0.95
APD QE @680	0.70

Figure 4.6: Calculation of the collection efficiency of the setup used for the experiment presented in Sec. 6. The values for the transmission of the individual optical elements were taken from the product specification sheets provided by the manufacturer. QE stands for quantum efficiency.

the setup to the totally emitted photons. It is a figure of merit for how well a single photon source system, in this case the NV defect center - solid immersion lens system directs the single photon emission to be collected by the first optical element, e.g. an objective lens. A high source collection efficiency is of importance for future single photon applications.

4.4 Low temperature setup

For the low temperature experiments carried out in the course of this thesis, a continuos flow cold finger cryostat (Type Microscope, Cryovac, Germany) was used. It was mainly operated with liquid Helium at temperatures from 4.2 K to 10 K. For some experiments, a temperature range from 4.2 K to 293 K was bridged by internal electrical heating to observe the change in behavior of quantum systems that are heated up or cooled.

In its original configuration, it is operated with an objective lens placed in front of the vacuum chamber window for optical access.

4.4.1 Original confocal cryostat setup

In its original configuration the cryostat was mounted with the vacuum window aligned horizontally as can be seen in the photographic image in Fig. 4.7. It was mounted

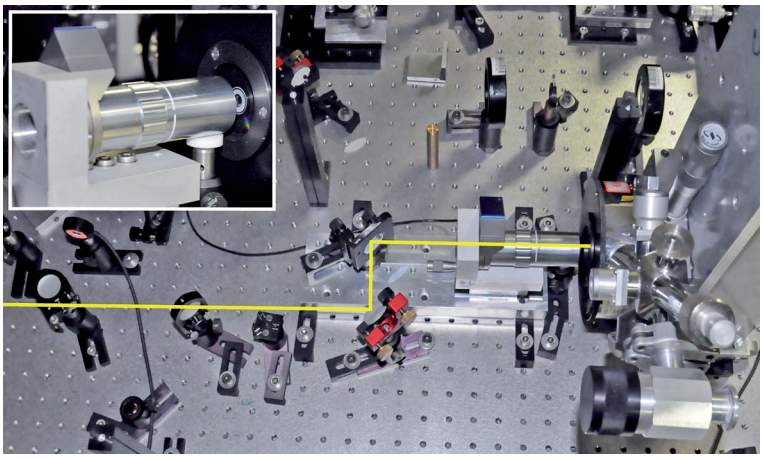

Figure 4.7: Photographic image of the optical access to the cryostat in a configuration where the objective lens is placed in front of the optical window of the vacuum chamber. The inset in the top left corner shows an objective with an NA of 0.7 and a working distance of 6 mm. The cryostat is mounted on two manual linear translation stages for lateral position control in x- and y-direction with about 0.5 µm position accuracy. By moving the cryostat, the sample is moved relative to the optical axis. The z-position of the focus is controlled via a coarse manual stage and a precise piezo z-axis lens positioner with 1 nm resolution (Mipos 100, Piezosystems Jena, Germany). The fine x-y-position control of the focus is realized via laser scanning (see Sec. 4.1.1).

on two linear stages for coarse x-y-control. Coarse and fine z-alignment were realized with a linear stage integrated with the objective, and an objective piezo (Mipos 100, Piezosystems Jena, Germany), respectively. The fine x-y-control was realized by a laser scanning system as introduced in Sec. 4.1.1.

For optical access a long distance objective with an NA of 0.7 was used (Mitutoyo, Japan). There are two major disadvantages of this configuration regarding an efficient excitation and collection. The first one is the limited NA. A higher NA can be implemented only under costs of a reduced working distance which is not allowed geometrically. The collection with an NA of 0.9 for example is much more efficient. The other disadvantage is the vacuum window that the light needs to pass, i.e. the laser on the way to the sample, and the single photons on their way towards the detection. This introduces further losses due to reflection. Also the focus quality and hence the collection efficiency is reduced. These losses were observed for measurements with and without a window under ambient conditions. They have a major impact and reduce the overall collection efficiency. These last difficulties could be partly overcome by a corrected objective. However, such an objective was not available and could only

increase the focus quality.

4.4.2 Highly efficient cryostat setup

To overcome the previously mentioned disadvantages, an advanced cryostat setup was developed. A photographic image is displayed in Fig. 4.8. This new configuration allows placement of an objective lens behind the window inside the isolation vacuum. Hence, the two major disadvantages discussed in the previous section can be surpassed. The focussed light is not refracted at the window and transmission losses were reduced.

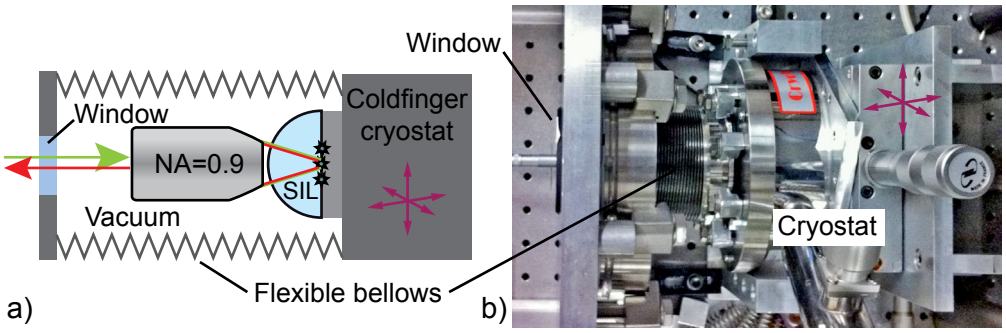

Figure 4.8: a) Sketch of the highly efficient cryostat setup. The vacuum is extended with a diaphragm bellows. The objective lens is placed inside the isolation vacuum of a cold finger cryostat. The cold finger holds the sample. The cryostat is mounted on three manual translation stages for coarse 3d-alignment. Fine x-y-alignment is carried out via a beam control. Fine z-alignment is performed via an objective lens piezo. b) Photographic image of the extended cryostat configuration where the objective lens is placed inside the vacuum chamber.

Furthermore, an objective with an NA of 0.9 was implemented in the cryostat (Type Microscope, Cryovac, Germany). This already improves the collection efficiency and resolution of the setup. However, most thrivingly, the solid immersion microscope (SIM) introduced in Chapter 6 can also be implemented inside the cryostat. In contrast to an oil immersion microscope such a SIM can be used at cryogenic temperatures. This allows the ultra-efficient collection even at liquid Helium temperatures and opens the way towards experiments that could not be realized before. Experimental results are presented in Sec. 7.2.

The implementation of the objective inside the isolation vacuum of the cryostat is straight forward. The vacuum is extended with a diaphragm bellows (Trinos, Germany). The bellows is attached to the cryostat and to a solid board. The cryostat is held by three linear stages to allow coarse 3d-positioning. The solid board is fixed to the table. It has a vacuum window opening and supports the objective via a z-piezo (Mipos

100, Piezosystems Jena, Germany) for fine focus adjustment. Fine x-y-positioning is realized with an external beam control (Sec. 4.1.1). The forces caused by vacuum under-pressure are compensated with three springs according to Hooke's law $F = -kx$. The flexibility of the diaphragm bellows allows comfortable position control even under full isolation vacuum.

The extended cryostat allows collection of single photos from NV^- defect centers with 5.4 times enhanced collection efficiency compared to the original configuration from Sec. 4.4.1. It was used for the efficient measurement of optical properties of NV^- defect centers at cryogenic temperatures presented in Chapter 7.

5 Integrated single photon generation and collection systems

Most of the applications of quantum optics, quantum key distribution and quantum information processing have been realized with macroscopic table-top confocal setups, limiting their use to specialized optical laboratories [11, 42, 83, 115]. Such setups allow fundamental lab-incorporated experiments, but are less appropriate for compact, mobile and portable devices that can be installed in everyday work environments. Such implementations require fiber coupled photons for highest practicability. Fiber coupling can be realized after photon collection via an objective lens, free beam propagation, and fiber launching with a second objective. In the free beam path, other optical elements such as filters, dichroic beam splitters etc. can be included for mandatory suppression of excitation and stray light. Such free beam elements are bulky and prohibit compact and integrated implementation.

In this chapter, three conceptually different approaches to realize integrated single photon devices are introduced. Consequently, the dimensions of these devices were reduced from millimeters for the gradient index lens - fiber array in Sec. 5.1, over micrometers for the facet-coupled photonic crystal fiber system in Sec. 5.2, to nanometers for the tapered fiber device in Sec. 5.3. Vice versa, the complexity and challenges to assemble the systems decrease from the smallest to the largest. This allows for the first time a very simple and low cost realization of a single photon source (Sec. 5.1). Further advantages and limitations will be discussed in detail in each section.

Furthermore, controlled coupling to resonant structures is also highly desirable. The efficient and small-scale coupling of single photon emitters to such structures is an essential requirement to build complex quantum systems [116]. In Sec. 5.4 the controlled coupling of pre-selected single quantum emitters to different types of resonators is demonstrated. These experiments are an important step towards realizing strongly Purcell enhanced spontaneous emission rates and towards cavity quantum electrodynamics with single defect centers in diamond.

The results introduced in Sec. 5.1, Sec. 5.2, Sec. 5.3, Sec. 5.4.2, and Sec. 5.4.3 were published in Schröder *et al.* 2012b, Schröder *et al.* 2011b, Schröder *et al.* 2012a, Schietinger *et al.* 2008a and Barth *et al.* 2010a, and Gregor *et al.* 2009a, respectively.

5.1 Gradient index lens - fiber array: A compact single photon system

5.1.1 Motivation

One approach to replace the bulky free beam elements of a table-top confocal setup is introduced in this section. An integrated optical system that features only single photon emitters, gradient index (GRIN) lenses and integrated optical fibers was developed.

In such a system, the number as well as the size of the implemented optical elements are reduced. E.g. the integration of a beam splitter (BS) is not necessary. BS are used in common table-top setups for the separation of excitation laser light and signal photons as described in Sec. 4. Separation of the excitation laser beam and single photons is realized here with a miniaturized and integrated filter system. Furthermore, the GRIN system measures only a few millimeters in diameter and a few centimeters in length. Also, free space light propagation is reduced to a few hundred micrometers. In particular, the collection GRIN lens can simultaneously serve as a sample holder, further reducing the amount of optical elements as will be shown later.

Therefore, diamond nanocrystals are directly deposited on the facet via spin-coating. The emission of optical dipoles located at the interface between air and glass is preferentially directed towards the lens. This results in an increased collection efficiency compared to standard optics (see Finite Difference Time Domain (FDTD) simulations in Sec. 6.1.5). A sketch of such a miniaturized single photon collection system is presented in Fig. 5.1 a).

5.1.2 Gradient index lenses: General functionality and optical properties

A GRIN lens (also called SELFOC lens) is based on the principle of a continuously changing refractive index of a transparent material. The change of refractive index is described by a continuous function n(r) where r is the radial position relative to the optical axis of the lens. Thereby, the ray of light, in the picture of linear ray optics, will not follow a straight line but a curved way of light with continuous change of direction. The electromagnetic wave is minimizing its effective optical path length as

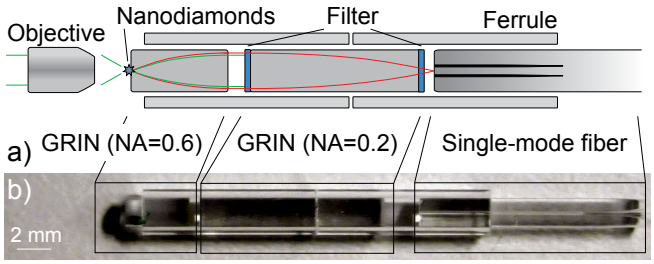

Figure 5.1: a) Schematic of the compact single photon collection system. Single photon emission of defect centers in diamond nanocrystals, deposited on the facet of a high numerical GRIN lens (NA = 0.6), is coupled into a single mode fiber via a second GRIN lens (NA = 0.2). The depicted Bragg filters block the excitation laser. They are attached by a special filter transfer technology (O.I.B. GmbH, Jena, Germany). b) Photographic image of the assembled single photon collection system. Not displayed is the 3d-stage that controls the position of the fiber.

predicted by Fermat's principle.

n(r) can be designed in such a way, that the GRIN lens refracts light like a conventional lens, e.g. a positive double-convex lens. In contrast to conventional lenses where at least one surface is non-planar, GRIN lenses have two planar surfaces as indicated by the photographic image in Fig. 5.1 b).

GRIN lenses are cylindrical glass rods. They are doped with a combination of different elements to create an index of refraction radially decreasing parabolic like from the center to the outside of the rod [117].

For the implemented GRIN lenses, the refractive index profile n(r) can be described as:

$$n(r) = n_0(1 - \frac{1}{2}(\sqrt{A}r)^2,$$

where n_0 is the index of refraction at the optical axis of the rod and $\sqrt{A}$ the index gradient constant. This constant characterizes the gradient of the refractive index.

The length is defined as $z_l = \frac{2\pi p}{\sqrt{A}}$. Here, p is the pitch of the lens, i.e. the number of optical periods of a light ray inside the lens, see Fig. 5.2.

Typical diameters and lengths are 1.5 mm to 3.5 mm and 1 mm to 10 mm, respectively. Available numerical apertures range from NA = 0.05 to NA = 0.6, while n_0 is typically between 1.4 and 1.658, $\sqrt{A}$ lays between 0.6 mm^{-1} and 0.15 mm^{-1}. By adapting the length, n_0 and the refractive index profile, the position of the focal plane in relation to the facet of the lens can be controlled, defining the effective focal length. Thereby, the focal plane can be superimposed with the facet. Such a GRIN lens has a pitch of 0.25. Light from a quantum emitter that is deposited on one end facet will be guided through

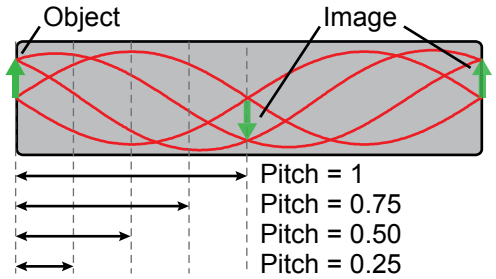

Figure 5.2: Schematic of the light propagation in a GRIN lens. The red lines indicate the trace of light inside a GRIN lens with a pitch of 2. The object in the left plane is imaged onto the right plane. The pitch represents, as indicated, the number of optical periods of a light ray inside the lens.

the lens and collimated when exiting the lens. This enables collection of single photon fluorescence from a quantum emitter, e. g. a defect center in a diamond nanocrystal, in an integrated way. The GRIN lens serves as substrate holder (for the diamond nanocrystal) and collection optics at the same time.

A key problem is fluorescence from the dopant as it may overlap with the defect center's fluorescence. Therefore, fluorescence stemming from the dopant under green 532 nm excitation was spectrally determined to be in the range from 540 nm to 570 nm (see spectrum in Fig. 5.5 d)), hence not overlapping with the fluorescence from the neutral and the negatively charged NV centers investigated here. Their emission occurs between 575 nm and 690 nm [5]. Therefore, the background fluorescence can easily be cut off with a spectral long pass filter edged at 590 nm.

5.1.3 GRIN lens - fiber array: Preparation and integration

The envisioned GRIN lens - fiber array was assembled of a collecting and a coupling GRIN lens, a single mode fiber, and a ferrule to support these components.

For the collection of photons emitted by NV defect centers in diamond, a lens with a pitch of 0.25 and a numerical aperture of NA = 0.6 (NSG Europe, UK, now Go!Foton Group, USA) was chosen. This is the highest NA commercially available for such type of GRIN lenses. The length of the lens is 3.65 mm, its diameter 1.8 mm and its focal length is 1.41 mm.

For coupling to a single mode fiber, a second GRIN lens with the smallest deliverable NA of 0.2 was selected (GRINTECH, Germany), not matched to the NA of 0.13 of the fiber mode (S630HP, Thorlabs, Germany). This lens has a different index gradient but

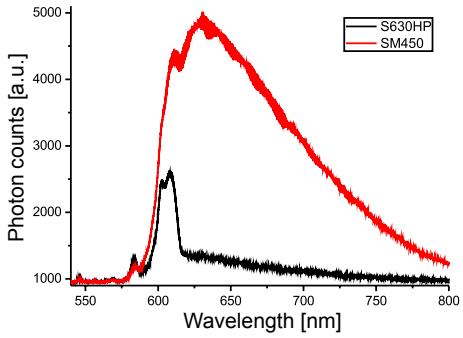

Figure 5.3: Background fluorescence of two single mode fibers under 532 nm laser excitation. Care was taken to coupled the same laser power (some mW) into both fibers. Clearly, the SM450 (red line, Thorlabs, Germany) fiber generates much more intrinsic fluorescence. The integrated area from 575 nm to 800 nm is 7 times larger than for the S630HP (black line, Thorlabs, Germany). The S630HP is therefore better suited for optical experiments at the single photon level where laser light is coupled into the fiber.

also a diameter of 1.8 mm. It has a pitch of 0.23 and a focal length of 4.52 mm.

The collection lens was prepared with diamond nanocrystals via a self-developed spin-coating procedure as described in Sec. 3.3. With this procedure, nanocrystals with mean sizes of 25 nm, 50 nm and 100 nm were uniformly deposited in the center of the front facet of various collection lenses. A x-y-intensity scan of a representative distribution is shown in Fig. 5.5 b).

The coupling lens was equipped with one integrated laser stop filter on each of its two facets. The filters were designed, grown and implemented by Optische Interferenz Bauelemente (O.I.B.) in Jena, Germany. For their integration, a special transfer technique was used. With this technology, arbitrary filter layers can be designed and fabricated on external glass substrates. Subsequently, these filter layers are directly deposited on the facets of the GRIN lenses as depicted in Fig. 5.1. First, the filter layers are grown on a decimetre-sized substrate with low adhesion. Then, the facet of a GRIN lens is glued to these filter layers. Subsequently, the lens is removed with the glued filter part sticking to it. This transfer technique (O.I.B. GmbH, Jena, Germany) can be applied to any optical component with sizes down to some ten micrometers [118]. It is thus versatile and particularly useful for integrated micro-optical systems.

Each of the filters achieves a laser suppression of 10^{-4}. The filters prevent the laser excitation light from being coupled into the fiber mode where it would cause fiber background fluorescence in the same spectral region as the single photons. Such fluorescence was observed and has to be considered. If total suppression of laser light

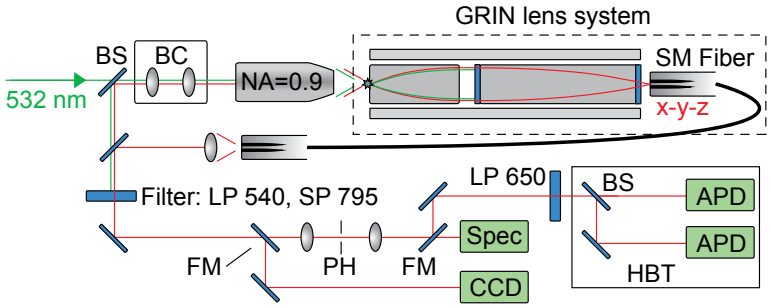

Figure 5.4: Schematic of the table-top setup. The light collected with a single mode fiber is coupled out to free space and sent to the detector unit. A green 532 nm laser was used to excite defect centers in diamond nanocrystals. BS stands for beam splitter, BC for beam control, FM for flip mirror, PH for pinhole, HBT for Hanbury Brown and Twiss setup, Spec for spectrometer, and APD for avalanche photo diode.

can not be guaranteed it is advantageous to utilize a low background fiber. The fiber background fluorescence was analyzed for two different fibers. The recorded spectra of such fiber fluorescence are shown in Fig. 5.3. Clearly, the S630HP fiber (Thorlabs, Germany) shows far lower fluorescence than the SM450 (Thorlabs, Germany) at 532 nm excitation. Integrated over the NV defect center typical spectral range from 600 nm to 790 nm, the S630HP has a 7 times reduced background intensity.

The single mode fiber was placed inside a glass ferrule with an outer diameter of 1.8 mm and an inner diameter of 125 µm. The ferrule can also be equipped with other types of fibers, e.g. multi-mode fibers which would increase the collection efficiency, but would prevent the system from delivering single spatial mode single photons.

All experiments were carried out with the collection lens fixed via a ferrule to the coupling lens in the configuration shown in Fig. 5.4. For pre-selection of a suitable quantum emitter, the laser-scanner of the home-built setup was used while the GRIN lenses were fixed. For fiber coupling, the fiber was mounted on a 3d-stage (Thorlabs) with sufficient resolution of 10 nm.

For fiber coupling of fluorescence emission of a quantum emitter located on the front facet of the collection lens, an image of this emitter needs to be mapped onto the single mode fiber core with a precision of about 100 nm. This requires precise alignment of the fiber in all three dimensions relative to the focal point of the coupling lens. This alignment was achieved with the 3d-stage.

However, it would be most suitable, to align and subsequently fix all three optical elements in a final stable position with the help of a ferrule. Such a ferrule has an

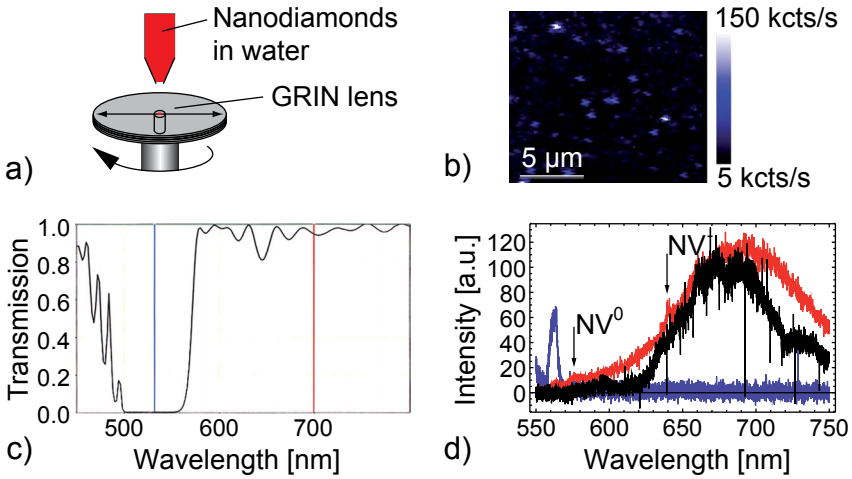

Figure 5.5: a) Schematic picture of the diamond nanocrystal deposition technique. The GRIN lens is used as a sample holder and placed inside a home-built spin-coating setup. b) x-y-distribution of fluorescent diamond nanocrystals (50 nm average size) on the facet of a GRIN lens taken with a standard confocal microscope. c) Transmission curve of integrated long-pass filters from Fig. 5.1 a). d) Fluorescence of GRIN lens under 532 nm laser excitation (blue curve). Fluorescence of a few neutral (NV^0) and negatively charged (NV^-) nitrogen vacancy defect centers (indicated by arrows) collected via an air objective and via the GRIN lens single mode fiber system (red curve and black curve, respectively, see figure of setup in Fig. 5.4).

inner diameter matched to the diameter of the optical elements of 1.8 mm. The optical components could be fixed with glue, as sketched in Fig. 5.1 b). This was already realized for a compact external cavity laser with sufficient accuracy of 100 nm [119]. As applying such a procedure is non-trivial and out-reaches the scope of this thesis, it was not realized.

5.1.4 Theoretical investigation of dipole - GRIN lens interaction

The emission pattern of a single dipole close to the surface of a dielectric material with n = 1.658 was simulated with a finite-difference time-domain (FDTD) software (Lumerical, see Sec. 6.1.5). The distance of the dipole to the surface was 10 nm, according roughly to the average distance of a dipole inside diamond nanocrystals with a mean size of 25 nm. The refractive index was chosen to be equal to the refractive index at the center of the collecting GRIN lens. The emission pattern was analyzed in the far field. This analysis predicts, that about 30 % of the light emitted by a perpendicular dipol will be directed into the collection cone of the GRIN lens. This collection efficiency $\epsilon = 0.3$ of the first optical element of the setup [114] was calculated for a light cone

with a half angle smaller than 37° according to the NA of 0.6 of the GRIN collection lens. This efficiency is much higher than $\epsilon = 0.12$ for an air objective with the same numerical aperture of 0.6. This is due to the enhanced density of states offered by the high index material with an index of refraction n = 1.66, see Sec. 6.1.5. However, due to strong chromatic aberration, imperfections in assembly and a mismatch in mode overlap, the collection efficiency of single photons coupled to a single mode fiber was much smaller in the performed experiments, but can be improved by far as desribed in Sec. 5.1.6.

5.1.5 Operation of the system: Experimental results

Free beam operation

Before the system is operated in the intended fiber configuration, analysis of the deposited diamond nanocrystals on the surface of the collection GRIN lens was performed with the table-top confocal microscope described in Sec. 4.1 to allow a pre-selection of a suitable defect center. Spectral analysis of the NV defect centers inside the nanocrystals reveals neutral or negatively charged defects. A spectrum of a crystal containing several neutral and negatively charged defects is depicted in Fig. 5.5 d). Clearly, zero phonon line (ZPL) peaks at 575 nm and 637 nm are visible, indicating neutral and negative defects, respectively.

As expected, the fluorescence light of such a defect center shows quantum behavior as proven by a dip in the normalized second order auto-correlation function of $g^{(2)}(\tau) = \frac{\langle I(t)\, I(t+\tau)\rangle}{\langle I(t)\rangle^2} = 0.84$ for $\tau = 0$ (see Fig. 5.6). For a perfect single photon source $g^{(2)}(0)$

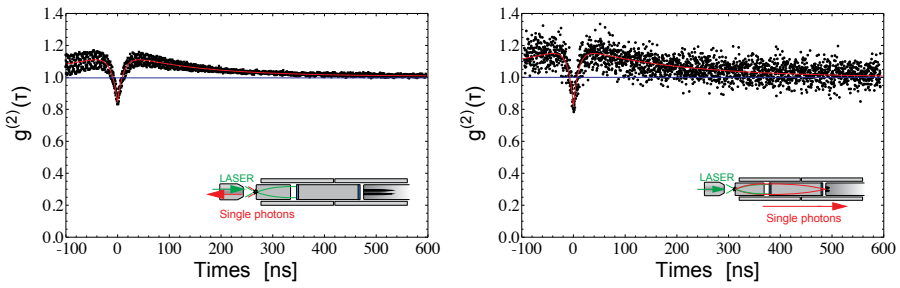

Figure 5.6: a) Measured normalized second order auto-correlation function $g^{(2)}(\tau)$ taken via the air objective for the same diamond nanocrystal as in Fig. 5.5d) with $g^{(2)}(0) = 0.84$. This value indicates that the nanocrystal contains only six or less defect centers, see text. b) Auto-correlation function of the same nanocrystal collected via the single mode fiber with $g^{(2)}(0) = 0.76$. This corresponds to five or less single photon emitters, see text. The red curves are fits according to a three level model (see App. A).

would be zero. $g^{(2)}(0) = 0.84$ and a fluorescence count rate stable over long time periods indicate that more than one emitter are contributing to the fluorescence rather than high background fluorescence. With $g^{(2)}(0) = 1 - \frac{1}{n}$ (see Sec. 2.1) one can estimate an upper limit for the number of equally bright single emitters. For $g^{(2)}(0) = 0.84$, n = 6.3, indicating that only very few (less than 6) quantum emitters contribute. As more than one emitter contributes photons, the fluorescence signal is much higher compared to a single one. This will facilitate fiber coupling which is challenging for small signals. Also, for a first proof-of-principle experiment it would be sufficient to couple more than one emitter.

However, for true single photon applications, $g^{(2)}(0)$ needs to be at least smaller than 0.5. Therefore, also a single emitter was identified in free beam operation with $g^{(2)}(0) = 0.21$ (see Fig. 5.7 c). Spectral analysis confirmed an NV^- defect center. Due to its lower photon rate, fiber coupling is more challenging.

Fiber operation

After identification of two nanocrystals containing multiple and a single defect center, the system can be used in its fiber mode. In principle, the identification of a suitable emitter would also be possible when the system is operated in fiber mode. However, as the quantum emitter has to be imaged onto the single mode core of the fiber, simultaneous scanning of the excitation laser and fiber core is more challenging to implement. Already general alignment of the system is non-trivial, a coupling routine was developed featuring back-coupling of a red laser at 637 nm [120].

Successful fiber coupling of multiple NVs was proven by guiding the fiber coupled light via a free-space track to a spectrometer and the HBT setup respectively. The according spectrum is shown in Fig. 5.5 d). The spectral width of the light is reduced due to inefficient coupling for wavelengths shorter or longer than the central wavelength of the broad NV emission. This effect is caused by chromatic aberration of the GRIN lenses.

The auto-correlation function of this emitter has a dip of $g^{(2)}(0) = 0.76$, deeper than for collection via the air objective. $g^{(2)}(0) = 0.76$ theoretically limits the amount of equally bright defect centers inside the crystal to four ($g^{(2)}(0) = 1 - \frac{1}{n} \rightarrow n = 4.2$).

This upper limit reveals that four or less single emitters and higher classical background fluorescence rather than sixth emitters contributed to the correlation measurement for free beam collection. This background reduction is a feature of increased spatial filtering. The lens system with fiber core coupling represents a confocal micro-

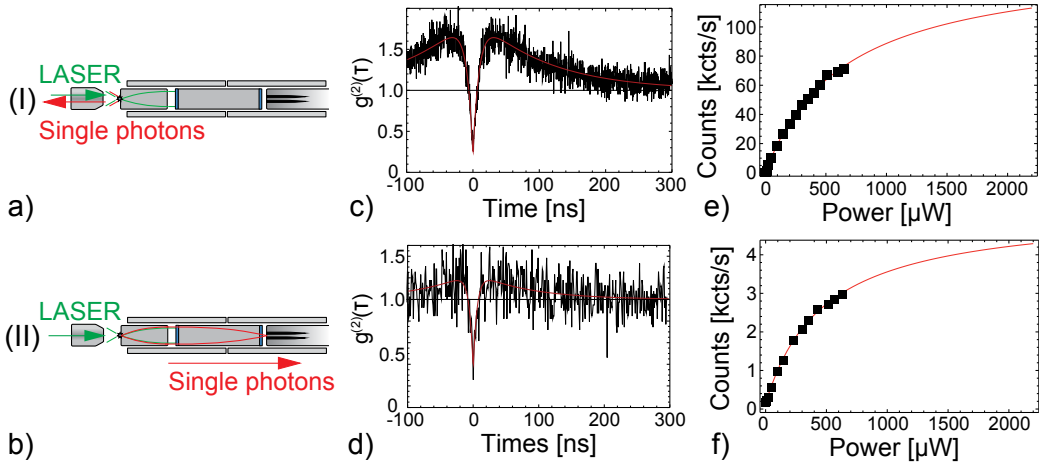

Figure 5.7: a) Schematic of configuration (I) for free beam operation, when excitation and fluorescence collection is performed via the air objective. b) Schematic of configuration (II) for fiber operation, when fluorescence collection is realized via the GRIN lens collection system and a single mode fiber. c) Measured normalized second order auto-correlation function $g^{(2)}(\tau)$ for configuration (I) with $g^{(2)}(0) = 0.21$. d) Auto-correlation function of the same defect center in configuration (II) with $g^{(2)}(0) = 0.36$. $g^{(2)}(0) < 0.5$ indicates single photon character of the measured fluorescence light. e,f) Plots of the measured single photon counts as function of laser excitation intensity. e) for collection in configuration (I), and f) for configuration (II) of 146 kcts/s and 5 kcts/s, respectively. The red curves are fits according to App. A.

scope with a relatively smaller pinhole size than the 100 µm pinhole used in the free beam. One finds a fiber pinhole diameter reduced by a factor of 1.8 compared to the iris pinhole by taking into consideration the focal length of the objective lens (2 mm), of the lens in front of the pinhole (100 mm), of the collection GRIN lens (1.41 mm), of the coupling GRIN lens (4.52 mm) and the diameters of the iris pinhole (100 µm) and of the fiber pinhole (3.5 µm). Please refer to Sec. 4.1 for further details about confocal microscopy.

For real single photon applications, a single photon emitter needs to be fiber coupled. Identification of a single emitter was already carried out in free beam operation. Fiber coupling of such an emitter is more challenging as overall detection rates are lower. However, single photons of the identified emitter with $g^{(2)}(0) = 0.21$ were fiber coupled and examined as described above. Measurement reveals a dip in the auto-correlation function of $g^{(2)}(0) = 0.36$, proving single photon character of the fiber coupled emission of a defect center in a diamond nanocrystal (Fig. 5.7 d)).

To further evaluate the system and to determine the collection and fiber coupling

efficiencies, saturation measurements were performed. Therefore, APD count rates at different excitation intensities were recorded. For analysis of the data, a fit was made according to App. A. For collection in free beam configuration via an air objective lens with a numerical aperture of 0.9 and air guidance to the APDs, 146 kcts/s in saturation were found (Fig. 5.7 e)). For collection in fiber configuration via the GRIN lens and direct coupling into a single mode fiber, 5 kcts/s in saturation were measured (Fig. 5.7 f)).

At first glance, 5 kcts/s single mode fiber coupled photons appears very low compared to 146 kcts/s free beam photons. However, this count rate has to be compared to fiber coupled photons collected by the objective lens. Assuming a single mode fiber coupling efficiency of 15 %, a reasonable efficiency according to experimental experience, 22 kcts/s of the 146 kcts/s photons could be fiber coupled. This reveals that the GRIN lens collection system only lacks a 4-fold collection shortage in comparison with the NA = 0.9 air objective.

5.1.6 Improvement of operation parameters

There are several straightforward experimental improvements promising much higher collection efficiencies. Ray-tracing simulations were performed to estimate fiber coupling losses introduced by length deviation of the GRIN lenses of 5 % to a factor of 1.5 and chromatic aberration for a broad emitter (FWHM of 100 nm) to a factor of 2. Chromatic aberration is negligible if a narrow band emitter (FWHM of 1 nm) is utilized. Furthermore, the coupling GRIN lens has an NA = 0.2 much higher than the NA of 0.12 of the single mode fiber causing high coupling losses of a factor of about 3. Also an increased mode overlap by aligning the dipole inside the diamond nanocrystal, e. g. via rotating it with an atomic force microscope manipulation technique [121], could lead to an enhancement of up to 1.1 as estimated above. As alternative for an NV defect a silicon-vacancy (SiV) defect center [11] in diamond nanocrystals may be used (see Sec. 2.5). Its spectral width of 1 nm is centered around 740 nm, outside of the GRIN lens' intrinsic fluorescence. It has a 10 times reduced lifetime compared to an NV defect center. Yet, it must be pointed out, that its internal quantum efficiency (QE) varies. For simplicity, a QE of 1 is assumed.

All the before discussed improvements accumulate to a factor of about 100 of improvement in fiber coupling efficiency. Hence, an improved GRIN lens system could couple up to 500 kcts/s of single photons to a single mode fiber.

5.1.7 Summary and outlook

In this section, a fiber coupled single photon collection system based on two gradient index lenses was presented. With its dimensions of only 2.5 cm x 2.5 cm x 5.5 cm, it is super compact and can be integrated into portable and mobile applications. Non-blinking, non-bleaching, room temperature single photon operation was realized with single nitrogen-vacancy defect centers in diamond nanocrystals as quantum emitters. Such a system was realized for the first time.

The presented system is not only interesting from a fundamental point of view, as a new concept of integration was implemented, but also from an applied perspective. It should be pointed out, that all compoments, such as gradient index lenses, filter technology, diamond nanocrystals, as well as single mode fibers, are commercially available. Furthermore, the deposition of single fluorescent particles is straight forward. For excitation, a low cost diode laser can be used. These off the shelve components and their simple assembly allow the implementation of a compact and low cost single photon system. Such single photon systems could be used for non-scientific applications. For example, high school students could benefit from such devices by performing real quantum experiments.

5.2 Fiber single photon source: The most simple and direct single photon source

5.2.1 Motivation

The experimental realization of a fiber-based single photon source described in this section was driven by the question: How can one realize the most simple and direct fiber based single photon source? The idea was to take a quantum emitter (single NV defect center in a diamond nanocrystal) and place it directly in the core region of the facet of an optical fiber. By doing so, the NV center is near-field coupled to the fiber mode, and its emission is directly launched into the fiber core. Such a system is alignment free, µm-sized and can be operated at room as well as cryogenic temperatures. Furthermore, it easily integrates into fiber optic networks for quantum cryptography or quantum metrology applications [122]. A sketch of such a micrometer sized single photon collection system is presented in Fig. 5.8.

To realize such a system, a nanometer-sized object has to be deposited on a micro-

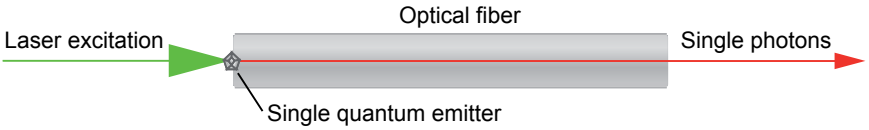

Figure 5.8: Idea of the most simple and direct fiber coupled single photon source: A quantum emitter, e.g. a single NV center inside a diamond nanocrystal, is deposited directly on the fiber core. A part of its single photon emission is near-field coupled to the fiber mode and guided through the fiber core.

meter-sized object with nanometer precision. Previous attempts to construct such a system have been made by growing diamond crystals directly on fiber facets [123] or by depositing pre-selected diamond nanocrystals on specially prepared fibers [108]. However, a direct near-field coupling of single photons from a single emitter to guided optical modes of a fiber has not been achieved.

The hybrid bottom-up approach presented in this chapter utilizes the self-developed pick-and-place technique via an atomic force microscope (AFM) as was described in Sec. 3.5.3. This pick-and-place technique allows pre-selection of a diamond nanocrystal with required properties, such as emission wavelength and brightness, and its subsequent deposition directly on a pre-selected structure, e.g. the fiber facet of an optical fiber.

5.2.2 Pre-selection of optical fiber

The pre-selection of an optical fiber is a critical task for the successful realization of the system. The intended configuration causes one main difficulty: The laser light that is used to excite the NV center will also be coupled into the fiber if not blocked by a spectral or spatial filter. Neither spectral nor spatial filtering were applied in this proof-of-principle experiment. Therefore, a fiber had to be chosen that will only generate laser induced fiber fluorescence in the same order-of-magnitude as the fiber coupled single photons or less. This, expressed as background fluorescence per excitation power, is one crucial fiber parameter. This parameter can be experimentally measured. It turned out, that only one type of investigated fiber was suitable in terms of fiber background. This was a pure silica photonic crystal fiber (PCF) with air guiding as depicted in Fig. 5.9.

Another crucial parameter is the ability to fiber couple as much NV fluorescence as possible. This can be expressed as coupling efficiency. It mainly depends on the numerical aperture of the fiber: The higher the collection angle is, the higher the collection efficiency will be.

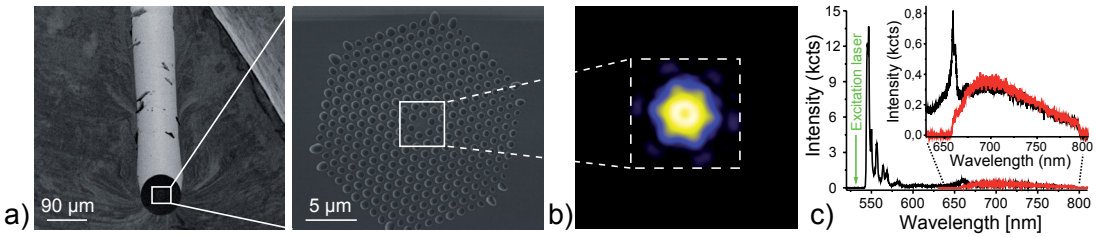

Figure 5.9: Properties of the photonic crystal fiber used for the experiments. a) Scanning electron microscope pictures of the PCF with a diameter of 90 µm. The white box indicates a zoom in on the fiber facet. b) CCD-camera image of the light collected from the fiber under 532 nm excitation. The color coding is logarithmic from white (bright) to black (dark). c) Spectrum of this light (black line) and the spectrum after adding a 650 nm longpass filter (red line). The inset displays a section of the entire spectrum as indicated by the dashed lines.

Based on these assumptions, a pure silica PCF (NL-1.5-590, NKT Photonics, Denmark) was chosen. It has a high numerical aperture of 0.45, a diameter of 90 µm, a hole pitch (hole distance) of 1.07 µm, a hole diameter of 0.7 µm, a core region of about 1.65 µm, and a length of about 10 cm. Fig. 5.9 a) shows an image of the fiber taken with a scanning electron microscope. In b), a CCD camera picture in color coding of the fiber mode intensity distribution under 532 nm laser excitation is depicted. The scale is logarithmic, it goes from white as the highest intensity, to yellow, to blue and to black as the lowest intensity. In c), the spectrum of this fiber background fluorescence is shown. With the help of a 650 nm long pass filter, most of the background light can be suppressed.

A numerical study presented in Sec. 5.2.4 shows the theoretically expected collection efficiencies of different dipole orientations for the selected fiber.

5.2.3 Pre-selection and assembly of a diamond nanocrystal

A 30 nm sized diamond nanocrystal containing just a single NV^- defect center was pre-selected. The pre-selection process and verification of single photon emission was carried out with the inverted confocal microscope described in Sec. 4.1.2 and Sec. 3.5.3.

The diamond deposition via the pick-and-place manipulation technique was carried out in a two-step process as described in Sec. 3.5.3. A direct placement of the crystal from the nanocrystal cover slip reservoir to the fiber core is technically not possible due to alignment limitations and the only 1.65 µm sized core. Therefore, the nanocrystal was first deposited in the non-structured, relatively large area (roughly 30 µm × 30 µm) outside the cladding hole region. Then, a large scan over an area including the position

of the nanocrystal and the fiber core was performed to measure their relative position. After that, in a second pick-and-place step, the diamond was deposited in the core region. Finally, it was moved close to the center of the core where a maximum coupling efficiency is expected from the FDTD simulations (Sec. 5.2.4). An AFM surface scan that clearly shows the position of the diamond is depicted in Fig. 5.11 a).

5.2.4 Theoretical investigation

Finite difference time domain (FDTD) simulations were carried out using a commercial software package (Lumerical FDTD Solutions, Canada). The simulated geometry consists of a section of 10 µm × 10 µm × 15 µm of the fiber with a dipole emitter placed 12.5 nm above the fiber facet. The pitch of the holes as well as the hole diameters were adapted to the original fiber.

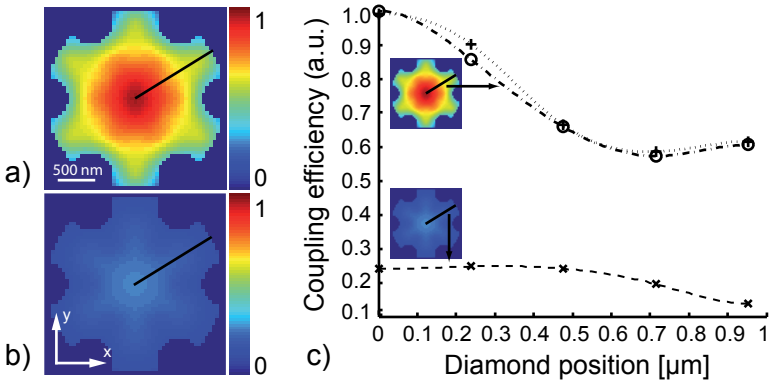

Figure 5.10: Results of a FDTD simulation showing the coupling efficiency of a single dipole emitter to the fiber modes versus the dipole's position at a fixed distance of 12.5 nm to the fiber facet. In a) and b) two-dimensional position images with the dipole axis orthogonal and parallel to the optical axis of the fiber, respectively, are plotted while c) shows the coupling along the black line in a) and b). Crosses represent dipole orientation in y-direction, circles in x-direction and x marks orientation perpendicular to the x-y-plane. Maximum coupling efficiency is achieved in the center of the core.

The dipole x-y-position as well as the dipole orientation was varied. To obtain a quantitative result for the dipole-fiber coupling light arriving at the end of the fiber within a circle of radius 1.65 µm from the center was considered to be guided by the fiber.

The results of this simulation are displayed in Fig. 5.10. It is clearly visible that the coupling efficiency strongly depends on the position and on the orientation of the dipole relative to the center and the facet of the fiber. The coupling to the fiber mode is much

higher for a position at the center of the core as well as for a dipole oriented parallel to the facet. This has to be taken into account for an experimental optimization of the system. For best fiber coupling, the dipole has to be placed in the center of the core, and aligned in the plane of the facet.

The simulation was also used to estimate the relative collection efficiency of the fiber compared to an objective with an NA of 0.9. For that purpose, the emission coupled to the fiber mode was divided by the emission of a dipole within a cone of 64°(according to an NA of 0.9) into the free space. This gives the effective NA_{Eff} of the fiber. For a perpendicular dipole $NA_{Eff} = 0.77$ and for a parallel dipole $NA_{Eff} = 0.68$. Surprisingly the effective NA_{Eff} is higher for the perpendicular dipole despite the lower coupling efficiency. This can be explained easily. The effective NA_{Eff} is a relative value comparing the fiber collection to the collection of an air objective. For a perpendicular dipole the collection efficiency for an air objective is low compared to a parallel dipole.

5.2.5 Operation of assembled system

Continuous wave operation

The deposited diamond nanocrystal emitter was optically excited on the fiber facet by CW laser radiation of 532 nm with a typical excitation power of 1.1 μW in the focus of the scanning confocal microscope (details in Sec. 4.1) with an NA of 0.9. Figure 5.9 b) depicts a fluorescence image taken with a CCD camera while filtering the excitation laser light. This figure clearly shows the structure of the fluorescence modes of the PCF. However, the NV center's emission is outshined by strong background fluorescence below 670 nm as indicated in the spectrum in Fig. 5.9 c). This background light stemming from inelastic Raman scattering and fluorescence emitted from fiber impurities can be significantly suppressed with spectral filtering. Figures 5.11 c) and 5.11 d) show the filtered fluorescence light collected by the confocal microscope and the fiber, respectively. In Fig. 5.11 c) excitation and confocal detection were both performed on the diamond-loaded side of the fiber, whereas in 5.11 d) the excitation laser was scanned across the diamond-loaded facet of the fiber while the fluorescence was detected through the fiber (see configurations (I) and (II) sketched in 5.11). The NV center's emission appears as diffraction limited spot with high intensity (about 9 kcts/s and 20 kcts/s for configuration (I) and (II), respectively) while the holes of the PCF emit a six times lower intensity. This proves that the NV center emission couples directly to optical modes of the fiber and can be separated from background

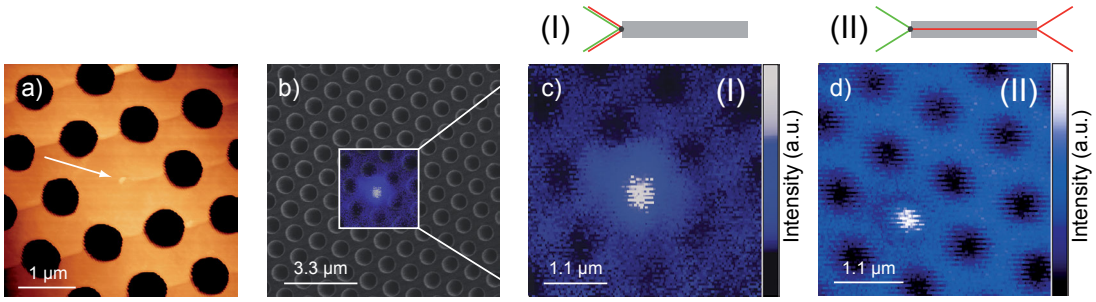

Figure 5.11: a) Atomic force microscope (AFM) image of the fiber core region. The diamond in the middle of the core (marked by an arrow) has a diameter of about 30 nm and was placed via an AFM pick-and-place technique. It contains a single NV center as single photon emitter. b) Overlay image of the fiber core consisting of a scanning electron and a corresponding confocal microscopy photoluminescence excitation (PLE) image. The white dot represents the fluorescence of the NV center. c) Scanning confocal microscopy PLE image in experimental configuration (I), with excitation and detection on the diamond-loaded side of the fiber. d) Scanning confocal microscopy PLE image in experimental configuration (II), with excitation on the diamond-loaded side of the fiber and detection through the fiber. This PLE image already indicates, that the emission of the single NV is coupled to the fiber mode and outshines the background fluorescence.

fluorescence.

The light emitted by the NV center on the fiber facet shows strong single photon character. This is indicated by the measured auto-correlation functions at zero time delay $g^{(2)}(0)$ displayed in Fig. 5.12 a,b). The photons measured on the diamond-loaded side in configuration (I) have $g^{(2)}(0) = 0.45$ at 40 µW excitation power in the focus. The light collected by the fiber in configuration (II) has $g^{(2)}(0) = 0.36$ at 49 µW excitation power. No background correction was applied to the data.

Effective NA of the system

A comparison of the measured photon rates at saturation in configurations (I) and (II) (see Fig. 5.12) reveals an effective numerical aperture $\mathrm{NA_{eff}} = 0.82$ of the fiber. The far field pattern of the radiation was assumed to be isotropic as the real dipole orientations of the defect center are not known. The experimental results are in agreement with the FDTD simulations of dipole emission patterns presented in Sec. 5.2.4. The simulations reveal an $\mathrm{NA_{eff}}$ of 0.77 and 0.68 for single dipole emitters orthogonal and parallel to the optical axis of the fiber, respectively. Compared to the far field NA of 0.45 of the fiber this is a tremendous improvement. The relative increase is caused by the near-field emitter to fiber coupling and the refractive index $n = 1.46$ at 637 nm of the fiber [124].

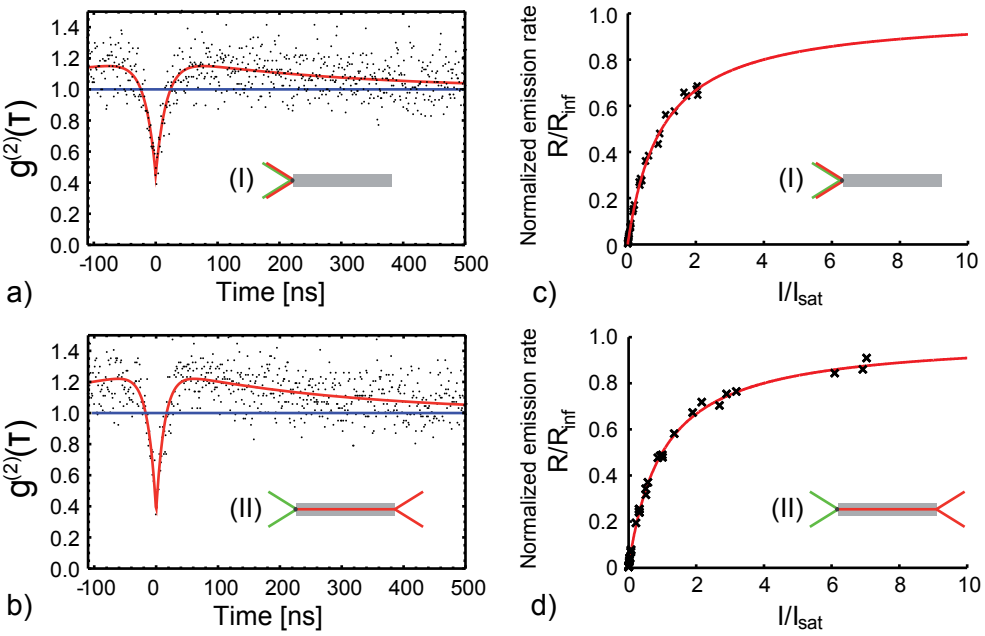

Figure 5.12: Characterization of the NV's fluorescence emission. a,b) Autocorrelation function $g^{(2)}(\tau)$ measured in configurations (I) and (II) as shown in the insets, respectively, under continuous wave excitation. $g^{(2)}(0) = 0.45$ and $g^{(2)}(0) = 0.36$ for (I) and (II) demonstrate the single photon character. c,d) Saturation measurements in configurations (I) and (II). The maximum count rate is 52.6 kcts/s for configuration (I) where light was collected via an objective with NA of 0.9. In configuration (II) where light was collected via the fiber the maximum count rate is 43.2 kcts/s. This corresponds to an effective NA of about 0.82 of the fiber. Refer to the text for further details.

Such near-field coupling improves the collection in a similar way as a solid immersion lens [125] as will also be discussed in detail in Chapter 6.

It should be pointed out that such a high collection efficiency is achieved with a device only 90 µm in diameter. This is remarkable compared to the size of an objective lens. A size reduction by more than two orders of magnitude has been achieved.

Pulsed excitation

A true on-demand single photon source requires pulsed excitation which confines the single photon in a time interval determined by the spontaneous lifetime. If the fiber integrated NV defect center is excited with a pulsed 532 nm laser, a $g^{(2)}(0)$ of about 0.5 is measured. However, due to the larger power density of the pulsed excitation, single photon emission is accompanied by strong background fluorescence with lifetimes below 3.5 ns. These background lifetimes are much shorter than the lifetime of the NV

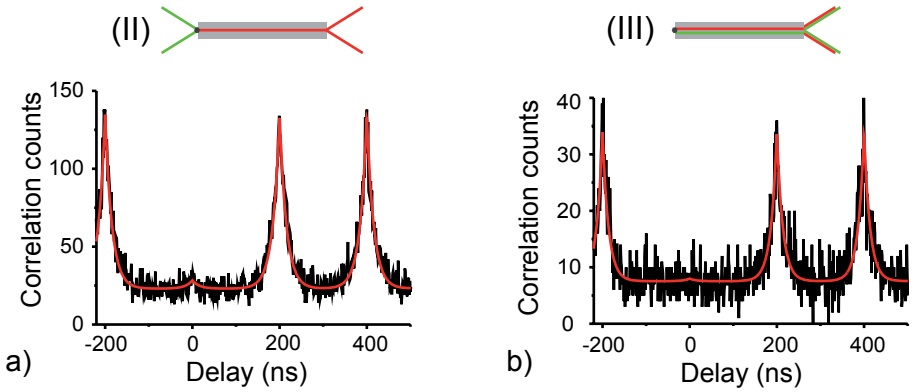

Figure 5.13: Characterization of the NV's fluorescence emission under pulsed excitation. a) Autocorrelation function $g^{(2)}_{\mathrm{Pulse}}(0) = 0.21$ of the NV center fluorescence in configuration (II) for a laser repetition rate of 5 MHz. b) Autocorrelation function $g^{(2)}(\tau)$ of the single photons collected in another configuration (III) where excitation and collection are realized through the fiber. The laser repetition rate was again 5 MHz and $g^{(2)}_{\mathrm{Pulse}}(0) = 0.23$. The data in a) and b) was post-processed to imitate gating with an offset of 3.5 ns. Red curves are fits to the data. Refer to the text for further details.

center of about $\tau = 25$ ns. Therefore, temporal filtering allows partly suppression of background fluorescence. Computational post-processing of the data was performed to mimic a physical temporal filter, e.g. a fast shutter in front of the APDs opening 3.5 ns after the excitation pulse. As expected, the autocorrelation function $g^{(2)}_{\mathrm{Pulse}}(\tau)$ calculated from the post-processed data shows a deeper antibunching of $g^{(2)}_{\mathrm{Pulse}}(0) = 0.21$. This value was taken from the fit to the data in Fig. 5.13 a). Details about the fitting function can be found in App. A.

For pulsed excitation measurements the time-tagged-time-resolved mode of the PicoHarp 300 was used. This mode records the excitation pulses and the arrival times of all photons with a timestamp. Calculation of the autocorrelation function is done afterwards. The time differences of all events are calculated and written into a time-event histogram. To suppress fast decaying background fluorescence, photon events in an interval of 3.5 ns after the laser pulse were excluded from the correlation calculations.

Polarization properties

The polarization properties of the NV center's fluorescence were analyzed for detection through the fiber. For that purpose, a $\lambda/2$-plate and a polarization filter were introduced in the optical path towards the detector. The waveplate was used to rotate the

linear fraction of the photons, while the polarization filter was kept fixed to avoid polarization dependencies of the setup. Figure 5.14 a) shows the measured polarization properties of the light after the fiber (measured in configuration (II)). The visibility $V = (I_{max} - I_{min})/(I_{max} + I_{min})$ was determined to be 0.48 mainly due to high background fluorescence as determined by the auto-correlation measurements.

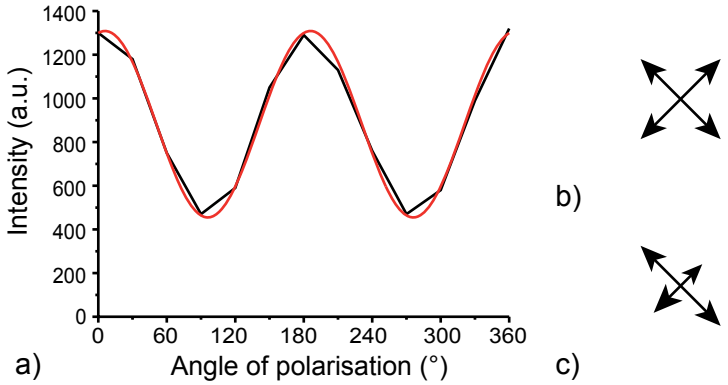

Figure 5.14: a) Polarization properties of the NV center fluorescence detected through the fiber. The observed modulation accounts for the symmetry of the NV center resembling an emission pattern of two orthogonal dipole emitters. The visibility $V = (I_{max} - I_{min})/(I_{max} + I_{min})$ of 0.48 indicates that one of the dipoles is strongly inclined relative to the optical axis [65]. b) Illustration of two equally strong perpendicular dipoles in the plane of the page. c) Illustration of the same dipoles if one them is oriented under an angle relative to the plane. Its effective strength relative to plane is reduced.

The C_{3V} symmetry of the NV center determines two orthogonal dipole emitters as illustrated in Fig. 5.14 b) and c). Their relative alignment to the fiber facet can be deduced from the measured polarization of the fluorescence [65]. One of the two dipoles is inclined strongly relative to the optical axis and therefore only weakly contributes to the fluorescence guided by the fiber. Numerical simulations (Sec. 5.2.4) confirm this behavior as can be seen in Fig. 5.14 a).

The measurement implies that coupling of the emitter to the fiber modes and thus photon collection efficiency can be further improved by optimizing the orientation of the diamond nanocrystal. If both dipoles are aligned parallel to the surface, the coupling efficiency would be maximized. Such an alignment of the dipoles relative to the facet of the fiber could be achieved by rotating the diamond nanocrystal with the help of an AFM similar to the procedure described in Sec. 3.5.3.

5.2.6 Improvements of system

To further improve the performance of the system, some direct means can be realized. First, to experimentally improve the single photon character of the fiber coupled photons, i.e., to get a deeper dip at $g^{(2)}(0)$, a Bragg mirror could be coated on the diamond loaded facet to suppress fiber coupling of laser excitation light and thus prevent fiber background fluorescence. Although the maximum single photon emission at saturation is already very high for such a device of only 90 µm in diameter ($R_{inf} = 43.2\,kcts/s$ for configuration (II), see Fig. 5.12 d)), photon collection efficiency could be further improved. One possibility is to coat a Bragg mirror on top of the diamond, suitable to reflect single photon emission into the core of the fibre. Furthermore, as the emission patterns of the NV dipoles depend on the dielectric environment (see Sec. 6.1.5), an adaption of the dielectric structure surrounding the dipole could be realized. The most simple one would be increasing the index of refraction of the core structure, e.g. by doping the core. Also, an optimization of the dipole orientation could be achieved in an in-situ feedback process by simultaneously manipulating the diamond nanocrystal with the AFM and maximizing the fluorescence intensity coupled into the fibre. By choosing a brighter defect center, such as a Si- or Cr-related defect [11, 37], an approximetly ten times higher fiber coupled photon rate could be achieved.

5.2.7 Fiber quantum sensor

The robust on-facet integration of a single defect diamond nanocrystal has another thriving feature. It was also possible to excite the NV center through the fiber while its emission is simultaneously collected through the same fiber. This new operation configuration (III) is sketched in Fig. 5.15). The collected light still shows single photon character with $g^{(2)}_{Pulse}(0) = 0.23$ if temporal filtering is applied as discussed in Sec. 5.2.5. The auto-correlation data is displayed in Fig. 5.13 b).

The fiber-integrated single emitter thus represents a versatile quantum light source for optical scanning probe imaging [126] or as local source of quantum light, e.g., to launch single photons in the evanescent field of other optical components such as micro-cavities [127]. Moreover, the optical read-out of the spin-state of the single defect center at the end of a fiber tip resembles a small and robust magnetic field probe [49, 128]. In all cases operation is at room temperature and all optical components are fiber coupled.

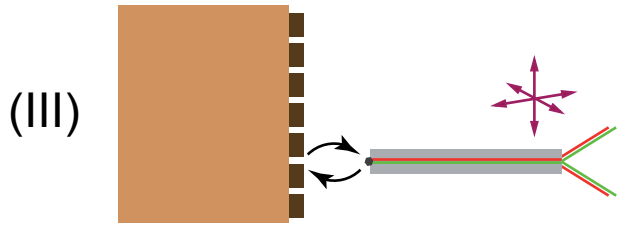

Figure 5.15: Schematic illustrating how the fiber coupled single NV defect center could be used for probing. It is possible to excite the NV defect through the fiber and collect its emission through it. That this configuration is still working in the single photon regime is shown in Fig. 5.13 b) under pulsed excitation. By approaching it to other materials and structures, one could analyze the interaction of the intrinsic NV center's dipoles with these samples. Plasmonic, photonic, electronic and also magnetic samples could be probed.

5.2.8 Summary and outlook

Concluding this section, a fully integrated single photon source was realized by facet-coupling a diamond nanocrystal with a commercial optical fiber using the atomic force microscope manipulation technique introduced in Sec. 3.5.3. The single photon source has a pronounced antibunching dip of $g^{(2)}_{\mathrm{Pulse}}(0) = 0.21$ under pulsed excitation. This technique is independent of emitter type and sample geometry and thus not limited to optical fibers as described in Sec. 3.5.3.

Figure 5.16: Schematic showing the different experimental configurations, i.e. (I) excitation and detection on the diamond-loaded side of the fiber, (II) excitation on the diamond-loaded side of the fiber and detection through the fiber, and (III) detection and excitation through the fiber.

The assembled system can be operated in three different configurations as illustrated in Fig. 5.16. As a light collecting fiber objective it reaches an effective numerical aperture of 0.82 while having only micrometer dimensions (configuration (II)). It therefore allows integration into ultra-compact quantum photonic devices or fiber networks. Since the direct fiber-emitter coupling is ultra-stable, these devices would be maintenance-free, and scalability to more complex systems is feasible. Such fiber-based sources can be bundled to launch a larger, yet precisely defined number of photons into on-chip photonic structures for an integrated quantum optical technology. The possibility to simultaneously excite the NV center and recollect its single photon emission through the fiber will open the way towards new devices where single emitters need to be

coupled directly to photonic structures or where they are used as local quantum sensors (configuration (III)).

5.3 Tapered fiber single photon system: Efficient single mode fiber coupling

5.3.1 Motivation

The system that will be described in this section is a consequent development of the facet near-field coupled single photon system (SPS) introduced in Sec. 5.2. It was realized in cooperation with the group of Shigeki Takeuchi during a research visit to his laboratory at The Institute of Scientific and Industrial Research, Osaka.

As illustrated in Fig. 5.17 near-field coupling to the fiber mode is achieved at the tapered region of a single mode fiber. This implementation offers various advantages. In contrast to the device introduced in the last section, where photon collection is

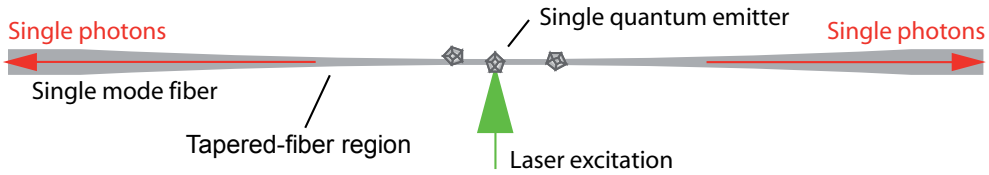

Figure 5.17: Schematic of a tapered fiber equipped with diamond nanocrystals. Single incorporated NV centers are excited with a 532 nm laser, their single photon emission is collected via the fiber ends.

limited by the NA of the fiber mode, theoretical models have predicted a coupling efficiency of up to 28 % for a cesium atom [129] to a 200 nm tapered fiber. Furthermore, such a tapered fiber coupled single emitter could be used for transmission control of a coherent laser beam and other building elements for quantum information processing as will be sketched in the outlook [130--132].

5.3.2 Preparation of diamond - fiber system

Production of tapered fibers

The tapered fibers were fabricated from standard single-mode optical fibers (630HP, Thorlabs). The production process is described in Sec. 3.4.1. To generate a large evanescent field strength, the tapered fibers were pulled down to a diameter of 273 nm

in the tapered region, as measured by scanning electron microscopy (VE9800, Keyence) while still maintaining a transmission higher than 90 %. All experiments were performed in a class 100 cleanroom for which transmission degradation is negligible during the optical experiment. The experimental procedure is described in Sec. 3.4.1.

Deposition of diamond nanocrystals

For the preparation of the single photon system, a dip-coating technique was developed that allows controlled deposition of diamond nanocrystals. The experimental procedure is sketched in Fig. 5.18 b), a detailed description can be found in Sec. 3.4.

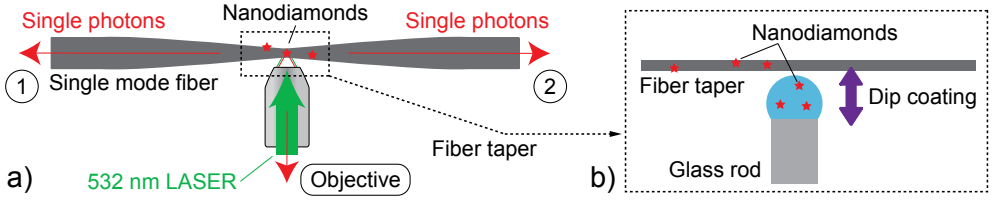

Figure 5.18: a) Schematic of a tapered fiber equipped with diamond nanocrystals. Via excitation with a 532 nm laser, single photons were collected either through the objective or the fiber ends. Tapered fibers with diameters down to 273 nm were applied. 1 and 2 indicate fiber end one and fiber end two, respectively. b) Schematic of dip coating technique: A small droplet of an aqueous diamond nanocrystal solution was given onto the facet of a thin glass rod with a diameter of about 1 mm. The tapered fiber was dipped into the solution. By moving the tapered fiber via a linear stage along the fiber axis through the droplet, diamond nanocrystals were deposited. This deposition was controlled by the laser scattering signal of the deposited nanoparticles and allowed for controlling the deposition of an approximate number of scatterers, please refer to Sec. 3.4 for more details.

5.3.3 Analysis of deposited nanoparticles

To find and analyse deposited nanoparticles, a microscope image of the tapered fiber was taken. To make the particles optically visible, red laser light was sent through the fiber. At the positions of nanoparticles, parts of the guided light are scattered and collected by the objective (NA = 0.8) of the microscope. Such an image, taken with a conventional CCD camera, is depicted in Fig. 5.19 a), four scatterers can be seen. To identify single photon emitting defect centers, lateral x-y-intensity scans with a home-built confocal microscope featuring a multi-mode fiber as pinhole (1550HP, Thorlabs, core diameter $\sim 10\,\mu m$) and a x-y-piezo scanner were performed, see Fig. 5.19 a). For excitation, a CW 532 nm laser was used, while the laser fluorescence was blocked with two 565 nm long pass filters. Doing so, fluorescent particles such as the NV were identified. Such a

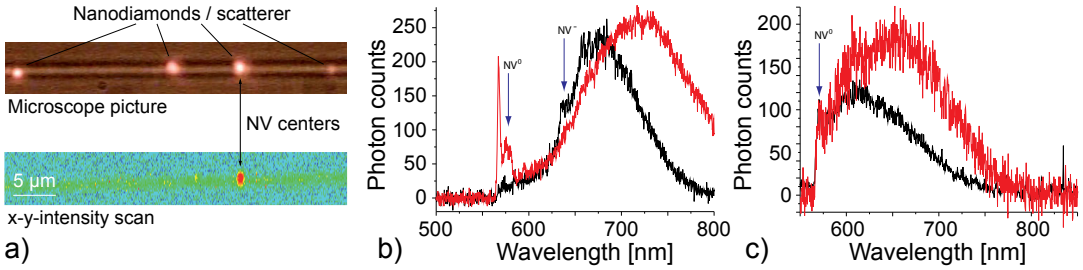

Figure 5.19: a) Top: Microscope picture of a 40 µm long tapered fiber section. Laser is guided through the fiber. The scattered light from four scatterers is visible. Bottom: x-y-intensity scan of the same region. While the tapered fiber is scanned, 532 nm laser light is focussed on the tapered fiber. The laser is blocked with a 565 nm long pass filter before the detection of fluorescence > 565 nm. One of the four scatterers contains several nitrogen vacancy centers. b) Spectrum of the fluorescence of the light emitter depicted in the lower panel of Fig. 5.19 a) at excitation intensity of 500 µW. Several nitrogen vacancy centers contribute to the emission. Clearly visible are the zero phonon lines of the neutral (575 nm) and the negatively charged (637 nm) centers. c) Spectrum of the fluorescence of a single neutral nitrogen vacancy center excited with 500 µW, normalized to the zero phonon line at 575 nm. The black and red line in b) and c) represent the fluorescence collected via an air objective and via one end of the fiber, respectively. The red spectra appear redshifted due to chromatic dependence of the fiber filter stage transmission.

scan is shown at the bottom panel of Fig. 5.19 a) where a single diamond nanocrystal containing multiple NVs is present. Both panels (top and bottom) in Fig. 5.19 a) depict the same tapered fiber region. By comparing both images, fluorescent nanoparticles can be distinguished from merely scattering ones.

First evidence for the fluorescence indeed stemming from NV centers can be retrieved from spectral analysis. The black and the red graph in Fig. 5.19 b) show the fluorescence of the diamond nanocrystal in Fig. 5.19 a) collected by the confocal microscope and by one end of the fiber, respectively, when excited with 500 µW. The spectrum collected by the fiber appears red-shifted due to fiber background fluorescence and due to wavelength dependent transmission of the laser light filter stage. This free space filter stage with two aspherical lenses for fiber in- and out-coupling shows high chromatic aberration. Therefore, wavelengths around 800 nm have a higher transmission than wavelengths around 600 nm. Nevertheless, zero phonon lines (ZPLs) of neutral and of negatively charged NVs can be identified in both spectra around 575 nm and 637 nm, originating from several NVs. Fig. 5.19 c) shows a fluorescence spectrum of a single NV excited with 500 µW. The peaks in the spectra around 575 nm indicate a neutral NV. The spectrum shows the emission collected by the confocal microscope and by one end of the fiber, displayed with black and red graphs, respectively. The intensity of these

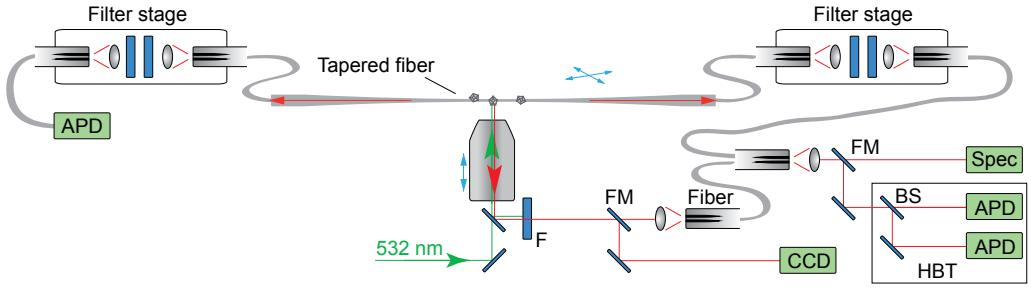

Figure 5.20: Illustration of the setup to measure the fiber coupled single photons. A green 532 nm laser was used to excite the defect centers inside the diamond nanocrystals via an air objective with an NA of 0.8. The fluorescence light was either collected with the same objective or via the tapered fiber. The light collected with the tapered fiber is either send to a fiber coupled APD after passing a filter stage or coupled out to free space and sent to the detector unit after passing a filter stage. In this setup, the pinhole was replaced by a fiber with a core diameter of roughly 10 µm. F stands for filter, FM for flip mirror, BS stands for beam splitter, HBT for Hanbury Brown and Twiss setup, Spec for spectrometer, and APD for avalanche photo diode.

peaks was used to normalize both spectra. The spectrum collected by the fiber was corrected by substraction of the fiber fluorescence background.

5.3.4 Single photon fiber coupling

The Hanbury Brown and Twiss setup was used to perform auto- and cross-correlation measurements [21]. As done before, the photon statistics were derived from the normalized second-order autocorrelation function $g^{(2)}(\tau)$. In Fig. 5.21 a) the auto-correlation function of the same NV as depicted in Fig. 5.19 c) is displayed. The data in Fig. 5.21 a) was collected via the confocal microscope. A deep antibunching dip $g^{(2)}(0) = 0.11 < 0.5$ is visible. This proves, that the collected light originates from a single photon emitter, in this case from a single neutral NV, in reference to the spectrum in Fig. 5.19 c). For both fiber ends cross-correlation measurements with the photons collected via the objective were performed (see Fig. 5.21 b)). $g^{(2)}(0) = 0.29$ and $g^{(2)}(0) = 0.29$ for fiber end one and fiber end two (not shown here, see Fig. 5.18 a)), respectively. This clearly proves that the photon flux in the fiber is stemming from a single light emitter even in the cross correlation measurement. The less pronounced dip indicates higher background fluorescence generated mainly in the tapered fiber region. This background has stronger influence on the cross-correlation measurements taken between the two fiber ends as it is present in both channels of the HBT setup as illustrated in the sketch of the setup in Fig. 5.20. Therefore, the antibunching dip

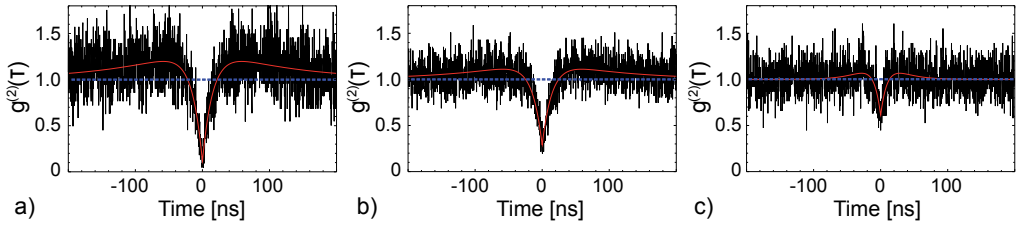

Figure 5.21: a) Normalized auto-correlation function of the same single NV center as in Fig. 5.19 c). Light was collected via the air objective (see Fig. 5.18 a)). A deep antibunching dip $g^{(2)}(0) = 0.11$ is visible. According to the spectrum in Fig. 5.19 c) this correlation measurement confirms a single neutral NV defect center as single photon source. b) Cross-correlation measurement for fiber end one with the photons collected via the objective (see Fig. 5.18 a)). $g^{(2)}(0) = 0.29$ proves single photon statistics for the fiber coupled light. For an equivalent measuremtent for fiber end two $g^{(2)}(0)$ was 0.29 (not displayed for redundance). c) Cross-correlation measurements between the two fiber ends. The antibunching dip $g^{(2)}(0) = 0.61$ is slightly higher than 0.5, yet indicating strong quantum character of the light. The correlation functions in a), b), c) were taken at excitation intensities of 450 µW, 500 µW and 400 µW, respectively.

$g^{(2)}(0) = 0.61$ is slightly higher than 0.5, yet indicating strong quantum character of the light. All correlation measurements were performed while blocking the laser light with a 565 nm long-pass filter.

To estimate the total amount of single photons coupled from the NV emission into the single-mode fiber, saturation measurements and setup efficiency analysis were carried out. For saturation measurements, detected photon events were recorded at different excitation intensities. Fitting to the experimental curves was done according to $\mathrm{R(I)} = \frac{\mathrm{R_{Inf}\ I}}{\mathrm{I_{Sat}+I}} + (\alpha)\mathrm{I} + \beta$, where R is the single photon count rate, $\mathrm{R_{Inf}}$ the count rate at infinite excitation intensities, I the excitation intensity, $\mathrm{I_{Sat}}$ the saturation excitation intensity, while α and β are fit parameters for linear background stemming from the diamond and tapered fiber and additional background such as dark counts from the avalanche photo diodes (APD) and residual stray light, respectively. Further details regarding the saturation fitting can be found in App. A.

For the same neutral NV as discussed in the paragraphs above, this analysis reveals 74±2 kcps, 104±1 kcps and 107±3 kcps for collection via the objective, fiber end one and fiber end two, respectively (see Fig. 5.18 a) and Fig. 5.22). In total 211 ± 3 kcps single-mode single photons originating from the fiber were measured. The efficiency to detect such a fiber coupled single photon was limited by the transmission of the filter stages and the quantum efficiency of the APDs (taken from APD datasheets). These efficiencies were determined to be $\nu = 0.33$ for emission from fiber end one and $\nu = 0.29$ for fiber

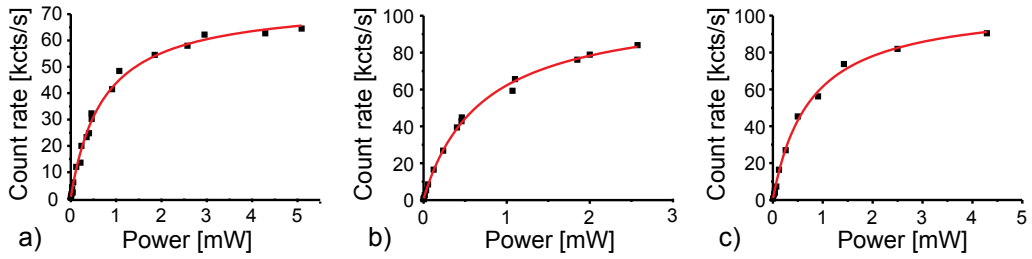

Figure 5.22: a-c) Saturation measurements of the NV from Fig. 5.19 c). Fitting (red solid lines) was done according to text. This analysis reveals a) 74 ± 2 kcps, b) 104 ± 1 kcps and c) 107 ± 3 kcps for collection via the objective, fiber end one and fiber end two, respectively (see Fig. 5.18 a)). In total 211 ± 3 kcps single-mode single photons from the fiber were measured. The efficiencies to measure a single photon from the tapered region are $\nu = 0.33$ for emission from fiber end one and $\nu = 0.29$ for fiber end two. Taking these efficiencies into consideration, a total number of $(689 \pm 12) \cdot 10^3$ single photons are coupled to the single-mode fiber at saturation intensities.

end two. Taking these efficiencies into consideration, a total number of $(689 \pm 12) \cdot 10^3$ single photons are coupled to the single-mode fiber at saturation intensities. This is the highest reported number of single-mode fiber coupled single photons originating from an NV center. This number corresponds to an estimated near-field coupling efficiency of 1.7 %, assuming an internal NV quantum efficiency of one [133] and using a lifetime of 25 ns [134] for a diamond nanocrystal ($690{,}000 \cdot 25\,\text{ns} = 1.7\,\%$). Sending all collected photons to one end of the fiber for accumulated collection is straightforward, e.g., by adding a fiber Bragg grating mirror to the other side [135].

5.3.5 Experimental challenges

Despite the presented advantages, some drawbacks of the tapered fiber system have to be pointed out. The tapered fiber is very sensitive to any kind of particle deposition, for example caused by dust from normal air environments where its transmission degrades within minutes. Therefore the tapered fiber has to be operated in a clean-room environment of at least class 1000 [97]. If operated in a class 10 environment, transmission endures for months as was tested within adequate clean-room facilities.

Background fluorescence plays a major role when working in the regime of single photons. Background fluorescence originating from fiber coupled excitation laser light could not always be neglected. At 1 mW excitation, a typical NV excitation power for the setup, 10 nW are coupled to the fiber and cause background in the orders of magnitude of 10^3 to 10^4 kcps. To overcome this problem, a bleaching method was

developed. Substantial reduction of background fluorescence can be achieved with such a bleaching method. About 100 µW of 532 nm laser light was guided for several minutes up to several ten minutes through the fiber to the tapered region. Thereby, fluorescent particles are bleached and fluorescent background was reduced one to two orders of magnitude. Over a time period of ten minutes, the fluorescence recovered partly.

When this bleaching method was applied, cross-correlation measurement between fiber end one and fiber end two revealed $g^{(2)}(0) = 0.28$ for an NV center. This proves real single photon character of the fiber coupled photons, even when taken several ten minutes after bleaching.

Note also, that the coupling efficiency of the laser pump to the tapered fiber mode can be controlled by the laser polarization. By changing the excitation laser light from circular to linear polarization and by appropriate rotation, background could be reduced irrevocably by a factor of up to six.

5.3.6 Fiber-integrated 50:50 beam splitter

The correlation measurement shown in Fig. 5.21 c) already demonstrates that the tapered fiber represents a beam splitter (BS). In order to quantify the branching ratio fluorescence spectra taken from a single diamond nanocrystal at both fiber ends were quantitatively evaluated, see Fig. 5.23. A splitting ratio of 56:44 was found. The

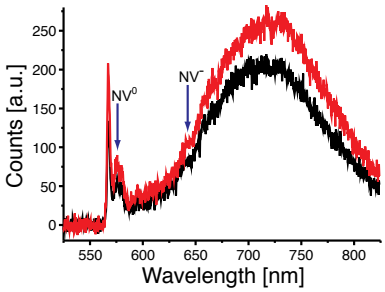

Figure 5.23: Spectra of several NVs from a single diamond nanocrystal measured via fiber end one and fiber end two (see Fig. 5.18 a)), depicted with a black and a red line, respectively. The integrated intensities have a ratio of 56:44. Blue arrows indicate the zero phonon lines of neutral (575 nm) and negatively charged (637 nm) centers.

deviation from a perfect 50:50 ratio is comparable to commercially available cube BS. Yet, such an integrated nearly 50:50 beamsplitter has some advantages over a bulky cube BS or a lossy fiber BS. The tapered fiber integrated BS could be exploited for the realization of a quantum number generator [136, 137]. True random number generation

is an important building element for the realization of e.g. quantum key distribution schemes (see Sec. 8.2).

5.3.7 Summary and outlook

In summary, a new fiber coupled diamond-based single photon system was introduced in this section. Single diamond nanocrystals containing nitrogen vacancy defect centers are deposited on a tapered fiber of 273 nm in diameter providing a record-high number of 689,000 single photons per second from a defect center in a single-mode fiber. The system can be cooled to cryogenic temperatures and coupled evanescently to other nanophotonic structures, such as microresonators. It is suitable for integrated quantum transmission experiments, two-photon interference, quantum-random-number generation and nano-magnetometry. The system represents a flexible tool for integrated quantum technology and nanophotonics.

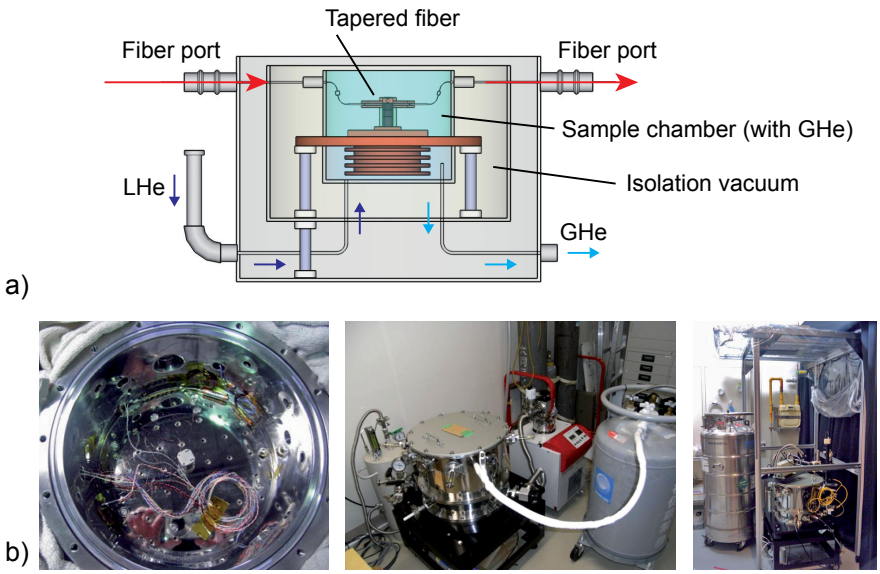

Figure 5.24: a) Sketch of the home-built cryostat developed in the group of Prof. Takeuchi [138]. The chamber has a diameter of roughly 30 cm, 8 optical fiber I/O ports and can be cooled down to temperatures around 10 K. LHe stands for liquid helium, GHe for gaseous helium. b) Photographic images of the chamber, the cryostat and the arrangement of the cryostat inside a home-built clean-room housing, respectively.

The efficiently single mode fiber coupled single photons could be used for various quantum optical experiments. One is the generation of indistinguishable photons for a

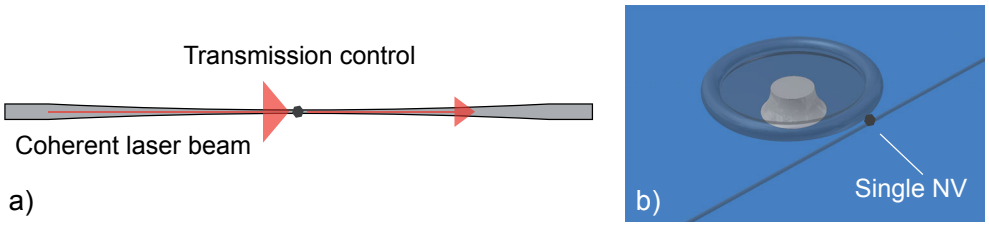

Figure 5.25: a) Sketch of a transmission control scheme via a single NV defect center coupled to a tapered fiber mode [143]. b) Sketch of using the tapered fiber system to couple a single NV to toroidal microresonators. The fiber simultaneously serves as nanopositioning system for the NV and efficient in- and out-coupler of the resonator mode [146].

Hong-Ou-Mandel interference experiment [139]. Such an experiment with NVs has been realized for bulk diamond [140], but not yet for nanocrystals. It is more challenging to find lifetime limited emitters in diamond nanocrystals with low spectral diffusion [86]. For such an experiment a pulsed excitation at low temperatures ($< 10\,\mathrm{K}$) and a length difference of the two fiber ends matching the time difference between repeated excitation events can be used [141]. Indeed, a tapered fiber with a diameter of 300 nm was successfully cooled to 7 K and subsequently heated to room temperature without breaking. For cooling of the tapered fiber system, a home-built cryostat system was used. It was developed in Prof. Takeuchi's group [138]. A photographic image of the cold finger exchange gas cryostat 'Taiko' is depicted in Fig. 5.24.

Moreover, the tapered fiber system as opposed to other fiber coupling architectures, e. g. end-facet coupling (see Sec. 5.2), allows measurements in transmission as sketched in Fig. 5.25 a). This is a requirement for the implementation of single photon nonlinearities [142], single photon transistors [143] or quantum phase gates [144, 145].

Finally, the NV center - tapered fiber system can be mounted on a piezo translation stage and used as a nano-probe. One application would be to locally probe the magnetic field via the NV^- center's electron spin [147]. In this way the NV center on the tapered fiber could also be coupled evanescently to microresonators in order to enhance the spontaneous emission rate [8, 146] or to perform cavity quantum electrodynamics [148] as sketched in Fig. 5.25 b). Evanescent coupling of about five NVs inside a diamond nanocrystal to a toroidal resonator was also demonstrated within this thesis and is described in Sec. 5.4.3. The next step would be to combine both experiments, i.e. couple a single NV to the optical mode of a resonator.

5.4 Coupling to resonant structures

5.4.1 Introduction

The controlled coupling of single quantum emitters to resonant structures allows implementation of a wide range of applications. For example, reducing the emitter's fluorescence lifetime would allow higher bit rates in quantum communication induced by the so called Purcell factor $F_c \propto Q/V_{Eff}$ [149]. Here, Q is the quality factor $Q = \frac{\Delta\nu}{\nu_0}$ which describes the energy loss of a cavity with ν_0 the frequency of the light and $\Delta\nu$ the resonance width. $V_{Eff} = \left(\int_V \mathrm{d}\boldsymbol{r}\, \varepsilon(\boldsymbol{r})\left|\boldsymbol{E}(\boldsymbol{r})\right|^2\right) / \left(\max\{\varepsilon(\boldsymbol{r})\left|\boldsymbol{E}(\boldsymbol{r})\right|^2\}\right)$ is the effective mode volume of the resonator with E the electric field. Q and V_{eff} are the key parameters for an efficient emitter-cavity coupling. For a maximum Purcell factor, Q/V_{eff} should me maximized [150, 151].

In this section, the controlled coupling of quantum light sources to different types of resonators is presented. Again, similar to the previous sections, a hybrid bottom-up approach was pursued.

5.4.2 Coupling of an NV defect center to a spherical resonator

Motivation

To realize a controlled bottom-up assembly of a coupled system consisting of a single quantum emitter and a resonant structure, two approaches can be taken. The first one is the manipulation of single nanoparticles and its controlled deposition on the structure. This approach was used in the previous sections. Yet, it is more challenging to manipulate nanoparticles than spherical microparticles. Single spherical microresonators for example can be assembled to more complex structures such as photonic molecules [152, 153]. Also coupled resonator optical waveguides have been realized in a bottom-up approach with the help of a fiber tip manipulator [100, 154]. This integrability and their high quality factors of up to 10^6 make these microresonators an ideal cavity system for the controlled coupling to single defect centers in diamond nanocrystals.

Preparation of diamond nanocrystals and microresonators

Diamond nanocrystals containing single NV centers (25 nm average size) were spin-coated on a cover slip as described in Sec. 3.3. Again, their single NV defect centers are employed as single photon emitters. Polystyrene microspheres (MicroParticles, Germany) with a diameter of roughly 5 µm were applied as spherical microresonators.

They were dissolved in isopropanol. A suitably concentrated solution was drop-casted onto the prepared diamond sample to assure homogeneous distribution on the cover slip as described in Sec. 3.2. The sample was then placed in the inverted confocal microscope for optical access to the diamonds. A scanning near-field optical microscope (SNOM) can be integrated into the setup with manipulation access from top (Sec. 4.1.2).

Coupling multiple single NVs to the same optical modes of a resonator

The position of microspheres can be controlled via the tip of the SNOM as described in detail in Sec. 3.5.1. A single one can be picked up from the cover slip and kept in an uphold position until a suitable diamond nanocrystal with a single NV has been selected via measurements of its spectrum and its second order auto-correlation function as is illustrated in Fig. 5.26 a-c). Subsequently, with the diamond in the focus, the microsphere is lowered on top of it. With successful assembly of the system and its removal from the cover slip (as sketched in Fig. 5.26 d)), the optical signal of the NV will diminish. Focus re-adjustment allows recovery of the signal and furhter analysis.

If the crystal is attached to the sphere, not only can it be manipulated. Also, and more interesting under quantum optical considerations, the NV couples to the high Q modes of the resonator. The coupling can be seen in the spectrum in Fig. 5.26 e). The most pronounced resonances have a modal number of $l = 1$ and a Q factor of about $3.0 \cdot 10^3$ to $3.5 \cdot 10^3$. A more detailed analysis of these modes can be found in [155]. $g^{(2)}(0) = 0.37$ proves, that resonator coupled light still has single photon character (Fig. 5.26 f)).

After deposition of a first NV containing diamond crystal, a subsequent deposition step can be performed to couple a second diamond to the microsphere as illustrated in the sketch of Fig. 5.26 g). The procedure is the same as before. While the diamond-resonator system is retracted from the surface, a second fluorescent diamond crystal can be selected and kept in the focus of the laser. The spectrum and the auto-correlation function of such pre-selected fluorescent diamonds are depicted in Fig. 5.26 h) and i) (black and red curves: diamond one and two, respectively). Then, by approaching and retracting the microsphere, the second diamond is picked up and its single NV is coupled to the same high Q modes of the resonator. This behavior is visible in the spectra of the collected single photons (Fig. 5.26 j)). Both NV defect centers can be addressed separately. The comparison of both spectra reveals that they share the same resonator modes.

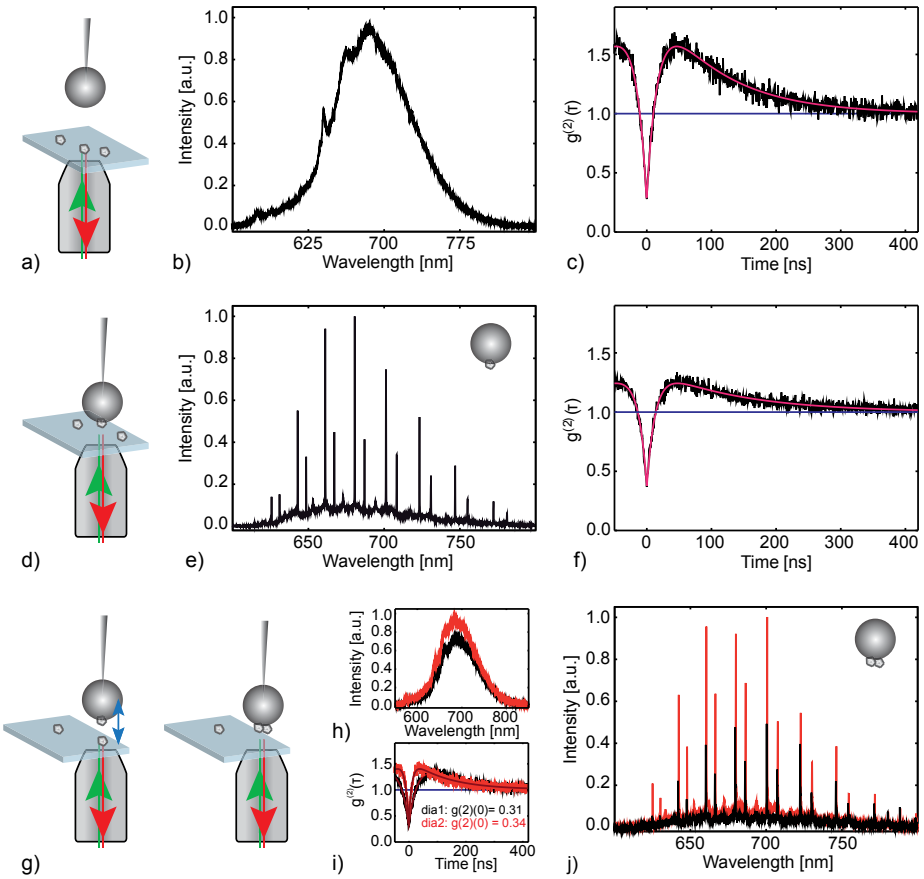

Figure 5.26: a) Sketch of the analysis of a single NV defect center isolated on the cover slip. The defect inside the diamond nanocrystal is excited with a 514 nm laser. It is separated from the NV emission with a 550 nm longpass filter. b) Spectrum of such a single NV defect center. The appearance of two ZPLs at 575 nm and 637 nm indicates that it is undergoing a continuous change between a neutral and a negative charge state, respectively. c) $g^{(2)}(\tau)$ of the same NV indicating its single photon emission with $g^{(2)}(0) = 0.27$. d) Sketch of a microresonator coupled to a single NV defect. For analysis of the fluorescence emitted by the NV directly and via the modes of the resonator the diamond microsphere system is lifted two to three micrometers away from the cover slip. e) Spectrum of the single photon emission of such a coupled system. Clearly visible are the different mode families of the resonator [156] and the wide direct emission of the NV. The highest modes have a radial mode number of $l = 1$. f) $g^{(2)}(\tau)$ of the same coupled NV proving that the single photon character is preserved with $g^{(2)}(0) = 0.37$, yet is reduced due to increased background fluorescence. g) Sketch of a system consisting of a resonator and two single NVs that are coupled to the same modes. h) Spectra of diamond one and two taken on cover slip (black and red line, respectively). i) $g^{(2)}(0) < 0.5$ for both diamonds reveals single photon emission. j) These spectra of diamond one and two prove for the first time that two single emitters are coupled to the same high Q modes of a microresonator. The red lines in c), f) and i) are theoretical fits (see App. A) to the data.

5.4.3 Coupling of NV defect centers to a toroidal resonator

Motivation

In Sec. 5.4.2, a coupled single emitter - resonator system was presented. It was assembled by bringing a sphere resonator to a diamond nanocrystal containing a single NV defect center. Such a manipulation is only possible for mobile resonators. Future implementations however, will be integrated into semiconductor chips. These on-chip

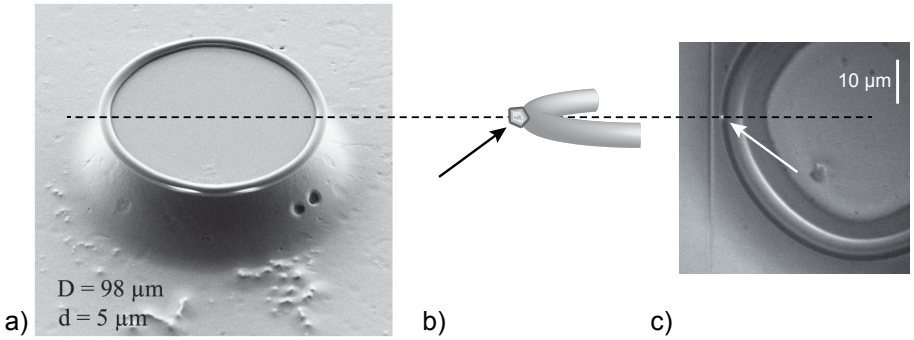

Figure 5.27: a) Scanning electron microscope picture of a toroidal SiO_2 microresonator on a silicon substrate. Such resonators were home-fabricated as described in [106]. D and d represent the outer diameter of the toroid and the diameter of the tube of the toroid, respectively. b) Illustration of a diamond nanocrystal deposited at the equatorial plane of the toroidal SiO_2 structure on the silicon chip. c) Photographic image of a toroidal resonator and a fluorescent diamond nanocrystal. The arrows in b) and c) indicate the position of a diamond nanocrystal containing fluorescent NV defect centers.

devices can be fabricated in a scalable way and complex optical structures can be designed. One type of optical microresonator that was implemented in such a structure, was a toroidal microresonator [157]. It is a whispering gallery mode type resonator based on the same principle as a sphere resonator (see Sec. 5.4.2). Such toroidal resonators achieve even higher Q factors of up to 10^8 [158] and are therefore even more suited for cQED experiments than the applied sphere resonators. The toroidal microresonators were produced as described in [106]. A scanning electron microscope image of such a home-fabricated resonator is depicted in Fig. 5.27 a).

Preparation of the single emitter - microresonator system

A pre-selected diamond nanocrystal containing only several NV defect centers was deposited in the equatorial plane of the toroidal SiO_2 structure as illustrated in Fig. 5.27 b), where the overlap with the evanescent field from fundamental whispering

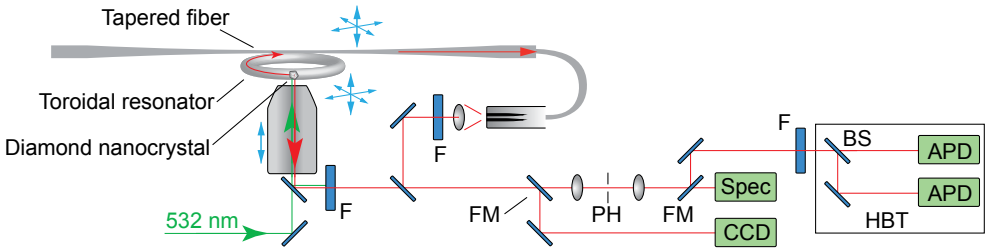

Figure 5.28: Illustration of the setup to investigate the diamond nanocrystal deposited on a toroidal microresonator. A green 532 nm laser was used to excite the defect centers inside the diamond nanocrystals via an air objective with an NA of 0.9. The fluorescence light was either collected with the same objective or via the tapered fiber and sent to the detection unit. F stands for filter, FM for flip mirror, PH for pinhole, BS for beam splitter, HBT for Hanbury Brown and Twiss setup, Spec for spectrometer, and APD for avalanche photo diode.

gallery modes has a maximum [159]. The quantum character of the diamond fluorescence was confirmed by measurements of the second order auto-correlation function. A detailed description of the procedure which was applied to deposit the nanocrystal, was introduced in Sec. 3.5.2.

Optical properties of the NV defect center - resonator system

The single photon emission of the fluorescent diamond nanocrystal deposited at the equator of the toroid was analyzed spectrally. The spectra in Fig. 5.29 a) clearly indicate, that the emission is stemming from NV defect centers. The peaks around 575 nm and 637 nm indicate that the NV defect centers are undergoing a charge state conversion process between NV^0 and NV^- as discussed in Sec. 2.4.1.

Furthermore, the black curve in the spectrum in Fig. 5.29 a) indicates, that the defect centers couple to the optical modes of the toroidal resonator. The spectrum is strongly modulated in comparison to the red curve. The black curve was recorded via a tapered fiber (diameter of 900 nm, see Sec. 3.4.1) that allows efficient coupling of the fiber mode to the high Q optical resonator modes. Therefore, only single photons were detected, that first coupled from the defect centers to the resonator modes and then from the resonator modes to the tapered fiber. In contrast, the emission from the defect centers in the red spectrum was recorded directly via the confocal microscope. The single photons did not couple to the resonator mode. Therefore, the spectrum is not modulated.

To confirm that the modulation is caused by the resonator and not by interference in the mode of the tapered fiber, a Fourier transformation was performed. The spectrum

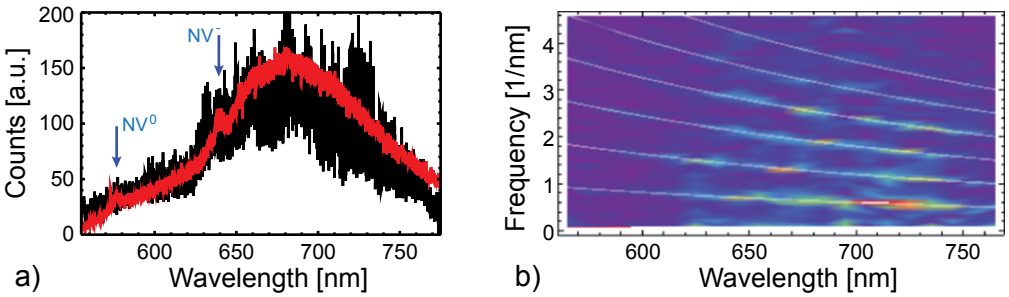

Figure 5.29: a) Spectra of the emission of several NV defect centers deposited on a toroidal resonator. The red curve represents the spectrum of the photons collected via the confocal microscope. These photons did not couple to the modes of the resonator. The black curve represents the spectrum of the photons collected by a tapered fiber which was coupled to the modes of the resonator (see Fig. 5.28). These photons first coupled to the resonator and from there to the tapered fiber. Therefore, a modulation caused by the resonator modes is clearly visible. b) Frequency amplitudes of Fourier transformed 10 nm wide segments of the black spectrum in a). Red color coding represents a high intensity, dark blue color coding a low intensity. The white lines indicate the theoretically calculated resonances for a free spectral range of a toroid with a diameter of 65 µm.

was divided into segments of 10 nm width. Each segment was Fourier transformed. The frequency amplitudes of each segment are plotted together in Fig. 5.29 b). Red color coding represents high intensities, dark blue color coding low intensities. The regions of high intensity agree well with the theoretical expectations for a toroid with a diameter of 65 µm (white lines in Fig. 5.29 b)). The diameter of the toroid was confirmed by a microscopic measurement which revealed a diameter of 64.3 ± 1 µm.

To prove that the quantum character of the light is conserved even if the diamond nanocrystal is deposited on the toroid, the second order auto-correlation function was measured. The result is shown in Fig. 5.30 a). After normalization, $g^{(2)}(0) = 0.84$ indicates that, in fact, the light collected has non-classical single photon character. With $g^{(2)}(0) = 1 - 1/\mathrm{N} = 0.84$, a number of $\mathrm{N} = 6$ single emitters is determined (see Sec. 2.1).

This value is confirmed by cryogenic experiments at about 5 K. For these measurements, the chip with the toroid was placed inside a cold finger cryostat (see Sec. 4.4.1). A spectrum of the NV defect centers was collected via the confocal microscope with an NA of 0.7 through the vacuum window of the cryostat. The evaluation of the spectrum reveals five or six NV^- ZPLs. The peak at 637 nm cannot be resolved but is wider than the others. Therefore, it is possible that two defect centers contribute to this peak. However, both values for the number of single defect centers of five or six, are in

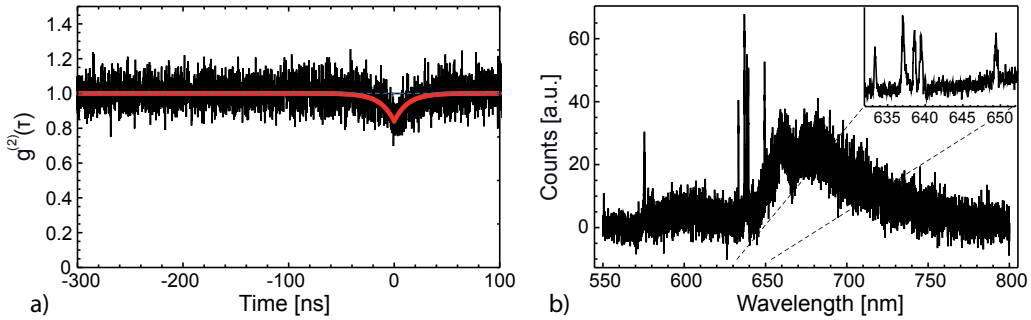

Figure 5.30: a) Second order auto-correlation data of the NV defect centers inside the diamond nanocrystal deposited on the toroidal resonator. $g^{(2)}(0) = 0.84$ indicates, that roughly six single quantum emitters contribute to the fluorescence (see Sec. 2.1). b) Spectrum of the emission of the same NV defect centers at a cryogenic temperature of about 5 K. The inset shows a zoom in on the ZPLs from 632 nm to 652 nm. Five to six ZPLs are visible. Around 637 nm, either one or two ZPLs are present. This is in accordance with the correlation data in a).

agreement with the measured second order auto-correlation function.

Furthermore, the cryogenic measurement shows, that indirect cooling of the diamond matrix down to about 5 K is possible by thermal heat conduction via the silicon wafer and the silica toroid. This is an important pre-requisite for further cryogenic experiments with diamond nanocrystals coupled to SiO_2 toroidal resonators.

5.4.4 Summary and outlook

In this section, controlled coupling of single emitters to high-Q whispering gallery resonators was shown for two different resonator designs.

In Sec. 5.4.2, a single photon emitter was coupled to a high-Q whispering gallery mode resonator in a controlled manner for the first time. Furthermore, a second single photon emitter was coupled to the same resonator modes, showing the scalability of such systems.

In Sec. 5.4.3, it was shown for the first time, that diamond nanocrystals containing only several NV defect centers can be coupled to the optical modes of a toroidal resonator in a controlled manner. This is also the first experiment, in which such few defect centers in diamond were coupled to an integrated on-chip system. Furthermore, the system was cooled down to cryogenic temperatures of about 5 K where the ZPLs of the defect centers were clearly visible in the spectrum. Due to the strain induced spectral shift of the individual ZPLs, they can be clearly distinguished. This even allows coupling of a single ZPL to the optical modes of the toroidal resonator. However,

the coupling of the NV defect centers to the resonator modes was too weak to confirm significant influence on the quantum system. This might be due to the size of the nanocrystal that was deposited on the toroidal resonator. In Sec. 5.3, a tapered fiber system was presented with a roughly 30 nm sized diamond nanocrystal coupled to it which contains only a single NV^- defect center. The defect center in such a small crystal could be coupled stronger to the resonator modes. Combining both techniques would therefore allow the assembly of advanced single emitter - resonator systems.

The two experiments introduced in this section are remarkable steps towards scalable cavity quantum electrodynamics (cQED) experiments at cryogenic temperatures around 5 K to either realize experiments in the strong coupling regime or Purcell enhancement of emission stemming from the ZPL [8, 104, 138, 160].

6 Solid immersion microscopy

In this chapter, a solid immersion microscope (SIM) is presented. This conceptually new method for optical investigations of diamond nanocrystals was developed in the course of this thesis. The idea is to exploit the advantages of solid immersion microscopy [125] and build a bright single photon source with collection efficiencies that have not been achieved with conventional techniques.

In Sec. 6.1 the basic principle of a SIM and pre-characterizing studies of the implemented SIM are discussed. In Sec. 6.2 experimental results are presented of integrating diamond nanocrystals containing single NV defects into the SIM. It provides the highest collection efficiencies for single NV defects reported. It can be applied at room temperature and also at cryogenic temperatures.

Parts of the results of this chapter were published in Schröder *et al.* 2011a.

6.1 Solid immersion microscope

The solid immersion microscope that was developed in the course of this thesis follows the same basic principles that were first introduced by Mansfield and Kino in 1990 [125, 161]. Its principle is very similar to the idea of an oil immersion microscope which has become standard equipment today. In contrast to oil immersion techniques, the solid immersion microscope can be used at cryogenic temperatures in a helium cryostat as described in Sec. 4.4.

The basic idea is to increase the resolution of a microscope by reducing the effective wavelength of the analyzing light by the refractive index n of the material adjacent to the sample (see Fig. 6.1). It has become a powerful tool for many different applications where maximal light sensitivity and resolution are a crucial property of an optical experiment [162].

To benchmark the resolution of a microscope the Rayleigh criterium can be applied. It is defined as the minimal distance r between two point like objects when these can

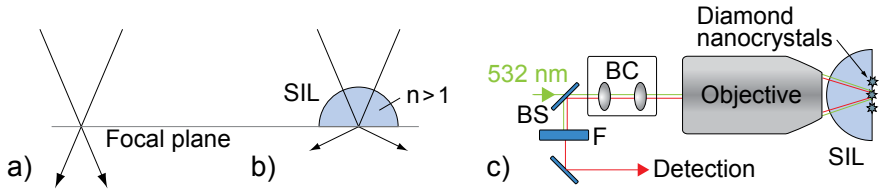

Figure 6.1: a) Sketch of a focussed laser beam by means of ray optics. The path of light is not altered in the focal plane. b) Sketch of a focussed laser beam with a hemispherical solid immersion lens (SIL). The SIL is placed in such a way that the flat air interface is located in the focal plane and the center of the hemisphere in the focal spot. The light is refracted at the air interface. c) Sketch of a solid immerison microscope. The principle is equivalent to a standard air microscope, except that the SIL serving as optical element and sample holder is placed in the light beam. For example, diamond nanocrystals can be deposited on the flat side. BS stands for beam splitter and BC for beam control.

still be resolved, $r = 0.61\lambda/NA$. The refractive index n is hidden in the expression of the numerical aperture $NA = n \cdot \sin(\alpha)$. For example, in the case of an oil immersion microscope, $n_{Oil} \approx 1.5$, the resolution is increased by a factor of 1.5. For a material with $n = 2.1$ the resolution could be enhanced by a factor of 2.1.

Additional to the increase in optical resolution, four other (partly correlated) effects make immersion microscopes attractive for the investigation of classical and quantum optical systems.

I) **Reduction of the focal spot size** as direct consequence of the enhanced resolution. Due to the reduced spot size, the intensity of a focussed laser increases. Therefore, the interaction of the light with the dipole is enhanced and less excitation power is needed to excite a quantum system, e.g. a single dipole. The experimental evaluation of the spot size of the implemented SIM is presented in Sec. 6.1.4.

II) **Enhancement of the objective acceptance cone** of a point like source and hence an increase in light collection efficiency is achieved. This is expressed by $NA = n \cdot \sin(\alpha)$ and illustrated in Fig. 6.1 b).

III) **Increase of the collection angle for bulk material.** For a SIL that is processed into a high index bulk material like diamond, the angle of internal reflection for light leaving the bulk at the usually planar surface is enhanced by far. For example, as illustrated in Fig. 6.2 e), for a hemispherical SIL in diamond with $n = 2.4$, the collection angle would increase from 24.6° to 62.2° for an objective lens with NA of 0.9.

IV) **Modification of the emission pattern of a dipole** in the vicinity of material interfaces with different refractive indices. This modification is a result of the altered density of states $\rho(\omega) = \mathrm{nV}\omega^2/(\pi^2\mathrm{c}^3)$, where ω is the emission frequency and c the speed of light in vacuum. The altered spontaneous emission rate can be derived from Fermi's golden rule [163] and expressed as $\Gamma_0(\omega) = \frac{\mathrm{n}|\boldsymbol{\mu}|^2\omega^3}{3\pi\varepsilon_0\hbar\mathrm{c}^3}$, with μ the transition dipole moment, ϵ_0 the dielectric constant and and $\hbar$ the reduced Planck constant [87]. The modification of the emission patern only emerges when the flat side of the SIL adjoins to a material with a different refractive index. In this scenario the SIL acts as a near field optical element. The modification of the emission that can be theoretically expected was simulated with a FDTD method. The results are presented in Sec. 6.1.5.

All these effects induced by a solid immersion microscope are very important properties for some of the experiments that have been carried out during this thesis. Furthermore, they allow investigations of the properties of single NV defect centers, that would not be possible with standard microscopes due to insufficient collection efficiencies, e.g. the incoherent down-conversion of single photons into the infrared wavelength regime (see Sec. 8.3).

6.1.1 Principle of a solid immersion microscope

The functional principle of the SIM is very similar to that of an oil immersion microscope as was already pointed out in the introduction. The higher the index of refraction of the immersion medium, the higher the resolution, the collection angle and the collection efficiency. In contrast to oil immersion microscopy, the light passes from the immersion medium to air and then to the objective or vice versa. Two different lens designs have been studied, the hemispherical SIL [125, 164, 165], and the so called super-hemispherical, or Weierstrass SIL [166--168].

In the case of a hemispherical solid immersion lens design, the light passes the air interface via perpendicular incidence. Hence, no refraction takes place, and the optical path is not altered. For perfect alignment and fabrication properties, no chromatic aberration would take place. Yet, for imperfect hemispheres and alignment, chromatic aberration is observed as will be discussed later.

The Weierstrass SIL is a refracting optical element itself, as is illustrated in Fig. 6.2 c). It can be described as a ball lens that is truncated at the inner aplanatic point [169]. The height of the truncated sphere is $(1 + 1/\mathrm{n})\mathrm{r}$ with the radius of curvature r. It will

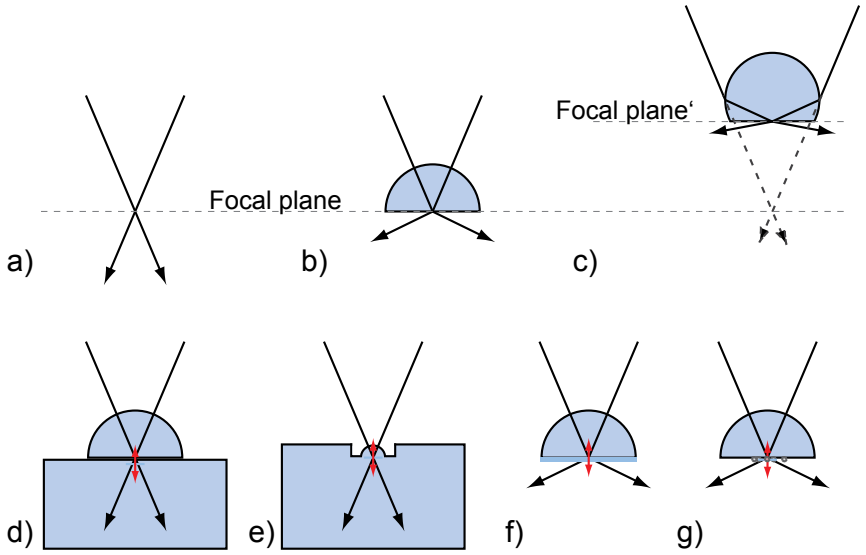

Figure 6.2: a) Sketch of a focussed laser beam by means of ray optics. The path of light is not altered in the focal plane. b) Sketch of a focussed laser beam with a hemispherical SIL. c) Sketch of a focussed laser beam with a super-hemispherical SIL. In contrast to a hemisphere the light is refracted at the spherical side of the SIL. d-g) Sketches of different configurations of a diamond solid immersion microscope that were realized. In d) a mm-sized SIL is placed on top of a bulk diamond sample [10, 170]. e) A µm-sized SIL is etched into a bulk diamond [82]. f) A mm-sized SIL is fabricated into diamond. The SIL is made of ultra-pure diamond but the backside is made of diamond containing NV defect centers. As both components were grown onto each other, no air layer reduces the imaging quality [83]. g) A mm-sized SIL is used as a substrate holder for diamond nanocrystals. This configuration was realized in the course of this thesis. The black arrows indicate two rays of a focussed light beam. The red arrows indicate an optical dipole.

change the actual geometrical NA of the system and reduce the focal spot to $1/n^2$ of its value in vacuum. Disadvantages are the monochromatic performance, restricting its application to one wavelength, the strongly reduced field of view by $1/n^2$, and reduced tolerances for fabrication imperfections and alignment.

As all experiments described in this thesis were carried out with hemispherical SILs, the theoretical treatment is only carried out for this design. Various modifications of such hemispherical SILs have been studied in the literature. They are introduced in the next section and are sketched in Fig. 6.2 d-g).

6.1.2 Solid immersion lenses

The solid immersion lens is the main element of a SIM. Hemispherical SILs can be realized with different geometries and modifications. Presently, the following

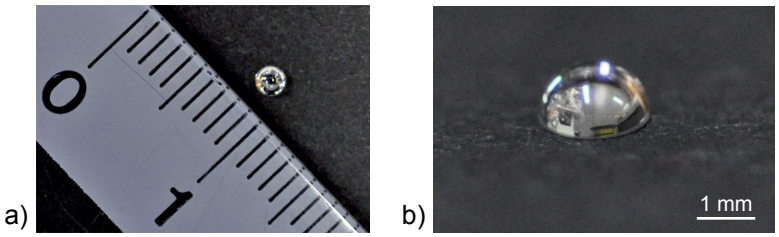

Figure 6.3: a) and b) Photographic images of the applied SIL type. The hemisphere has a radius of 1 mm and consists of cubic zirconium (ZrO_2). It is transparent in the visible spectral region. Details are described in the text.

configurations have been studied in the context of single defect centers in diamond. The configurations are sketched in Fig. 6.2 d-g).

The first experiments with diamond SILs were performed in 1996 with a diamond hemispherical SIL that was placed on top of a bulk diamond as illustrated in Fig. 6.2 d) [10, 170]. The collection efficiency of single SiV defect centers was enhanced by a factor of six but overall count rates were limited to roughly 1.5 kcts/s in saturation, about 1000 times less than realized within this thesis. Manufacturing imperfection and particularly the air gap existent between the SIL and the bulk caused collection inefficiencies, suggesting other configurations.

Very recently, three different configurations were realized by different groups. A 5 µm hemisphere was fabricated via focussed ion beam etching (FIB) at an arbitrary position of a bulk diamond (see Fig. 6.2 e)), resulting in 345 kcts/s of single photons from a single NV^- defect center [82]. This technique was further developed to etch 8 µm SILs at initially located suitable defects with respect to registration marks [171]. Secondly, monolithic SILs (see Fig. 6.2 f)) with a radius of 1 mm were processed into synthetic diamond using a combination of laser and mechanical processing stages. From an incorporated NV^- defect, 493 kcts/s single photons were collected [83]. Finally, a configuration with preselected diamond nanocrystals was realized in the course of this thesis (see Fig. 6.2 g)). The results [115] will be presented in detail in the following sections. In the beginning, a pre-characterizing study of the optical properties of the SILs is presented.

Properties of implemented SILs

The implemented SILs are hemispheres with a radius of 1 mm. They consist of cubic zirconium (ZrO_2). ZrO_2 is a transparent ceramic and has similar properties to diamond

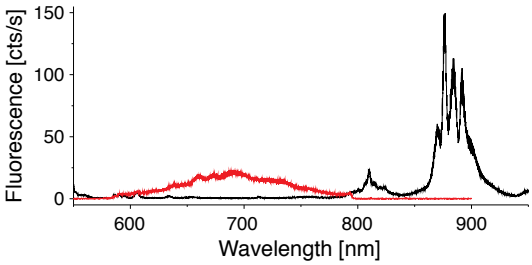

Figure 6.4: Spectrum of the fluorescence of a SIL (black curve) under 532 nm excitation with an excitation power of 933 µW. Spectrum of a single NV^- center deposited on a SIL, emission cut off by 590 nm long pass and 795 nm short pass filters (red curve) for similar excitation powers.

[172]. Figure 6.3 shows a photographic image of such a SIL. As well as diamond, ZrO_2 is also particularly hard and has a similar refractive index n of 2.17 at $\lambda = 600\,\text{nm}$. Hence, it almost matches the index $n_{\text{Diamond}} = 2.4$ of diamond. A strong deviation $> 30\%$ from n_{Diamond} would result in reduced optical performance [166].

The SILs were purchased from a commercial vendor (Mikrop, Switzerland). They had been fabricated from spheres that were ground to a hemisphere. The process accuracy is limited to $1\,\text{mm} \pm 2\,\mu\text{m}$; not precise enough to meet the requirements as discussed in Sec. 6.1.3. Therefore, pre-selection of the SILs was necessary, see Sec. 6.1.4.

The particular ZrO_2 ceramic that the applied SILs have been fabricated of, has fluorescence properties well suited for the investigation of quantum systems with emission between 620 nm to 790 nm. The spectrum under green 532 nm excitation in Fig. 6.4 indicates, that the SIL background fluorescence can be filtered with a 590 nm or 620 nm long pass filter and a 790 nm short pass filter.

6.1.3 Theoretical treatment: Magnification and aberration

A perfect hemispherical SIL does not alter the optical path of the illumination light for a perfect on-axis positioning and illumination. In this case, all light rays pass the air interface on the spherical side under normal incidence. For a non-perfect hemisphere, misalignment, and off-axis illumination, the SIL will introduce aberrations and reduce the focus quality. For off-axis illumination or off-axis imaging, a simple model can be derived by trigonometry and means of approximations for small shifts. A detailed analysis of the influence of fabrication imperfections and misalignment can be found in the literature [173, 174]. The following equation describes the lateral displacement r'

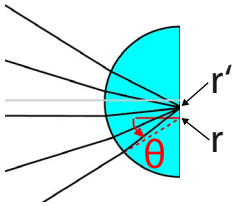

Figure 6.5: Sketch of the optical path of light inside a SIL. In this configuration with off-axis illumination the light rays are being refracted at the spherical side. This causes a shift of the focus from position r to posititon r' = r/n towards the center of the SIL. The angle θ quantifies the refraction at the spherical air interface.

of a ray that would have hit the focal plane at r under an angle θ without the SIL.

$$\mathrm{r'} = \frac{\mathrm{r}}{\mathrm{n}} + \frac{\mathrm{r}^2}{\mathrm{na}}\left(1 - \frac{1}{\mathrm{n}}\right)\sin(\theta) + \mathrm{O}(\mathrm{r}^3) \tag{6.1}$$

Here, n is the refractive index of the SIL, and a is its radius. The equation is valid for any angle θ as defined in Fig. 6.5.

The first order term describes the focus shift from position r to position r' = r/n towards the center of the SIL in the presence of the SIL. This shift is equivalent to a magnification by a factor of n = 2.17 for ZrO_2. This effect takes place for imaging extended objects and for scanning the focus across the flat back surface of the SIL or vice versa.

The second order term is a function of θ as defined in Fig. 6.5. It can be interpreted as a wavefront curvature at the position of the focus. The bigger the angular misalignment of incoming light beam, objective lens and SIL, the bigger the reduction of focus quality. For estimating a field of view for which a certain image quality can be expected, the so called $\lambda/4$ criterion can be considered [173, 174], where the aberration of the focus can be neglected.

$$2\mathrm{r'} < \left[\frac{2\mathrm{a}\lambda}{\mathrm{n}(\mathrm{n}-1)\sin(\theta_{\mathrm{Max}})}\right]^{1/2} \tag{6.2}$$

For a maximum angle θ_{Max} of 64.1° for an NA of 0.9 of the objective lens, this equation gives a spot diameter of 23.6 µm at 637 nm. Only within this region aberration free access to diamond nanocrystals containing defect centers is achieved. Therefore, to still have access to a high number of defects, the density of nanodiamonds on the backside of the SIL needs to be adjusted properly.

Yet, it has to be denoted, that the area with an acceptable fluorescence collection efficiency can be larger. The experiments described in Sec. 6.2.3 show, that an area of

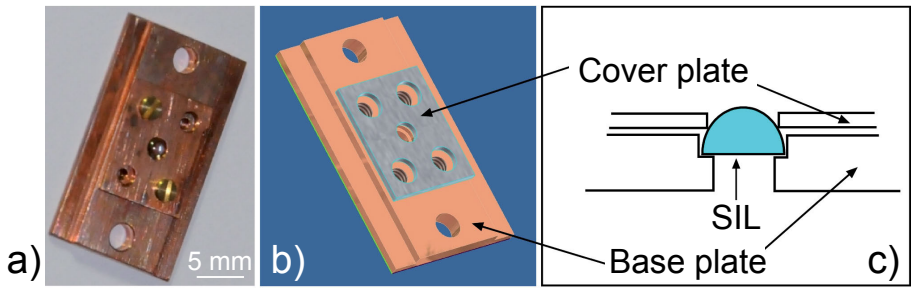

Figure 6.6: a) Photographic image of a copper SIL holder. b) Rendered 3d model of a SIL holder. c) Sketch of the mechanism that clamps the SIL to the base plate.

100 μm^2 around the center of the SIL contains quantum emitters with single photon count rates exceeding 400 kcts/s. Therefore, more than 100 such bright emitters could be found within this region.

6.1.4 Experimental evaluation of microscope properties

Pre-selection of SILs

Not all purchased ZrO_2 hemispheres have the same properties. Due to fabrication faults, a SIL can be limited in its performance. The following imperfections were observed. Material inhomogeneities, like air bubbles inside or scratches outside, of some SILs introduced refraction and thereby reduction of excitation and collection efficiencies. Furthermore, due to fabrication tolerances, some SILs are more congruent with a mathematical hemisphere than others. The differences can be diameter deviation, height deviation, or deviations of the round side from a mathematical circle. Details about the faults and their influence on the optical properties can be found in the literature [173].

To identify the best suited hemispheres, a pre-selection was carried out. The hemispheres were first inspected visually under a commercial microscope. Only those with an adequate appearance were implemented into the confocal microscope, where their focus quality was measured by imaging the reflection of a laser focus onto a CCD camera. The focus quality was evaluated qualitatively by experience and the focus diameter was measured with the CCD camera. Those with acceptable focus properties were used for further experiments.

SIL holder

The SILs were mounted with a self-constructed sample holder as sketched in Fig. 6.6 c). It was designed to guarantee optical access for objectives up to an NA of 0.9 (half angle of 64.2°). Therefore the hole of the cover plate and the step height of in the ground plate were chosen adequately.

Minimal focus size

The minimal focus size of a laser spot on the backside of a SIL was determined experimentally for an objective lens with a numerical aperture of 0.7. To determine this spot diameter, the laser focus was scanned over 50 nm sized beads (Fluosphere, Molecular Probes) imitating a point-like source. The beads were spin-coated onto the

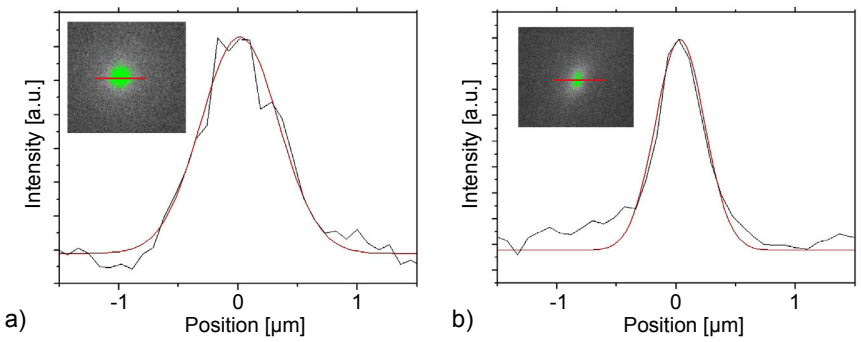

Figure 6.7: Determination of the minimal focus diameter for a focussed laser in a) and with SIL in b). 50 nm sized fluorescent particles were used as point-like light sources and imaged onto a CCD camera. The data points were taken at a longitudinal cut through this intensity distribution (see text for more details). The red curves are Gaussian fits to the data. The inset show the intensity distribution. The green regions are positions where a certain intensity threshold is reached to simulate the spot size as a function of the FWHM.

flat side of the SIL (see Sec. 3.3). They are equipped with fluorescent molecules having an emission wavelength of 605 nm. A green 532 nm laser is used to excite these molecules. The resulting signal was recorded with a CCD camera for each raster position while the laser was blocked with a long pass filter. The intensity distributions of all pictures were added maintaining the original positioning. Thereby, a two-dimensional intensity profile of the focus was rebuilt. The results are displayed in Fig. 6.7. The FWHM of the focus with SIL was determined to be 656 nm and to 376 nm with a particular SIL. This results in a reduction by a factor of 1.74, deviating 20 % from the expected factor of 2.17. For other SILs a factor of 1.9 was estimated, only deviating 12 % from the theoretically

expected value. The mismatch can be explained by fabrication imperfections which cause a deviation from a perfect hemisphere and by misalignment of the objective lens and the SIL relative to the optical axis of the beam. A SIL with theoretically expected properties was not spotted in the batch of SILs investigated.

Magnification

A direct consequence of the reduced focus size and thereby increased resolution is an enhanced magnification. The magnification enhancement of the solid immersion microscope was measured with the help of a micrometer grid with known lattice constant. The grid was illuminated with a white light source and imaged onto the chip of a CCD camera. Although the white light reduces the image quality because the non-perfect hemisphere introduces chromatic aberrations to the image, it turned out to be a reliable method.

By comparing the grid with and without SIL, the magnification ratio can be determined. In Fig. 6.8 the CCD camera image is displayed. The ratio of magnification is 1.9, deviating from the theoretically expected value of 2.17 by 12 %. Hence, the point of view is also reduced by a factor of 1.9. The deviation of 12 % from the expected value can be explained by fabrication imperfections of the hemisphere as was discussed in more detail in the sections above. The results of determining the magnification by simply imaging a grid agree well with the experimental values for the minimal spot size and thereby enhanced resolution.

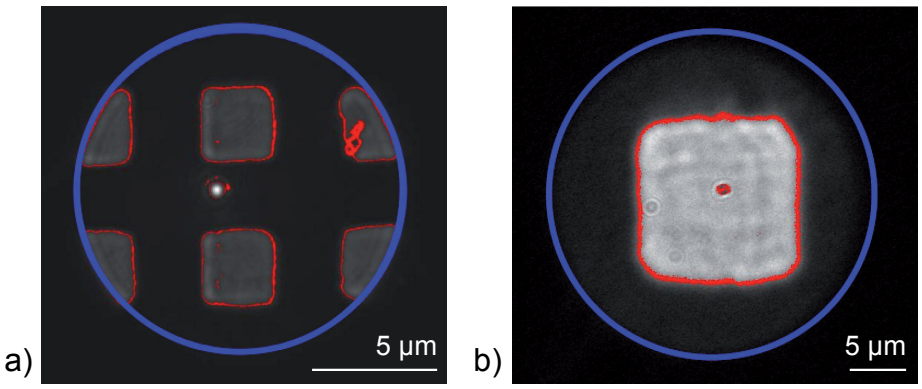

Figure 6.8: Determination of the magnification of the solid immersion microscope for an NA of 0.7. In a) the CCD image of a micrometer grid is displayed taken with an objective lens with an NA of 0.7. The field of view is roughly 28 µm in diameter. In b) the same grid is imaged with the same objective and a SIL. Therefore, the grid is attached to the backside of the SIL. The field of view is roughly 12 µm.

Collection efficiency

The collection efficiency of the solid immersion microscope was determined experimentally. For a SIM with an objective lens with an NA of 0.7 the same fluorescent beads were used as in Sec. 6.1.4. For an objective with an NA of 0.9 a single diamond defect center was used. Both emitter types were excited with a green 532 nm laser. The laser was blocked with a long pass filter.

For an NA of 0.7 the intensities for both directions of emission, through the SIL as well as from the air side, were measured with the same laser intensity. For the beads a 16-fold enhancement of the fluorescence intensity was measured through the SIL compared to the collection from the backside. To reduce measurement uncertainties, the measurement was repeated with eight single beads and averaged. A CCD camera picture for both directions is shown in Fig. 6.9.

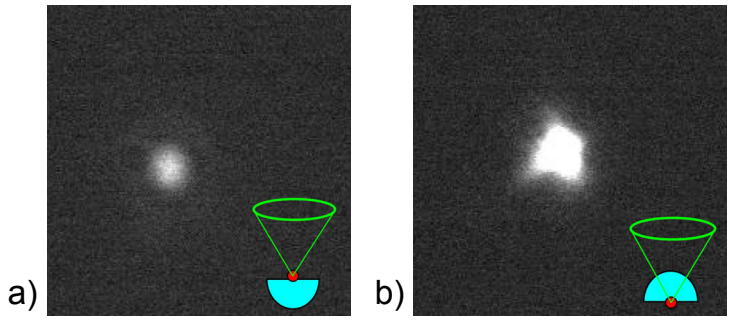

Figure 6.9: Determination of the collection efficiency of the solid immersion microscope with an objective NA of 0.7. Fluorescent beads are used as point-like sources. In a) the fluorescence was collected via the air side and in b) through the SIL. The blurred image in b) is caused by aberration of the SIL.

The result has to be evaluated critically. The molecules incorporated in the beads were not excited in saturation, hence the fluorescence intensity is a function of the laser intensity in the focal spot. This intensity will differ for both directions. Theoretically, the intensity in the focus exactly at the air interface should be enhanced by n^2 for the SIM, resulting in a correction factor of 4.7. This theoretical value needs to be adopted for the experimental situation. The focus will have increased in size by roughly 30 % in diameter for the beads with a size of 50 nm and and an increased interface distance caused by the polymer matrix they are inhibited in [166]. This reduces the excitation intensity enhancement to a factor of only 2.3. This results in an enhancement of the fluorescence intensity through the SIL by a factor of 7.0. This is in very good agreement with the theoretical expectations for an NA of 0.7 as discussed in Sec. 6.1.5. For a

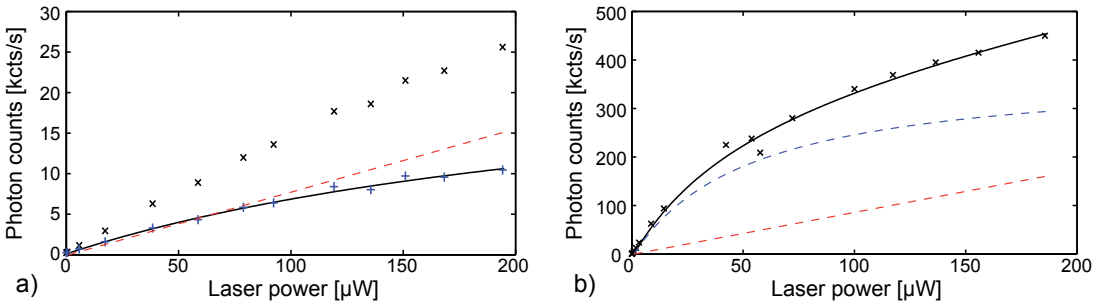

Figure 6.10: Determination of the collection efficiency of the solid immersion microscope with an objective NA of 0.9 for a particular SIL. A single fluorescent NV^- defect is used as a point-like source. The maximum count rates in saturation were determined as a function of excitation power (see Sec. 6.2.3). The data in a) was taken from the air side, the data in b) through the SIL. For the air side, 25 kcts/s in saturation with a saturation power of 279 µW was determined, for the collection through the SIL, 379 kcts/s in saturation with a saturation power of 54 µW. The crosses represent data points, the black lines a fit to the data, the red dashed lines linear background signal, the blue dashed line fluorescence stemming from the NV^- defect center, the blue plus signs data subtracted of measured background.

dipole in front of a dielectric with n = 2.15 (see Fig. 6.15) an enhanced emission into the dielectric of a factor of 7.2 for an NA of 0.7 was calculated.

A very similar analysis was carried out for single NV^- defect centers inside a diamond nanocrystal. This time, the single photons were collected via an objective lens with an NA of 0.9. In this measurement, fluorescence intensities in saturation were calculated (see Sec. 6.2.3). This has the advantage over the previous method, that the increase in excitation for the SIM can be neglected.

For the emission in direction of a particular SIL, 379 kcts/s in saturation for a particular NV^- was measured. For emission into air, 25 kcts/s in saturation was determined, resulting in a factor of 15.2. It can not be guaranteed that the same defect was measured, yet, the excitation intensities for other defects only varied by a factor of 1 to 2 on average for the corresponding direction. Hence, a factor of 7.6 to 15.2 for the intensity enhancement in the SIM is achieved. For another SIL, hence another single defect center, the brightest that was found from the flat side, shows count rates at saturation of 50 kcts/s, which is about 10 times lower than typical count rates of 500 kcts/s from defect centers emitted through this particular SIL. Both results agree with the result determined via the beads (factor of 7 for NA = 0.7) and the theoretical predictions (factor of 7.2 for NA = 0.7 and factor 4.4 to 7, depending on the dipole orientation, for NA = 0.9).

Furthermore, the efficiencies to excite an NV^- defect center can be considered for

both sides. The excitation saturation power for the first NV^- was 54 µW for the air side and 279 µW for the SIL, resulting in a factor of 5.2. For the second defect center analyzed, the saturation power of 440 µW is about 5.5 times higher than average 80 µW for the SIL side, indicating, that the focus spot size is much larger for the air side as expected, see Sec.6.2.3. This agrees well with the theoretically expected spot size reduced by a factor of $n^2 = 4.7$.

Profile of collimated beam of single photons

The far field emission pattern of a single NV^- defect center was measured experimentally. Therefore, a lens with a long focal length was placed into the collimated beam in front of the CCD camera. The resulting image of the intensity distribution of an exemplary single photon emitter is depicted in Fig. 6.11 b). A theoretically determined far field image for a dipole perpendicular to the air interface is depicted in Fig. 6.11 c), according to the simulations presented in Sec. 6.1.5. Both images can only be compared qualitatively. The theoretical simulations predict a far narrower emission cone than found in the experiment. This is difficult to quantify but can qualitatively be explained by a deviation of the SIL from a perfect hemisphere and a distance of the NV defect center of more than 10 nm.

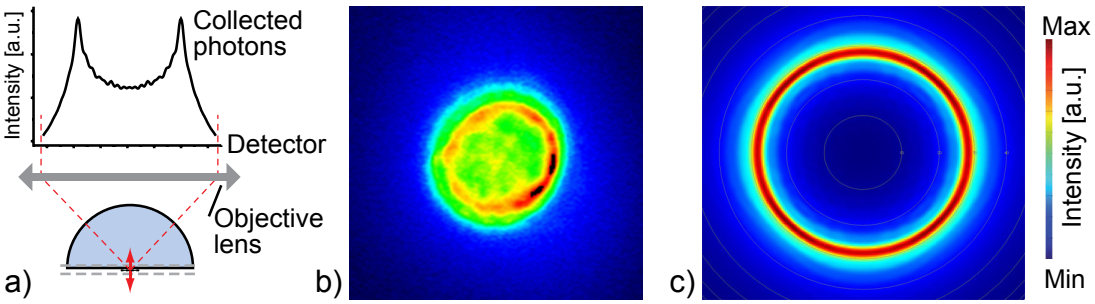

Figure 6.11: Far field emission patterns of photons collected via a high refractive index SIL. a) Schematic of the experimental setup to determine the lateral intensity distribution in the beam. Not shown is the lens system for downsizing the beam diameter to be detected with a CCD chip. b) Lateral intensity distribution of a collimated beam of single photons emitted by a single NV^- center. In contrast to c) a high ratio of evenly distributed fluorescence is found (green colour coding) due to deviations from the spherical symmetry of the SIL. c) Theoretical far field emission pattern of an electric dipole with an emission wavelength of 600 nm. It is located at a distance of 10 nm from a high refractive index dielectric with n = 2.15 (see Sec. 6.1.5).

Confocal implementation

The imperfections of the implemented SIL cause chromatic aberrations. This strongly influences the collimation of the emitted photons, especially for an emitter with a spectrally wide emission like the NV defect center (FWHM of about 100 nm). Because of the badly collimated beam, the confocal behavior at the pinhole is also influenced. Not all wavelengths will be focussed perfectly by the first focussing lens in front of the pinhole as their wavefronts do not arrive perfectly perpendicular to the lens. Therefore,

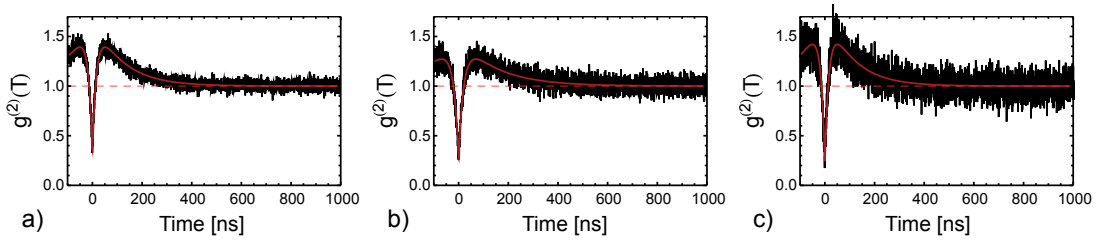

Figure 6.12: Second order autocorrelation functions of a single NV^- defect center recorded with different pinhole diameters. In a) the pinhole was 100 µm, in b) 50 µm and in c) 25 µm. The corresponding $g^{(2)}(0)$ values are 0.34, 0.27 and 0.22, respectively. The count rates at an excitation power of 215 µW (3 times of the saturation power) also deviate correspondingly. The count rates were 440 kcts/s, 220 kcts/s and 76 kcts/s.

only a fraction of the light passes the pinhole and a part of the single photon emission is lost. Theoretically, for a focus diameter of 300 nm, and no aberration, the pinhole size in this particular setup should be around 15 µm (focal length of objective is 2 mm, of confocal lens 100 mm).

Yet, to reduce these losses due to aberration, one could choose a bigger pinhole at the cost of increased background. A bigger pinhole in the confocal microscope will reduce its function as a spacial filter (see Sec. 4.1). On the other hand, a high signal to noise ratio is important for many experiments. By reducing the pinhole diameter, the signal to noise ratio could be increased on the cost of single photons.

As the real SIL imperfections are not known it is difficult to determine the chromatic

Pinhole	Counts at $3 \cdot P_{Sat}$	$g^{(2)}(0)$
25 µm	76 kcts/s	0.22
50 µm	220 kcts/s	0.27
100 µm	440 kcts/s	0.34

Table 6.1: Values of detected single photon rates for different pinhole sizes and the corresponding photon autocorrelation at zero time delay $g^{(2)}(0)$. For further details see text.

aberration and hence calculate theoretically the optimum pinhole size. Yet, to gain further insights into the behavior of the signal photons and background fluorescence, an experimental evaluation with different pinhole sizes was performed. Therefore, the $g^{(2)}(\tau)$ functions for a single NV^- center were recorded with pinholes of diameter 25 µm, 50 µm, and 100 µm.

The results can be found in Fig. 6.12 and Tab. 6.1. They do not give an unambiguous indication. Depending on the application, either a low single photon rate with low background fluorescence has to be chosen or a high single photon rate with increased background. For example, for the QKD experiments presented in Sec. 8.2, a high single photon rate is of great interest, while a low background fluorescence is not of importance as long as $g^{(2)}(0) < 0.5$.

6.1.5 Modification of emission of a dipole at material interfaces

To learn more about the interaction of single dipoles in the vicinity of dielectric interfaces and photonic structures, finite difference time domain (FDTD) calculations were performed. The simulations were realized with a commercial FDTD package (Lumerical, Canada).

The FDTD method has become a state of the art tool to simulate the evolution of electro-magnetic fields inside complex electro-magnetic and photonic structures. It was first introduced in 1966 [175]. The FDTD method gives the direct time and space solution of a system. By applying a Fourier transform, solutions in the frequency domain can also be calculated.

Therefore, the structure of the system is implemented into the software and sources (e.g. dipoles) as well as monitors (to record the field evolution at a certain position) are added. The structure is then divided into so called Yee cells forming the fundamental lattice for all calculations. At the edges of these cells, the E-field components are calculated while the H-field components are centered surface normals. The differentials are based on the fundamental Maxwell equations for the E- and H-fields. The differentials of these field equations are expressed as differences at the equivalent lattice points. Simplified, this can be expressed as

$$\frac{\delta \mathrm{f(x)}}{\delta \mathrm{x}} \rightarrow \lim_{\delta \mathrm{x} \rightarrow 0} \frac{\mathrm{f(x} + \delta \mathrm{x}/2) - \mathrm{f(x} - \delta \mathrm{x}/2)}{\delta \mathrm{x}}, \tag{6.3}$$

where f(x) is replaced by the E- or H-field.

The electric field (E-field) and the magnetic field (H-field) are calculated subsequently

in an iterated manner. For all times t the H-field $H(\mathbf{r}, t)$ is calculated. Subsequently, the E-field $E(\mathbf{r}, t + \delta\frac{t}{2})$ is estimated and then again, $H(\mathbf{r}, t + \delta t)$ and so forth. The process is repeated until an adequate evolution has been achieved defined by a termination criterion.

Air interface of dielectric

The emission pattern of a single NV defect center inside a diamond nanocrystal deposited on the flat side of a SIL was estimated via various FDTD simulations. To imitate the defect center - interface system, a single transverse magnetic (TM) dipole source was placed 10 nm away from a dielectric material with a refractive index of 2.15 (see Fig. 6.13). The diamond nanocrystal was not imitated as its influence can be neglected due to its size (30 nm), which is much smaller than the vacuum wavelength of the

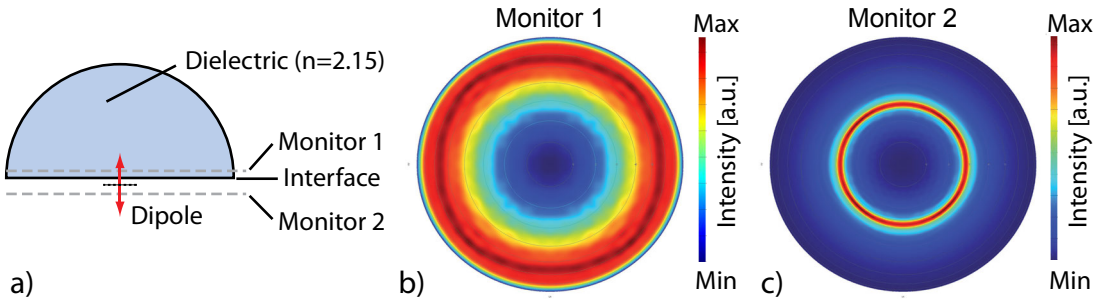

Figure 6.13: a) Sketch of the simulated configuration. An electric dipole with an emission wavelength of 600 nm is oriented perpendicular to the air interface. It is located at a distance of 10 nm from a high refractive index dielectric with n = 2.15. The field monitors are located at a distance of 100 nm from the dipole. Only a volume of about 10 µm by 10 µm by 10 µm around the dipole was simulated. b) Far field emission pattern into the direction of the vacuum (air). c) Far field emission pattern into the direction of the dielectric material (SIL). The intensity contrast in c) is roughly 10 times higher than in b).

simulated dipole. The dipole source had a center wavelength of 600 nm and a pulse length of 1 ns. To simplify the monitoring, only two 2d-monitors where placed parallel to the interface, one in air, one in the dielectric, at a distance of 100 nm from the dipole. The grid cells had dimensions of 6 nm.

For this simulation, the far field pattern of the emission was calculated. A typical intensity picture is depicted in Fig. 6.13 b,c). There are two interesting findings. First, the ratio of the emission into the dielectric to the emission into air is increased. Secondly, the emission into the direction of the high refractive index material is altered in such a way that most of the emission is emitted within an angle of less than 40°. The dielectric

acts as a nearfield antenna. Two situations have to be distinguished for both cases, a dipole oriented parallel and a dipole oriented perpendicular to the the air interface.

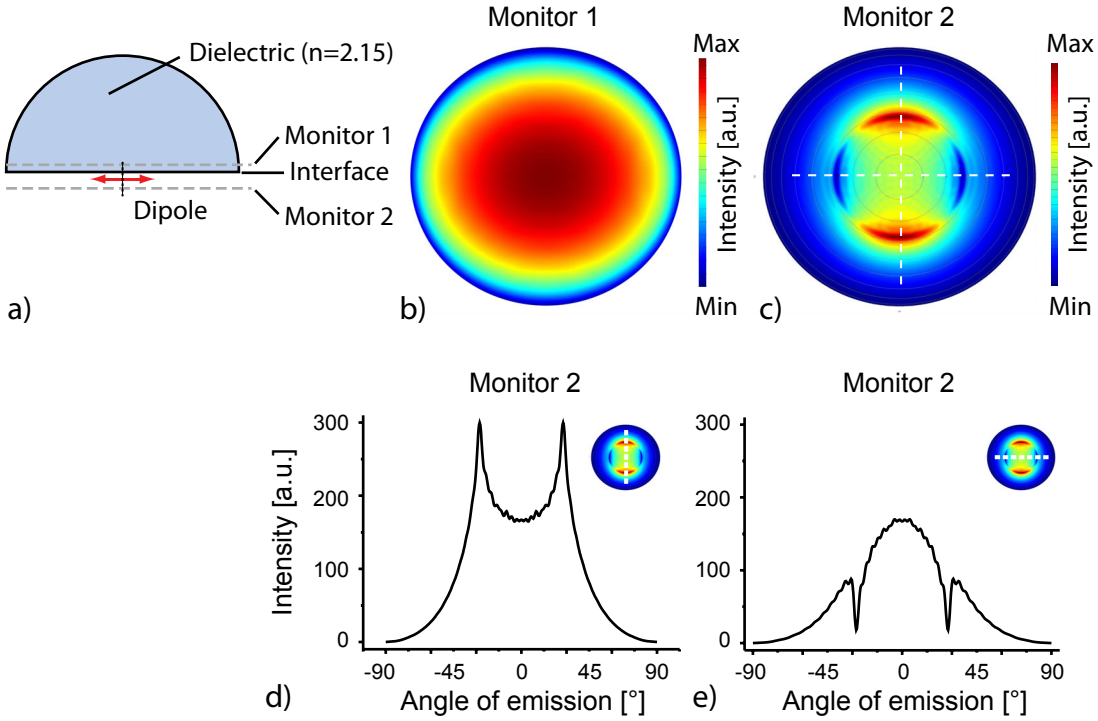

Figure 6.14: a) Sketch of the simulated configuration. An electric dipole with an emission wavelength of 600 nm is oriented parallel to the air interface. It is located at a distance of 10 nm from a high refractive index dielectric with n = 2.15. The field monitors are located at a distance of 100 nm from the dipole. Only a volume of about 10 µm by 10 µm by 10 µm around the dipole was simulated. b) Far field emission pattern into the direction of the vacuum (air). c) Far field emission pattern into the direction of the dielectric material (SIL). The intensity contrast in c) is roughly 10 times higher than in b). d) and e) show the intensities of the far field emission as indicated by the white lines.

For the case that the ratio of the emission into the dielectric is increased, the following phenomena can be observed in the simulations. For a dielectric with n = 2.15, and a dipole oriented parallel to the air interface, 86.2 % of the total emission is emitted into the direction of the dielectric while only 13.7 % are emitted into the air. The missing 0.1 % fraction of the total emission is caused by the simple monitor design which allows radiation under very high angles to escape without monitoring (see Fig. 6.14). This gives a factor of about 6.3 higher emission intensity into the direction of the dielectric. For a dipole perpendicular to the interface, 74.7 % of the total emission is emitted into the direction of the dielectric while 25.2 % are emitted into the air (see Fig. 6.13).

Again, the missing 0.1 % fraction of the total emission is caused by the simple monitor design which allows radiation under very high angles to escape without monitoring. This results in a factor of 3 for the increased emission into the dielectric. Both results indicate, that depending on the orientation of the dipole the emission into the dielectric relative to air is increased by a factor 3 to 6.3. These results are in agreement with an analytical evaluation of a dipole emitter in front of a flat dielectric interface [176]. Also a simulation taking into account the modification of the radiative recombination rate induced by air interfaces and the spatial re-distribution of the emitted radiation gives very similar results [177].

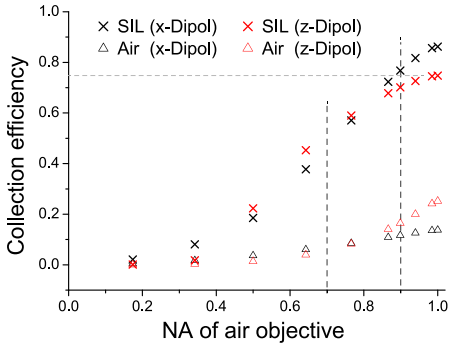

Figure 6.15: Simulated collection efficiency for different collection angles α spanning from 0° to 90° (corresponding to the NA = sin(α)) for an electric dipole with an emission wavelength of 600 nm. It is located at a distance of 10 nm from a high refractive index dielectric with n = 2.15 (see Fig. 6.13 and 6.14). The dashed vertical lines represent an NA of 0.7 and 0.9 as implemented in the experiment. The dashed horizontal line indicates the ratio of light that would be emitted on average into the dielectric for randomly oriented dipoles for an NA of 0.9.

The case in which the dielectric acts as an antenna is visualized in Fig. 6.15. Here, the collection efficiency is plotted against the NA of an air objective lens for both directions of emission and both dipole orientations. Crosses represent the emission into the dielectric, triangles into air. Red symbols are used for a perpendicular dipole orientation, black for a parallel orientation. At high NAs the collection of a parallel dipole into the dielectric is more efficient.

Most interesting are the cases for an NA of 0.7 and 0.9 matching the used objective lenses. For an NA of 0.9, 70.1 % for a perpendicular and 76.8 % for a parallel dipole are emitted within an angle of 64 degrees (equivalent to NA = 0.9). Compared to the collection from the air side this gives an enhancement factor of 4.4 to 7. The same calculation for an NA of 0.7 gives a factor of 7.2 of enhanced collection in direction of the dielectric for an ensemble of dipoles. This represents the experimental situation of

a fluorescent bead, where the far field emission pattern is determined by roughly 10^4 randomly oriented dipoles.

For a perfect SIL, 66 % and 60 % respectively of the total emission could be guided into air to be collected by an objective lens with NA of 0.9 (see Fig. 6.1). This estimation accounts for the reflection loss at the spherical SIL-air interface for perpendicular incidence ($(n_{2.17} - n_{Air})^2/(n_{2.17} + n_{Air})^2$, with $n_{Air} = 1$). These theoretical estimations agree well with the measured values.

6.2 Application to diamond nanocrystals containing single NV^- defects

6.2.1 Room temperature solid immersion microscope equipped with diamond nanocrystals

In this section, the feasibility of the implemented SIM as an efficient single photon source is discussed. Maximum single photon count rates were measured for CW and pulsed excitation. Furthermore, an overall collection efficiency for single NV^- defect centers in diamond nanocrystals was determined.

Preparation of SIL - diamond sample

The dense distribution of nanocrystals on the SIL is important for experimental convenience. For example, for certain applications it can be necessary to have access to single photons with a well defined spectral position. Yet, as was discussed in Sec. 2, each NV defect inside a nanocrystal has unique electronic and optical properties. In particular, the wavelength of the zero phonon lines (ZPLs) can differ by far. Therefore, pre-selection of a certain single NV defect can be necessary. To guarantee a wide range of NVs and hence a wide range of ZPL, the nanocrystal density on the limited accessible region on the SIL needs to be high.

To ensure a dense distribution with distances around 1 µm, spin-coating of a solution with 0.01 % polyvinyl alcohol and with suitable diamond density was performed with 2000 rpm. The diamond nanocrystals (Microdiamant, Switzerland) have a mean size of 25 nm. Further experimental details of the spin-coating process can be found in Sec. 3.3.

Figure 6.16 shows a x-y-intensity scan of a 10 µm by 10 µm region with typical diamond distribution and fluorescence intensity, indicating an NV density of 12 in this

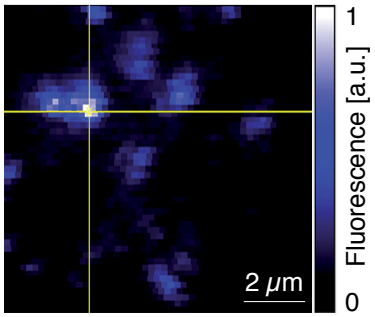

Figure 6.16: 10 μm by 10 μm fluorescence intensity scan of an area close to the center of the SIL. Such scans typically feature a few bright (R_{Inf} =400 kcts/s to 700 kcts/s) and many darker (R_{Inf} <400 kcts/s) NV centers.

area. This accords well with a distribution of 100 nanocrystals within 10 μm^2 and an NV defect density of 1 per 10 crystals of this size (see Sec. 3.3).

6.2.2 Analysis of single photon character

In order to prove the single photon character of the light emitted from a specific colour center under study, autocorrelation measurements in a Hanbury-Brown and Twiss (HBT) setup were performed. Details of this measurement can be found in Sec. 4.2.4. As was explained in detail in Sec. 2.1, the normalized intensity autocorrelation function $g^{(2)}(\tau) = \frac{\langle I(t)\, I(t+\tau)\rangle}{\langle I(t)\rangle^2}$ is a measure of the single photon character of the detected light. If it has values at zero time delay $\tau = 0$ of $g^{(2)}(0) < 0.5$, emission should occur basically from a single NV center. The measured $g^{(2)}(\tau)$ functions of single NV centers implemented in the SIM show that the single photon character of the emission is well preserved. The fluorescent background from the SIL can be suppressed strong enough by spectral filtering.

In Fig. 6.17 a) and c) the normalized autocorrelation functions for two different single NV defects are shown. For the NV^- defect in a), which was also the brightest non-blinking defect, $g^{(2)}(0) = 0.3$ for an excitation power of roughly 213 mW (3 times the value of the saturation excitation intensity). For the defect in c), $g^{(2)}(0)$ was 0.16 for 1 mW excitation power. The fits to the data were done according to a 3-level model (see App. A)

For all other defects investigated, typical $g^{(2)}(\tau)$ functions of the measured NV centers have a $g^{(2)}(0)$ between 0.1 and 0.3, depending on excitation intensities and intrinsic nanocrystal fluorescent background. Further suppression could be achieved

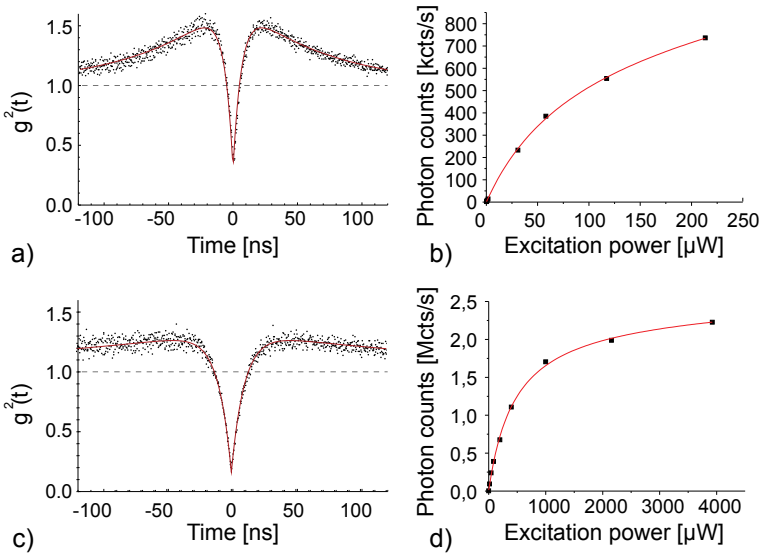

Figure 6.17: a)Normalized autocorrelation function $g^{(2)}(\tau)$ of the brightest stable emitter found with $g^{(2)}(0) < 0.3$. b) Saturation measurement of same emitter. R_{Inf} is 853 kcts/s while the saturation excitation power is 88 μW. c) Normalized autocorrelation function $g^{(2)}(\tau)$ of the brightest blinking emitter found with $g^{(2)}(0) < 0.16$ at excitation of 1 mW. d) Saturation measurement of the same emitter. R_{Inf} is 2.4 Mcts/s on a time basis of several ten seconds while the saturation excitation intensity is 464 μW. The averaged count rate is 477 kcts/s for an excitation intensity of 2.6 mW. The red curves are theoretical fits to the data (see text).

via closer spectral filtering, e.g. with a long pass filter at 620 nm and a short pass at 780 nm.

6.2.3 Saturation measurements: Single photon count rates

In order to determine the maximum accessible photon flux, saturation measurements were performed as discussed in detail in App. A. In Fig. 6.17 b) and d) the data for the two single defects from a) and c) is displayed. Fits to the experimental curves were done according to $\mathrm{R(I)} = \frac{\mathrm{R_{Inf}\ I}}{\mathrm{I_{Sat}+I}} + (\mathrm{A} + \alpha)\mathrm{I} + \beta$. Here, R is the single photon count rate, $\mathrm{R_{Inf}}$ the count rate at infinite excitation intensities, I the excitation power, $\mathrm{I_{Sat}}$ the saturation excitation power, A represents the measured background fluorescence 1 µm away from the NV center, while α and β are fit parameters for linear background stemming from the diamond and additional background such as APD dark counts and residual stray light, respectively.

Emitters with more than 400 kcts/s

Twelve single NV centers of similar brightness were analyzed by saturation measurements. The typical single photon count rate R was 500 kcts/s with background subtraction as can be seen in Fig. 6.18 a). Although most saturation excitation intensities were around 80 µW in the focus, some of them have quite different saturation intensities as can be derived from Fig. 6.18 a). One of the reasons for this observation originates from intrinsic properties of the NV defect. The randomly distributed dipole orientations, caused by a randomly oriented nanocrystal, cause different emission patterns resulting in different collection efficiencies as was investigated in detail via FDTD simulations in Sec. 6.1.5. Furthermore, the nanodiamonds have mismatched physical and optical contact to the SIL surface resulting in diverse optical coupling of the nanodiamonds to the SIL. Thereby, the excitation efficiency as well as the emission profile is influenced.

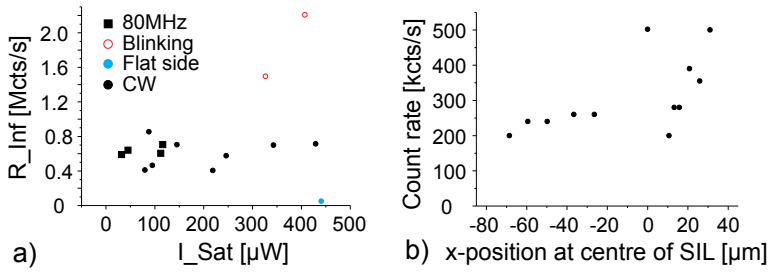

Figure 6.18: a) Saturation count rates of different NV centers as function of saturation excitation intensities. Black symbols represent stable emitters, open red circles blinking ones and the blue dot represents a NV center probed from the flat side of the SIL. Square symbols denote quasi-CW excitation with 80 MHz laser repetition rate while circles relate to CW excitation. b) Photon count rates of different NV centres under pulsed excitation of 80 MHz and excitation intensities of 148 µW in the focus. The count rates of 12 NV centres along one scan direction (x-axis) across the centre of the flat SIL surface were investigated. All emitters provide single emitter characteristics proven by a measured value of the normalized 2nd order correlation function $g^{(2)}(0) < 0.5$.

In a similar experiment with the same SIL, a rectangular array of about 10 µm by 100 µm around the center of the SIL was analyzed for maximum count rates (not count rates at saturation) where the background is still small with $g^{(2)}(0) < 0.16$. More than 10 diamonds showed count rates of more than 250 kcts/s when excited with 148 µW of a pulsed laser (Picoquant, Germany, 532 nm, pulse width about 110 ps) with a repetition rate of 80 MHz, whereas many more diamonds showed count rates around 200 kcts/s (see Fig. 6.18 b)). An excitation with 80 MHz represents quasi-CW excitation

for NV centers with a typical lifetime of 18 ns. The count rates of the 12 measured defect centers were extrapolated. Thereby, saturation count rates under CW excitation between 400 kcts/s and 500 kcts/s were derived.

For an area of 100 µm by 100 µm more than 100 colour centers with similar emission rates could be found on the investigated SIL. This offers the opportunity to select suitable diamonds out of a large ensemble for special applications, e.g., a specific ultra-bright NV or two NV^- with matching zero phonon line emission for two-photon interference experiments at cryogenic temperatures (see Sec. 4.4).

The brightest emitter: Maximum stable single photon count rates

One outstanding NV^- center with a stable single photon count rate at saturation of 853 kcts/s was found. This is the highest reported number of detected single photon counts of a single NV^-. Its saturation curve is depicted in Fig. 6.17 b). Even at excitation intensities of 213 µW and count rates of 736 kcts/s its $g^{(2)}(0)$ value was smaller than 0.3.

Blinking single defect centers

Besides the stable single NV^- defect center with 853 kcts/s, another remarkable single defect center was found. This defect center was ultra-bright, it had single photon count rates of up to 2.4 Mcts/s at saturation on a time base up to several ten seconds alternating with darker periods. There was no pronounced on-off behaviour, but rather jumps between a very bright state and several states with a far less intensity. Blinking NV defects have been studied but the behavior of this particular defect is different from the simple on-off behavior reported [47]. On average, the single photon emission rate was 400 kcts/s at an excitation power of 2.6 mW. Its autocorrelation function at count rates of up to 1.1 Mcts/s was smaller than $g^{(2)}(0) < 0.16$.

In the ensemble of diamond NC investigated there exist a few ultra-bright NV defect centers with rates > 1 Mcts/s. However, this large rate seems to be accompanied by pronounced blinking behaviour. Not only these ultra-bright defects showed blinking but about 30% of the diamonds investigated. The reason for this is not yet understood. Photochromic behaviour may play a role [54]. Compared to recent studies of blinking in very small (5 nm) diamond nanocrystals [47] the size of the diamond nanocrystals used is much larger (25 nm). Yet, with NV centers located close to the surface the situation may be similar to the small ones. Since only few ultra-bright blinking NV defect centers have been investigated, a solid statement concerning the reason for the blinking is

not possible yet. However, the correlation of brightness and blinking warrants further studies.

6.2.4 Pulsed excitation

For most applications of single photons in QIP an on-demand generation is required [178]. One possibility is to use pulsed excitation. A crucial parameter of such a source is the collection efficiency per excitation pulse. A perfect single photon on-demand device would deliver exactly one detected single photon per pulse in a well defined optical mode. Such performance is limited in real devices mainly by the efficiency to collect single photon emission with the first lens, losses in the optical path towards the detector as well as by detector efficiencies.

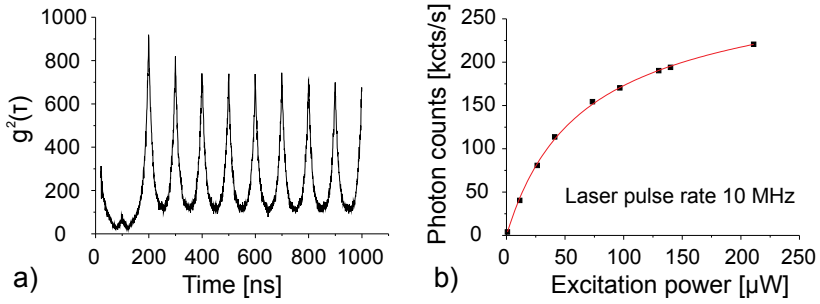

Figure 6.19: a) Pulsed autocorrelation measurement with $g^{(2)}(0) = 0.16$ of the stable, bright emitter from Sec. 6.2.3 excited with 532 nm laser wavelength. The excitation intensity was 77 µW, the laser repetition rate 10 MHz and count rates were 221 kcts/s. b) Saturation curve of the same emitter as in a), again under pulsed excitation of 10 MHz. The red curve is a theoretical fit to the data (see App. A). This plot shows, that an overall collection efficiency $\eta = 2.7\,\%$ was achieved for a stable single NV^- defect center.

Emission under pulsed excitation generally provides a better suppression of background photons compared to CW excitation as excitation radiation is limited to periods when the electron is in the ground state, i.e. can be excited and emit a single photon. This is proven by measuring the single photon character of the emitters under pulsed 532 nm laser excitation by analyzing their normalized intensity autocorrelation function $g^{(2)}(\tau)$. Fig. 6.19 a) depicts the pulsed autocorrelation function of the NV center examined in Sec. 6.2.3 with 10 MHz laser repetition rate. It has $g^{(2)}(0) = 0.16$ instead of $g^{(2)}(0) = 0.3$ at an excitation intensity of 77 µW and count rates of 221 kcts/s. Also the bright blinking defect center from Sec. 6.2.3 was investigated under pulsed excitation. It had $g^{(2)}(0) = 0.11$ instead of $g^{(2)}(0) = 0.16$ while excited with laser rates of 10 MHz and 385 µW excitation power.

Overall collection efficiency

To determine the overall collection efficiency of single NV defect centers in diamond nanocrystals, the collection efficiency per excitation pulse was determined. The repetition rate of the pulsed excitation laser was limited to 10 MHz, such that the time interval between pulses was 100 ns, i.e. much larger than the lifetime of 18 ns of the NV center. With these numbers the probability for excited NV centers to decay before the arrival of the next excitation pulse was 0.97. Furthermore, the excitation probability is considered to be one, which is justifiable because the count rates are taken for excitation at saturation. The photon count rate at different excitation powers was measured and plotted as saturation curve in the graph in Fig. 6.19. From this saturation behavior, the collection efficiency of the setup can be directly deduced. A stable collection efficiency of $\eta = 2.7\,\%$ in saturation was achieved, estimated from experimental collection efficiency at 10 MHz laser rate, while having a total single photon count rate of 267 kcts/s in saturation (see Fig. 6.19).

A more detailed analysis can be based on a simple two-level model. It can confirm the results estimated above. Furthermore, it can be used to calculate the maximally expected count rate for a certain laser repetition rate. Such a model neglects the metastable singlet (shelving) state of the NV^- center (see App. A). However, good agreement with respect to the saturation behaviour is obtained. This simple model describes the measured count rate $r(\Gamma)$ as a function of the laser repetition rate Γ. Assuming an excitation probability of one which is justifiable as explained above, only the collection efficiency η, the lifetime of the emitter γ^{-1} and the laser repetition rate Γ influence the single photon count rate

$$r(\Gamma) = \eta \cdot \Gamma \cdot \gamma \cdot \int_0^{1/\Gamma} e^{-\gamma t} dt = \eta \cdot \Gamma \cdot (1 - e^{-\gamma/\Gamma}).$$

This model was used for the fit in Fig. 6.20 where the count rate in saturation is displayed as a function of the laser repetition rate. From the fit the photon collection efficiency of the entire setup η can be derived. A value of $\eta = 2.6\,\%$ for the overall collection efficiency is found in agreement with the estimated η of 2.7 %. This is the highest yet reported collection efficiency for a stable NV defect center in diamond.

Furthermore, the collection efficiency for the blinking defect center from Sec. 6.2.3 with count rates up to 2.4 Mcts/s at CW excitation was determined to be even higher.

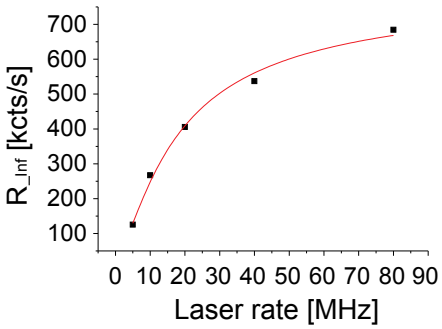

Figure 6.20: Photon count rate at saturation R_{Inf} as function of laser repetition rate. The theoretical fit to the data (red curve) is further explained in the text.

With a lifetime of 17.6 ns it also emits an ultra-high single photon flux when excited with pulsed laser light. At laser repetition rates of 10 MHz and 385 µW up to 420 kcts/s were detected. This determines a collection efficiency of 4.2 % on a timescale of several ten seconds.

Source collection efficiency

The determination of a value for the source efficiency is also of particular interest to compare different single photon source designs [114]. The source efficiency is the ratio of photons collected by the first optical element in the setup to the total emitted photons.

For its determination, the setup efficiency η_{Setup} of the elements beyond the flat surface of the SIL was estimated. The setup efficiency was calculated from reflection and transmission parameters of all optical elements according to their data sheet values and presents the optimistic upper boundary. The data sheet parameters are listed in Sec. 4.3. For the particular setup used for the measurements, it was determined to be $\eta_{\text{Setup}} < 0.23$. From this value, the source efficiency ϵ, i.e. the fraction of light collected by the first objective, was calculated. For the brightest stable NV^- (see Sec. 6.2.3) $\epsilon > 11.7\,\%$. For the blinking defect (see Sec. 6.2.3), it was even higher with $\epsilon > 18.3\,\%$.

6.3 Summary and outlook

In conclusion, an experimentally simple, but efficient way was developed to strongly enhance the collection of single photons emitted by NV centers in diamond at room temperature. A ZrO_2 solid immersion lens with spin-coated nanodiamonds on its flat

surface was integrated into a solid immersion microscope. Count rates in saturation of up to 853 kcts/s for a stable NV center and up to 2.4 Mcts/s for a blinking defect center were measured. Furthermore, the compact SIL design provides access to about 100 NV centers that emit more than 400 kcts/s. The overall collection efficiency of the setup is up to 4.2 % while having a source efficiency ϵ of up to $\epsilon > 18.3\,\%$ [114], opening the way towards much more efficient diamond-based on-demand single photon sources.

Furthermore, the setup is versatile and allows the implementation of any kind of defect center located in a diamond nanocrystal. This is thus very attractive for an integration of even brighter emitters with smaller bandwidth. For a single SiV center with a lifetime of 1.2 ns as was very recently presented [11] count rates of up to 10 Mcts/s could be expected. Cryogenic experiments will also be possible as the immersion microscope works oil free leading off towards two-photon interference experiments which are only possible with ultra-high single photon rates. First low temperature results are presented in the next Chapter 7.

7 Experimental investigation of fundamental properties of NV defect centers at low temperatures

In this chapter, the particular advantages of solid immersion microscopy at cryogenic temperatures are exploited. In contrast to oil immersion microscopy it is suitable for low temperature experiments and hence allows efficient excitation of quantum systems and ultra-efficient collection of its fluorescence.

In Sec. 7.1 the cryogenic solid immersion microscope is evaluated. It is applied for spectral diffusion measurements based on spectroscopic analysis of single photons. Time resolution down to 30 ms is achieved. In Sec. 7.2 a novel method for spectral diffusion measurements is applied. It was used to determine spectral diffusion times of single NV^- defect centers with higher time resolution. The efficient method also allowed systematic studies of spectral diffusion. They give deeper insight into the underlying processes.

Parts of this chapter were published on *arXiv* [Wolters *et al.* 2012a] and were accepted by *Phys. Rev. Lett.* for peer reviewing.

7.1 Low temperature solid immersion microscope for spectral diffusion measurements

In this section, an efficient cryogenic temperature setup is introduced and evaluated concerning its single photon collection efficiencies. Furthermore, it is applied for investigation of optical properties of single NV^- defect centers.

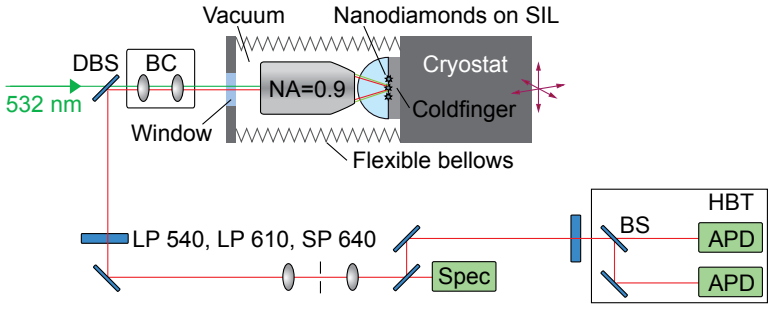

Figure 7.1: Schematic of the extended cryogenic solid immersion microscope. It allows ultra-efficient collection of single photons which are generated by a quantum emitter at temperatures down to 4.2 K. Technical details are described in Sec. 4.4.2. DBS stands for dichroic beam splitter, BC for beam control, LP and SP for long pass and short pass filter, Spec for spectrometer, BS for beam splitter and HBT for Hanbury Brown and Twiss setup.

7.1.1 Motivation

Efficient low temperature analysis of single quantum systems is necessary for a deeper understanding of their fundamental properties and characteristics. Furthermore, for the realization of certain optical quantum information processes, lifetime limited emission [84, 179] generated at cryogenic temperatures is crucial.

For example, to realize a simple Hong-Ou-Mandel interference experiment [139], two photons with the same frequency have to be interfered. This was recently achieved with NV^- defect centers in pure type IIa bulk diamond under off-resonant excitation [140, 180].

However, for individual NV^- defect centers in diamond nanocrystals the situation is different. Although NV^- defect centers with almost lifetime limited ZPL emission can be found on small time scales [86], it spectrally shifts over time, causing an inhomogeneous broadening of the ZPL of about 0.5 nm (see exemplary spectrum in Fig. 7.2 b). This phenomenon is called spectral diffusion and limits the applicability of an NV^- defect center for quantum information processing as discussed above. Such line broadening was observed for different solid state quantum systems. It is widely assumed, that it is caused by a fluctuating electrostatic environment [181]. In diamond nanocrystals it is induced by ionized impurities [182, 183] or charge traps on the surface. However, the phenomenon of spectral diffusion in diamond nanocrystals and mechanisms causing it are not well understood [140]. For a better understanding, measurements of the diffusion rate of NV^- defect centers have been carried out for the first time in the course of this thesis.

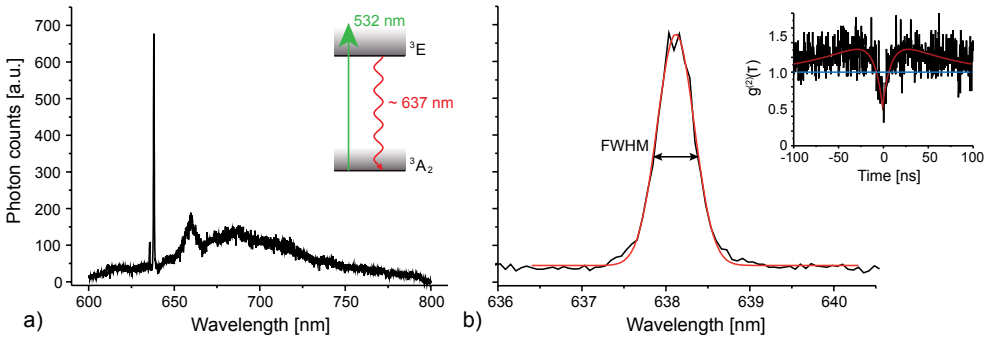

Figure 7.2: a) Spectrum of a single NV^- defect center at 5 K. Integration time was 5 s under 22 µW 532 nm laser excitation. The ZPL emission peak is located at 638.1 nm. The inset shows the excitation scheme. b) Zoom-in into the ZPL. The FWHM of 0.52 nm was determined with a Gaussian fit (red curve). The inset shows the normalized second order auto-correlation function $g^{(2)}(\tau)$.

7.1.2 Spectral diffusion: A simple model

To illustrate and estimate the dominating mechanism of spectral diffusion in diamond nanocrystals, a simple toy model is introduced. A sketch of the model is shown in Fig. 7.3. Spectral diffusion is much higher in crystals than in bulk, it is therefore assumed, that the main cause of spectral diffusion are fluctuating charges on the surface of the crystal. These charges induce an electric field and cause a Stark-shift of the excited states $\Delta E_{x/y} = d \cdot E$. By using data from Refs. [184, 185] it was estimated, that in crystals of a size of a few 10 nm, a single elementary charge can induce a Stark-shift of several hundred GHz, corresponding to the observed linewidth of about 0.5 nm. Thus, individual fluctuating surface charges can well explain changes in the electrostatic environment that cause typical inhomogeneous linewidths. Fluctuation of surface charges can be caused by laser irradiation. Loosely bound surface charges can be ionized by photons stemming from the laser light.

The time interval during which the probability that the electrostatic environment remains unchanged is reduced to 1/e can be defined as the spectral diffusion time τ_D. Within τ_D, the system can be assumed to be free of spectral diffusion, and all photons emitted within τ_D have the same spectral position and should be nearly indistinguishable.

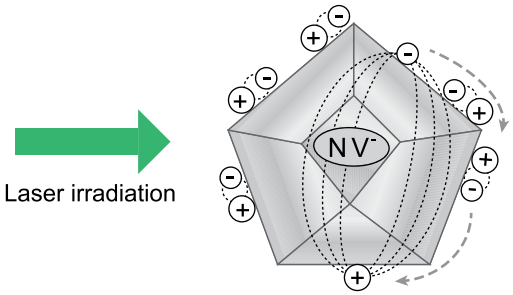

Figure 7.3: Schematic of the toy model used to illustrate the cause of spectral diffusion. A diamond nanocrystal of a size of a few 10 nm containing a single NV^- defect center is illustrated with additional charge states and corresponding fields (dotted lines). Most of the electrons (-) are locally bound to a positive charge state (+). However, already a single elementary charge can induce a Stark-shift of several hundred GHz. Fluctuation of surface charge states can be caused by laser irradiation (green arrow), indicated by dashed grey arrows. The electrostatic fields are indicated by dotted black lines. N stands for nitrogen, and V for vacancy. Details are described in the text.

7.1.3 Experimental realization and characteristics

Before spectral diffusion measurements are carried out, the cryogenic temperature setup is evaluated. Technical specifications were already discussed in Sec. 4.4. The sketch in Fig. 7.1 illustrates the experimental configuration.

Setup efficiency

To determine maximum single photon detection rates, a saturation measurement was carried out for a single NV^- defect center. The second order auto-correlation measure-

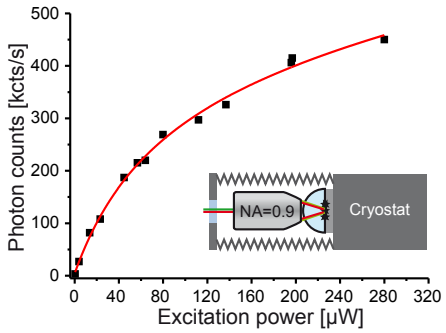

Figure 7.4: Saturation measurement of a single NV^- defect center at around 5 K under 532 nm excitation. Single photon count rate at saturation is 461 kcts/s under saturation excitation power of 80 µW.

ment proving single photon character is not shown for redundancy. The fit to the data in Fig. 7.4 reveals a maximum single photon detection rate of 461 kcts/s under saturation excitation power of 80 µW. This is a typical number for investigated single defect centers. Compared to the standard cryogenic setup (see Sec. 4.4.1), this is an improvement of a factor of 5.4 of single photon detection rates for a typical single NV^- defect center. A typical maximum count rate is only 85 kcts/s for the standard cryostat configuration under saturation excitation power of about 700 µW.

Overall photon rates of about 500 kcts/s result in single photon count rates from ZPL transitions only of around 25 kcts/s. This is an extra-ordinarily high number compared to other cryostat setups and allows efficient investigation of ZPL photons, i.e. photons stemming from the ZPL transition.

7.1.4 Analysis of spectral diffusion via time series of spectra

The most straightforward method to measure spectral diffusion in a single NV^- defect center is to take a time series of spectra. By doing so, spectral wandering of the ZPL could be directly visualized [186, 187]. Such time series are shown in Fig. 7.5.

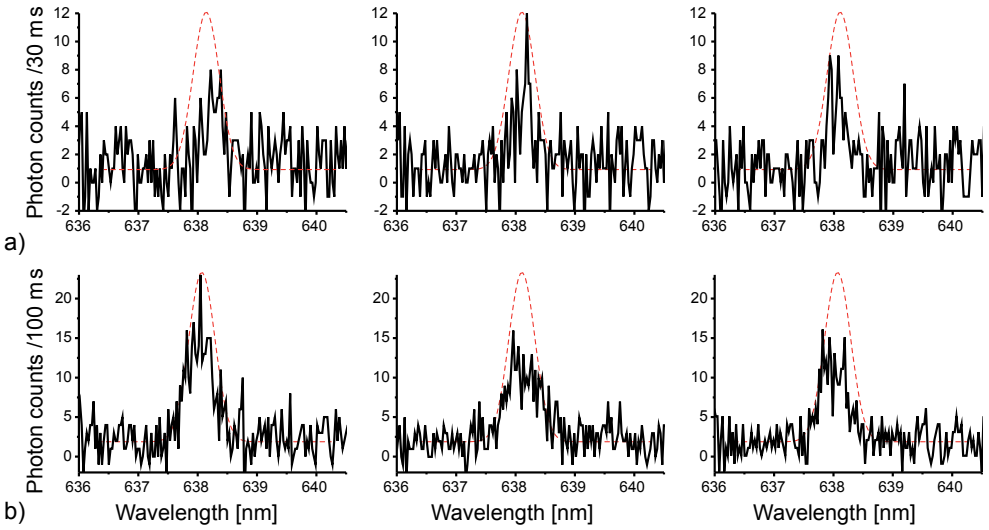

Figure 7.5: Time series of spectra of the ZPL line emission of a single NV^- defect center. In a) and b) the integration time was 30 ms and 100 ms, respectively. The dashed red line represents an inhomogeneous Gaussian line shape determined for the same defect center for 5 s integration time (see Fig. 7.2). The height was adapted to the maximum count rate.

They were recorded for the same NV^- defect center as investigated in Fig. 7.2. In Fig. 7.5 a) and b) the integration time was 30 ms and 100 ms, respectively. Clearly

visible are peaks at different spectral positions with linewidths much smaller than the inhomogeneously broadened envelope (dashed red line). The envelope function was taken from the fit of the ZPL in Fig. 7.2. The height was adapted according to the maximum count rate.

The spectra indicate, that spectral wandering is caused by random jumps of the much narrower ZPL. This is in particular visible in the spectra with integration time of 30 ms. However, the time resolution is still not high enough to determine the spectral diffusion time τ_D.

7.1.5 Summary and outlook

A novel cryogenic solid immersion microscope for the investigation of single NV defect centers was introduced. It achieves single photon count rates of up to 461 kcts/s and about 25 kcts/s of photons stemming from the ZPL line only. However, despite its efficient single photon collection capability, the time resolution of direct spectral analysis is not high enough to determine spectral diffusion times of single NV^- defect centers.

To overcome the limitations in time resolution and efficiency of the applied spectral analysis method, a novel method was applied. It is introduced in the following section.

7.2 Ultra-fast spectral diffusion measurement: Correlation interferometry

In this section a novel method is applied that allows measurement of spectral diffusion times of single NV^- defect centers with ultra-fast time resolution. Compared to the time resolution accomplished in Sec. 7.1 and previous experiments from the literature [86], an improvement by five to six orders of magnitude is achieved.

Furthermore, in combination with efficient photon collection available with the cryogenic temperature SIM introduced in Sec. 7.1, the method allows systematic studies due to moderate time consumption of the method. Therefore, it was possible, to analyze the spectral diffusion rate as function of excitation power, temperature, and excitation wavelength under off-resonant excitation.

7.2.1 Motivation

The limited time resolution of the spectral diffusion measurement presented in Sec. 7.1 demands an advanced experimental method that provides ultra-fast time resolutions. Different methods with ultra-fast time resolutions have been presented in the literature. One approach relies on the idea of conversion of frequency fluctuations into intensity fluctuations [188, 189]. However, its experimental realization is quite complex, moving mechanical setup components reduce the time resolution to the order of 100 µs [189]. Another approach, conceptually related, achieves sub-nanosecond resolution. However, by this approach, only spectrometer limited spectral resolution with reduced detection efficiencies was achieved [187].

To overcome the limitations of both methods and to combine their inherent advantages, a novel method is introduced in the following. The time resolution of this method is limited only by single photon counting and correlation instrumentation, while its spectral resolution can almost reach conventional Fourier spectroscopy. Therefore, time resolution down to 50 ps and spectral resolution down to some kHz can be achieved. Furthermore, its photon detection efficiency is enhanced by a factor of two or more compared to the latter method [187].

7.2.2 Method

A pre-adjusted Mach-Zehnder interferometer was used as dispersive element. It converts the spectral modulation of ZPL emission into intensity modulation. The intensity modulation was measured by cross-correlating the photons from both interferometer outputs. These photon statistics are used to derive the timescale of spectral diffusion. The setup is illustrated in Fig. 7.6.

Theoretical introduction

The theoretical introduction in the following describes, how the cross-correlation function between the outputs of the interferometer determines the timescale of the spectral diffusion. For simplicity, the wavelength index λ of the photon number operator $\hat{n}_\lambda(t)$ is suppressed.

The time averaged photon detection rate in the left or right output port of the interferometer is $< \hat{I}(t)_{L/R} >_t$, with

$$\hat{I}(t)_{L/R} \quad = \quad \eta_{L/R}\, \hat{n}(t)\, m_{L/R}(t). \tag{7.1}$$

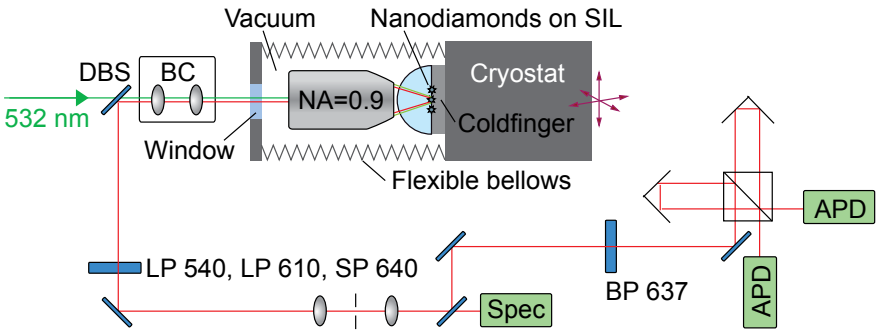

Figure 7.6: Sketch of the setup. The setup was the same as in Sec. 7.1, but extended by a folded Mach-Zehnder interferometer. DBS stands for dichroic beam splitter, BC for beam control, LP, SP and BP for long pass, short and band pass filter, Spec for spectrometer, respectively.

Here, $\eta_{L/R}$ is the overall quantum efficiency in the left and right exit of the interferometer, respectively. $m_{L/R}(t)$ describes the modulation introduced by the interferometer

$$m_{L/R}(t) \quad = \quad 1 \pm c \, \sin[2\pi x/\lambda(t)]. \tag{7.2}$$

Here, c is the contrast of the interference fringes and x is the path length difference of the interferometer arms. The plus and minus signs correspond to the left and right arm, respectively. The cross-correlation between the two arms $g^{(2)}_{LR}(\tau) = \frac{<:\hat{I}_L(t)\hat{I}_R(t+\tau):>_t}{<\hat{I}_L(t)>_t<\hat{I}_R(t)>_t}$ can also be expressed as

$$g^{(2)}_{LR}(\tau) \quad = \quad g^{(2)}(\tau) < m_L(t) m_R(t+\tau) >_t . \tag{7.3}$$

Here, $g^{(2)}(\tau) = \frac{<:\hat{n}(t)\hat{n}(t+\tau):>_t}{<\hat{n}(t)>^2_t}$ is the direct second order auto-correlation function of the emitter determined without interferometer. $<: \ldots :>_t$ denotes normal ordering before time averaging.

It is assumed, that spectral diffusion occurs in form of random jumps of the narrow emission line within a broad envelope [86]. This was also confirmed by the spectral measurements presented in Sec. 7.1 and is illustrated in Fig. 7.5. For the calculation of $< m_L(t) m_R(t+\tau) >_t$ the characteristic function $X(t,\tau)$ is introduced. It is 1, if no spectral jump occurred within the time interval $(t, t+\tau)$ and it is zero, if a spectral jump has occurred. For the averaged values, terms with and without spectral jump are separated.

In the case, that no jump occurred, $\lambda(t) = \lambda(t+\tau)$. In the case, that a jump occurred, $\lambda(t+\tau) = \lambda(t') \neq \lambda(t)$. Furthermore, the probability that the spectral position remains

unchanged after time τ can be expressed with $p(\tau) =< X(t,\tau) >_t$. By furthermore separating $X(t,\tau)$, one finds

$$\begin{aligned} < m_L(t)m_R(t+\tau) >_t = \quad & p(\tau) \quad < m_L(t)m_R(t) >_t + \\ & [1-p(\tau)] \quad < m_L(t)m_R(t') >_{t,t'} . \end{aligned} \tag{7.4}$$

The sine terms average out, if the interferometer is adjusted in such a way, that several fringes can be found within the inhomogeneous width of the ZPL as can be seen in Fig. 7.7 b). Therefore, $< m_L(t) \cdot m_R(t') >_{t,t'} = 1$, and $< m_L(t)m_R(t) >_t = 1 - c^2/2$. This results in

$$< m_L(t)m_R(t+\tau) >_t \quad = \quad 1 - c^2/2 \cdot p(\tau). \tag{7.5}$$

Finally, one can derive the probability, that the spectral position of the ZPL has not changed after time τ as

$$p(\tau) \quad = \quad 2/c^2 \cdot \left(1 - \frac{g^{(2)}_{LR}(\tau)}{g^{(2)}(\tau)}\right). \tag{7.6}$$

The equation shows, that for determination of the spectral dynamics of an emitter, only measurement of the direct auto-correlation function $g^{(2)}(\tau)$ of the emitter and the cross-correlation between the two outputs L/R of the interferometer $g^{(2)}_{LR}(\tau)$ are necessary.

7.2.3 Experimental implementation

For the experimental realization, the highly efficient cryostat solid immersion microscope (see Sec. 4.4.2) was expanded by a folded Mach-Zehnder interferometer in the detection path. The sketch of the setup is shown in Fig. 7.6. The SIL was equipped with diamond nanocrystals as described in Sec. 3.2. It was cooled down to about 5 K. NV^- defect centers were excited with 532 nm CW laser light of several µW power. Single photons are separated from the excitation laser light by a dichroic mirror and a longpass filter. For suppression of phonon side band emission, a removable bandpass filter (FWHM of 7 nm) centered around 637 nm was used. Residual ZPL photons were sent through the Mach-Zehnder interferometer before detection by two APDs. APD detection events were time correlated by a standard correlation device (PicoHarp300, PicoQuant, Germany, see Sec. 4.2.4).

Prerequisite alignment of the interferometer

The interferometer arms were adjusted prior to correlation measurements in such a way, that their length difference caused four fringes per nanometer at roughly 639 nm. The alignment was carried out as follows. One of the APDs was replaced by a

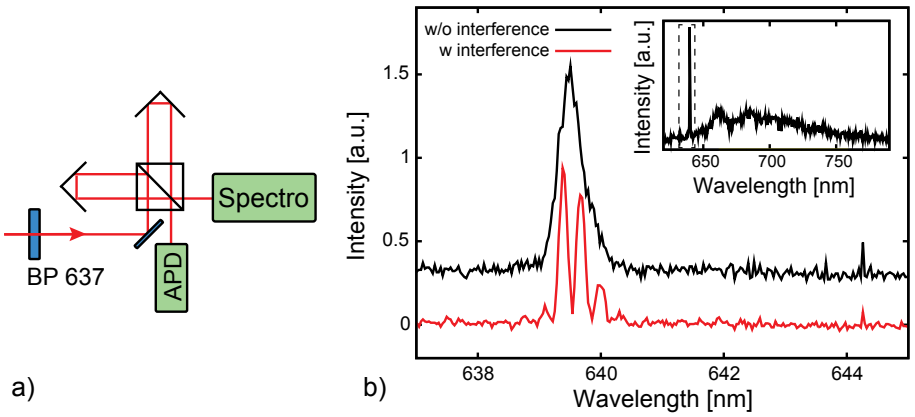

Figure 7.7: a) Sketch of the prerequisite setup for alignment of the interferometer. The spectrometer is used to determine the adequate arm length difference. The band pass (BP) filter has a spectral width of about 7 nm. b) Spectra of the ZPL of a single NV^- defect center at 5 K; the black curve (upshifted by 0.3 for clarity) for a configuration without interferometer, and the red curve for a configuration with interferometer as illustrated in a). The interferometer arms were aligned such that 4 interference fringes appear within 1 nm. The contrast is about 90 %. The zoom-out shows the complete NV^- spectrum including phonon side-bands. The dashed rectangular denotes the transmission of the BP filter.

spectrograph (Acton SpectraPro 500i, Roper Scientific, USA) with cooled CCD camera and resolution of about 0.1 nm. This preliminary configuration permitted to determine the interferometric and spectral properties of the interferometer directly from a spectral measurement. To do so, spectra of the fluorescence of single NV^- defects were taken. Such a measurement is shown in Fig. 7.7 b). Clearly visible are the interferometric fringes in the fluorescence of the ZPL of a single NV^- defect center. From the spectra, a contrast of 0.9 of the interferometer at around 639 nm was determined.

Data acquisition

The spectral diffusion time can be extracted from the probability $p(\tau)$ that the spectral position has not changed after the time τ (see Eq. 7.6). For experimental determination of $p(\tau)$ of a single NV^- defect center, the direct second order auto-correlation function $g^{(2)}(\tau)$ and the cross-correlation function $g^{(2)}_{LR}(\tau)$ between the interferometer arms have

to be measured.

$g^{(2)}(\tau)$ can be determined directly by auto-correlation measurements without removing the interferometer in front of the APDs for the following reason. If the complete fluorescence spectrum including phonon side band emission of a single NV^- is sent through the interferometer, it acts as a common HBT setup because the coherence length L of the photons is too short ($L \propto \lambda^2/\Delta\lambda$ with $\Delta\lambda \approx 100\,nm$). This was also confirmed by experimental means.

For determination of $g^{(2)}_{LR}(\tau)$, the 637 nm band pass filter is introduced in the optical path and the cross-correlation measurement between the interferometer arms can be carried out. The coherence length L of the ZPL is long enough to measure interference fringes in the spectrometer. Therefore, spectral jumps of the narrow ZPL emission cause intensity fluctuations. Although the collection efficiency of the cryogenic setup is exceptionally high, acquisition times for $g^{(2)}_{LR}(\tau)$ were roughly 30 min. During acquisition time, care was taken to keep laser power stable and adjustment unchanged.

7.2.4 Data analysis

Spectral diffusion rate

For a specific NV^- defect center, both $g^{(2)}(\tau)$ and $g^{(2)}_{LR}(\tau)$ were determined. The results are shown in Fig. 7.8 a). Excitation power was 23 µW in front of the cryostat corresponding to about 12 µW in the focus.

These correlation measurements are used to determine the spectral diffusion probability $p(\tau)$ according to Eq. 7.6. The resulting function is shown in Fig. 7.8 b). A fit to the data according to Eq. 7.6 reveals a single exponential decay for the spectral diffusion probability $p(\tau)$. This supports the assumption that spectral diffusion is indeed caused by uncorrelated (surface) charge fluctuations.

The fit also gives a number for the spectral diffusion time τ_D. For this particular NV^- defect center, $\tau_D = 2.2 \pm 0.4\,\mu s$ with a spectral diffusion rate $\gamma_D = 1/\tau_D$ of about 450 kHz. This is almost 100 times faster than the single photon detection rate of about 4.6 kHz for photons stemming from the ZPL only.

Furthermore, the interferometer contrast c was determined to be 0.45 from the fit. This is much lower than the contrast of $c = 0.9$ that was measured before with the spectrometer. Washing out of the contrast can be explained by fluorescence background, and by the two non-degenerate NV dipole transitions [185].

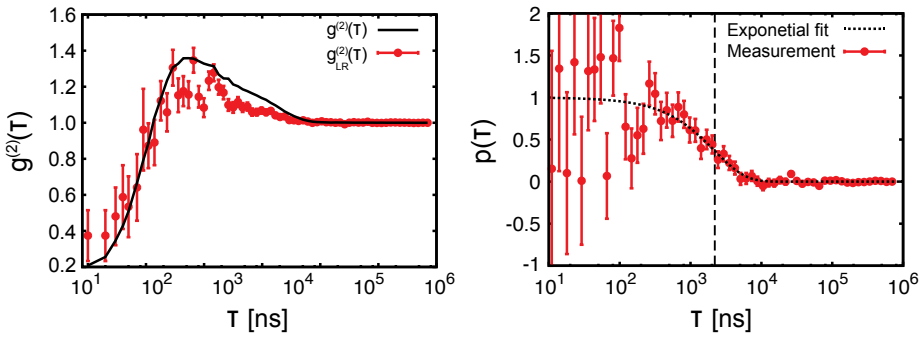

Figure 7.8: a) Measured second order auto-correlation function $g^{(2)}(\tau)$ (black solid line) and cross-correlation $g^{(2)}_{\mathrm{LR}}(\tau)$ (red dots) under laser excitation power of 12 µW in the focus. The error of $g^{(2)}(\tau)$ is on the order of the linewidth. Further details are described in the text. b) Probability $p(\tau)$ that the spectral position of the ZPL does not jump within the time interval τ calculated from the data in a) according to Eq. 7.6. The black dotted line is an exponential fit to the data revealing a spectral diffusion time τ_{D} of 2.2 ± 0.4 µs. The dashed black line indicates the spectral diffusion time τ_{D}, where $p(\tau)$ has decreased to 1/e.

Power dependence

The dependence of spectral diffusion on laser excitation power can reveal new insights into the mechanisms causing spectral diffusion. The spectral diffusion rate γ_{D} was determined for various laser powers ranging from 3 µW to 23 µW. The data in jumps per microsecond is shown in Fig. 7.9.

A linear dependency of the spectral diffusion rate on the excitation power is visible. The fit also reveals, that spectral diffusion $\gamma_{\mathrm{D}} \to 0$ for zero excitation power. Two conclusions can be drawn. First, spectral diffusion is primarily caused by 532 nm laser excitation light. This is in agreement with the simple surface charge trap model introduced in Sec. 7.1.2. Furthermore, it also supports the assumption, that substitutional nitrogen atoms in the diamond lattice create donor levels which are ionized by 532 nm excitation laser light [182, 183]. Floating charges provided by such defects can be trapped in other charge traps and hence change the electric field distribution in the vicinity of an NV^- defect center.

Secondly, the number of ZPL photons detected per spectral jump is constant for excitation powers far below saturation powers. This implies that it is independent of the excitation power. This number gives direct information on the quality of single photon emission concerning the possible number of subsequent indistinguishable photons provided by an NV^- defect center. This is a key figure of merit for future quantum optics experiments as will also be discussed in Sec. 9.2.

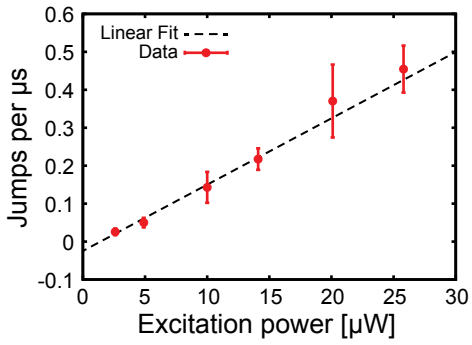

Figure 7.9: Measured spectral diffusion rate for varying excitation powers. The black dashed curve is a linear fit to the data. The jump rate at zero excitation power was a free fit parameter and was determined to approach zero.

Temperature dependence

Temperature dependent spectral diffusion measurements were carried out for a deeper understanding of mechanisms causing it and to possibly identify strategies to increase the number of collected photons per spectral jump. Temperature measurements throughout a temperature range of 5 K to 20 K did not reveal a change in the spectral diffusion rate. This supports the findings from above, that ionization of charge traps by laser excitation light is the main cause of spectral diffusion. In this temperature range, ionization energies exceed k_bT. Therefore, thermal energy does not play a significant role.

Dependence on the laser excitation wavelength

Another essential property of the experimental configuration is the laser excitation wavelength. It has crucial influence on the electron dynamics, as it directly corresponds to the photon energy. Excitation is carried out non-resonantly into the phonon sideband of the NV^- defect center. However, this excitation is not limited to a single wavelength, but can be carried out with excitation light ranging from around 480 nm to about 580 nm.

In order to determine the influence of the laser wavelength, spectral diffusion measurements were carried out for varying excitation wavelengths. To do so, the 532 nm CW laser was replaced by a pulsed super continuum source (SuperK, NKT Photonics, Denmark). Its emission was spectrally filtered with exchangeable bandpass filters of 10 nm width, centered at various wavelengths ranging from 510 nm to 580 nm, corre-

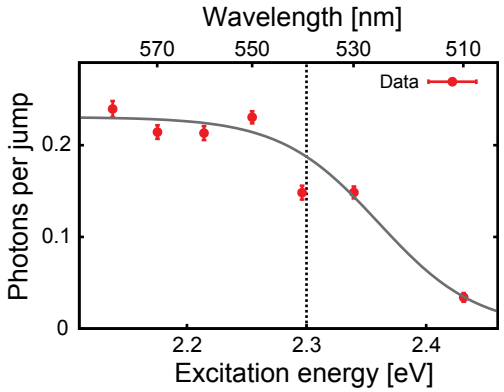

Figure 7.10: Number of collected photons from the ZPL transition per spectral jump as a function of the excitation photon energy (wavelength). The data points were determined at equal photon count rates but varying excitation powers. It is clearly visible, that the spectral diffusion rate increases dramatically above the threshold of about 2.3 eV indicated by the dotted line. The grey curve is a guide to the eyes.

sponding to photon energies from 2.4 to 2.1 eV. For each wavelength, spectral diffusion rates γ_D were determined.

The measurement reveals increasing γ_D with increasing excitation energy. To make this characteristic comparable as figure of merit, again, the number of detected ZPL photons per spectral jump was determined. It is shown in Fig. 7.10. The plot clearly indicates, that the number of collected photons per spectral jump decreases with increasing excitation energy. At about 2.3 eV, a pronounced threshold is visible. This threshold indicates the existence of a deep (surface) charge trap with an ionization energy close to 2.3 eV.

7.2.5 Summary and outlook

In this section, an interferometric method to measure the spectral diffusion of the ZPL of single NV^- defect centers in diamond nanocrystals was introduced. The method works even for spectral diffusion rates orders of magnitudes higher than photon detection rates. Systematic studies of milled and purified type Ib nanodiamonds (see Sec. 3.2) were carried out and give the following insights.

I) **The spectral diffusion probability $\mathbf{p}(\tau)$ decays exponentially,** with a single exponential decay. This supports the assumption that spectral diffusion is indeed caused by uncorrelated (surface) charge fluctuations.

II) **A spectral diffusion time $\tau_D = 2.2 \pm 0.4\,\mu s$ was determined** with a spectral

diffusion rate $\gamma_D = 1/\tau_D$ of about 450 kHz. This is almost 100 times faster than the single photon detection rate of about 4.6 kHz for photons stemming from the ZPL only.

III) **A linear dependency of spectral diffusion rates on excitation power was determined, while spectral diffusion rate approaches zero $\gamma_D \to 0$ for zero excitation power.** This indicates, that spectral diffusion is primarily caused by laser excitation light. This is in agreement with a simple surface charge trap model introduced here.

IV) **The number of ZPL photons detected per spectral jump is constant for excitation powers far below saturation powers.** It is therefore independent of the excitation power. This number is a key figure of merit for future quantum optics experiments. It gives direct information on the quality of single photon emission concerning the possible number of subsequent indistinguishable photons provided by an NV^- defect center.

V) **Temperature measurements throughout a temperature range of 5 K to 20 K did not reveal a change in the spectral diffusion rate.** This supports the findings from above, that ionization of deep charge traps by laser excitation light is the main cause of spectral diffusion.

VI) **The number of collected photons per spectral jump decreases with increasing excitation energy.** At about 2.3 eV, a pronounced threshold was found, emphasizing the use of excitation wavelengths above 540 nm.

The determined number of photons per jump of about 0.3 in NV^- defect centers in diamond nanocrystals indicates, that experiments are not feasible where spectral overlap of consecutive photons is necessary. Therefore, new approaches have to be developed to annihilate spectral diffusion in diamond nanocrystals. For example, novel surface treatments could provide reduction of spectral diffusion. Also improved collection rates would facilitate equal consecutive photons. Another way could be the active enhancement of optical transition rates via optical resonators or plasmonic structures [7, 8, 107].

8 Compact and mobile single photon generation system: Application for quantum key distribution and single photon conversion

In the first section of this chapter, a compact stand-alone single photon generation system is presented. It is based on single NV defect centers integrated in a solid immersion microscope as already introduced for a table-top setup in Chapter 6 and achieves similar photon collection efficiencies. However, its implementation on a ground plate with dimensions of only 7 x 19 x 23 cm^3 makes it an ultra-compact and mobile device. It can therefore be installed and operated outside of laboratory environments as one of the brightest stable room temperature single photon sources. Furthermore, the direct integration of common samples, i.e. non solid immersion lens samples, is also possible. This makes it a versatile microscopy system beyond its single photon source application.

Two of various possible applications of the single photon system are presented in Sec. 8.2 and Sec. 8.3. In Sec. 8.2 a quantum key distribution (QKD) experiment is introduced. It was realized by applying the compact single photon source system with single NV defect centers. Furthermore, for the first time, a silicon vacancy (SiV) defect center was applied to implement a QKD experiment in cooperation with the group of Christoph Becher in Saarbrücken. Such defect centers are ultra-bright and stable room temperature single photon emitters with almost linearly polarized emission (see Sec. 2.5). This makes them a very promising candidate for efficient implementation of QKD based data transfer as introduced here.

In Sec. 8.3, a conceptually new method is suggested for the generation of true single photons. The method is of particular interest for spectral domains where stable room temperature single photon sources are not available, e.g. the near-infrared. This makes it an interesting candidate for the generation of single photons in the telecom band.

This wavelength regime is important for data transfer over long distances where optical losses in fibers are minimal. Therefore, quantum communication schemes could be realized with infrared single photons on-demand as realized in Sec. 8.2, or entanglement transfer [190].

Parts of Sec. 8.3 were published in Jiang *et al.* 2012a.

8.1 Single photon generation system: Principle and performance

8.1.1 Motivation

True single photon applications will have increasing impact in different fields of quantum technology. Besides implementation as a single pump photon source and for quantum key distribution, further applications in quantum optics and quantum metrology, in microscopy and optical sensing are in the scope of such stand-alone single photon sources. Furthermore, a high impact application would be the absolute calibration of quantum efficiencies of single photon detectors [191]. Moreover, a low-cost single photon system could be introduced to physics classes in high schools. It would finally allow the students to perform real quantum experiments and thereby experience physics beyond it classical borders for the first time in class rooms, more than a hundred years after the discovery of quantum physics.

At present, there is already one single photon system commercially available (SPS 1.01, Quantum Communications Victoria, Australia, [9]). However, the system lacks in performance and usability. It is housed in a comparably large 19 inch ($> 48\,\mathrm{cm}$) box, and its data sheet states an unspecified operation frequency of $> 150\,\mathrm{kHz}$, which is much smaller than a photon rate of 853 kHz measured in this thesis (Sec. 6.2).

The broad scientific and applied demand and the limited commercial availability of bright single photon systems warrant further technical progress. The developed solid immersion microscope (SIM) could be one possible way to further reduce the dimension of such a system and increase its performance. Figure 8.1 illustrates, how such a SIM could be realized in dimension of 7 x 19 x 23 cm^3, smaller than a standard piece of paper (i.e. US letter size or DIN A4). This concept was implemented, the results are presented in the following.

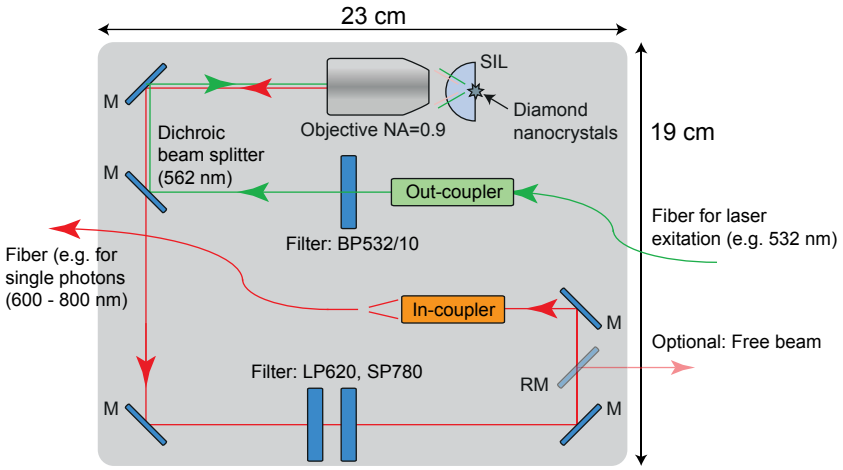

Figure 8.1: Sketch of the small scale integration of optical components of a solid immersion microscope (see Sec. 6.2). All components can be placed on a base plate with dimensions of only 19 x 23 cm^2. With its fiber coupled laser input and its fiber coupled single photon output, it is highly versatile and portable. Furthermore, beam splitter and filters can be exchanged easily for use with other wavelengths. M stands for mirror, and RM for removable mirror

8.1.2 Experimental realization

The properties of the single photon system presented in the following are very similar to the table-top system presented in Chapter 6. The system is based on a solid immersion microscope. The solid immersion lens is made of ZrO_2 (Mikrop, Switzerland), has a radius of 1 mm, and the same optical properties as discussed in Sec. 6.1. Therefore, also mounting was realized very similar as presented in Fig. 6.6. Again, diamond nanocrystals containing single NV defect centers were integrated via a spin-coating technique (Sec. 3.3). The same objective lens was implemented (NA = 0.9, Mitutoyo, Japan). Separation of excitation light and single photon fluorescence was also carried out with a dichroic beam splitter and two 620 nm long pass filters (3rd Millenium, Omega Optical Inc, USA) and a 785 nm short pass filter (Raman filter, Semrock, USA).

Besides these similarities, instead of using a beam steering unit to move the laser relative to the sample, the sample position is controlled via a 3d piezo stage (SLC-1720-S-HV, SmarAct, Germany) with nanometer precise sensors. The 3d piezo stage has only centimeter dimensions. Furthermore, the introduced system offers direct fiber coupling in addition to free beam disposition of the generated single photons. For excitation of quantum emitters, arbitrary fiber coupled laser sources (CW and pulsed mode) can be directly connected to the integrated fiber out-coupler.

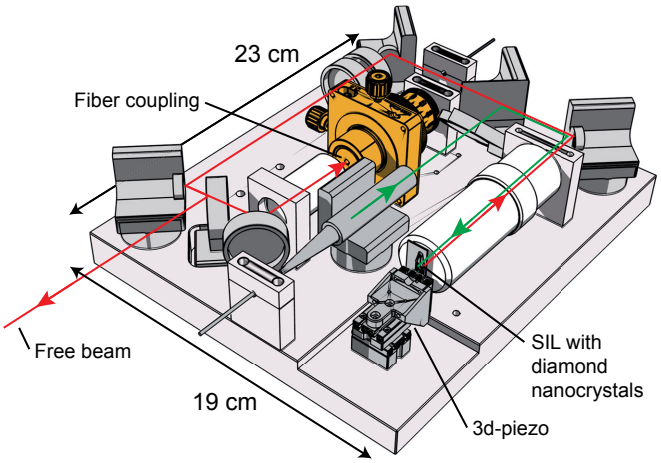

Figure 8.2: Rendered graphic of a 3d model of the single photon generation system. The 3d piezo stage with nanometer precise position sensors and 12 mm translation per axis allows large scale sample analysis (SLC-1720-S-HV, SmarAct, Germany). The system has a height of only 7 cm.

The arrangement of optical elements on a customized aluminum base plate can be seen in Fig. 8.2.

Additional components for mobile operation

The aluminum plate with the integrated SIM is the core component of the mobile stand-alone system. Additionally to this main device, some components for the operation of the system were implemented. A laptop computer controls the single photon generation system and reads out the following measurement devices. The measurement devices are either a fiber-coupled Hanbury Brown and Twiss (HBT) setup (see Fig. 8.3 a,b), with a mobile USB-integrated time correlation device, or a fiber coupled APD with a USB-integrated event counter. A sketch of the system in Fig. 8.4 gives a detailed overview of the complete application.

The computer (Thinkpad Edge E320, Lenovo, China) controls the 3d piezo stage via a home-written Labview software (National Instruments, USA). Integrated position sensors allow feedback control and large scale sample analysis. The computer also visualizes the detected count rates of either a single APD or the APDs integrated into the HBT setup. Event counting is performed either with a simple counter (NI USB-6210, National Instruments, USA) or with a time correlation device (Picoharp, Picoquant, Germany). The latter device also enables measurement of the second order auto-correlation function via the HBT setup.

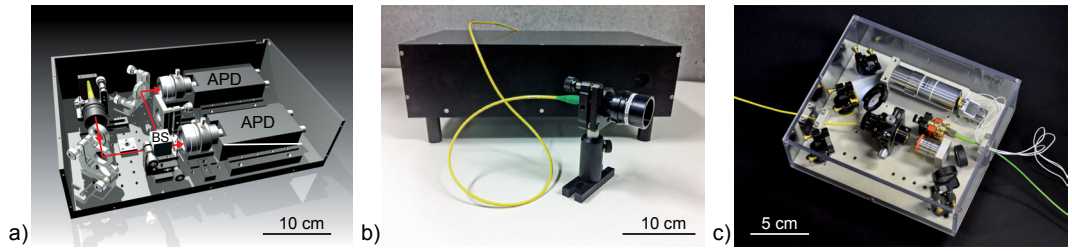

Figure 8.3: a) Rendered graphic of a 3d model of the mobile fiber coupled HBT setup. BS stands for 50:50 beam splitter, APD for avalanche photo diode. b) Photographic image of the mobile HBT device with fiber coupler. c) Photographic image of the assembled single photon generation system. The acrylic boxing protects the optical components. In a blackened version it also reduces background light.

8.1.3 Operation of the system

Free beam single photon mode

Free beam out-coupling is realized via a removable mirror as indicated in Fig. 8.1. In free beam mode, photon rates were found comparable to the table-top setup introduced in Sec. 6.2. The saturation measurement in Fig. 8.5 reveals a single photon count rate of 512 kcts/s in saturation for an excitation saturation power of 148 µW in the focus. The normalized second order auto-correlation function $g^{(2)}(\tau)$ of this specific single NV^- defect is not shown for redundancy. However its antibunching dip $g^{(2)}(0)$ was measured to be much smaller than 0.5, indicating, that true single photons were generated.

Fiber coupled single photon mode

For stand-alone operation outside of laboratory environments, fiber coupling of single photons is more suitable than free beam delivery. Fiber coupling of generated single photons is realized via an objective lens (Plan-Neofluar 5x, NA = 0.15, Zeiss, Germany. Various fibers can be integrated via a FC-PC fiber connector, e.g. single mode fibers, or multi mode fibers with core diameters ranging from about 10 µm to several 100 µm.

Fiber coupling efficiency was estimated for a standard single mode telecom fiber (SMF28e, Thorlabs, Germany). In order to do so, free beam count rates were compared to fiber coupled count rates for the same NV^- defect center and the same excitation power of 310 µW in the focus. Table 8.1 shows the result. In free beam mode, 325 kcts/s of single photons were detected, for fiber coupling 120 kcts/s. This implies a fiber coupling efficiency $\eta_{\text{Fiber}} = 0.37$. Considering this fiber coupling efficiency and a

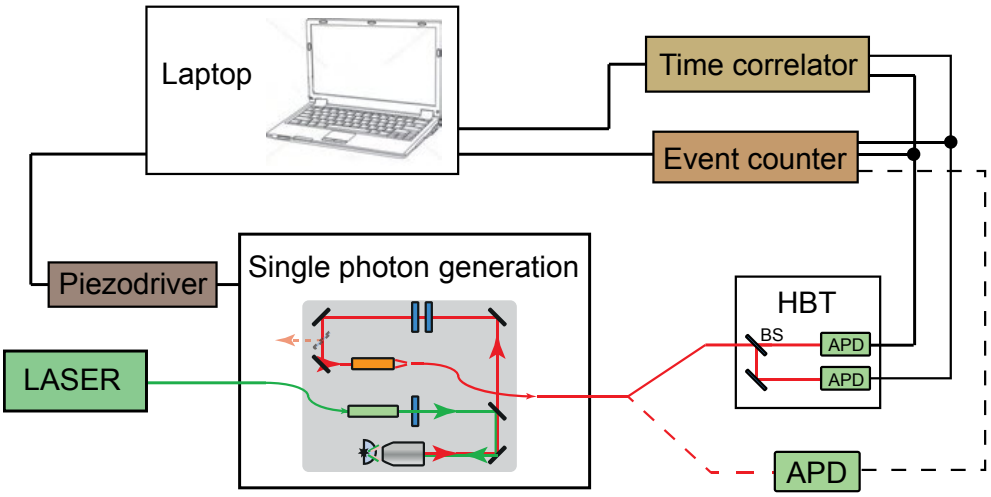

Figure 8.4: Sketch of components of the mobile stand-alone single photon system. A laptop computer controls and records the experiment. APD stands for avalanche photo diode, HBT for Hanbury Brown and Twiss setup, BS for beam splitter.

maximum count rate in saturation of 853 kcts/s (see Sec. 6.2.3), 315 kcts/s fiber coupled single photons could be delivered in saturation. The corresponding second order auto-correlation functions in Fig. 8.5 b,c) show, that true single photons were measured for free beam detection with $g^{(2)}(0) = 0.24$ as well as for fiber coupling with $g^{(2)}(0) = 0.22$. The excitation intensities were 310 µW and 765 µW for free beam and fiber coupling, respectively.

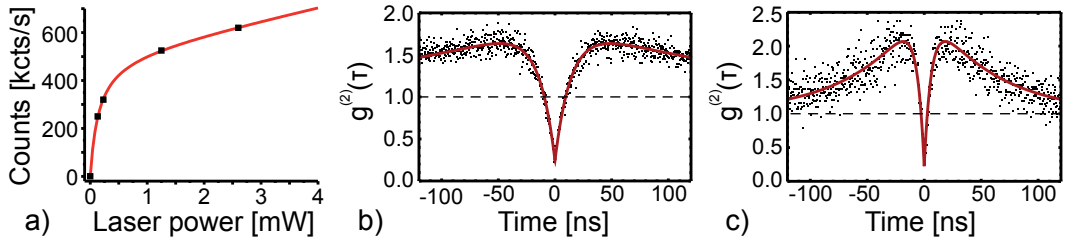

Figure 8.5: a) Saturation measurement of a single NV^- defect center. Single photon count rate of 512 kcts/s in saturation were found for an excitation saturation power of 148 µW in the focus. b,c) Measured second order auto-correlation curve for free beam detection with $g^{(2)}(0) = 0.24$ as well as for fiber coupling with $g^{(2)}(0) = 0.22$. Laser excitation power was 310 µW and 765 µW for free beam and fiber coupling, respectively

8.1.4 Summary and outlook

The compact and mobile single photon system provides reliable and efficient performance as a stand alone device (see photographic image in Fig. 8.3 c). In principle, single photon fiber out-put count rates of 315 kcts/s can be achieved for the determined fiber coupling efficiency $\eta_{\text{Fiber}} = 0.37$. Furthermore, also other fluorescent emitters like the SiV defect center can be implemented. Such emitters can be used as single photon sources. Furthermore, the emitter itself can be optically analyzed. A spectrometer or other analysis devices can be directly connected optically to the system via free-beam or fiber. This makes the device a portable high-resolution microscope.

Comparison of free beam operation to fiber operation			
	Exit. Power	Count rate	Auto-correlation
Free beam single photons	310 µW	325 kcts/s	$g^{(2)}(0) = 0.24$
Fiber coupled single photons	310 µW	120 kcts/s	$g^{(2)}(0) = 0.22$
Fiber coupling efficiency		$\eta_{\textbf{Fiber}} = \mathbf{0.37}$	
Maximum fiber count rate*	315 kcts/s		

Table 8.1: Determined single photon count rates for fiber operation mode and achieved fiber coupling rates. The excitation power was 310 µW. For a fiber coupling efficiency$\eta_{\text{Fiber}} = 0.37$ and a maximum count rate in saturation of 853 kcts/s (see Sec. 6.2.3), 315 kcts/s fiber coupled single photons could be found in saturation (indicated by the asterisk). Furthermore, the antibunching dip of the second order auto-correlation function is given for excitation intensities of 310 µW and 765 µW for free beam and fiber coupling, respectively. The corresponding data curves are depicted in Fig. 8.5 b,c).

Operation of the system is simple, all relevant components can be computer controlled. Positioning and selection of single NV defect centers repeatable due to sensor based feedback control. This even allows employment of the system by a trained person without detailed background knowledge. Therefore, the system opens up implementations outside the scientific community. Yet, for employment in e.g. school environment, further development is necessary.

However, such implementations are interesting, but are not the direct scope of the developed system. Scientific applications are still the major aim. Such experiments are presented in the following sections.

8.2 Quantum key distribution with true single photons

8.2.1 Motivation

Modern classic cryptography schemes based on so-called asymmetric (public-key) cryptosystems are widely spread and applied in almost all of our daily encrypted communication. It was first introduced in 1976 [192]. In such asymetric cryptography two different, but mathematically related keys are used: a public key and a private key. The public key is transfered in a public channel, while the corresponding private key must stay secret. The public key is used for encryption, while the private key is used for decryption. The main advantage of asymmetric cryptography is its simplicity: It allows sharing of an encrypted message in a public place or over a public channel - peer to peer communication is not necessary. It is based on multiplication of long prime numbers that need to be factorized for decryption. Despite its elegance, this scheme suffers from major disadvantages. This scheme can theoretically be cracked. While limited computational power still prevent cracking at present, factoring could be achieved by stronger computational power in reasonable time. Furthermore, new classical algorithms could be found that allow faster factoring. And finally, a quantum computer would be particularly crucial - it was already shown in 1994, that such a quantum system could factorize prime numbers using a polynomial quantum algorithm [193, 194]. This would allow factoring in reasonable time, much faster than classic computers with present protocols.

However, existing classical cryptography schemes would allow inherently secure, i.e. impossible to crack, data transfer. This is the case if a so-called one-time pad encryption scheme is used. In such a scheme, every bit of a message is encrypted by addition with a bit from a secret random key used only once (the one-time pad) of the same length as the message. The result of this procedure is a so-called ciphertext. Such a ciphertext is also truly random. Therefore, it is impossible to crack the encryption if the key is truly random, kept secret and has never been used before [195]. Hence, the ciphertext can be send via a public channel. The message can only be decrypted by a receiver who has been provided with the key, for example by physically exchanging the somehow stored one-time pads. This causes practical problems in every day communications. Providing one-time pads in the present world is not reasonable, because physically exchanging one-time pads is not practical.

Quantum key distribution (QKD) schemes can provide one-time pad security via means of telecommunication, hence in a much more convenient way than by physically

exchanging keys. As will be discussed in the following, such schemes allow the exchange of a secret key without the necessity to exchange one-time pads stored on physical systems. In 1984 a QKD scheme was suggested the first time, the BB84 protocol [4]. Its first experimental realization dates 1992 [196]. Up to today, whilst other QKD protocols exist [195], the widely explored BB84 remains one of the most relevant protocols. Therefore, further progress of implementing this protocol experimentally stays relevant. Such experimental progress was achieved in this thesis and is introduced in this section.

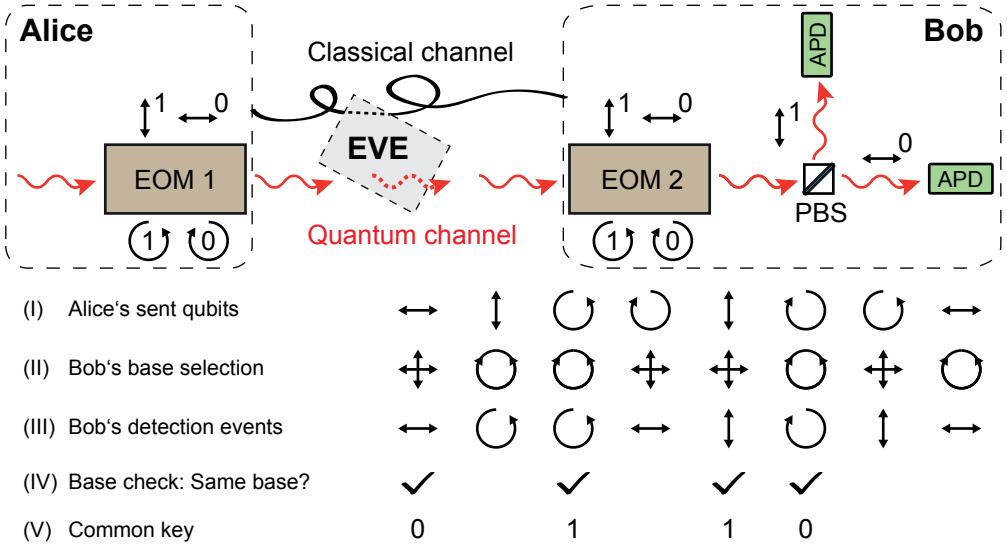

Figure 8.6: Schematic of the BB84 protocol for quantum key distribution [4]. Alice and Bob can communicate via two channels, Eve could interfere with both of them. Via the quantum channel, polarized single photons are used as information carrier (indicated by waved arrows). The polarization properties of the photons are controlled via two electro-optical modulators (EOMs) and a polarizing beam splitter (PBS). Via EOM 1, Alice can chose between two bases, linear or circular polarized. By doing so, a polarization state is prepared (indicated by the black arrows). Via EOM 2, Bob again choses a bases and measures the photon, either on APD 1 or APD 2. Via the classical channel, they select those transmission events with the same bases and create a common key. This key is used for encrypting private information. (I) - (V) Exemplary process sequence of the BB84 protocol. Details are described in the text.

The BB84 protocol describes a scheme for the inherently secure transfer of a private message from a sender (by convention called Alice) to a receiver (by convention called Bob). The protocol will be introduced by means of polarized single photons and according to reference [195]. It is illustrated in the sketch of Fig. 8.6. The protocol applies four quantum states that build two conjugate bases. For example, these could

be the polarization states horizontal (H), vertical (V), left circular (L), and right circular (R). The binary value 0 is attributed by convention to horizontal and right circular states and the value 1 to vertical and left circular states. The states will be called qubits (for quantum bits).

In a first step, Alice generates single photons in one of the four randomly chosen states. This random choice is crucial for security, therefore, truly random numbers should be used to make the choice. The photons are then send to Bob via a one-to-one correspondence.

In the next step, Bob measures the transmitted photons in one of the two bases, again, chosen randomly and independent from Alice. The events (bits) when Alice and Bob have chosen the same bases by chance, give them perfectly correlated results. However, for different bases, they get uncorrelated results. Therefore, on average, Bob receives a sequence of bits with an error rate of 25 %, the so-called raw key.

Now, Alice and Bob compare their choice of bases via a public channel and hence determine those bits which are perfectly correlated (for matching bases) and those which are completely uncorrelated. Bob can publicly announce his choice of bases for each bit, without announcing the result of his measurement. Alice then tells him which bits he should keep. Both only keep the bits for matched bases, and thereby generated a bit sequence of about 50 % of the original bit sequence. This bit sequence is called the sifted key.

The public channel used by Alice and Bob only needs to be authenticated. Hence any eavesdropper, by convention called Eve, is permitted to listen to all exchanged information on the public channel, but is not able to modify it.

What could Eve do to get information about the shared key of Alice and Bob? The most simple way would be to intercept a qubit propagating in the quantum channel. However, Eve does not know in which bases (just as Bob) the qubit was prepared by Alice. And, since diminished reception of bits on Bob's side would uncover Eve, she is forced to send a qubit to Bob to try to stay incognito. This eavesdropping strategy is called intercept-resend. In the ideal case, Eve would like to send the intercepted qubits in their original state, while keeping a copy for herself.

This, however, is prohibited by the so-called non-cloning theorem [197]. It predicts that quantum mechanics forbids the splitting or replication of a single quantum state, e.g. a single photon. Only imperfect copies are possible. Therefore, Eve can only send a newly generated qubit to Bob according to her measurement. However, only in roughly 50 % of the cases, Eve will choose the same bases as Alice. In all other cases, Eve

creates a state with a bases incompatible with the choice of Alice. Eve cannot avoid this, as no information about Alice's strategy of choosing bases is available (as it should be truly random). Therefore, Alice and Bob get uncorrelated results in about 50 % of the cases, resulting in an error rate of 25 % and thus can reveal Eve's intervention. By applying this intercept-resend strategy for all qubits, Eve could thus receive 50 % information, while Alice and Bob would find an error of about 25 % in their sifted key. However, Eve could also use this strategy for a reduced fraction of qubits, e.g. of 12 %. In this case, the sifted key error rate will be about 3 %, while Eve's information will be about 6 %. This is a relevant scenario: Typical quantum bit error rates (QBER) in present QKD schemes (including the error rates measured in the presented experiment), are of this order of magnitude. Hence, sifted keys contain errors - caused either by an Eavesdropper, by technical imperfections, or both. Though, due to their unknown origin, all errors have to be attributed to Eve.

Fortunately, such errors can be corrected by error correction protocols. Such protocols use classical algorithms to correct the errors. After error correction, Alice and Bob have identical copies of the key, but Eve may still have some information about it. However, Alice and Bob have a tool to minimize the information Eve has of their final key. This tool is the so-called privacy amplification [198]. By applying privacy amplification protocols, Eve's information can be reduced to an arbitrarily low value.

After error correction and privacy amplification, the key is used for encrypting a private message by means of the one-time-pad encryption scheme as introduced earlier. The thereby encrypted message can be send via a public channel to Bob as it can not be decrypted by any means without knowing the key.

8.2.2 Experimental implementation

Setup

The experimental setup is illustrated in Fig. 8.7. A pulsed single photon source with either NV or SiV defect centers was used as introduced in Sec. 8.1. A polarizing filter was inserted into the optical path to linearly polarize the single photons vertically. The polarization state of a photon was controlled via two EOMs (LM0202 P VIS with KD*P crystal, Linos, Germany), operated by home-built EOM drivers. These EOMs were used to rotate the polarization by the linear electro-optic effect (Pockels effect). They were oriented in a way, that their fast and slow axis is oriented $\pm 45\,^{\circ}$ and thus can either act as $\lambda/2$ or $\lambda/4$ wave plates, depending on the applied voltage. Hence, they

could either rotate the incoming polarization by 90 °, turn linear polarized light into circular, or vice versa. On Alice's side, they prepared either of the states H, V, L, or R. On Bob's side, they are used to chose a polarization bases of either H/V or R/L. The choice of state and choice of bases were determined independent and randomly by using true random numbers from a quantum random number generator (QRNG)[137]. On Bob's side, the incoming photon state was determined via a polarizing beam splitter.

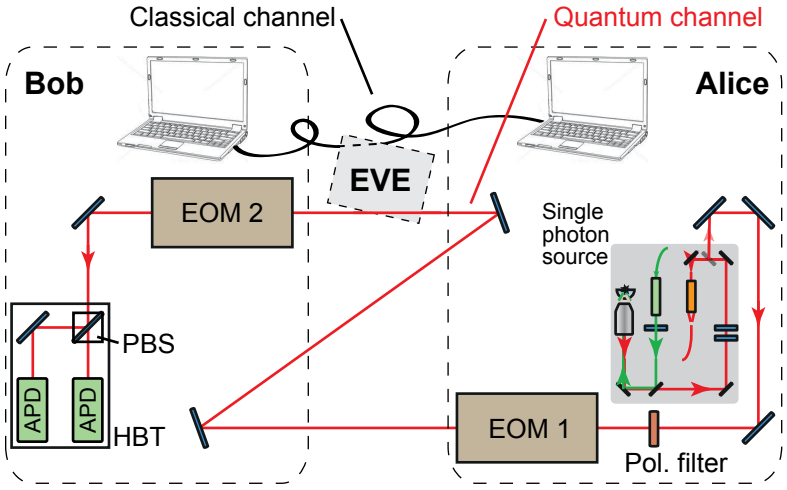

Figure 8.7: Schematic of the implemented QKD setup. Alice and Bob can communicate via two channels, Eve could interfere with both of them. Single photons are generated with a pulsed source introduced in Sec. 8.1 and detected with avalanche photo diodes. The polarization properties of the photons are controlled and measured via a polarizing filter (pol. filter), two electro-optical modulators (EOMs), and a polarizing beam splitter (PBS). In contrast to the illustration, Alice and Bob were controlled by a single computer to reduce the experimental complexity.

For the intended proof-of-principle experiment, a simple experimental configuration was chosen. To reduce the complexity of the setup, only one computer was used to control the experiment. A field programmable gate array (FPGA, NI-R7813, National Instruments, USA) was implemented for fast and potent control of the experiment. The FPGA's cycle rate is 40 MHz. It allows massive parallel computing in realtime with high accuracy. It can thus be used to control all dynamic components of the experiment, such as EOMs, laser trigger, and APD read-out. It was fed with real quantum random numbers. These were generated by a QRNG, the bits were downloaded from a public online service: http://qrng.physik.hu-berlin.de, provided by our group. The implemented control cycle is illustrated in Fig. 8.8. However, in the experiment we used only repetition rates of up to 1 MHz due to limited EOM driving speed.

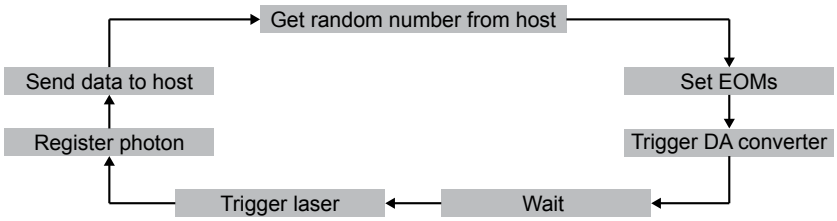

Figure 8.8: Process diagram of a FPGA cycle. First, it gets random number from the host computer. Then it sets the EOMs randomly with this number. Then it triggers the digital-analog (DA) converters that set the EOM voltages. After initialization of the EOMs, they need some time to adjust, the FPGA waits until it triggers the laser. The triggered single photon passes both EOMs where it is polarized according to the initialized state. It is detected by one of the APDs. This count event is registered and send to the host computer.

Performance of the EOMs

The most crucial devices within the setup are the single photon source and the EOMs including their drivers. The single photon generation has been discussed in Sec. 8.1. It is presently the most efficient and stable room temperature single photon source. Besides its still limited efficiency, the EOM driving frequency is the main limiting factor of this experiment. The driving speed of the EOMs has direct impact on the bit rate. A faster EOM - driver system needs to be applied to further enhance the performance. Also the polarization properties influence the outcome of the experiment. Therefore,

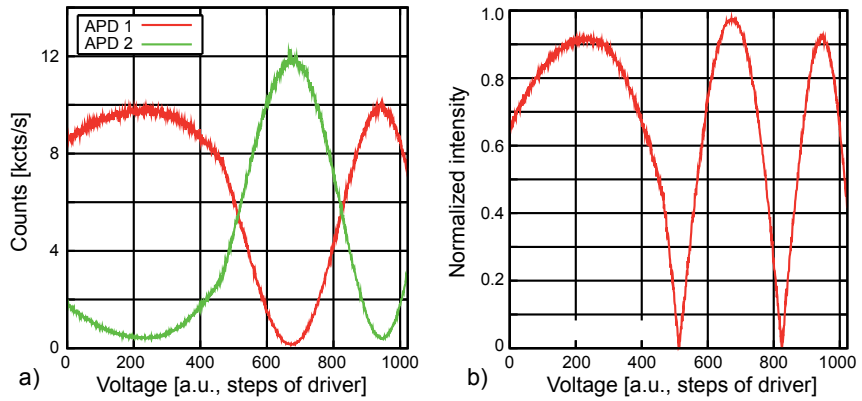

Figure 8.9: Performance of the EOMs a) APD count rates for varying the driver voltage of one EOM and thus varying the polarization of the photons. b) Contrast between the count rates of the two APDs.

the EOMs were tested regarding their ability to polarize incoming light. The results are depicted in Fig. 8.9. The graph in Fig. 8.9 a) shows APD count rates for varying

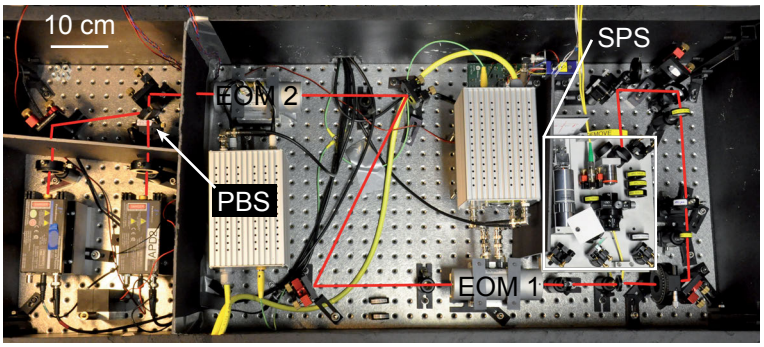

Figure 8.10: Photographic image of the experimental setup used for the QKD experiment. SPS stands for single photon source, EOM for electro optical modulator, and PBS for polarizing beam splitter. The red line represents the path of the single photons. Other components are according to Fig. 8.7.

EOM driver voltage and thus varying polarization. Increasing voltage causes stronger rotation of the polarization of incoming light. APD 1 and APD 2 detect horizontal and vertical polarized light, respectively. The graph indicates that the polarization can be turned by more than 180 °. It is also visible, that the APDs were not perfectly balanced. The graph in Fig. 8.9 b) shows the contrast $C = \frac{I_1 - I_2}{I_1 + I_2}$ between the two APDs indicating a high contrast of $C > 0.9$.

8.2.3 QKD with single NV^- defect centers

To show the capability of the developed compact single photon system (see Sec. 8.1) and its possible implementation as stand alone device, a QKD experiment was realized using a single NV defect center [199].

Operation parameters with NV defect centers

The developed QKD system was tested in the laboratory. Successful quantum cryptography was performed using a mobile room temperature single photon generation system. A quantum bit error rate (QBER) of $\approx 3.3\,\%$ was reached, which is far below the limit of 11 % [200], necessary for suitable error correction. The sifted key rate was 2.5 kBits/s for a cycle rate of 1 MHz. This is comparable to key rates achieved in the literature of 17.7 kBits/s for a cycle rate of 5.3 MHz [199]: Extrapolation from 1 MHz to 5.3 MHz gives 13.3 MHz of key rate for the experiment, only slightly smaller than 17.7 kBits/s.

The main limitation of the presented device is the limited cycle rate caused by a

relatively slow EOM driving rate of 1 kHz. Extrapolating the achieved key rate gives a key rate of 50 kBits/s for the same system with enhanced cycle rate of 20 MHz. This cycle rate is possible with the implemented FPGA and also adequate for an NV defect center with a lifetime of 18 ns. Furthermore, extrapolation for the same cycle rate and for best setup efficiency of 4.2 % achieved (Sec. 6.2.4), would enable sifted key rates of up to 420 kBits/s. Table 8.2 gives an overview of achieved and possible and bit rates.

QKD with single **NV** defect centers	
	Comp. single photon system
Cycle rate	1 MHz
Raw bit rare	5 kBits/s
Sifted key rate	2.5 kBits/s
Quantum bit error rate	$\approx 3.3\,\%$
Possible sifted key rate*	50 kBits/s
Improved possible sifted key rate*	420 kBits/s

Table 8.2: Performance of the implemented QKD experiment. The main limitation was a driving rate of the EOM of 1 MHz. The value for a maximum possible sifted key rate was estimated based on a maximum repetition rate of 20 MHz suitable for an NV defect center with a lifetime of about 18 ns. The improved possible bit rate was determined for the same cycle rate and a maximum setup efficiency of 4.2 % as achieved before (see Sec. 6.2.4).

8.2.4 QKD with SiV defect centers: First time implementation

The performance of a QKD scheme with an NV defect center is inherently limited by the lifetime of the defect center. Also, the relatively low degree of polarization of the NV defect centers limits the performance. The required polarization filtering causes a loss of 10 % to 50 % the emission. Furthermore, the spectrally broad emission of the NV defect center of about FWHM = 100 nm causes problems in imaging and polarization control via the EOM. These constraints can be overcome by SiV defect centers as introduced in detail in Sec. 2.5. They have a lifetime of down to 0.2 ns and a polarization of up to 0.91 with a spectral width of down to 0.7 nm at room temperature. It is therefore a promising system for fast quantum key distribution.

The same compact single photon generation system was applied as for the NV. The SIL was exchanged with a sample of diamond nanocrystals containing SiV defect centers provided by the group of Christoph Becher in Saarbrücken. The roughly 100 nm sized nanocrystals were grown by chemical vapor deposition from 10 nm - 20 nm sized diamond seeds on an iridium substrate [11].

Operation parameters with SiV defect centers

Successful quantum cryptography was performed for the first time with a single SiV defect center. The quantum bit error rate (QBER) was ≈ 6 %, slightly higher than for the NV. The sifted key rate was 890 Bits/s for a cycle rate of 0.5 MHz.

QKD with single **SiV** defect centers	
	Comp. single photon system
Cycle rate	0.5 MHz
Raw bit rare	1780 Bits/s
Sifted key rate	890 Bits/s
Quantum bit error rate	≈ 6 %
Possible sifted key rate*	360 kBits/s
Improved possible sifted key rate*	3.6 MBits/s

Table 8.3: Performance of the SiV - QKD experiment. The main limitation were a driving rate of the EOM of 0.5 kHz and emitter quantum efficiency (QE). The value for a maximum possible sifted key rate was estimated based on a maximum repetition rate of 20 MHz suitable for a SiV defect center with a lifetime of down to 0.2 ns and a 10 times improved emitter QE. The improved possible bit rate was determined for the same QE and for a cycle rate of 200 MHz. For details refer to text.

Two main experimental shortcomings were determined which prohibited higher key rates. First, accordant to the experiment with the NV defect center, a limited cycle rate limited the key rate. However, extrapolating the achieved sifted key rate gives a key rate of 36 kBits/s for the same system with enhanced cycle rate of 20 MHz. This cycle rate is possible with the implemented FPGA and also adequate for SiV defect center lifetimes of down to 0.2 ns. For a lifetime of 1 ns, even faster cycle rates of 200 MHz are reasonable, resulting in a sifted key rate of 360 kBits/s, outreaching key rates for NV defect centers.

The second and equally severe reason for limited key rates was the 'quality' of applied SiV defect centers. Maximum count rates under CW excitation of 4.8 Mcts/s have been reported in the literature [11]. However, these are maximum values for selected defect centers. Effort has to be made to find such a bright center. In the performed experiment (and for corrected setup efficiencies), SiV defect centers did not reach such high photon rates. About 10 times smaller photon rates were measured. This is mainly assigned to limited quantum efficiencies of the defect centers. Significant improvements of key rates are simply achievable by optimizing the fluorescent properties of the single photon emitter. For a SiV defect center with 10 times improved photon rate, 8.9 kBits/s sifted key rate would be achieved.

Combination of these possible experimental improvements would provide much higher key rates than achieved to date. For a maximum repetition rate of 200 MHz suitable for a SiV defect center with a lifetime of down to 0.2 ns and a 10 times improved emitter quantum efficiency, up to 3.6 MBits/s sifted key rate could be reached. Table 8.3 gives an overview of achieved and possible bit rates.

8.2.5 Summary and outlook

Successful quantum cryptography was performed for the first time with a single SiV defect center. This is a major step towards MHz quantum key rates due to the short lifetime of the SiV of down to 0.2 ns. The achieved QBER was about 6 %, low enough for inherently secure application via public channels. For a single NV defect center 2.5 kcts/s sifted key rate with a QBER of only 3.3 % was achieved. This key rate is in the range of before reported rates [199].

These experiments prove that the developed compact system is well suited for the application of QKD schemes. However, the performance of the experiment is limited by slow EOM drivers and limited quantum efficiencies of the SiV defect centers. Assuming faster EOMs and a by 10 improved QE, a sifted key rate of 3.6 MBits/s could be achieved with a SiV for a cycle rate of 200 MHz. For an NV defect center, the bit rate could be 420 kBits/s, assuming 20 MHz driving rate and an improved setup efficiency as was achieved before (see Sec. 6.2.4).

8.3 A novel method for single photon generation: Incoherent photon conversion in selectively infiltrated hollow-core photonic crystal fibers

In this section, a conceptually new method for the creation of single photons is suggested. It is based on a complementary approach to single photon generation via a single photon emitter. The emission of a bright and stable single photon source is applied to pump an ensemble of emitters.

The suggested method is applied to realize a novel, stable, non-blinking, room temperature infrared single photon source. In the particular implementation presented here, visible single photons from a defect center in diamond are converted to the near infrared. The theoretical conversion efficiency was estimated to be 26 %.

8.3.1 Motivation

Single photons in the near infrared, particularly the telecom band, are highly desirable for long-distance fiber-based quantum key distribution [201] or entanglement transfer [190]. They can be generated by parametric conversion processes [202, 203], however, such processes are not suitable for on-demand single photon generation which is advantageous for various communication protocols. At present, there exist a number of on-demand single photon sources with high emission rates and stability even at room temperature as was introduced earlier in this thesis. However, only few quantum systems with strong transitions in the near-infrared wavelength regime have been developed. Self-organized quantum dots are in principle capable to emit in the infrared, e.g. at 1.3 µm [204], but they require cryogenic temperature operation and their growth with low density is challenging. Individual lead chalcogenide colloidal quantum dots (such as PbS) or CdHgTe quantum dots (QDs) can provide single photons in the near-infrared wavelength range, but they are not photo-stable over longer periods of laser excitation [205]. These examples show, that on-demand single photon generation in the near infrared, possibly within the telecom band, though most urgently needed, is particularly crucial.

The approach presented in the following overcomes the limitations of photo-stability of quantum dots by relying on an ensemble of quantum dots and addressing them individually with low light powers. Hence, maintaining their functionality for time periods much longer than that of individual quantum dots under strong laser excitation.

8.3.2 Fundamental concept

What is the fundamental requirement for the generation of a single on-demand photon by spontaneous decay of a fluorescent system? A closer look reveals, that the fundamental key requirement is the generation of a *single excitation* in an optically active system.

A single quantum system fulfills this requirement automatically, since it can only absorb a single quantum of light, even if pumped with an ensemble of photons (see Fig. 8.11 a) and Sec. 2.1). After absorption, a single photon is emitted.

A complementary approach is to utilize an ensemble of photon emitters, but to pump it with only a single quantum of light as illustrated in Fig. 8.11 b). By doing so, a single photon is converted by single photon absorption and subsequent single photon re-emission.

For the implementation of the latter concept, there are three main requirements: (I)

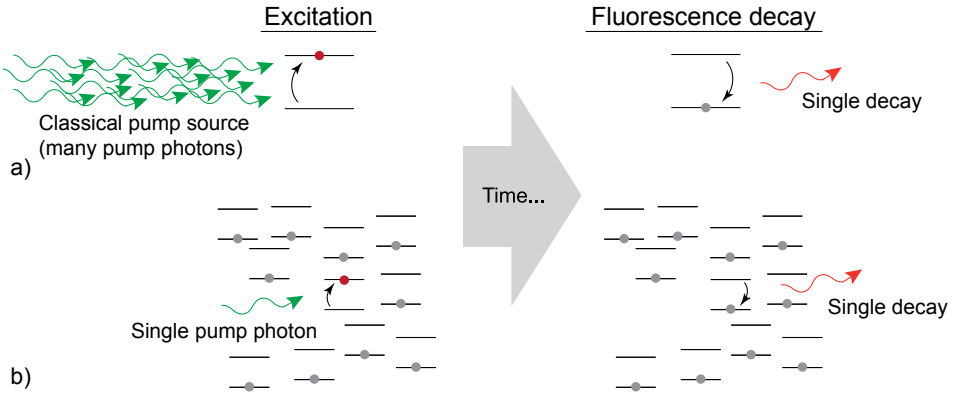

Figure 8.11: Two complementary approaches for on-demand single photon generation. a) Excitation of a single quantum system with a classical pump source of many photons and subsequent spontaneous emission of a single photon. b) Excitation of an arbitrary ensemble of quantum emitters with a single pump photon. Also in this case only a single excitation is present, hence decay of the ensemble also leads to emission of a single photon only.

a bright single pump photon source, (II) an efficient absorber and re-emitter with an appropriate Stokes-shifted emission spectrum in the targeted optical spectrum, and (III) an efficient conversion system that provides high absorption of the incoming single pump photon and efficient re-collection of the re-emitted single photons to provide them for further application.

8.3.3 Experimental implementation

(I) Efficient source of single pump photons

The compact and mobile single photon source introduced in Sec. 8.1 is a well suited pump source. It is based on a solid immersion lens microscope and a single nitrogen vacancy (NV) center in diamond. Its maximum single photon count rate was determined in Sec. 6.2 to be 2.4 Mcts/s and could possibly be increased by applying a SiV defect center (Sec. 2.5).

(II) Optical absorber and fluorescence re-emitter with high quantum efficiency

A suitable absorber, for example, is an ensemble of colloidal QDs. Such QDs are room temperature stable and only photo-bleach under high excitation power. Furthermore, they have large above-band absorption and their Stokes-shifted fluorescence emission spectrum can be tailored by choosing the right size and material [206], for example, in the telecom band.

(III) Efficient conversion system

The most direct conversion system would be a dense sample of QDs. Single pump photons could be focussed onto such a sample of QDs by a high NA objective. The QD emission could be collected via the same objective. However, an estimation based on the absorption cross section of similar QDs, the maximum density of QDs in a spin-coated or drop-casted sample, and an NA of 0.95 reveals a very small conversion efficiency of $\eta_{\mathrm{Tot}} = 0.01\,\%$. This estimation indicates the limitation of this direct absorption and re-collection approach.

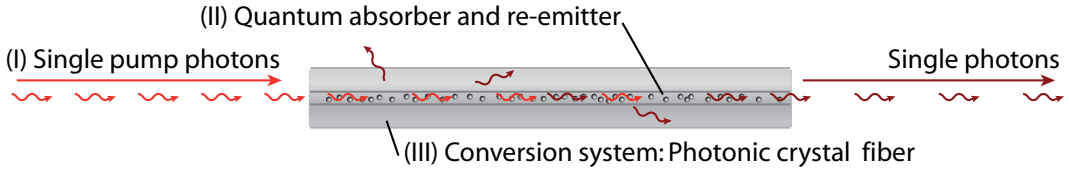

Figure 8.12: Sketch of the concept of using a stream of single pump photons to generate single photons in a pre-selected wavelength regime.

Therefore, in order to achieve both a large single photon absorption probability and a very high re-collection efficiency of Stokes-shifted fluorescence a hollow-core photonic crystal fiber (HCPCF) was applied as efficient conversion system. It was infiltrated with a solution of pre-selected colloidal QDs for absorption and re-emission [207]. By adopting the concentration of QDs and fiber length, the absorption can approach unity. However, an increase in absorption causes an increased re-absorption as will be discussed in the experimental section. At the same time, a selectively filled HCPCF provides a large numerical aperture for collection and guiding of a large fraction of re-emitted fluorescence.

Utilizing a bright single photon source, specific, pre-selected QDs, and a HCPCF, a novel kind of fiber-coupled single photon source in the telecom band can be realized. The single photon system is sketched in Fig. 8.12.

8.3.4 Hollow-core photonic crystal fibers

Micro-structured optical fibers allow for light confinement in microscopic dimensions and guiding over macroscopic distances. Therefore, these fibers are ideally suited for enhanced interaction between light and matter. Many of these micro-structured fibers feature a hollow center hole which can be filled with various substances. Such filled HCPCFs allow strong and well-controlled interactions with solid state, fluidic

and gas systems. In recent years, such micro-structured optical fibers have been used for absorption [208], fluorescence [209], Raman [210], and surface enhanced Raman scattering (SERS) [211, 212] experiments and have shown great potential for chemical, biological, and environmental sensing applications. Due to the much longer interaction length between the guided light and the sample (e.g., gases or liquids), accomplished sensitivities and detection signals are orders of magnitudes higher than in unguided beam light - matter interaction experiments.

Efficient light collection by waveguide light guiding

Generally, HCPCFs confine and guide light within the lower dielectric material in the central core via the photonic band-gap effect [213]. This allows infiltration of gases in the hollow core without substantially changing the band-gap properties. When the hole is filled with liquid, the band-gap effect and therefore band-gap light-guiding are destroyed due to the high refractive index of liquids. Yet, another optical process enables light guiding within the filled hole of the fiber. The refractive index of liquids of about $n = 1.4$ to $n = 1.6$ is higher than the surrounding microstructure which consists mainly of hollow regions. The filled region forms a dielectric rod waveguide and total internal reflection happens at the interface of the filled core and the holey cladding. This results in a high collection efficiency for the applied HCPCF system. However, other waveguiding structures, e.g. on chip silicon nitride (Si_3N_4) waveguides [214, 215] or tapered fibers (see Sec. 5.3), could also be used.

Theoretical collection efficiency

The collection efficiency of QD fluorescence for a selectively filled HCPCF, as used in the presented experiment, can be estimated as follows. A solution of QDs and polystyrene dissolved in toluene can be infiltrated into the hollow core of the fiber ($n_{Tol} = 1.49$, $n_{Poly} = 1.57$ with 1:1 proportion). This results in a refractive index of the liquid in the fiber of $n = 1.53$. For the structured, hollow part surrounding the center hole (see Fig. 8.13 b) the effective index of refraction is estimated to be about $n = 1.05$. The emission of quantum dots is totally reflected inside the fiber, when the radiation angle is greater than the angle of total internal reflection of $43\,^\circ$ ($\arcsin(1.05/1.53)$). Via this reflection mechanism, 26 % of the total emission is guided inside the fiber core to the end of the fiber to be detected or further guided in air. A similar portion of the emission is guided to the front facet of the fiber. Both fractions could be easily sent to one end of the fiber by adding a reflective filter on the facet of the other fiber end. In

this way a re-collection efficiency of 52 %, collected at both ends of the fiber, can be achieved when neglecting re-absorption.

8.3.5 Preparation of conversion system

Synthesis of CdHgTe quantum dots

Synthesis of CdHgTe quantum dots was carried out at th TU Dresden in the group of Prof. Eychmüller. Aqueous mercaptopropionic acid (MPA)-capped CdHgTe QDs have been synthesized according to the method reported in reference [216]. In a typical synthesis, 0.562 g of $Cd(ClO_4)_2 \times 6H_2O$, 0.014 g of $Hg(ClO_4)_2 \times 6H_2O$ and 0.189 g of MPA were dissolved in 60 mL of Milli-Q (Millipore) water. The pH of the resulting mixture was adjusted to 12 using 1 M NaOH solution and subsequently was deaerated by bubbling with Ar for 30 min. Then, under stirring, H_2Te gas (generated by the reaction of 0.1 g of Al_2Te_3 lumps with an excess of 0.5 M H_2SO_4 solution) was bubbled into the solution together with a slow argon flow. The molar ratio of $Cd^{2+}/Hg^{2+}/Te^{2-}$/MPA was 0.98/0.02/0.5/1.3. Further nucleation and growth of the nanocrystals proceeded by refluxing the solution at 100 °C for 30 min - 35 min under open-air conditions. The obtained QD colloid was purified by reprecipitation of the particles by addition of 2-propanol to the concentrated (on a rotor evaporator) crude solution with subsequent dissolving of the QD precipitate in ∼2 mL of Milli-Q water.

Thus obtained CdHgTe QDs were transferred from water into toluene utilizing octadecyl-p-vinylbenzyldimetylammonium chloride (OVDAC) as a transfer agent according to a procedure described in reference [217]. Briefly, ∼2 mL of the reprecipitated QD water solution, 70 mg of OVDAC and 2 mL of toluene were vigorously stirred for 30 min. Toluene layer containing QDs was separated and mixed with 6 mL of acetone with subsequent centrifugation. The QD precipitate was dissolved in ∼3 mL of toluene.

The ultraviolet to visible absorption spectrum was recorded using a Cary 5000 spectrophotometer (Varian Inc., USA). Fluorescence measurement was performed with a Fluorolog-3 spectrofluorometer (HORIBA Jobin Yvon Inc., Japan).

Assembly of the conversion system: Integration of QDs into the PCF

The commercial hollow-core photonic crystal fiber (HC-800-01, NKT Photonics) employed in the experiment is made of fused silica (refractive index $n_2 = 1.45$) and produced from a preform by a heating and stretching process in a drawing tower (so-called stack-and-draw method) [218]. The fiber is designed for the operation in air

via the photonic band-gap effect at a central wavelength of 830 nm with a transmission bandwidth larger than 70 nm. Its hollow cladding structure exhibits an air filling fraction f > 90 % and has a diameter of 40 µm while the central core diameter is about 9.5 µm.

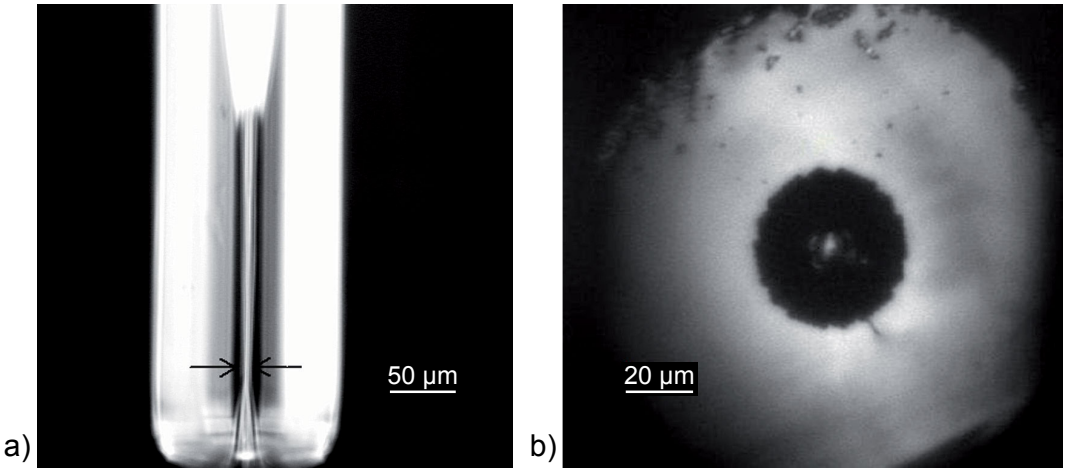

Figure 8.13: a) Optical microscope image of a hollow-core fiber (side view) after treatment in the fusion splicer. The arrows indicate the region of the open core hole, while the cladding holes are sealed. b) Optical microscope image of a hollow-core photonic crystal fiber selectively filled with liquid.

When preparing the hollow-core fiber, liquid should be selectively injected into the core hole only. Therefore, additional preparation steps prior to the infiltration are needed. A selective melting method for the holes in the facet was applied [219] in order to selectively seal the cladding holes, while the central core hole remains open. An optical microscopy image of a melted hollow-core fiber after the treatment in the fusion splicer is shown in Fig. 8.13 a).

After the cladding holes are sealed, the core hole is equipped with colloidal quantum dots dissolved in toluene. In order to suppress evaporation of toluene, a polymer (polystyrene) is dissolved in the solution containing the quantum dots. It dries fast and blocks the end of the core hole, stopping the evaporation of toluene. Furthermore, the polymer has a higher refractive index than toluene, resulting in improved collection efficiency due to a higher angle of total internal reflection. To equip the core hole, the fiber is glued to a syringe that is filled with the polymer QD solution. Pressure is applied until the core is entirely filled [209]. After infiltration, the fiber is cleaved for smooth facets. As shown in Fig. 8.13 b), after selective infiltration and cleaving, only the core hole is filled with liquid while other cladding holes are empty.

8.3.6 Experimental setup: Integration of pump and conversion source

A sketch of the experimental setup used for the measurement is shown in Fig. 8.14. Single photons were generated by single NV centers that emit in the visible at 690 nm with a FWHM of the fluorescence spectrum of approximately 100 nm (see Sec. 2.4 and red curve in Fig. 8.16). For efficient photon collection, the home-built compact and mobile single photon generation system was used as introduced in Sec. 8.1. For filtering the green 532 nm laser excitation and guiding the red single photons to the functionalized fiber core, a dichroic beam splitter with a 625 nm edge was used. The transmission rate of the red photons through the dichroic beam splitter was about 89 %. The other 11 % of single photons were reflected back to single photon counting modules in order to monitor the total single photon generation rate, align the setup, and estimate the number of visible photons directed to the HCPCF.

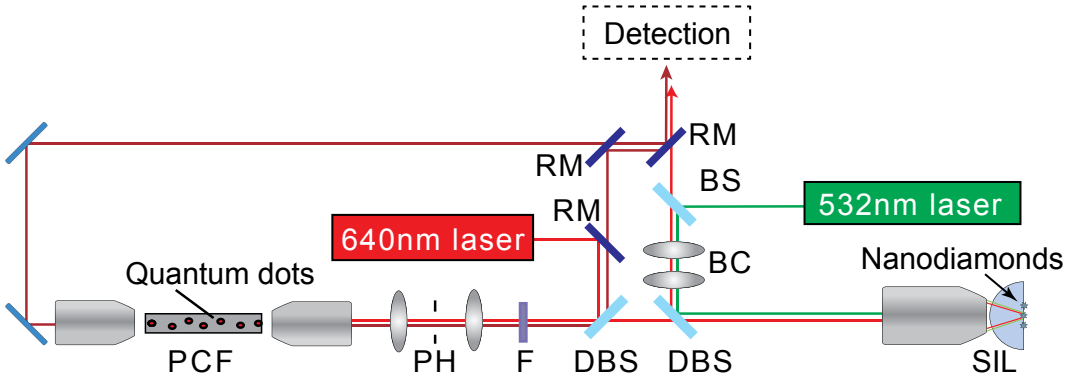

Figure 8.14: Experimental setup. PCF, BC, BS, DBS, RM, F, PH, SIL, refer to photonic crystal fiber, beam control, beam splitter, dichroic beam splitter, removable mirror, filter, pinhole, solid immersion lens, respectively.

The HCPCF which had been functionalized with QDs, was mounted on a mechanical 3d translation stage. The red single photon emission was coupled in and out of the fiber via two microscope objectives (20 ×, NA = 0.4, Olympus, Japan), which were also mounted on a mechanical translation stage. Before coupling into the filled fiber, a 540 nm long pass filter was used to block the remaining green laser light. After the absorption and re-emission process of photons by the quantum dots inside the fiber, the photoluminescence of the QDs was detected by a spectrograph (SpectraPro 500i, Princeton Instruments, USA) or with a CCD camera (SPEC-10, Roper Scientific, USA). Detection was carried out either in transmission or backward direction (see Fig. 8.14). For doing so, the fluorescence light was collected by the microscope objective at the end

of the fiber and guided to the detection systems after passing a 540 nm long-pass filter and a 790 nm long-pass filter. In this setup, removable mirrors were put on magnetic stages to change the direction of the signal path. In backward direction, a dichroic plate beam splitter (801 nm single-edge, BrightLine, Semrock, USA) was used. It has a high transmission for the red photons and a high reflectivity for near-IR photons (above 801 nm). Thereby, converted near-IR emission from the front facet of the fiber could be detected. To verify single photon character of the converted photons, autocorrelation measurements were performed in an HBT setup [14]. The 640 nm laser was used for preliminary analysis of the fiber system to determine the optimum concentration of QDs inserted into the fiber. It was also used to determine the overall conversion efficiency of the single photon system.

8.3.7 Operation of system

Single pump photon source

For preparing the conversion experiment, at first, single photon generation from a single NV^- center in the SIM was optimized (see Sec. 6.2.3). For this particular experiment, a single NV^- with 31 kcts/s under an excitation power of 230 µW was detected after reflection by the dichroic beam splitter with a reflection coefficient of 11 %. Hence, 280 kcts/s of single photons were guided to the fiber (transmission of the dichroic beam splitter was 89 %). The measured and normalized autocorrelation function (collected with the HBT setup) is shown in Fig. 8.15. $g^{(2)}(0) = 0.2$ indicates strong single photon character stemming from a single NV center.

Conversion system: Evaluation of functionalized PCF system

To evaluate the fiber system, the transmission properties of a HCPCF filled only with liquid (toluene with dissolved polymer, but without QDs) were analyzed. The black curve in Fig. 8.16 shows the measured fluorescence spectrum of light under 532 nm excitation stemming directly from the SIL. A pronounced fluorescence was observed above 795 nm which stems from the ZrO_2. This fluorescence can be blocked by a 795 nm short pass filter. The red and blue curves in Fig. 8.16 indicate the spectrum of the NV center on the SIL and the total fluorescence from the end of the filled fiber, respectively. The blue curve was normalized to the red one by means of the zero phonon line emission of the NV center at 637 nm. Comparing both spectra reveals, that the spectrum of the fluorescence light that has passed through the polymer filled fiber

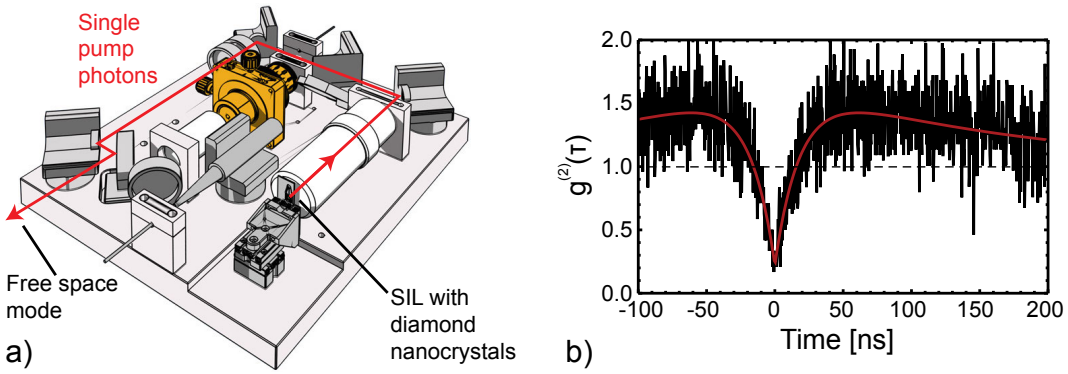

Figure 8.15: a) Rendered graphic of the compact single photon generation system used for pumping the ensemble of quantum dots. b) Normalized second-order correlation function of the fluorescence of a single NV center used for pumping. The data shows a deep dip at zero, indicating single photon statistics with $g^{(2)}(0) = 0.2$. The red curve is a fit to the data according to a three level model (see App. A).

was qualitatively the same as that of the directly measured NV center. Only below the wavelength of 625 nm, a strong suppression of fluorescence is visible for the blue curve, caused by the dichroic beam splitter in the setup. The measurement proves, that single photons stemming from the NV center were transmitted through the fiber without spectral changes. Yet, a high transmission loss of 86 % was observed. This is mainly due to the scattering out of the core mode induced by tiny bubbles in the polymer toluene solution in the fiber. Moreover, the coupling efficiency from free space to the filled fiber was reduced by partial sputtering of polymer around the core region when the fiber is cleaved as is clearly observable in Fig. 8.17 b).

In a next step, the optical properties of an active, functionalized HCPCF were determined. It was selectively filled with a solution of colloidal CdHgTe QDs, emitting in the near-infrared region (see Fig. 8.18, black curve) [216]. The central photoluminescence (PL) wavelength of the QDs is 850 nm (see Fig. 8.18 a). After the deposition of the QDs in an HCPCF, they have a small chance to be exposed to air due to the partly evaporation of toluene. Therefore, their survival in air, e.g. the time before they stop to convert photons, was experimentally determined to be at least three days, long enough to carry out the performed optical experiments.

The concentration of the QDs is a crucial parameter for preparing the QD - HCPCF system. Absorption of single photons in the visible should be maximized while re-absorption of infrared photons should be minimized. Generally, absorption and re-

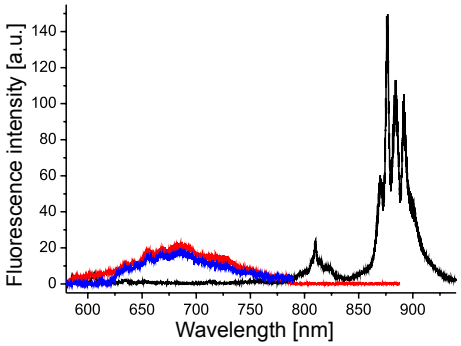

Figure 8.16: Measured spectral properties of the liquid-filled HCPCF, the NV center, and the solid immersion lens (SIL). The black curve shows the fluorescence from the bare ZrO_2 SIL. The red and blue curves are spectra of NV centers on a SIL and the total fluorescence from the end of the filled fiber, respectively. The blue curve is normalized to the red one. The edges in the spectrum are caused by a 590 nm and a 625 nm long pass and a 795 nm short pass filter. The excitation wavelength was 532 nm.

absorption depend on the concentration of emitters and can be estimated theoretically by the absorption cross-section. As the exact concentration of CdHgTe QDs after the transfer from aqueous solution into toluene was not accessible a priori, the optimum concentration was determined directly from spectral measurements.

This was done by utilizing a diode laser emitting at a wavelength of 640 nm. The laser is coupled into a HCPCF selectively filled with QD-polymer solution (see Fig. 8.14) where it excites the QDs. Fluorescence from the QDs centered at around 850 nm (Fig. 8.17 b) was filtered out with the help of a 790 nm long pass filter. As can be seen in Fig. 8.17 b), most emission from the CdHgTe QDs was confined inside the filled core region and could be collected selectively. The dotted circle line indicates the region from where fluorescence was collected in the measurements. Although the highest intensity (red and yellow color encoding) was collected at the core region of the fiber, a significant fraction of fluorescence was also found in the cladding region. This lost fraction is fluorescence light that does not satisfy the total reflection condition, or which is scattered into the cladding by small air bubbles in the liquid. An additional loss channel was scattering due to the polymer sputtering around the core region close to the facets caused by cleaving the fiber.

Photoluminescence spectra under 640 nm laser excitation (see Fig. 8.14) collected at the end of the fiber with different CdHgTe QD concentrations are shown in Fig. 8.18 b). The PL intensity increases with increasing concentration, which represents higher

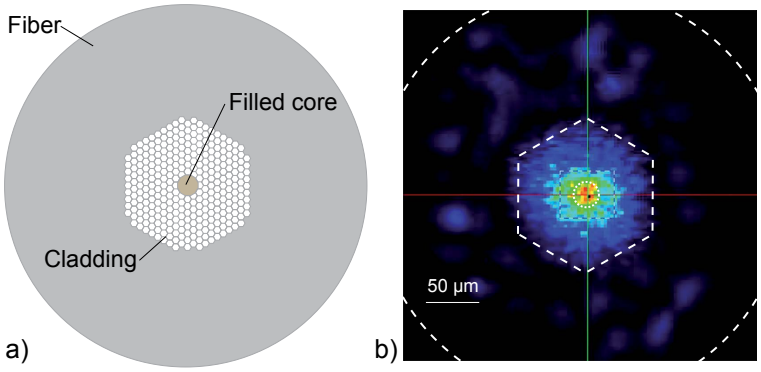

Figure 8.17: a) Sketch of the HCPCF as in b). The fiber has a diameter of 135 µm, the core a diameter of 9.5 µm. The cladding consists of a hexagonal glass structure with a pitch of 2.3 µm and an air fraction of 0.9. b) CCD image of the photoluminescence from the CdHgTe QD-solution in the HCPCF collected at the end of the fiber. The white dashed lines indicate the fiber and the cladding region, the dotted line shows the core. The largest fraction of light is guided in the central core region.

conversion efficiency from visible light at 640 nm to the near infrared. However, at higher concentration, re-absorption appears. It can be observed in the near infrared spectrum as a re-distribution of light towards longer wavelengths. In Fig. 8.18 b) (red and blue curves), this effect is already quite pronounced and is observed as the onset of additional peaks at around 900 nm.

Re-absorption has to be avoided in the incoherent photon emission via absorption and Stokes-shifted emission. In order to maintain single photon statistics, the excitation rate of the QDs has to be smaller than the emission rate of the converted photons. Otherwise, the probability to emit more than one photon at a time increases. In the experiment, the generation rate of visible photons was kept far below the reciprocal of the lifetime $\tau_{\mathrm{Life}} = 150\,\mathrm{ns}$ of the CdHgTe QDs. A re-absorption of converted photons would double the effective lifetime which enhances the probability of two-photon events. To avoid this, a concentration corresponding to that of the black curve in Fig. 8.18 b) with negligible re-absorption was used for the conversion experiments.

Conversion efficiency of the assembled system

The onset of re-absorption limits the maximum concentration of QDs. This leads to a lower conversion efficiency of visible to infrared light. To measure the absolute conversion efficiency, the red diode laser (640 nm) was applied as classical photon source and coupled into the HCPCF. The intensity, i.e. the photon generation rate, of

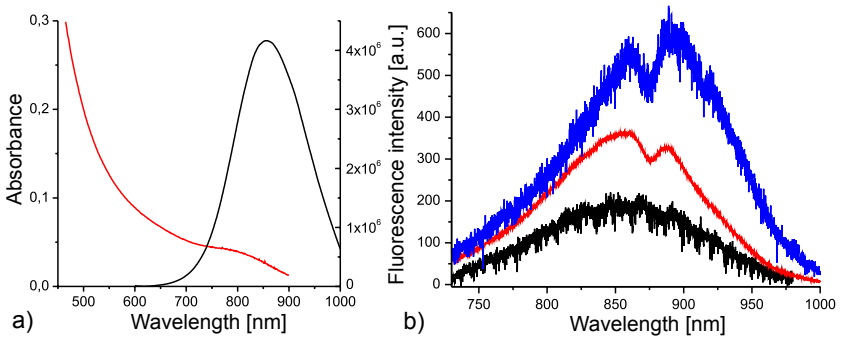

Figure 8.18: a) Absorption (red) and PL (black) spectra of CdHgTe QDs in toluene. b) PL spectra collected at the end of the HCPCF fiber (see Fig. 8.17 b) with different CdHgTe QD concentrations (increasing from the black to the blue curve). The black curve represents the appropriate concentration used for the experiment, where re-absorption is absent. The red and the blue curve correspond to a two times and five times higher concentration than in the black curve, respectively.

the red laser was compared to the photon rate of near-infrared photons collected at the end of the fiber. The ratio is the total conversion efficiency of the system. It was determined to be $\eta_{\mathrm{Tot}} = 0.1\,\%$. This number includes the coupling efficiency of laser light from free space to the fiber, the transmission of the fluorescence light inside the fiber and the collection efficiency of the photoluminescence from the QDs at the end of the fiber, all together having a total efficiency $\eta_{\mathrm{Trans}} = 14\,\%$. From this number the probability can be derived that a single visible photon at 640 nm is absorbed by a QD in the HCPCF and re-emitted as infrared photon at 850 nm to be $\eta_{\mathrm{Convert}} = 3\,\%$. This number is quite large compared to simply focusing and collecting on a QD solution with high NA objectives [209].

With these numbers, the expected rate of single infrared photons can be estimated for the case that the attenuated red laser is replaced by the true single photon source as discussed earlier. For a total conversion efficiency of 0.1 %, the photon rate of the converted near-infrared single photons will only be about 280 cts/s, when 280 kcts/s of visible single photons are launched into the fiber. Unfortunately, this photon number is similar to the accumulated number of dark counts of the APDs of 159 cts/s, and not sufficient for spectral analysis and autocorrelation measurements with the available equipment. However, direct improvements of the experimental setup would increase the conversion efficiency as discussed in the next section.

8.3.8 Towards single photon generation in the infrared

As seen in the previous section, the photon conversion process requires very high total conversion efficiency, and bright single photon sources. Here, possible improvements of the experimental implementation are discussed.

Since re-absorption of infrared photons limits the maximum concentration of QDs, a large Stokes shift between absorption and emission spectrum (see properties of QDs in Fig. 8.18 a) would be desirable. Colloidal chemistry holds promising prospects to develop QDs with a large Stokes-shift and high quantum efficiency at the same time [220--225].

Another improvement of the conversion efficiency concerns infiltration of the fiber. It is also possible to use infiltration only for coating the inner wall of the hollow core in the HCPCF [226]. In this case, light guiding and a large NA are maintained by the photonic band-gap effect, yet scattering by air bubbles in the liquid is absent.

Finally, QDs with shorter lifetime would allow for a higher single photon excitation rate. At the same time, they would also reduce the problem of re-absorption. Figure 8.19 compares the state of the art of stable single photon sources in the visible with the source used in the experiment.

8.3.9 Summary and outlook

In conclusion, a conceptually new method was suggested for the generation of single photons by pumping an ensemble of quantum emitters with a stream of pump photons. By doing so, single photons are generated by incoherent absorption and Stokes-shifted re-emission, e.g. from the visible to the infrared.

Furthermore, experimental studies were performed to demonstrate feasibility of the method. Selectively infiltrated hollow-core photonic crystal fibers equipped with colloidal quantum dots are very promising systems for an implementation in an integrated platform. With this system, a total conversion efficiency of 0.1 % could be realized in a first proof-of-principle experiment. Although this number was yet too small to verify conversion of single photons from a true single photon source, it is still quite large compared to simply focusing and collecting with high-NA objectives. As discussed above already, an estimation based on the absorption cross section of similar QDs, the maximum density of QDs in a spin-coated or drop-casted sample, and an NA of 0.95 reveals at least an order of magnitude better conversion efficiency with the presented approach.

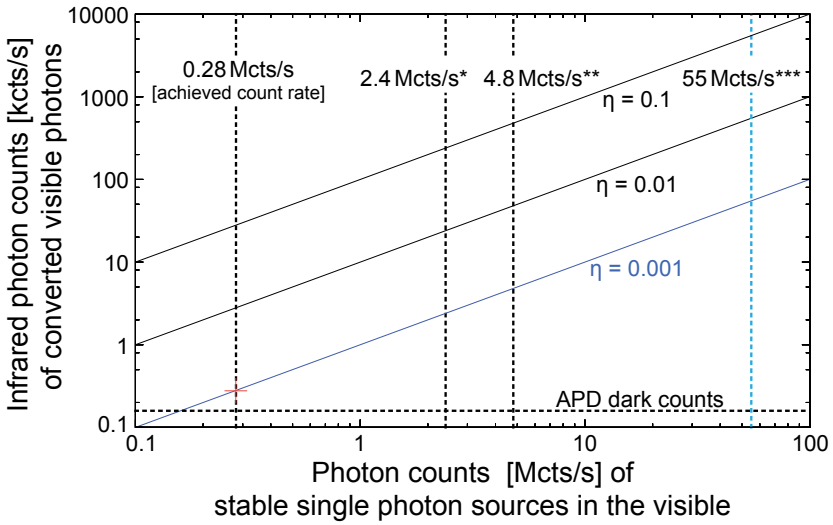

Figure 8.19: Overview of single photon sources realized so far and expected single photon count rates from incoherent photon conversion to the near infrared using the presented HCPCF system. The red cross marks the achieved conversion rate of 0.1 (blue line) and the resulting single photon counts of 280 cts/s for the conversion of NV centers in diamond to CdHgTe QDs emitting at 850 nm. The black lines show the expected infrared single photon counts for $\eta_{\mathrm{Tot}} = 1\,\%$ and $\eta_{\mathrm{Tot}} = 10\,\%$. These conversion efficiencies can be achieved with experimental improvements. The black vertical dotted line indicated by an asterisk represents the maximum count rate of the employed single photon source (see Sec. 6.2.3). The black vertical dotted line indicated by two asterisks represents the maximum count rate achieved with SiV defect centers [11]. The light blue vertical dotted line, indicated by three asterisks, gives an outlook of a possible implementation of NV centers in a dielectric layer system with a collection efficiency of 99 % as has been realized with single molecules [227]. Conversion with the present efficiency of such high flux would generate 80 kcts/s infrared single photons.

With improvements by two orders of magnitude, which are experimentally feasible, as well as visible photon sources approaching 10 Mcts/s, the generation rate of single photons in the infrared could be as high as several 100 kcts/s, much higher than existing true single photon sources in the infrared [201]. With the suggested method, single photon generation in the near infrared, e.g. the telecom band at around 1550 nm, is accessible without the need of photo-stable quantum emitters in that wavelength regime.

Finally, it should be pointed out, that the HCPCF can be filled with arbitrary materials. Also, cooling of the fiber to cryogenic temperatures is straightforward. In this way, converted photons could have much better properties, e.g., in terms of linewidth, coherence, or indistinguishability than pump photons. In this respect, the

presented experiments show, that ultra-bright single photon sources even of poor optical quality may be very useful as pump sources to generate single quanta of excitation with exceptional properties.

8.4 Summary and outlook

In this chapter, a compact and mobile single photon system was presented. It provides reliable and efficient performance as a stand alone device. For NV defect centers, single photon count rates of 315 kcts/s can be achieved via the fiber out-put. Similar count rates have been achieved with SiV defect centers. The system is also suitable as a portable device for optical analysis, e.g. by means of a spectrometer. Operation of the system is simple, therefore, the system opens up implementations outside the scientific community. Yet, for employment in every day environment, further development is necessary but feasible.

The system was applied for the first time realization of a quantum cryptography experiment with a single SiV defect center. This is a major step towards MHz quantum key rates. Sifted key rates of 3.6 MBits/s could be achieved with a SiV for a cycle rate of 200 MHz and for improved quantum efficiencies by a factor of 10. For an NV defect center, the bit rate could be 420 kBits/s, assuming 20 MHz driving rate and an improved setup efficiency as was achieved before. These numbers show the potential of the developed device for highly efficient quantum cryptography.

In another experiment, the single photon system was used as pump source for single photon generation in the infrared. This generation is based on a conceptually novel method for single photon generation. The concept was introduced for the first time in this thesis. By pumping an ensemble of quantum emitters with a stream of pump photons, single photons are generated by incoherent absorption and Stokes-shifted re-emission, e.g. from the visible to the infrared. In the experimental implementation a total conversion efficiency of 0.1 % was achieved in a first proof-of-principle experiment. With experimentally feasible improvements by two orders of magnitude as well as visible photon sources approaching 10 Mcts/s, the generation rate of single photons in the infrared could be as high as 1 Mcts/s, much higher than existing on-demand true single photon sources in the infrared [201]. Furthermore, also cooling of the conversion system to cryogenic temperatures is straightforward. In this way, photons could be generated with much better optical properties than pump photons, e.g., in terms of linewidth, coherence, or indistinguishability. In this respect, the presented experiments

show, that ultra-bright single photon sources even of poor optical quality may be very useful as pump sources to generate single photons with exceptional properties.

9 Summary and outlook

9.1 Summary

The experiments which were performed in the frame of this thesis cover a broad variety of current research topics in nanophotonics, single photon generation, and single photon applications. In particular, five major novel achievements were discussed, (1) the development of particle deposition techniques of quantum emitters for nano-assembly of photonic systems, (2) their application for miniaturization and integration of single photon systems and coupling to resonant structures, (3) development of a highly efficient solid immersion microscope for room and cryogenic temperature experiments of single quantum emitters, (4) its application to study fundamental properties of single nitrogen vacancy defect centers in diamond nanocrystals, (5) realization of a mobile single photon source and its application for quantum key distribution and single photon generation in the infrared. All experiments are based on diamond nanocrystals containing single (or only few) nitrogen vacancy (NV) or silicon vacancy (SiV) defect centers.

In the first topic, various deposition and integration techniques of diamond nanocrystals were introduced. In particular, novel nano- and micro-manipulation techniques were developed. For deposition of a controlled number of nanocrystals on tapered fibers, a dip-coating technique was developed and applied [Schröder *et al.* 2012a]. A pick-up technique via a functionalized fiber tip, controlled by a SNOM probe, enables assembly of sphere - diamond systems [Schietinger *et al.* 2008a]. Furthermore, a pick-and-place method with a tapered fiber was introduced for coupling nanocrystals to toroidal microresonator or other geometries, such as sphere resonators or fiber integrated resonators [Gregor *et al.* 2009a]. Finally, a pick-and-place method with an atomic force microscope with nanometer deposition precision was developed. The method enables positioning of pre-selected particles to a variety of structures at ambient environments [Schröder *et al.* 2011b, Schell *et al.* 2011a].

In the second topic, three different integrated single photon systems and controlled coupling of quantum emitters to two different whispering gallery mode resonator designs were realized. These achievements are listed in the following.

(I) For the first time, a fiber coupled single photon collection system based on two gradient index lenses was presented [Schröder *et al.* 2012b, Schröder *et al.* Patent I]. Single photons stemming from a single NV defect center were coupled to a single mode fiber, enabling stable non-blinking, non-bleaching, room temperature operation. The system was assembled using only commercially available compoments, such as gradient index lenses, filter technology, diamond nanocrystals, as well as single mode fibers, allowing implementation of a low cost single photon system. With its dimensions of only 2.5 cm x 2.5 cm x 5.5 cm, it is super compact and can be integrated into portable and mobile applications.

(II) For the first time, a fully integrated single photon source was realized by facet-coupling of an NV defect center inside a diamond nanocrystal to a commercial optical fiber [Schröder *et al.* 2011b]. This system is the most simple fiber coupled single photon source, no additional optical components are necessary. Therefore, it is ultra-stable, maintenance-free, and scalability to more complex systems is feasible. Two configurations of operation are highly interesting. First, as a light collecting fiber-objective it reaches an effective numerical aperture of 0.82 while having only micrometer dimensions. It therefore allows integration into ultra-compact quantum photonic devices or fiber networks. Such fiber-based sources can be bundled to launch a larger, yet precisely defined number of photons into on-chip photonic structures for an integrated quantum optical technology. Secondly, the possibility to simultaneously excite the NV center and recollect its single photon emission through the fiber will open the way towards new devices where single emitters need to be coupled directly to photonic structures or where they are used as local quantum sensors.

(III) For the first time, a tapered fiber diamond-based single photon system was realized [Schröder *et al.* 2012a]. Single diamond nanocrystals containing NV defect centers were deposited on a tapered fiber of only 273 nm in diameter for efficient evanescent fiber coupling. The system provides a record-high number of 689,000 single photons per second from a defect center in a single-mode fiber. It is maintenance free and no additional components are necessary for fiber coupling. The system can be cooled to cryogenic temperatures. The possibility to couple both the tapered fiber as well as the single defect center evanescently to other nanophotonic structures, such

as microresonators, makes it a promising system for integrated quantum transmission experiments, two-photon interference, quantum-random-number generation and nano-magnetometry.

(IV) For the first time, controlled coupling of a single emitter to a high-Q whispering gallery mode (WGM) resonator was shown [Schietinger *et al.* 2008a, Barth *et al.* 2010a]. A pre-selected NV defect center in a diamond nanocrystal was attached to a polystyrene microsphere and thereby coupled to its high-Q WGMs. Its resonances were observed within the emission of the NV defect center, while its single-photon character was preserved. Q-values as high as $5.5 \cdot 10^3$ were determined. Furthermore, a second pre-selected single photon emitter was coupled to the same resonator modes, proving the possibility to up-scale the system. This is a remarkable result towards the observation of future collective effects in a cQED system [104, 160].

(V) It was shown for the first time, that pre-selected diamond nanocrystals containing only several NV defect centers can be coupled to the optical modes of a toroidal resonator in a controlled manner with a novel pick-and-place method [Gregor *et al.* 2009a]. The resonator was integrated in an on-chip system. The system was cooled down to cryogenic temperatures of about 5 K to prove the feasibility of coupling a single ZPL to a high-Q resonator mode. This is an important step towards the realization of strong Purcell enhancement or cQED experiments.

In the third topic, a solid immersion lens microscope was developed for the investigation of single defect centers in diamond [Schröder *et al.* 2011a]. The microscope is based on a ZrO_2 solid immersion lens and enables ultra-efficient single photon collection with highest count rates published in the literature of up to 853 kcts/s for a stable and up to 2.4 Mcts/s for a blinking defect center. Furthermore, the compact design provides access to about 100 NV centers that emit more than 400 kcts/s. The overall collection efficiency of the setup is up to 4.2 % while having a source efficiency ϵ of up to $\epsilon > 18.3\,\%$, opening the way towards much more efficient diamond-based on-demand single photon sources. For example, by integration of single SiV defect centers with a lifetime of about 1 ns, count rates of up to 10 Mcts/s could be expected. The microscope can also be operated at cryogenic temperatures and therefore enables fundamental investigation of single defect centers in diamond and leads off towards two-photon interference experiments which are only possible with ultra-high single photon rates.

In the fourth topic, a novel cryogenic solid immersion microscope for the in-

vestigation of single defect centers in diamond nanocrystals was introduced. For a single NV^- defect center, it achieves single photon count rates of up to 461 kcts/s and about 25 kcts/s of photons stemming from the ZPL line only. The microscope was applied to investigate their spectral diffusion times. Systematic studies of milled and purified type Ib nanodiamonds were carried out. With the help of a novel interferometric method, it was possible to determine the spectral diffusion time of the ZPL of a single NV^- defect center in a diamond nanocrystal to be $\tau_D = 2.2 \pm 0.4\,\mu s$ [Wolters *et al.* 2012a]. This indicates, that the spectral diffusion rate $\gamma_D = 1/\tau_D$ of about 450 kHz is almost 100 times faster than the single photon detection rate of about 4.6 kHz for photons stemming from the ZPL only. This result is an important insight into the mechanism causing spectral diffusion towards new methods to suppress it. Suppression of spectral diffusion rates or at least reduction to rates smaller than photon detection rates is necessary, e.g. for the realization of 2-photon-interference experiments.

In the fifth topic, a novel compact, mobile single photon system was introduced based on solid immersion microscopy [Schröder *et al.* 2012c]. It provides reliable and efficient performance as a stand alone device. Single photons are either provided via a free beam or fiber coupled, with principally possible count rates of up to 853 kcts/s or 315 kcts/s for single NV defect centers, respectively. Furthermore, other fluorescent emitters, for example the SiV defect center, can also be implemented, promising even higher single photon rates. In addition to its main purpose as single photon source, the system can also be used as a portable high-resolution microscope for optical analysis of fluorescent emitters. A spectrometer or other analysis devices can be directly connected to the system. Such implementations are interesting for the future, however, within this thesis, the device was exclusively used as a single photon source for quantum key distribution [Leifgen *et al.* 2012a] and for stable single photon generation in the infrared [Jiang *et al.* 2012a].

For the first time, quantum cryptography was performed with single SiV defect centers [Leifgen *et al.* 2012a]. This is a major step towards MHz quantum key rates due to the short lifetime of the SiV of down to 0.2 ns. The achieved quantum bit error rate (QBER) was about 6 %, low enough for inherently secure application via public channels in combination with error correction. For a single NV defect center 2.5 kcts/s sifted key rate with a QBER of only 3.3 % was achieved. This key rate for NV defect centers is in the range of previously reported rates [199]. The successful implementations prove that the developed mobile system is well suited for the application of QKD schemes.

To date, the performance of the experiment is mainly limited by slow EOM drivers and limited quantum efficiencies (QE) of the SiV defect centers. Assuming faster EOMs and a 10-fold improved QE, a sifted key rate of 3.6 MBits/s could be achieved with a SiV for a cycle rate of 200 MHz, making the system an interesting candidate for future QKD implementations.

A conceptually novel method was suggested and realized for the first time for the generation of single photons by pumping an ensemble of quantum emitters with a stream of single pump photons [Jiang *et al.* 2012a]. Single photons are generated by incoherent absorption and Stokes-shifted re-emission, e.g. from the visible to the infrared. Experimental studies revealed the feasibility of the method. Selectively infiltrated hollow-core photonic crystal fibers equipped with colloidal quantum dots are very promising systems for an implementation in an integrated platform. A total conversion efficiency of 0.1 % could be realized in a first proof-of-principle experiment. With experimentally feasible improvements by two orders of magnitude as well as visible photon sources approaching 10 Mcts/s, generation of on-demand single photons in the infrared could be as high as several 100 kcts/s, much higher than existing on-demand single photon sources in the infrared [201]. This is an important step towards efficient long-distance QKD with single photons in the telecom band at around 1550 nm. Also, the HCPCF can be filled with arbitrary quantum emitters, while cooling of the fiber to cryogenic temperatures is still possible. In this way, photons could be generated with much better properties, e.g., in terms of linewidth, coherence, or indistinguishability than those of the pump photons. This would make ultra-bright single photon sources, even of poor optical quality, useful as pump sources to generate single photons with exceptional properties.

9.2 Outlook

The developed experimental schemes and findings enable a broad variety of future experiments and progress in photonics, and nano and quantum optics. In the following, a selection of possible implementations is discussed.

Before going into detail, an interesting general characteristic of the introduced experiments should be pointed out. All experiments conducted with NV defect centers can in principle be realized with any other defect center, e.g., a SiV or a chromium [38] defect center. This allows application of developed techniques to single defect centers not known today. This might help to overcome disadvantages and limitations of NV

defect centers.

It should be furthermore noted, that the developed nano-manipulation techniques can be applied to build up complex hybrid photonic systems for a large variety of experiments. In particular, the combination of single NV defect centers in diamond nanocrystals with metallic structures featuring surface-plasmon polaritons might be a further step towards all-optical, on-chip solutions. Recently, first realizations were published [121].

The application of the fiber-facet coupled single NV^- defect center as **fiber quantum sensor** is straightforward. It is illustrated in Fig. 9.1. The possibility to excite the defect center through the fiber while its emission is simultaneously collected through the same fiber enables easy optical initialization and read-out of such a sensor. It could be applied as a versatile quantum light source for optical scanning probe imaging [126]

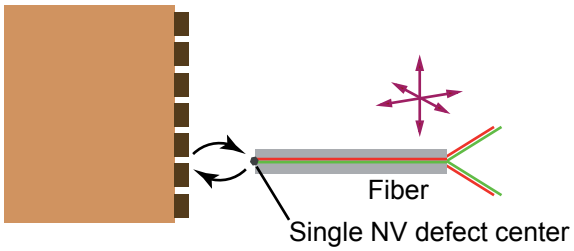

Figure 9.1: Schematic illustrating how a fiber coupled single NV defect center could be used for probing. The defect center is excited through the fiber and its single photon emission is collected through it. By approaching it to other materials and structures, one could analyze the interaction of the intrinsic NV center's dipoles with these samples. Plasmonic, photonic, electronic and also magnetic samples could be probed.

or as local source of quantum light, e.g., to launch single photons in the evanescent field of other optical components such as micro-cavities [127]. For example, the small and robust system could function as a stable local electromagnetic field probe. NV defect centers were recently applied as local magnetic field probes [128, 147] as well as for mode density measurement of plasmonic nanostructures [107, 228, 229]. Also other sensing applications with fiber-coupled optical initialization and read out are feasible. In particular, such sensing could be interesting for investigation and analysis of plasmonic and novel metamaterials with their ability to enhance the fluorescence [230, 231].

Similarly, as discussed for the facet-coupled quantum sensor above, the NV center -

tapered fiber system can also be mounted on a piezo translation stage and used as a **nano-probe**. Again, one application would be to locally probe the magnetic field via the NV^- center's electron spin [147]. The system is only several hundred nanometers in dimension, yet, in contrast to the approach discussed before, only optical read-out via the fiber is possible. Via 3d-translation stages, both the single NV center and the tapered fiber could also be **coupled evanescently to microresonators** in order to enhance the spontaneous emission rate [8, 232, 233] or to perform cavity quantum electrodynamics [148] as sketched in Fig. 9.2 a), similar to the experiment conducted with several defect centers, only with a single defect. Moreover, the tapered fiber

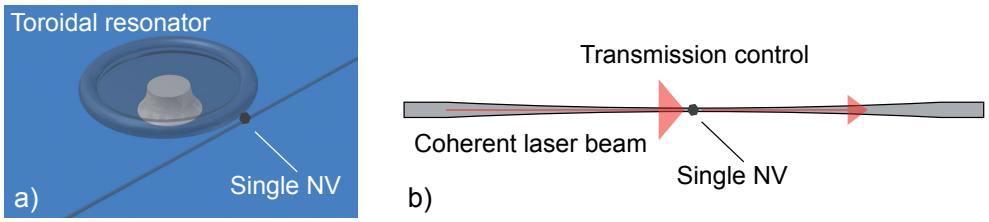

Figure 9.2: a) Sketch of how to use the tapered fiber system to couple a single NV defect center to a toroidal microresonator. The fiber simultaneously serves as nanopositioning system for the NV center and efficient in- and out-coupler to the resonator mode. b) Sketch of a transmission control scheme via a single NV defect center coupled to a tapered fiber mode [143].

system as opposed to other fiber coupling architectures, e. g. end-facet coupling (see Sec. 5.2), allows **measurements in transmission** as sketched in Fig. 9.2 b). This is a requirement for the implementation of single photon nonlinearities [142], single photon transistors [143] or quantum phase gates [144, 145].

Recently, photonic structures were introduced and realized which enable **collection efficiencies for single molecules of up to 96 % and 99 %** [227, 234], respectively. The system with up to 96 % source efficiency consists of a dielectric planar antenna, which uses a layered structure to tailor the angular emission of a single dipole oriented perpendicular to the structure. In the case with 99 % source efficiency, a dielectric layer system on a solid immersion lens was introduced for emitters with arbitrarily oriented dipole moments. Such a system would deliver up to 66 Mcts/s of single photons for an NV defect center with a lifetime of 15 ns. Hence, for a setup with 23 % setup efficiency, still a count rate of 15 Mcts/s could be reached. A first step towards such a system was developed in the course of this thesis. The sketch in Fig. 9.3 a) illustrates the system that was realized and tested. It consists of a solid immersion lens as used before and

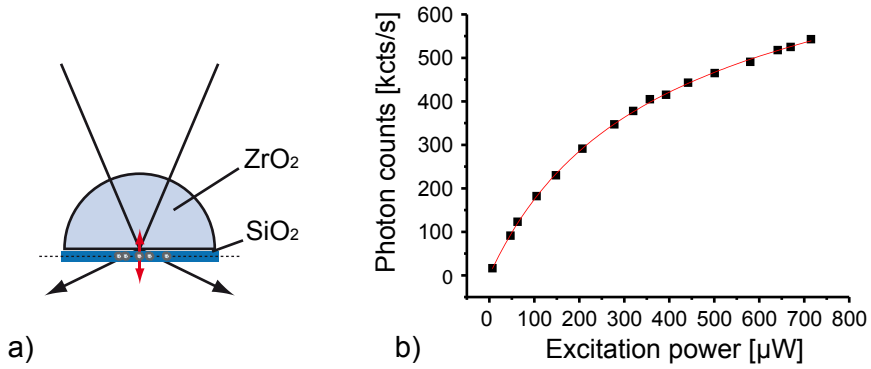

Figure 9.3: a) Sketch of the developed system. A ZrO_2 solid immersion lens was equipped with two 350 nm layers of SiO_2. In their middle, diamond nanocrystals were deposited. b) Saturation measurement of a single NV^- defect center incorporated in the middle of a 700 nm SiO_2 layer. Count rates were 718 kcts/s in saturation at 327 µW saturation power.

a SiO_2 layer with a thickness of roughly 700 nm. Diamond nanocrystals with sizes of about 25 nm were deposited in the middle of this SiO_2 layer. The maximum theoretical collection efficiency of such a structure is 96 % for perpendicular dipoles [234]. However, in the structure realized here, their dipole orientation is randomly distributed. Hence, only a small part of the NV defect centers, those oriented perpendicular to the SiO_2 plane, should show increased count rates. However, the maximum count rate measured was 718 kcts/s in saturation at 327 µW saturation power as shown in Fig. 9.3 b). This is much lower than theoretically expected results. Identification of the causes is challenging but it is assumed that mismatched layer thickness and false dipole position and orientation are limiting the performance. Therefore, further development could enable theoretically predicted collection efficiencies of 99 % for single defect centers in diamond, even at cryogenic temperatures. This would enable ultra-efficient single photon applications and quantum information schemes.

In addition to coupling single quantum emitters to whispering gallery mode resonators, coupling to other types of resonators is also promising. Recently, photonic crystal cavities and other resonators were coupled to single NV defect centers in diamond to reduce their radiative lifetime and enhance single photon rates in a small spectral regime, e.g., for the ZPL emission [8, 79, 232, 235, 236]. Another promising candidate are **fiber based Fabry-Perot cavities** [237] as illustrated in Fig. 9.4. Such cavities were developed in the group of Christoph Becher in Saarbrücken. In contrast to other resonator designs, resonator out-coupling and fiber in-coupling is directly provided

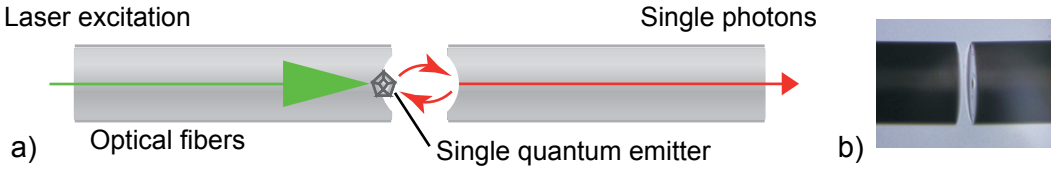

Figure 9.4: a) Sketch of a fiber based Fabry-Perot cavity. The laser excitation light is suppressed by an integrated filter before entering the second fiber. The coatings of the resonator are highly reflective for wavelengths around 637 nm. b) Image of an assembled cavity. Courtesy of Roland Albrecht, Saarbrücken. The fiber diameter is 125 µm.

by the resonator design and tuning is rather simple by controlling the length of the resonator. A cavity consisting of two fiber mirrors was equipped in the course of this thesis with a pre-selected diamond nanocrystal containing a single NV defect center. The crystal was deposited in the middle of one fiber mirror by the AFM pick-and-place technique introduced in this thesis.

Although the single NV defect center still showed antibunching with $g^{(2)}(0) < 0.5$ after deposition on the mirror, further investigation in cavity configuration was not possible because the NV defect center bleached probably due to electron irradiation when the structure was investigated inside an SEM. However, the obtained results show, that the realization of such a cavity can be achieved in a next experimental step enabling Purcell enhancement of the ZPL emission, e.g. for generation of indistinguishable photons.

Such generation of indistinguishable photons to realize Hong-Ou-Mandel interference [139] is another relevant experiment. Such an experiment with NV defect centers has been realized for bulk diamond [140, 180], but not yet for nanocrystals. It is more challenging to find lifetime limited emitters in diamond nanocrystals with low spectral diffusion [86]. Spectrally different photons can not be interfered efficiently. Therefore, as indicated by the results obtained in the course of this thesis, single photon detection rates need to be increased by a factor of 10 to 100 to overcome spectral diffusion in diamond nanocrystals. There are several promising strategies to implement single NV defect centers following the experimental schemes developed in this thesis.

By applying an advanced solid immersion lens design with dielectric antennas as discussed earlier, the cryogenic solid immersion lens microscope could reach a regime, where photon jump rates are lower than photon detection rates due to an up to 30-fold enhanced photon collection.

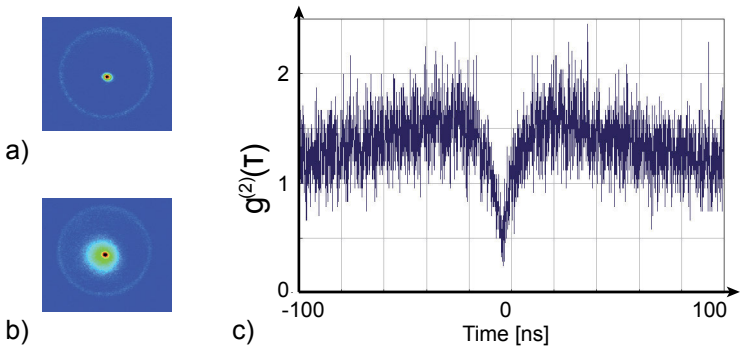

Figure 9.5: a) CCD camera image of a single NV defect center inside a diamond nanocrystal deposited in the middle of one fiber mirror. b) Same configuration as in a) with white light coupled to the other fiber end to envision the fiber core. c) Auto-correlation measurement of the same NV defect center prior to deposition on the fiber.

Another method is the application of resonant structures. For example, the Fabry-Perot cavity as discussed above could be used to enhance the overall ZPL emission via Purcell enhancement. Such enhancement could also be achieved by using a whispering gallery resonator in combination with a defect center attached to a tapered fiber as also discussed above. This scheme also enables direct out-coupling of the photons inside the resonator. Pre-requisite for such schemes is the possibility to cool the systems to cryogenic temperatures. Indeed, a tapered fiber with a diameter of only 300 nm equipped with diamond nanocrystals was successfully cooled to 7 K and subsequently heated to room temperature without breaking. This is a first step towards the application of such a scheme.

Finally, further development of the mobile single photon system is promising for various applications. By applying dielectric antennas as discussed earlier, up to 30 times higher single photon rates can be achieved than to date. This would make the system an even more interesting candidate for single photon applications such as quantum key distribution, or as a single photon source for pumping of conversion devices as introduced in this thesis. Another application for higher photon rates would be the absolute calibration of a single photon detector like an APD against a calibrated standard analogue detector with high gain amplifiers [191].

Furthermore, non scientific applications should also be considered. Operation of the mobile single photon system is simple, all relevant components are fiber coupled and can be computer controlled, enabling employment of the system by a trained

person without detailed background knowledge. This could open up implementations outside the scientific community, e.g. as a real quantum experiment in high school physics classes or other occasions. Yet, for employment in such an environment, further development towards a robust plug-and-play device is necessary.

In this short outlook, a few possible future experiments were proposed that are based on the findings of this thesis. They show, that further development is not only possible but would also enable interesting and relevant fundamental findings, experimental schemes, and applied devices.

A Adjusting correlation data and fitting the second order auto-correlation function and saturation measurements

A.1 Fitting second order auto-correlation data of NV^- or SiV defect centers

For adequate analysis of the recorded photon statistics, the experimental data was compared to a theoretical model. The free parameters of the theoretical model were therefore adopted to the data by means of a fitting function.

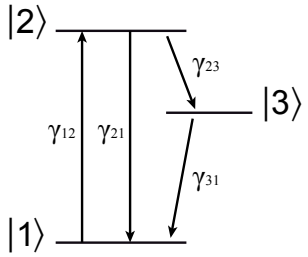

Figure A.1: Sketch of a simplified 3-level system that was applied to model the electron dynamics of the NV^- center. See text for further details.

Second order auto-correlation function

The photon statistics of the NV^- as well as the SiV defect center can be modeled using a three-level system. This simplified model reflects sufficiently the dynamics of the electron. Experimental data recorded in the course of this thesis can be well described by it. The simplified model does not consider the splittings of the ground and excited states and also neglects the two intermediate singlet states that have been observed very recently [61]. Furthermore, also very fast (in the order of picoseconds) non-radiative inter-band decays in the phonon sidebands are neglected.

Following these simplifications, the electron dynamics of such a three-level quantum system can be expressed via its rate equations. Its transition rates γ_{12}, γ_{21} ,γ_{23}, and γ_{31} are denominated as illustrated in Fig. A.1. The occupation probabilities ϱ_1, ϱ_2, and ϱ_3 for the levels $|1\rangle$, $|2\rangle$, and $|3\rangle$ have the following time dependence.

$$\frac{\partial \varrho_1(\mathrm{t})}{\partial \mathrm{t}} = -\gamma_{12}\varrho_1(\mathrm{t}) + \gamma_{21}\varrho_2(\mathrm{t}) + \gamma_{31}\varrho_3(\mathrm{t}), \tag{A.1}$$

$$\frac{\partial \varrho_2(\mathrm{t})}{\partial \mathrm{t}} = \gamma_{12}\varrho_1(\mathrm{t}) - (\gamma_{21} + \gamma_{23})\varrho_2(\mathrm{t}), \tag{A.2}$$

$$\frac{\partial \varrho_3(\mathrm{t})}{\partial \mathrm{t}} = \gamma_{23}\varrho_2(\mathrm{t}) - \gamma_{31}\varrho_3(\mathrm{t}). \tag{A.3}$$

This system of equations can be solved for the occupation probability ϱ_2 with the initial conditions $\varrho_1 = 1$, $\varrho_2 = 0$, and $\varrho_3 = 0$. $\varrho_2\gamma_{21}$ directly reflects the spontaneous emission probability and hence the photon statistics. The photon statistics are expressed by the second order auto-correlation function. By normalizing ϱ_2 for large times using $\varrho_2(\tau \to \infty) = 1$, the normalized second order auto-correlation function is expressed as

$$g^{(2)}(\tau) = 1 - (\mathrm{C}+1)\,\mathrm{e}^{\Gamma_1\tau} + \mathrm{C}\,\mathrm{e}^{\Gamma_2\tau} \tag{A.4}$$

with

$$\mathrm{C} = \frac{\Gamma_2 + \Gamma_{31} - \Gamma_{12}\frac{\Gamma_{23}}{\Gamma_{31}}}{\Gamma_1 - \Gamma_2},$$

$$\Gamma_{1,2} = -\frac{\mathrm{P}}{2} \pm \sqrt{\frac{\mathrm{P}^2}{4} - \mathrm{Q}},$$

$$\mathrm{P} = \gamma_{21} + \gamma_{12} + \gamma_{23} + \gamma_{31},$$

$$\mathrm{Q} = \gamma_{31}(\gamma_{21} + \gamma_{12}) + \gamma_{23}(\gamma_{31} + \gamma_{12}).$$

All second order auto-correlation fits were done using Equation A.4. An exemplary $g^{(2)}(\tau)$ of an NV^- defect center and a fit by Equation A.4 is displayed in Fig. A.2.

It has to be pointed out, that the fitting results of the transition rates were strongly dependent of the start values. For example, for many NV^- defect centers investigated, the determination of the excited state fluorescence lifetime deviated from direct lifetime measurements using pulsed excitation. Therefore, lifetime calculations have to be treated with care. A more quantitative analysis can be found in [155].

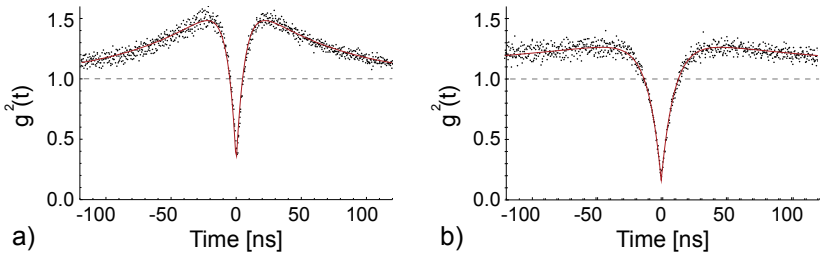

Figure A.2: a) Normalized auto-correlation function $g^{(2)}(\tau)$ of an exemplary single NV^- defect center with $g^{(2)}(0) < 0.3$. b) Normalized auto-correlation function $g^{(2)}(\tau)$ of another NV^- defect with $g^{(2)}(0) < 0.16$. Clearly visible is the difference of bunching strength. The red curves are theoretical fits to the data (see text).

Bunching behavior at $g^{(2)}(0)$

A bunching effect can be observed in Fig. A.2 and is present in all other second order auto-correlation function measured in this thesis. The magnitude of the bunching is determined by laser excitation intensities and intrinsic intersystem crossing rates into the metastable level $|3\rangle$. For high excitation intensities, bunching becomes more pronounced. This is due to the fact, that the meta-stable state $|3\rangle$ can capture the electron for much longer times than the excited state $|2\rangle$ (Fig. A.1). It has an average lifetime of about 200 ns at room temperature [72, 73] compared to around 18 ns excited state lifetime.

With higher excitation intensity, the probability that the electron is found in the excited state is increased. Therefore, also the probability for intersystem crossing k_{23} into the metastable state increases, hence, also the probability to be captured there is enhanced.

This phenomenon has direct influence on the bunching behavior of the correlation function of the 3-level system. Lets consider the system to be under CW excitation. In an arbitrary state (if no photon is detected) the system has a certain probability to be in the meta-stable state (only allowing photons to be detected at large times). This probability of a detection event at large times increases with higher excitation intensities. If the system is prepared in its ground state (by detection of a photon), the probability to emit (and to detect after a short time) a second photon is higher compared to the average case. Hence, the probability to detect a photon after a short time after a photon has just been detected (and the ground state prepared), is higher than the probability to detect a photon at large times.

A.2 Adjusting recorded correlation data

For the recording of correlation data, either a Timeharp 200 (Picoquant, Germany) or a Picoharp 300 (Picoquant, Germany) was applied. The Timeharp operates in a start-stop modus. For proper handling of the recorded correlation data $\mathrm{h}(\tau)$, one has to take into account a peculiarity of the implemented start-stop measurement. Due to this experimental configuration, the probability for a stop-event for $\tau \gg \tau_{\mathrm{Life}}$ approaches one, with $\tau_{\mathrm{Life}} \approx 18\,\mathrm{ns}$ the fluorescent lifetime of the emitter. Hence, the probability to measure a time-difference $\tau \to \infty$ of the start and stop events will run against zero. This behavior does not reflect the real correlation statistics of the photons. If the average photon intensity is stable for long time periods $\Delta\mathrm{t} \gg \tau_{\mathrm{Life}}$, the probability of a detection event with $\tau \gg \tau_{\mathrm{Life}}$ becomes one due to the loss of correlation for long times. Therefore, the data $\mathrm{h}(\tau)$ decreases too fast for $\tau \to \infty$. It is corrected with the following function

$$g^{(2)}(\tau) = \alpha \left(1 - \beta \int_0^{\tau} \mathrm{h}(\tau\prime) d\tau\prime\right)^{-1} \mathrm{h}(\tau).$$

Here, a normalization term α was added such that $g^{(2)}(\tau \gg \tau_{\mathrm{Life}}) = 1$. The integral $\int_0^{\tau} \mathrm{h}(\tau\prime) d\tau\prime$ weights events with $\tau \to \infty$ stronger than events with $\tau \to 0$. Hence, it runs against a constant for $\tau \to \infty$ and becomes zero for $\tau \to 0$. The parameter β needs to be adjusted in such a way, that $g^{(2)}(\tau \approx 1\,\mu\mathrm{s} \gg \tau_{\mathrm{Life}} \approx 13\,\mathrm{ns}) = \mathrm{const}$. This correction is approximate but is valid for events with $\tau \gg 1\,\mu\mathrm{s}$.

A.3 Fitting second order auto-correlation data for pulsed excitation

For pulsed excitation of the NV^- center, a simplified model was applied. This model is based on a mono-exponential decay of the excited state. Exemplary data with an according fitting function is shown in Fig. A.3. The fit $g^{(2)}_{\mathrm{pulsed}}(0) = 0.21$ for a laser repetition rate of 5 MHz, estimated by division of the maximum at $g^{(2)}_{\mathrm{pulsed}}(0)$ and the maximum at 200 ns. For the fit, the following function was used. It was adapted in such a way to the measured data that the free parameter B1 coincides with $g^{(2)}(0)$. Hence, B1 gives the peak height for $g^{(2)}_{\mathrm{pulsed}}(0)$, while A1 gives the peak height for the other laser excitation events.

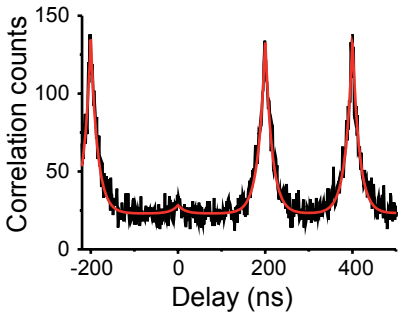

Figure A.3: a) Auto-correlation function $g^{(2)}(\tau)$ of an exemplary single NV^- defect center under pulsed excitation with a laser repetition rate of 5 MHz. $g^{(2)}_{\text{pulsed}}(0) = 0.21$ proves single photon detection. The red curve is a theoretical fit to the data (see text).

$$
\begin{aligned}
y = {} & ((A1) * (exp(-(x-T) * t1) * 1/2 * (erf((x-T) * 1) + 1))) \\
& + ((A1) * (exp((x-T) * t1) * 1/2 * (erf(-(x-T) * 1) + 1))) \\
& + ((B1) * (exp(-(x-T-1*p) * t1) * 1/2 * (erf((x-T-1*p) * 1) + 1))) \\
& + ((B1) * (exp((x-T-1*p) * t1) * 1/2 * (erf(-(x-T-1*p) * 1) + 1))) \\
& + ((A1) * (exp(-(x-T-2*p) * t1) * 1/2 * (erf((x-T-2*p) * 1) + 1))) \\
& + ((A1) * (exp((x-T-2*p) * t1) * 1/2 * (erf(-(x-T-2*p) * 1) + 1))) \\
& + ((A1) * (exp(-(x-T-3*p) * t1) * 1/2 * (erf((x-T-3*p) * 1) + 1))) \\
& + ((A1) * (exp((x-T-3*p) * t1) * 1/2 * (erf(-(x-T-3*p) * 1) + 1))) \\
& + y0\,.
\end{aligned}
$$

Here, T an offset parameter for the time x, y0 an offset parameter for linear background, p the period between laser pulses, t1 the decay rate, and erf(x) the error function (or normal error integral). The function has the limiting values erf(0) = 0, and erf(∞) = 1. Mathematically it is expressed as

$$\text{erf}(x) = \frac{2}{\sqrt{\pi}} \int_0^x e^{-u^2} du.$$

A.4 Maximum emission rate: Saturation measurements and fitting

For saturation measurements, fitting to the experimental curves was done according to

$$R(I) = \frac{R_{Inf}\ I}{I_{Sat} + I} + (A + \alpha)I + \beta.$$

Here, R is the single photon count rate, R_{Inf} the count rate at infinite excitation intensities, I the excitation power, I_{Sat} the saturation excitation power, A represents the measured background fluorescence 1 µm away from the NV center, while α and β are fit parameters for linear background stemming from the diamond and additional background such as APD dark counts and residual stray light, respectively. Exemplary data with an according fit function is shown in Fig. A.4. The fit gives a count rate at infinite excitation intensities R_{Inf} of 718 kcts/s with saturation excitation power $I_{Sat} = 327$ µW.

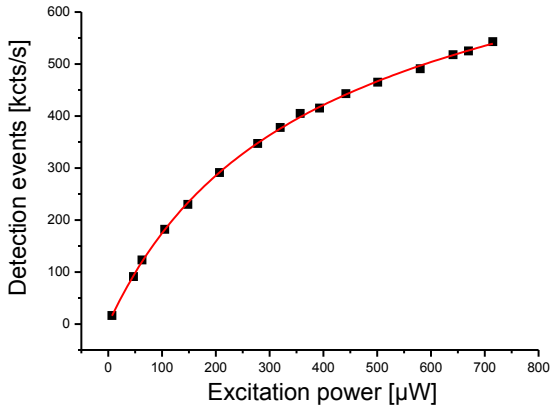

Figure A.4: Saturation measurement of a single NV^- defect center in a diamond nanocrystal on a SIL. It is incorporated in the middle of a roughly 600 nm SiO_2 layer. $R_{Inf} = 718$ kcts/s and $I_{Sat} = 327$ µW saturation excitation power. The red line is a fit to the data according to the text.

Bibliography

[1] D. P. Divincenzo. The physical implementation of quantum computation. In S. L. Braunstein and H. Lo, editors, *Scalable Quantum Computers*, pages 1--13. Wiley-VCH, 2005.

[2] D. Banerjee, M. Dalmonte, M. Müller, E. Rico, P. Stebler, U. Wiese, and P. Zoller. Atomic quantum simulation of dynamical gauge fields coupled to fermionic matter: From string breaking to evolution after a quench. *arXiv:1205.6366*, 2012.

[3] S. Ritter, C. Nölleke, C. Hahn, A. Reiserer, A. Neuzner, M. Uphoff, M. Mücke, E. Figueroa, J. Bochmann, and G. Rempe. An elementary quantum network of single atoms in optical cavities. *Nature*, 484(7393):195--200, 2012.

[4] C. Bennett and G. Brassard. Quantum cryptography: Public key distribution and coin tossing. *IEEE International Conference on Computers, Systems, and Signal Processing, Bangalore, India*, page 175, 1984.

[5] C. Kurtsiefer, S. Mayer, P. Zarda, and H. Weinfurter. Stable Solid-State source of single photons. *Physical Review Letters*, 85(2):290--293, 2000.

[6] I. Aharonovich, A. D. Greentree, and S. Prawer. Diamond photonics. *Nature Photonics*, 5(7):397--405, 2011.

[7] O. Benson. Assembly of hybrid photonic architectures from nanophotonic constituents. *Nature*, 480(7376):193--199, 2011.

[8] J. Wolters, A. W. Schell, G. Kewes, N. Nüsse, M. Schoengen, H. Doscher, T. Hannappel, B. Lochel, M. Barth, and O. Benson. Enhancement of the zero phonon line emission from a single nitrogen vacancy center in a nanodiamond via coupling to a photonic crystal cavity. *Applied Physics Letters*, 97(14):141108, 2010.

[9] Quantum Communications Victoria, www.qcvictoria.com, 2012.

[10] C. Wang, A. Ugur, V. Chernyshev, J. Meijer, and H. Weinfurter. A single photon source based on SiV centers in diamond. In *Frontiers in Optics*, OSA Technical Digest, page JWD106. Optical Society of America, 2006.

[11] E. Neu, D. Steinmetz, J. Riedrich-Möller, S. Gsell, M. Fischer, M. Schreck, and C. Becher. Single photon emission from silicon-vacancy colour centres in chemical vapour deposition nano-diamonds on iridium. *New Journal of Physics*, 13(2): 025012, 2011.

[12] M. Planck. Über das Gesetz der Energieverteilung im Normalspectrum. *Annalen der Physik*, 309(3):553--563, 1901.

[13] A. Einstein. Über einen die Erzeugung und Verwandlung des Lichtes betreffenden heuristischen Gesichtspunkt. *Annalen der Physik*, 322(6):132--148, 1905.

[14] H. J. Kimble, M. Dagenais, and L. Mandel. Photon antibunching in resonance fluorescence. *Physical Review Letters*, 39(11):691--695, 1977.

[15] R. J. Glauber. The quantum theory of optical coherence. *Physical Review*, 130 (6):2529--2539, 1963.

[16] R. Loudon. *The Quantum Theory of Light*. Oxford University Press, 2000.

[17] H. J. Carmichael and D. F. Walls. Proposal for the measurement of the resonant stark effect by photon correlation techniques. *Journal of Physics B: Atomic and Molecular Physics*, 9(4):L43--L46, 1976.

[18] L. Mandel and E. Wolf. *Optical coherence and quantum optics*. Cambridge University Press, 1995.

[19] V. Fock. Konfigurationsraum und zweite Quantelung. *Zeitschrift für Physik A Hadrons and Nuclei*, 75(9):622--647, 1932.

[20] D. Walls and G. J. Milburn. *Quantum Information*. Springer, 2008.

[21] R. Hanbuy Brown and R. Q. Twiss. Correlation between photons in two coherent beams of light. *Nature*, 177(4497):27–29, 1956.

[22] G. A. Steudle, S. Schietinger, D. Höckel, S. N. Dorenbos, V. Zwiller, and O. Benson. Quantum nature of light measured with a single detector. *arXiv:1107.1353*, 2011.

[23] G. Rebka and R. Pound. Time-correlated photons. *Nature*, 180:1035--1036, 1957.

[24] Z. Yuan, B. E. Kardynal, R. M. Stevenson, A. J. Shields, C. J. Lobo, K. Cooper, N. S. Beattie, D. A. Ritchie, and M. Pepper. Electrically driven single-photon source. *Science*, 295(5552):102--105, 2002.

[25] N. Mizuochi, T. Makino, H. Kato, D. Takeuchi, M. Ogura, H. Okushi, M. Nothaft, P. Neumann, A. Gali, F. Jelezko, J. Wrachtrup, and S. Yamasaki. Electrically driven single-photon source at room temperature in diamond. *Nature Photonics*, 6(5):299--303, 2012.

[26] J. G. Walker and E. Jakeman. Photon-antibunching by use of a photoelectron-event-triggered optical shutter. *Optica Acta: International Journal of Optics*, 32 (11):1303--1308, 1985.

[27] P. Grangier, G. Roger, and A. Aspect. Experimental evidence for a photon anti-correlation effect on a beam splitter: A new light on Single-Photon interferences. *Europhysics Letters*, 1(4):173--179, 1986.

[28] B. C. Jacobs, T. B. Pittman, and J. D. Franson. Single photon source using laser pulses and two-photon absorption. *Physical Review A*, 74(1):010303, 2006.

[29] M. C. Teich and B. E. A. Saleh. Observation of sub-Poisson Franck-Hertz light at 253.7 nm. *Journal of the Optical Society of America B*, 2(2):275–282, 1985.

[30] M. A. Albota and F. C. Wong. Efficient single-photon counting at 1.55 um by means of frequency upconversion. *Optics Letters*, 29(13):1449–1451, 2004.

[31] M. T. Rakher, L. Ma, O. Slattery, X. Tang, and K. Srinivasan. Quantum transduction of telecommunications-band single photons from a quantum dot by frequency upconversion. *Nature Photonics*, 4(11):786--791, 2010.

[32] S. Zaske, A. Lenhard, and C. Becher. Efficient frequency downconversion at the single photon level from the red spectral range to the telecommunications c-band. *Optics Express*, 19(13):12825, 2011.

[33] M. D. Eisaman, J. Fan, A. Migdall, and S. V. Polyakov. Invited review article: Single-photon sources and detectors. *Review of Scientific Instruments*, 82(7): 071101--071101--25, 2011.

[34] F. Diedrich and H. Walther. Nonclassical radiation of a single stored ion. *Physical Review Letters*, 58(3):203--206, 1987.

[35] T. Basché, W. E. Moerner, M. Orrit, and H. Talon. Photon antibunching in the fluorescence of a single dye molecule trapped in a solid. *Physical Review Letters*, 69(10):1516--1519, 1992.

[36] P. Michler, A. Kiraz, C. Becher, W. V. Schoenfeld, P. M. Petroff, L. Zhang, E. Hu, and A. Imamoglu. A quantum dot Single-Photon turnstile device. *Science*, 290(5500):2282--2285, 2000.

[37] I. Aharonovich, S. Castelletto, D. A. Simpson, A. Stacey, J. McCallum, A. D. Greentree, and S. Prawer. Two-Level ultrabright single photon emission from diamond nanocrystals. *Nano Letters*, 9(9):3191--3195, 2009.

[38] I. Aharonovich, S. Castelletto, B. C. Johnson, J. C. McCallum, D. A. Simpson, A. D. Greentree, and S. Prawer. Chromium single-photon emitters in diamond fabricated by ion implantation. *Physical Review B*, 81(12):121201, 2010.

[39] T. Gaebel, I. Popa, A. Gruber, M. Domhan, F. Jelezko, and J. Wrachtrup. Stable single-photon source in the near infrared. *New Journal of Physics*, 6:98--98, 2004.

[40] E. Wu, J. R. Rabeau, G. Roger, F. Treussart, H. Zeng, P. Grangier, S. Prawer, and J. Roch. Room temperature triggered single-photon source in the near infrared. *New Journal of Physics*, 9(12):434--434, 2007.

[41] J. R. Rabeau, Y. L. Chin, S. Prawer, F. Jelezko, T. Gaebel, and J. Wrachtrup. Fabrication of single nickel-nitrogen defects in diamond by chemical vapor deposition. *Applied Physics Letters*, 86(13):131926--131926--3, 2005.

[42] I. Aharonovich, C. Zhou, A. Stacey, J. Orwa, S. Castelletto, D. Simpson, A. D. Greentree, F. Treussart, J. Roch, and S. Prawer. Enhanced single-photon emission in the near infrared from a diamond color center. *Physical Review B*, 79:235316, 2009.

[43] D. A. Simpson, E. Ampem-Lassen, B. C. Gibson, S. Trpkovski, F. M. Hossain, S. T. Huntington, A. D. Greentree, L. C. L. Hollenberg, and S. Prawer. A highly efficient two level diamond based single photon source. *Applied Physics Letters*, 94(20):203107--203107--3, 2009.

[44] B. Naydenov, R. Kolesov, A. Batalov, J. Meijer, S. Pezzagna, D. Rogalla, F. Jelezko, and J. Wrachtrup. Engineering single photon emitters by ion implantation in diamond. *Applied Physics Letters*, 95(18):181109--181109--3, 2009.

[45] A. M. Zaitsev. Vibronic spectra of impurity-related optical centers in diamond. *Physical Review B*, 61(19):12909--12922, 2000.

[46] I. Aharonovich, C. Zhou, A. Stacey, F. Treussart, J. Roch, and S. Prawer. Formation of color centers in nanodiamonds by plasma assisted diffusion of impurities from the growth substrate. *Applied Physics Letters*, 93:243112, 2008.

[47] C. Bradac, T. Gaebel, N. Naidoo, M. J. Sellars, J. Twamley, L. J. Brown, A. S. Barnard, T. Plakhotnik, A. V. Zvyagin, and J. R. Rabeau. Observation and control of blinking nitrogen-vacancy centres in discrete nanodiamonds. *Nature Nanotechnology*, 5(5):345--349, 2010.

[48] Classification of Diamond, www.e6cvd.com/cvd, 2012.

[49] G. Balasubramanian, P. Neumann, D. Twitchen, M. Markham, R. Kolesov, N. Mizuochi, J. Isoya, J. Achard, J. Beck, J. Tissler, V. Jacques, P. R. Hemmer, F. Jelezko, and J. Wrachtrup. Ultralong spin coherence time in isotopically engineered diamond. *Nature Materials*, 8(5):383, 2009.

[50] S. Felton, A. M. Edmonds, M. E. Newton, P. M. Martineau, D. Fisher, and D. J. Twitchen. Electron paramagnetic resonance studies of the neutral nitrogen vacancy in diamond. *Physical Review B*, 77(8):081201, 2008.

[51] Y. Mita. Change of absorption spectra in type-Ib diamond with heavy neutron irradiation. *Physical Review B*, 53(17):11360--11364, 1996.

[52] M. V. Hauf, B. Grotz, B. Naydenov, M. Dankerl, S. Pezzagna, J. Meijer, F. Jelezko, J. Wrachtrup, M. Stutzmann, F. Reinhard, and J. A. Garrido. Chemical control of the charge state of nitrogen-vacancy centers in diamond. *Physical Review B*, 83(8):081304, 2011.

[53] N. Manson and J. Harrison. Photo-ionization of the nitrogen-vacancy center in diamond. *Diamond and Related Materials*, 14(10):1705--1710, 2005.

[54] T. Gaebel, M. Domhan, C. Wittmann, I. Popa, F. Jelezko, J. Rabeau, A. Greentree, S. Prawer, E. Trajkov, P. Hemmer, and J. Wrachtrup. Photochromism in single nitrogen-vacancy defect in diamond. *Applied Physics B: Lasers and Optics*, 82(2):243--246, 2006.

[55] H. Zhao, M. Fujiwara, and S. Takeuchi. Suppression of fluorescence phonon sideband from nitrogen vacancy centers in diamond nanocrystals by substrate effect. *Optics Express*, 20(14):15628, 2012.

[56] A. Lenef, S. W. Brown, D. A. Redman, S. C. Rand, J. Shigley, and E. Fritsch. Electronic structure of the N-V center in diamond: Experiments. *Physical Review B*, 53(20):13427--13440, 1996.

[57] N. B. Manson, J. P. Harrison, and M. J. Sellars. Nitrogen-vacancy center in diamond: Model of the electronic structure and associated dynamics. *Physical Review B*, 74(10):104303, 2006.

[58] A. Gali, M. Fyta, and E. Kaxiras. Ab initio supercell calculations on nitrogen-vacancy center in diamond: Electronic structure and hyperfine tensors. *Physical Review B*, 77(15):155206, 2008.

[59] F. M. Hossain, M. W. Doherty, H. F. Wilson, and L. C. L. Hollenberg. Ab initio electronic and optical properties of the N-V- center in diamond. *Physical Review Letters*, 101(22):226403, 2008.

[60] P. Tamarat, N. B. Manson, J. P. Harrison, R. L. McMurtrie, A. Nizovtsev, C. Santori, R. G. Beausoleil, P. Neumann, T. Gaebel, F. Jelezko, P. Hemmer, and J. Wrachtrup. Spin-flip and spin-conserving optical transitions of the nitrogen-vacancy centre in diamond. *New Journal of Physics*, 10(4):045004, 2008.

[61] L. J. Rogers, S. Armstrong, M. J. Sellars, and N. B. Manson. Infrared emission of the NV centre in diamond: Zeeman and uniaxial stress studies. *New Journal of Physics*, 10(10):103024, 2008.

[62] N. R. S. Reddy, N. B. Manson, and E. R. Krausz. Two-laser spectral hole burning in a colour centre in diamond. *Journal of Luminescence*, 38:46 -- 47, 1987.

[63] A. Batalov, V. Jacques, F. Kaiser, P. Siyushev, P. Neumann, L. J. Rogers, R. L. McMurtrie, N. B. Manson, F. Jelezko, and J. Wrachtrup. Low temperature studies of the Excited-State structure of negatively charged Nitrogen-Vacancy color centers in diamond. *Physical Review Letters*, 102(19):195506, 2009.

[64] G. Waldherr, J. Beck, M. Steiner, P. Neumann, A. Gali, T. Frauenheim, F. Jelezko, and J. Wrachtrup. Dark states of single Nitrogen-Vacancy cen-

ters in diamond unraveled by single shot NMR. *Physical Review Letters*, 106(15): 157601, 2011.

[65] T. P. M. Alegre, C. Santori, G. Medeiros-Ribeiro, and R. G. Beausoleil. Polarization-selective excitation of nitrogen vacancy centers in diamond. *Physical Review B*, 76(16):165205, 2007.

[66] A. T. Collins, M. F. Thomaz, and M. I. B. Jorge. Luminescence decay time of the 1.945 eV centre in type ib diamond. *Journal of Physics C: Solid State Physics*, 16(11):2177--2181, 1983.

[67] F. Jelezko and J. Wrachtrup. Read-out of single spins by optical spectroscopy. *Journal of Physics: Condensed Matter*, 16(30):R1089--R1104, 2004.

[68] J. Harrison, M. J. Sellars, and N. B. Manson. Optical spin polarisation of the N-V centre in diamond. *Journal of Luminescence*, 107:245 -- 248, 2004. Proceedings of the 8th International Meeting on Hole Burning, Single Molecule, and Related Spectroscopies: Science and Applications.

[69] C. Santori, D. Fattal, S. M. Spillane, M. Fiorentino, R. G. Beausoleil, A. D. Greentree, P. Olivero, M. Draganski, J. R. Rabeau, P. Reichart, B. C. Gibson, S. Rubanov, D. N. Jamieson, and S. Prawer. Coherent population trapping in diamond N-V centers at zero magneticfield. *Optics Express*, 14(17):7986–7993, 2006.

[70] N. Zhao, J. Honert, B. Schmid, J. Isoya, M. Markham, D. Twitchen, F. Jelezko, R. Liu, H. Fedder, and J. Wrachtrup. Sensing remote nuclear spins. *arXiv:1204.6513*, 2012.

[71] F. Jelezko, I. Popa, A. Gruber, C. Tietz, J. Wrachtrup, A. Nizovtsev, and S. Kilin. Single spin states in a defect center resolved by optical spectroscopy. *Applied Physics Letters*, 81(12):2160--2162, 2002.

[72] V. M. Acosta, A. Jarmola, E. Bauch, and D. Budker. Optical properties of the nitrogen-vacancy singlet levels in diamond. *Physical Review B*, 82:201202, 2010.

[73] L. Robledo, H. Bernien, T. v. d. Sar, and R. Hanson. Spin dynamics in the optical cycle of single nitrogen-vacancy centres in diamond. *New Journal of Physics*, 13 (2):025013, 2011.

[74] F. Jelezko, T. Gaebel, I. Popa, A. Gruber, and J. Wrachtrup. Observation of coherent oscillations in a single electron spin. *Physical Review Letters*, 92(7): 076401, 2004.

[75] T. Gaebel, M. Domhan, I. Popa, C. Wittmann, P. Neumann, F. Jelezko, J. R. Rabeau, N. Stavrias, A. D. Greentree, S. Prawer, J. Meijer, J. Twamley, P. R. Hemmer, and J. Wrachtrup. Room-temperature coherent coupling of single spins in diamond. *Nature Physics*, 2(6):408--413, 2006.

[76] L. Childress, G. Dutt, M. V, J. M. Taylor, A. S. Zibrov, F. Jelezko, J. Wrachtrup, P. R. Hemmer, and M. D. Lukin. Coherent dynamics of coupled electron and nuclear spin qubits in diamond. *Science*, 314(5797):281--285, 2006.

[77] M. V. Gurudev Dutt, L. Childress, L. Jiang, E. Togan, J. Maze, F. Jelezko, A. S. Zibrov, P. R. Hemmer, and M. D. Lukin. Quantum register based on individual electronic and nuclear spin qubits in diamond. *Science*, 316(5829):1312--1316, 2007.

[78] A. Stacey, I. Aharonovich, S. Prawer, and J. E. Butler. Controlled synthesis of high quality micro/nano-diamonds by microwave plasma chemical vapor deposition. *Diamond and Related Materials*, 18(1):51--55, 2009.

[79] T. v. d. Sar, J. Hagemeier, W. Pfaff, E. C. Heeres, S. M. Thon, H. Kim, P. M. Petroff, T. H. Oosterkamp, D. Bouwmeester, and R. Hanson. Deterministic nanoassembly of a coupled quantum emitter–photonic crystal cavity system. *Applied Physics Letters*, 98(19):193103, 2011.

[80] A. Beveratos, S. Kühn, R. Brouri, T. Gacoin, J. Poizat, and P. Grangier. Room temperature stable single-photon source. *The European Physical Journal D - Atomic, Molecular and Optical Physics*, 18(2):191--196, 2002.

[81] T. M. Babinec, B. J. M. Hausmann, M. Khan, Y. Zhang, J. R. Maze, P. R. Hemmer, and M. Loncar. A diamond nanowire single-photon source. *Nature Nanotechnology*, 5(3):195--199, 2010.

[82] J. P. Hadden, J. P. Harrison, A. C. Stanley-Clarke, L. Marseglia, Y. D. Ho, B. R. Patton, J. L. O'Brien, and J. G. Rarity. Strongly enhanced photon collection from diamond defect centers under microfabricated integrated solid immersion lenses. *Applied Physics Letters*, 97(24):241901--241901--3, 2010.

[83] P. Siyushev, F. Kaiser, V. Jacques, I. Gerhardt, S. Bischof, H. Fedder, J. Dodson, M. Markham, D. Twitchen, F. Jelezko, and J. Wrachtrup. Monolithic diamond optics for single photon detection. *Applied Physics Letters*, 97(24):241902, 2010.

[84] J. R. Rabeau, A. Stacey, A. Rabeau, S. Prawer, F. Jelezko, I. Mirza, and J. Wrachtrup. Single nitrogen vacancy centers in chemical vapor deposited diamond nanocrystals. *Nano Letters*, 7(11):3433--3437, 2007.

[85] F. Jelezko, C. Tietz, A. Gruber, I. Popa, A. Nizovtsev, S. Kilin, and J. Wrachtrup. Spectroscopy of single N-V centers in diamond. *Single Molecules*, 2(4):255–260, 2001.

[86] Y. Shen, T. M. Sweeney, and H. Wang. Zero-phonon linewidth of single nitrogen vacancy centers in diamond nanocrystals. *Physical Review B*, 77(3):033201, 2008.

[87] M. O. Scully and M. S. Zubairy. *Quantum optics*. Cambridge University Press, 1997.

[88] A. Beveratos, R. Brouri, T. Gacoin, J. Poizat, and P. Grangier. Nonclassical radiation from diamond nanocrystals. *Physical Review A*, 64(6):061802, 2001.

[89] K. Iakoubovskii and G. Adriaenssens. Optical detection of defect centers in CVD diamond. *Diamond and Related Materials*, 9(7):1349--1356, 2000.

[90] C. D. Clark, H. Kanda, I. Kiflawi, and G. Sittas. Silicon defects in diamond. *Physical Review B*, 51(23):16681--16688, 1995.

[91] I. Aharonovich, S. Castelletto, D. A. Simpson, A. D. Greentree, and S. Prawer. Photophysics of chromium-related diamond single-photon emitters. *Physical Review A*, 81(4):043813, 2010.

[92] S. Pezzagna, B. Naydenov, F. Jelezko, J. Wrachtrup, and J. Meijer. Creation efficiency of nitrogen-vacancy centres in diamond. *New Journal of Physics*, 12 (6):065017, 2010.

[93] S. Pezzagna, D. Rogalla, D. Wildanger, J. Meijer, and A. Zaitsev. Creation and nature of optical centres in diamond for single-photon emission—overview and critical remarks. *New Journal of Physics*, 13(3):035024, 2011.

[94] M. Gregor, C. Pyrlik, R. Henze, A. Wicht, A. Peters, and O. Benson. An alignment-free fiber-coupled microsphere resonator for gas sensing applications. *Applied Physics Letters*, 96(23):231102, 2010.

[95] M. Gregor, A. Kuhlicke, and O. Benson. Soft-landing and optical characterization of a preselected single fluorescent particle on a tapered optical fiber. *Optics Express*, 17(26):24234--24243, 2009.

[96] M. Gregor. *Fiber Taper-Coupled Microresonators for Applications in Sensing and Quantum Optics*. PhD thesis, Humboldt-Universität zu Berlin, Institut für Physik, AG Nano-Optik, 2010.

[97] M. Fujiwara, K. Toubaru, and S. Takeuchi. Optical transmittance degradation in tapered fibers. *Optics Express*, 19(9):8596–8601, 2011.

[98] D. W. Pohl, W. Denk, and M. Lanz. Optical stethoscopy: Image recording with resolution lambda/20. *Applied Physics Letters*, 44(7):651--653, 1984.

[99] E. Betzig, J. K. Trautman, T. D. Harris, J. S. Weiner, and R. L. Kostelak. Breaking the diffraction barrier: Optical microscopy on a nanometric scale. *Science*, 251(5000):1468--1470, 1991.

[100] T. Mukaiyama, K. Takeda, H. Miyazaki, Y. Jimba, and M. Kuwata-Gonokami. Tight-Binding photonic molecule modes of resonant bispheres. *Physical Review Letters*, 82(23):4623–4626, 1999.

[101] F. Müller. Detektion und Manipulation nanoskopischer Partikel mittels Nahfeld- und Fluoreszenzmikroskopie. Master's thesis, Humboldt-Universität zu Berlin, Institut für Physik, AG Nano-Optik, 2003.

[102] A. Mazzei, S. Götzinger, L. d. S. Menezes, G. Zumofen, O. Benson, and V. Sandoghdar. Controlled coupling of counterpropagating Whispering-Gallery modes by a single rayleigh scatterer: A classical problem in a quantum optical light. *Physical Review Letters*, 99(17):173603, 2007.

[103] E. Betzig, P. L. Finn, and J. S. Weiner. Combined shear force and near-field scanning optical microscopy. *Applied Physics Letters*, 60(20):2484--2486, 1992.

[104] S. Götzinger, L. d. S. Menezes, A. Mazzei, S. Kühn, V. Sandoghdar, and O. Benson. Controlled photon transfer between two individual nanoemitters via shared High-Q modes of a microsphere resonator. *Nano Letters*, 6(6):1151--1154, 2006.

[105] M. Pöllinger, D. O'Shea, F. Warken, and A. Rauschenbeutel. Ultrahigh-Q tunable Whispering-Gallery-Mode microresonator. *Physical Review Letters*, 103 (5):053901, 2009.

[106] T. Schröder. Herstellung und Vermessung von toroidalen Mikroresonatoren. Master's thesis, Humboldt-Universität zu Berlin, Institut für Physik, AG Nano-Optik, 2007.

[107] A. W. Schell, G. Kewes, T. Hanke, A. Leitenstorfer, R. Bratschitsch, O. Benson, and T. Aichele. Single defect centers in diamond nanocrystals as quantum probes for plasmonic nanostructures. *Optics Express*, 19(8):7914--7920, 2011.

[108] E. Ampem-Lassen, D. A. Simpson, B. C. Gibson, S. Trpkovski, F. M. Hossain, S. T. Huntington, K. Ganesan, L. C. Hollenberg, and S. Prawer. Nano-manipulation of diamond-based single photon sources. *Optics Express*, 17(14):11287--11293, 2009.

[109] R. H. Webb. Confocal optical microscopy. *Reports on Progress in Physics*, 59 (3):427--471, 1996.

[110] J. B. Pawley and B. R. Masters. Handbook of biological confocal microscopy, third edition. *Journal of Biomedical Optics*, 13(2):029902--029902--3, 2008.

[111] A. Gruber. Scanning confocal optical microscopy and magnetic resonance on single defect centers. *Science*, 276(5321):2012--2014, 1997.

[112] A. B. Shafer, L. R. Megill, and L. Droppelmann. Optimization of the Czerny-Turner spectrometer. *Journal of the Optical Society of America*, 54(7):879--886, 1964.

[113] G. N. Gol'tsman, O. Okunev, G. Chulkova, A. Lipatov, A. Semenov, K. Smirnov, B. Voronov, A. Dzardanov, C. Williams, and R. Sobolewski. Picosecond superconducting single-photon optical detector. *Applied Physics Letters*, 79(6):705--707, 2001.

[114] J. Claudon, J. Bleuse, N. S. Malik, M. Bazin, P. Jaffrennou, N. Gregersen, C. Sauvan, P. Lalanne, and J. Gerard. A highly efficient single-photon source based on a quantum dot in a photonic nanowire. *Nature Photonics*, 4(3):174–177, 2010.

[115] T. Schröder, F. Gädeke, M. J. Banholzer, and O. Benson. Ultrabright and efficient single-photon generation based on nitrogen-vacancy centres in nanodiamonds on a solid immersion lens. *New Journal of Physics*, 13(5):055017, 2011.

[116] J. L. O'Brien. Optical quantum computing. *Science*, 318(5856):1567--1570, 2007.

[117] F. P. Kapron. Geometrical optics of parabolic Index-Gradient cylindrical lenses. *Journal of the Optical Society of America*, 60:1433, 1970.

[118] Optische Interferenz Bauelemente GmbH, www.oib-jena.de, 2012.

[119] A. I. Bawamia, G. Blume, B. Eppich, A. Ginolas, S. Spießerger, M. Thomas, B. Sumpf, and G. Erbert. Miniaturized tunable external cavity diode laser with Single-Mode operation and a narrow linewidth at 633 nm. *IEEE Photonics Technology Letters*, 23(22):1676--1678, 2011.

[120] P. Engel. Realisation of a compact fiber-coupled diamond based single photon source in the visible spectrum. Master's thesis, Humboldt-Universität zu Berlin, Institut für Physik, AG Nano-Optik, 2010.

[121] A. W. Schell, G. Kewes, T. Schröder, J. Wolters, T. Aichele, and O. Benson. A scanning probe-based pick-and-place procedure for assembly of integrated quantum optical hybrid devices. *Review of Scientific Instruments*, 82(7):073709, 2011.

[122] J. L. O'Brien, A. Furusawa, and J. Vuckovic. Photonic quantum technologies. *Nature Photonics*, 3(12):687–695, 2009.

[123] J. R. Rabeau, S. T. Huntington, A. D. Greentree, and S. Prawer. Diamond chemical-vapor deposition on optical fibers for fluorescence waveguiding. *Applied Physics Letters*, 86(13):134104, 2005.

[124] I. H. Malitson. Interspecimen comparison of the refractive index of fused silica. *Journal of the Optical Society of America*, 55(10):1205--1208, 1965.

[125] S. M. Mansfield and G. S. Kino. Solid immersion microscope. *Applied Physics Letters*, 57(24):2615--2616, 1990.

[126] J. Michaelis, C. Hettich, J. Mlynek, and V. Sandoghdar. Optical microscopy using a single-molecule light source. *Nature*, 405(6784):325--328, 2000.

[127] P. E. Barclay, K. C. Fu, C. Santori, and R. G. Beausoleil. Chip-based microcavities coupled to nitrogen-vacancy centers in single crystal diamond. *Applied Physics Letters*, 95(19):191115--191117, 2009.

[128] J. R. Maze, P. L. Stanwix, J. S. Hodges, S. Hong, J. M. Taylor, P. Cappellaro, L. Jiang, M. V. G. Dutt, E. Togan, A. S. Zibrov, A. Yacoby, R. L. Walsworth, and M. D. Lukin. Nanoscale magnetic sensing with an individual electronic spin in diamond. *Nature*, 455(7213):644--647, 2008.

[129] F. Le Kien, S. Dutta Gupta, V. I. Balykin, and K. Hakuta. Spontaneous emission of a cesium atom near a nanofiber: Efficient coupling of light to guided modes. *Physical Review A*, 72(3):032509, 2005.

[130] D. E. Chang, A. S. Sorensen, E. A. Demler, and M. D. Lukin. A single-photon transistor using nanoscale surface plasmons. *Nature Physics*, 3(11):807–812, 2007.

[131] K. Y. Han, K. I. Willig, E. Rittweger, F. Jelezko, C. Eggeling, and S. W. Hell. Three-Dimensional stimulated emission depletion microscopy of Nitrogen-Vacancy centers in diamond using Continuous-Wave light. *Nano Letters*, 9(9):3323--3329, 2009.

[132] P. C. Maurer, J. R. Maze, P. L. Stanwix, L. Jiang, A. V. Gorshkov, A. A. Zibrov, B. Harke, J. S. Hodges, A. S. Zibrov, A. Yacoby, D. Twitchen, S. W. Hell, R. L. Walsworth, and M. D. Lukin. Far-field optical imaging and manipulation of individual spins with nanoscale resolution. *Nature Physics*, 6(11):912–918, 2010.

[133] S. Yu, M. Kang, H. Chang, K. Chen, and Y. Yu. Bright fluorescent nanodiamonds: No photobleaching and low cytotoxicity. *Journal of the American Chemical Society*, 127(50):17604--17605, 2005.

[134] B. R. Smith, D. Gruber, and T. Plakhotnik. The effects of surface oxidation on luminescence of nano diamonds. *Diamond and Related Materials*, 19(4):314--318, 2010.

[135] M. Fujiwara, K. Toubaru, T. Noda, H. Zhao, and S. Takeuchi. Highly efficient coupling of photons from nanoemitters into Single-Mode optical fibers. *Nano Letters*, 11(10):4362--4365, 2011.

[136] A. Stefanov, N. Gisin, O. Guinnard, L. Guinnard, and H. Zbinden. Optical quantum random number generator. *Journal of Modern Optics*, 47(4):595--598, 2000.

[137] M. Wahl, M. Leifgen, M. Berlin, T. Rohlicke, H. Rahn, and O. Benson. An ultrafast quantum random number generator with provably bounded output bias based on photon arrival time measurements. *Applied Physics Letters*, 98(17): 171105, 2011.

[138] H. Takashima, T. Asai, K. Toubaru, M. Fujiwara, K. Sasaki, and S. Takeuchi. Fiber-microsphere system at cryogenic temperatures toward cavity QED using diamond NV centers. *Optics Express*, 18(14):15169–15173, 2010.

[139] C. K. Hong, Z. Y. Ou, and L. Mandel. Measurement of subpicosecond time intervals between two photons by interference. *Physical Review Letters*, 59: 2044–2046, 1987.

[140] H. Bernien, L. Childress, L. Robledo, M. Markham, D. Twitchen, and R. Hanson. Two-Photon quantum interference from separate nitrogen vacancy centers in diamond. *Physical Review Letters*, 108(4):043604, 2012.

[141] R. B. Patel, A. J. Bennett, I. Farrer, C. A. Nicoll, D. A. Ritchie, and A. J. Shields. Two-photon interference of the emission from electrically tunable remote quantum dots. *Nature Photonics*, 4(9):632–635, 2010.

[142] I. Fushman, D. Englund, A. Faraon, N. Stoltz, P. Petroff, and J. Vuckovic. Controlled phase shifts with a single quantum dot. *Science*, 320(5877):769--772, 2008.

[143] J. Hwang, M. Pototschnig, R. Lettow, G. Zumofen, A. Renn, S. Gotzinger, and V. Sandoghdar. A single-molecule optical transistor. *Nature*, 460(7251):76–80, 2009.

[144] H. F. Hofmann, K. Kojima, S. Takeuchi, and K. Sasaki. Optimized phase switching using a single-atom nonlinearity. *Journal of Optics B: Quantum and Semiclassical Optics*, 5(3):218--221, 2003.

[145] K. Kojima, H. F. Hofmann, S. Takeuchi, and K. Sasaki. Efficiencies for the single-mode operation of a quantum optical nonlinear shift gate. *Physical Review A*, 70(1):013810, 2004.

[146] M. Gregor, R. Henze, T. Schröder, and O. Benson. On-demand positioning of a preselected quantum emitter on a fiber-coupled toroidal microresonator. *Applied Physics Letters*, 95(15):153110, 2009.

[147] G. Balasubramanian, I. Y. Chan, R. Kolesov, M. Al-Hmoud, J. Tisler, C. Shin, C. Kim, A. Wojcik, P. R. Hemmer, A. Krueger, T. Hanke, A. Leitenstorfer, R. Bratschitsch, F. Jelezko, and J. Wrachtrup. Nanoscale imaging magnetometry with diamond spins under ambient conditions. *Nature*, 455(7213):648--651, 2008.

[148] J. Vuckovic and Y. Yamamoto. Photonic crystal microcavities for cavity quantum electrodynamics with a single quantum dot. *Applied Physics Letters*, 82(15): 2374--2376, 2003.

[149] E. M. Purcell. Spontaneous emission probabilities at radio frequencies. *Physical Review*, 69:681, 1946.

[150] D. Englund, I. Fushman, and J. Vučković. General recipe for designing photonic crystal cavities. *Optics Express*, 12(16):5961--75, 2005.

[151] D. Englund, D. Fattal, E. Waks, G. Solomon, B. Zhang, T. Nakaoka, Y. Arakawa, Y. Yamamoto, and J. Vuckovic. Controlling the spontaneous emission rate of single quantum dots in a Two-Dimensional photonic crystal. *Physical Review Letters*, 95:013904, 2005.

[152] Y. P. Rakovich, J. F. Donegan, M. Gerlach, A. L. Bradley, T. M. Connolly, J. J. Boland, N. Gaponik, and A. Rogach. Fine structure of coupled optical modes in photonic molecules. *Physical Review A*, 70(5):051801, 2004.

[153] B. M. Möller, U. Woggon, M. V. Artemyev, and R. Wannemacher. Photonic molecules doped with semiconductor nanocrystals. *Physical Review B*, 70(11): 115323, 2004.

[154] B. M. Möller, U. Woggon, and M. V. Artemyev. Coupled-resonator optical waveguides doped with nanocrystals. *Optics Letters*, 30(16):2116–2118, 2005.

[155] S. Schietinger. *Investigation, Manipulation, and Coupling of Single Nanoscopic and Quantum Emitters*. PhD thesis, Humboldt-Universität zu Berlin, Institut für Physik, AG Nano-Optik, 2011.

[156] R. D. Richtmyer. Dielectric resonators. *Journal of Applied Physics*, 10(6): 391--398, 1939.

[157] D. K. Armani, T. J. Kippenberg, S. M. Spillane, and K. J. Vahala. Ultra-high-Q toroid microcavity on a chip. *Nature*, 421(6926):925--928, 2003.

[158] S. M. Spillane, T. J. Kippenberg, K. J. Vahala, K. W. Goh, E. Wilcut, and H. J. Kimble. Ultrahigh-Q toroidal microresonators for cavity quantum electrodynamics. *Physical Review A*, 71(1):013817, 2005.

[159] B. Min, L. Yang, and K. Vahala. Perturbative analytic theory of an ultrahigh-Q toroidal microcavity. *Physical Review A*, 76(1):013823, 2007.

[160] A. Imamoglu, D. D. Awschalom, G. Burkard, D. P. DiVincenzo, D. Loss, M. Sherwin, and A. Small. Quantum information processing using quantum dot spins and cavity QED. *Physical Review Letters*, 83(20):4204--4207, 1999.

[161] I. Ichimura, S. Hayashi, and G. S. Kino. High-density optical recording using a solid immersion lens. *Applied Optics*, 36(19):4339--4348, 1997.

[162] W. Barnes, G. Björk, J. Gérard, P. Jonsson, J. Wasey, P. Worthing, and V. Zwiller. Solid-state single photon sources: light collection strategies. *The European Physical Journal D*, 18(2):197--210, 2002.

[163] P. a. M. Dirac. The quantum theory of the emission and absorption of radiation. *Proceedings of the Royal Society of London. Series A*, 114(767):243--265, 1927.

[164] S. M. Mansfield, W. R. Studenmund, G. S. Kino, and K. Osato. High-numerical-aperture lens system for optical storage. *Optics Letters*, 18(4):305--307, 1993.

[165] Q. Wu, G. D. Feke, R. D. Grober, and L. P. Ghislain. Realization of numerical aperture 2.0 using a gallium phosphide solid immersion lens. *Applied Physics Letters*, 75(26):4064--4066, 1999.

[166] K. Karrai, X. Lorenz, and L. Novotny. Enhanced reflectivity contrast in confocal solid immersion lens microscopy. *Applied Physics Letters*, 77(21):3459--3461, 2000.

[167] B. D. Terris, H. J. Mamin, D. Rugar, W. R. Studenmund, and G. S. Kino. Near-field optical data storage using a solid immersion lens. *Applied Physics Letters*, 65(4):388--390, 1994.

[168] M. Yoshita, K. Koyama, Y. Hayamizu, M. Baba, and H. Akiyama. Improved high collection efficiency in fluorescence microscopy with a Weierstrass-Sphere

solid immersion lens. *Japanese Journal of Applied Physics*, 41(Part 2, No. 7B): L858--L860, 2002.

[169] A. T. Collins. The use of the weierstrass sphere geometry in luminescence spectroscopy. *Journal of Physics D: Applied Physics*, 10(8):1143--1150, 1977.

[170] A. Ugur. *Silicon Vacancy Defects in Diamond as Single Photon Source*. PhD thesis, Technical University Munich, 1996.

[171] L. Marseglia, J. P. Hadden, A. C. Stanley-Clarke, J. P. Harrison, B. Patton, Y. D. Ho, B. Naydenov, F. Jelezko, J. Meijer, P. R. Dolan, J. M. Smith, J. G. Rarity, and J. L. O'Brien. Nanofabricated solid immersion lenses registered to single emitters in diamond. *Applied Physics Letters*, 98(13):133107--133107--3, 2011.

[172] A. Krell, J. Klimke, and T. Hutzler. Transparent compact ceramics: Inherent physical issues. *Optical Materials*, 31(8):1144--1150, 2009.

[173] M. Baba, T. Sasaki, M. Yoshita, and H. Akiyama. Aberrations and allowances for errors in a hemisphere solid immersion lens for submicron-resolution photoluminescence microscopy. *Journal of Applied Physics*, 85(9):6923--6925, 1999.

[174] S. M. Mansfield. *Solid immersion microscopy*. PhD thesis, Department of Applied Physics, Stanford University, Stanford, Calif., USA, 1992.

[175] K. Yee. Numerical solution of initial boundary value problems involving maxwell's equations in isotropic media. *Transactions on Antennas and Propagation, IEEE*, 14(3):302 --307, 1966.

[176] W. Lukosz and R. E. Kunz. Light emission by magnetic and electric dipoles close to a plane interface. i. total radiated power. *Journal of the Optical Society of America*, 67(12):1607–1615, 1977.

[177] I. Sychugov, H. Omi, and Y. Kobayashi. On the role of substrate in light-harvesting experiments. *Optics Letters*, 33(16):1807–1809, 2008.

[178] T. D. Ladd, F. Jelezko, R. Laflamme, Y. Nakamura, C. Monroe, and J. L. O'Brien. Quantum computers. *Nature*, 464(7285):45–53, 2010.

[179] A. Stacey, D. A. Simpson, T. J. Karle, B. C. Gibson, V. M. Acosta, Z. Huang, K. M. C. Fu, C. Santori, R. G. Beausoleil, L. P. McGuinness, K. Ganesan,

S. Tomljenovic-Hanic, A. D. Greentree, and S. Prawer. Near-Surface spectrally stable nitrogen vacancy centres engineered in single crystal diamond. *Advanced Materials*, 24(25):3333–3338, 2012.

[180] A. Sipahigil, M. L. Goldman, E. Togan, Y. Chu, M. Markham, D. J. Twitchen, A. S. Zibrov, A. Kubanek, and M. D. Lukin. Quantum interference of single photons from remote nitrogen-vacancy centers in diamond. *Physical Review Letters*, 108(14):143601, 2012.

[181] A. Majumdar, E. D. Kim, and J. Vučković. Effect of photogenerated carriers on the spectral diffusion of a quantum dot coupled to a photonic crystal cavity. *Physical Review B*, 84(19):195304, 2011.

[182] R. Farrer. On the substitutional nitrogen donor in diamond. *Solid State Communications*, 7(9):685--688, 1969.

[183] J. Rosa, M. Vaněček, M. Nesládek, and L. Stals. Photoionization cross-section of dominant defects in CVD diamond. *Diamond and Related Materials*, 8(2–5): 721--724, 1999.

[184] P. Tamarat, T. Gaebel, J. R. Rabeau, M. Khan, A. D. Greentree, H. Wilson, L. C. L. Hollenberg, S. Prawer, P. Hemmer, F. Jelezko, and J. Wrachtrup. Stark shift control of single optical centers in diamond. *Physical Review Letters*, 97(8): 083002, 2006.

[185] V. M. Acosta, C. Santori, A. Faraon, Z. Huang, K. C. Fu, A. Stacey, D. A. Simpson, S. Tomljenovic-Hanic, K. Ganesan, A. D. Greentree, S. Prawer, and R. G. Beausoleil. Dynamic stabilization of the optical resonances of single nitrogen-vacancy centers in diamond. *Physical Review Letters*, 108(20):206401, 2012.

[186] D. W. Pohl. *Semiconductor Nanostructures*. Springer, 2008.

[187] G. Sallen, A. Tribu, T. Aichele, R. André, L. Besombes, C. Bougerol, M. Richard, S. Tatarenko, K. Kheng, and J. Poizat. Subnanosecond spectral diffusion measurement using photon correlation. *Nature Photonics*, 4(10):696--699, 2010.

[188] X. Brokmann, M. Bawendi, L. Coolen, and J. Hermier. Photon-correlation fourier spectroscopy. *Optics Express*, 14(13):6333–6341, 2006.

[189] L. Coolen, X. Brokmann, P. Spinicelli, and J. Hermier. Emission characterization of a single CdSe-ZnS nanocrystal with high temporal and spectral resolution by Photon-Correlation fourier spectroscopy. *Physical Review Letters*, 100(2):027403, 2008.

[190] N. Sangouard, C. Simon, H. d. Riedmatten, and N. Gisin. Quantum repeaters based on atomic ensembles and linear optics. *Reviews of Modern Physics*, 83(1): 33--80, 2011.

[191] W. Schmunk, M. Rodenberger, S. Peters, H. Hofer, and S. Kück. Radiometric calibration of single photon detectors by a single photon source based on NV-centers in diamond. *Journal of Modern Optics*, 58(14):1252--1259, 2011.

[192] W. Diffie and M. E. Hellman. Multiuser cryptographic techniques. In *Proceedings, National Computer Conference and Exposition*, AFIPS '76, pages 109--112. New York, NY, USA, 1976.

[193] P. Shor. Algorithms for quantum computation: discrete logarithms and factoring. In *Foundations of Computer Science, 1994 Proceedings., 35th Annual Symposium on*, pages 124 --134. 1994.

[194] P. W. Shor. Polynomial-Time algorithms for prime factorization and discrete logarithms on a quantum computer. *SIAM Journal on Computing*, 26(5):1484, 1997.

[195] N. Gisin, G. Ribordy, W. Tittel, and H. Zbinden. Quantum cryptography. *Reviews of Modern Physics*, 74(1):145--195, 2002.

[196] C. H. Bennett, F. Bessette, G. Brassard, L. Salvail, and J. Smolin. Experimental quantum cryptography. *Journal of Cryptology*, 5(1):3--28, 1992.

[197] W. Wootters and W. Zurek. A single quantum cannot be cloned. *Nature*, 299: 802--803, 1982.

[198] C. H. Bennett, G. Brassard, and J. Robert. Privacy amplification by public discussion. *SIAM Journal on Computing*, 17(2):210--229, 1988.

[199] A. Beveratos, R. Brouri, T. Gacoin, A. Villing, J. Poizat, and P. Grangier. Single photon quantum cryptography. *Physical Review Letters*, 89(18):187901, 2002.

[200] P. W. Shor and J. Preskill. Simple proof of security of the BB84 quantum key distribution protocol. *Physical Review Letters*, 85(2):441--444, 2000.

[201] P. M. Intallura, M. B. Ward, O. Z. Karimov, Z. L. Yuan, P. See, A. J. Shields, P. Atkinson, and D. A. Ritchie. Quantum key distribution using a triggered quantum dot source emitting near 1.3 um. *Applied Physics Letters*, 91(16): 161103--161103--3, 2007.

[202] M. Fiorentino, P. Voss, J. Sharping, and P. Kumar. All-fiber photon-pair source for quantum communications. *IEEE Photonics Technology Letters*, 14(7):983 --985, 2002.

[203] X. Li, P. L. Voss, J. E. Sharping, and P. Kumar. Optical-Fiber source of Polarization-Entangled photons in the 1550 nm telecom band. *Physical Review Letters*, 94(5):053601, 2005.

[204] M. B. Ward, T. Farrow, P. See, Z. L. Yuan, O. Z. Karimov, A. J. Bennett, A. J. Shields, P. Atkinson, K. Cooper, and D. A. Ritchie. Electrically driven telecommunication wavelength single-photon source. *Applied Physics Letters*, 90 (6):063512--063512--3, 2007.

[205] J. J. Peterson and T. D. Krauss. Fluorescence spectroscopy of single lead sulfide quantum dots. *Nano Letters*, 6(3):510--514, 2006.

[206] D. K. Harris, P. M. Allen, H. Han, B. J. Walker, J. Lee, and M. G. Bawendi. Synthesis of cadmium arsenide quantum dots luminescent in the infrared. *Journal of the American Chemical Society*, 133(13):4676--4679, 2011.

[207] A. R. Hawkins and H. Schmidt. *Handbook of Optofluidics - CRC Press Book*. CRC Press, 2010.

[208] F. M. Cox, A. Argyros, and M. C. J. Large. Liquid-filled hollow core microstructured polymer optical fiber. *Optics Express*, 14(9):4135–4140, 2006.

[209] S. Smolka, M. Barth, and O. Benson. Highly efficient fluorescence sensing with hollow core photonic crystal fibers. *Optics Express*, 15(20):12783, 2007.

[210] S. O. Konorov, C. J. Addison, H. G. Schulze, R. F. B. Turner, and M. W. Blades. Hollow-core photonic crystal fiber-optic probes for raman spectroscopy. *Optics Letters*, 31(12):1911, 2006.

[211] Y. Zhang, C. Shi, C. Gu, L. Seballos, and J. Z. Zhang. Liquid core photonic crystal fiber sensor based on surface enhanced raman scattering. *Applied Physics Letters*, 90(19):193504--193504--3, 2007.

[212] X. Yang, C. Shi, D. Wheeler, R. Newhouse, B. Chen, J. Z. Zhang, and C. Gu. High-sensitivity molecular sensing using hollow-core photonic crystal fiber and surface-enhanced raman scattering. *Journal of the Optical Society of America A*, 27(5):977, 2010.

[213] R. F. Cregan, B. J. Mangan, J. C. Knight, T. A. Birks, P. S. J. Russell, P. J. Roberts, and D. C. Allan. Single-Mode photonic band gap guidance of light in air. *Science*, 285(5433):1537--1539, 1999.

[214] W. Stutius and W. Streifer. Silicon nitride films on silicon for optical waveguides. *Applied Optics*, 16(12):3218--3222, 1977.

[215] S. Gaugiran, S. Gétin, J. Fedeli, G. Colas, A. Fuchs, F. Chatelain, and J. Dérouard. Optical manipulation of microparticles and cells on silicon nitride waveguides. *Optics Express*, 13(18):6956–6963, 2005.

[216] V. Lesnyak, A. Lutich, N. Gaponik, M. Grabolle, A. Plotnikov, U. Resch-Genger, and A. Eychmüller. One-pot aqueous synthesis of high quality near infrared emitting Cd1-xHgxTe nanocrystals. *Journal of Materials Chemistry*, 19(48): 9147--9152, 2009.

[217] H. Zhang, Z. Cui, Y. Wang, K. Zhang, X. Ji, C. Lü, B. Yang, and M. Gao. From Water-Soluble CdTe nanocrystals to fluorescent Nanocrystal–Polymer transparent composites using polymerizable surfactants. *Advanced Materials*, 15 (10):777–780, 2003.

[218] E. Chillcce, C. Cordeiro, L. Barbosa, and C. Brito Cruz. Tellurite photonic crystal fiber made by a stack-and-draw technique. *Journal of Non-Crystalline Solids*, 352(32–35):3423--3428, 2006.

[219] L. Xiao, W. Jin, M. Demokan, H. Ho, Y. Hoo, and C. Zhao. Fabrication of selective injection microstructured optical fibers with a conventional fusion splicer. *Optics Express*, 13(22):9014–9022, 2005.

[220] D. Dorfs, T. Franzl, R. Osovsky, M. Brumer, E. Lifshitz, T. A. Klar, and A. Eychmüller. Type-I and Type-II nanoscale heterostructures based on CdTe nanocrystals: A comparative study. *Small*, 4(8):1148–1152, 2008.

[221] S. Kim, B. Fisher, H. Eisler, and M. Bawendi. Type-II quantum dots: CdTe/CdSe(Core/Shell) and CdSe/ZnTe(Core/Shell) heterostructures. *Journal of the Optical Society of America*, 125(38):11466--11467, 2003.

[222] V. I. Klimov, S. A. Ivanov, J. Nanda, M. Achermann, I. Bezel, J. A. McGuire, and A. Piryatinski. Single-exciton optical gain in semiconductor nanocrystals. *Nature*, 447(7143):441--446, 2007.

[223] D. Oron, M. Kazes, and U. Banin. Multiexcitons in type-II colloidal semiconductor quantum dots. *Physical Review B*, 75(3):035330, 2007.

[224] S. Kumar, M. Jones, S. S. Lo, and G. D. Scholes. Nanorod heterostructures showing photoinduced charge separation. *Small*, 3(9):1633–1639, 2007.

[225] D. Dorfs, A. Salant, I. Popov, and U. Banin. ZnSe quantum dots within CdS nanorods: A Seeded-Growth Type-II system. *Small*, 4(9):1319–1323, 2008.

[226] S. Smolka, M. Barth, and O. Benson. Selectively coated photonic crystal fiber for highly sensitive fluorescence detection. *Applied Physics Letters*, 90(11):111101--111101--3, 2007.

[227] X. Chen, S. Götzinger, and V. Sandoghdar. 99% efficiency in collecting photons from a single emitter. *Optics Letters*, 36(18):3545, 2011.

[228] A. V. Akimov, A. Mukherjee, C. L. Yu, D. E. Chang, A. S. Zibrov, P. R. Hemmer, H. Park, and M. D. Lukin. Generation of single optical plasmons in metallic nanowires coupled to quantum dots. *Nature*, 450(7168):402--406, 2007.

[229] R. Kolesov, B. Grotz, G. Balasubramanian, R. J. Stöhr, A. A. L. Nicolet, P. R. Hemmer, F. Jelezko, and J. Wrachtrup. Wave–particle duality of single surface plasmon polaritons. *Nature Physics*, 5(7):470--474, 2009.

[230] K. Tanaka, E. Plum, J. Y. Ou, T. Uchino, and N. I. Zheludev. Multifold enhancement of quantum dot luminescence in plasmonic metamaterials. *Physical Review Letters*, 105(22):227403, 2010.

[231] O. Hess, J. B. Pendry, S. A. Maier, R. F. Oulton, J. M. Hamm, and K. L. Tsakmakidis. Active nanoplasmonic metamaterials. *Nature Materials*, 11(7): 573--584, 2012.

[232] A. Faraon, P. E. Barclay, C. Santori, K. C. Fu, and R. G. Beausoleil. Resonant enhancement of the zero-phonon emission from a colour centre in a diamond cavity. *Nature Photonics*, 5(5):301--305, 2011.

[233] C. Su, A. D. Greentree, and L. C. L. Hollenberg. Towards a picosecond transform-limited nitrogen-vacancy based single photon source. *Optics Express*, 16(9):6240, 2008.

[234] K. G. Lee, X. W. Chen, H. Eghlidi, P. Kukura, R. Lettow, A. Renn, V. Sandoghdar, and S. Götzinger. A planar dielectric antenna for directional single-photon emission and near-unity collection efficiency. *Nature Photonics*, 5(3):166--169, 2011.

[235] D. Englund, B. Shields, K. Rivoire, F. Hatami, J. Vuckovic, H. Park, and M. D. Lukin. Deterministic coupling of a single nitrogen vacancy center to a photonic crystal cavity. *Nano Letters*, 10(10):3922--3926, 2010.

[236] J. Riedrich-Möller, L. Kipfstuhl, C. Hepp, E. Neu, C. Pauly, F. Mücklich, A. Baur, M. Wandt, S. Wolff, M. Fischer, S. Gsell, M. Schreck, and C. Becher. One- and two-dimensional photonic crystal microcavities in single crystal diamond. *Nature Nanotechnology*, 7(1):69--74, 2012.

[237] D. Hunger, T. Steinmetz, Y. Colombe, C. Deutsch, T. W. Hänsch, and J. Reichel. A fiber fabry-perot cavity with high finesse. *New Journal of Physics*, 12(6): 065038, 2010.

List of own publications

The following articles have been published or submitted by the author.

Peer-reviewed journals

Wolters *et al.* 2012a Wolters J., Sadzak N., Schell A.W., Schröder T., and Benson O. Ultrafast spectral diffusion measurement on nitrogen vacancy centers in nanodiamonds using correlation interferometry. *arXiv*, arXiv:1206.0852v1, 2012.

Schröder *et al.* 2012b Schröder T., Engel P., Schmidt E., and Benson O. Integrated and compact fiber-coupled single-photon system based on nitrogen-vacancy centers and gradient-index lenses. *Optics Letters* 37, 2901-2903, 2012.

Jiang *et al.* 2012a Jiang P., Schröder T., Barth M., Lesnyak V., Gaponik N., Eychmüller A., and Benson O. Incoherent photon conversion in selectively infiltrated hollow-core photonic crystal fibers for single photon generation in the near infrared. *Optics Express* 20, 11536-11547, 2012.

Schröder *et al.* 2012a Schröder T., Fujiwara M., Noda T., Zhao H.-Q., Benson O., Takeuchi S. A nanodiamond-tapered fiber system with high single-mode coupling efficiency. *Optics Express* 20, 10490, 2012.

Schell *et al.* 2011a Schell A.W., Kewes G., Schröder T., Wolters J., Aichele T., Benson O. A scanning probe-based pick-and-place procedure for assembly of integrated quantum optical hybrid devices. *Review of Scientific Instruments* 82, 073709, 2011.

Schröder *et al.* 2011b Schröder T., Schell A.W., Kewes G., Aichele T., and Benson O. Fiber-Integrated Diamond-Based Single Photon Source. *Nano Letters* 11, 198Ð202, 2011.

Schröder *et al.* 2011a Schröder T., Gädeke F., Banholzer M.J., Benson O. Ultrabright and efficient single-photon generation based on nitrogen-vacancy centres

in nanodiamonds on a solid immersion lens. *New Journal of Physics* 13, 055017, 2011.

Barth *et al.* 2010a Barth M., Schietinger S., Schröder T., Aichele T., Benson O. Controlled coupling of NV defect centers to plasmonic and photonic nanostructures. *Journal of Luminescence* 130, 1628-1634, 2010.

Gregor *et al.* 2009a Gregor M., Henze R., Schröder T., Benson O. On-demand positioning of a preselected quantum emitter on a fiber-coupled toroidal microresonator. *Applied Physics Letters* 95, 153110, 2009.

Schietinger *et al.* 2008a Schietinger S., Schröder T., Benson O. One-by-One Coupling of Single Defect Centers in Nanodiamonds to High-Q Modes of an Optical Microresonator. *Nano Letters* 8, 3911-3915, 2008.

Conference proceedings

Schröder *et al.* 2012d Schröder T., Fujiwara M., Noda T., Zhao H.-Q., Benson O., Takeuchi S. Near-field coupling of a single NV center to a tapered fiber. *SPIE Conference Proceedings* 8272, 8, 2012.

Schröder *et al.* 2011c Schröder T., Schell A.W., Kewes G., Barth M., Aichele T., Benson O. Integrated photonic quantum technologies with fiber-integrated single photon emitters. *SPIE Conference Proceedings* 7943, 37, 2011.

Barth *et al.* 2010c Barth M., Höckel D., Koch L., Schietinger S., Schröder T., Aichele T., Benson O. Room-temperature single-photon sources: design, performance, and applications. *SPIE Conference Proceedings* 7681, 0I, 2010.

Barth *et al.* 2010b Barth M., Gregor M., Henze R., Schröder T., Nüsse N., Löchel B., Benson O. Hybrid approaches towards single emitter coupling to optical microresonators. *SPIE Conference Proceedings* 7579, 18, 2010.

Schietinger *et al.* 2010a Schietinger S., Barth m., Schröder T., Aichele T., Benson O. Plasmon-enhanced single photon emission from a nano-assembled metal-diamond hybrid structure. *Conference on Lasers and Electro-Optics & Quantum electronics and Laser Science Conference*, 2010.

Schietinger *et al.* 2009a Schietinger S., Schröder T., Benson O. One-by-one coupling of single photon emitters to high-Q modes of optical microresonators. *SPIE Conference Proceedings* 7211, 0K, 2009.

Patents

Schröder *et al.* Patent I Schröder T., Benson O., Schell A., Engel P., Banholzer M., Gädecke F., Birkl G.: Single Photon Emission System (Einzelphotonenemissionssystem). Submitted: U.S. Patent (Application No. 12/874,995, 2. September 2010), Deutsches Patent (amtl. Aktenzeichen 10 2011 005 327.1, 10.März 2011), Europäisches Patent (Aktenzeichen PCT/EP 2011/064223, 18. August 2011).

Abbreviations

3d	3-dimensional
a.u.	arbitrary units
AFM	atomic force microscope
APD	avalanche photodiode
BC	beam control
BP	band pass
BS	beam splitter
CCD	charge-coupled device
cQED	cavity quantum electrodynamics
cts	counts
CW	continuous wave
DA	digital-analog
DBS	dichroic beam splitter
DWF	Debye-Waller factor
e.g.	*exempli gratia* (for example)
EMCCD	electron multiplying CCD
EOM	electro optical modulator
erf	error function
FDTD	finite-difference time-domain
FIB	focussed ion beam etching
FPGA	field programmable gate array
FWHM	full-width at half-maximum
GHe	gaseous helium
GRIN	gradient index lens
HBT	Hanbury Brown and Twiss
HCPCF	hollow core photonic crystal fiber
HPHT	high pressure high temperature
i.e.	*id est* (that is)
LED	light emitting diode

LHe	liquid helium
LP	long pass
MPA	mercaptopropionic acid
NA	numerical aperture
NV	nitrogen-vacancy
NV^0	neutral NV
NV^-	negatively charged NV
ODMR	optically detected magnetic resonance
OVDAC	octadecyl-p-vinylbenzyldimetylammonium chloride
PBS	polarizing beam splitter
PCF	photonic crystal fiber
PL	photoluminescence
PLE	photoluminescence excitation
PS	polystyrene
PVA	polyvinyl alcohol
QBER	quantum bit error rate
QD	quantum dot
QE	quantum efficiency
QIP	quantum information processing
QKD	quantum key distribution
QRNG	quantum random number generator
qubit	quantum bit
SE	single emitter
SELFOC	self focussing
SEM	scanning electron microscope
SERS	surface enhanced Raman scattering
SIL	solid immersion lens
SIM	solid immersion microscope
SiV	silicon-vacancy
SNOM	scanning nearfield optical microscope
SP	short pass
SPS	single photon source
TM	transverse magnetic
TTTR	time-tagged time-resolved
WGM	whispering gallery mode
ZPL	zero phonon line

List of Figures

List of Tables

Danksagung

Ich werde meine Promotion als eine sehr schöne und intensive Zeit in Erinnerung behalten. Deshalb bedanke ich mich herzlich bei allen, die zum Gelingen dieser Doktorarbeit beigetragen und mich in den letzten Jahren begleitet haben.

Mein besonderer Dank gilt Herrn Professor Oliver Benson für die fachliche Betreuung dieser Arbeit und für die anregenden Diskussionen und Ratschläge. Auch die hervorragenden Arbeitsbedingungen, sowie die internationale Vernetzung waren für diese Arbeit mit entscheidend. Er hatte immer ein offenes Ohr für mich und konnte mir stets bei allen Fragen weiterhelfen.

Ebenso will ich gern Herrn Professor Shigeki Takeuchi und seinen Mitarbeitern meinen besten Dank für die aufregende, angenehme und konstruktive Zusammenarbeit in seiner Arbeitsgruppe aussprechen.

Darüber hinaus danke ich ganz besonders den Diplom- and Bachelorstudenten Friedemann, Philip, und Moritz, und all den Kollegen und Kooperationspartnern, mit denen ich während der letzten Jahre eng zusammengearbeitet habe und die sowohl mit ihrem Sachverstand als auch ihrer positiven Einstellung und guten Laune für eine angenehme Arbeitsatmosphäre gesorgt haben. Herrn Dipl. Ing. Klaus Palis danke ich ganz herzlich für die vielfätige Unterstützung bei der Realisierung verschiedener elektronischer Komponenten. Nicht zuletzt gilt Ben, Simon, Matthias und Katharina mein Dank für das Korrekturlesen dieser Arbeit.

All meine Zimmerkollegen, meine alten und meine gegenwärtigen, möchte ich mit einem Lachen auf den Lippen erwähnen, weil es stets eine Freude war, das Büro nicht ohne sie vorzufinden und über die vielen Dinge im Leben neben der Physik zu reden. Allen anderen Mitgliedern der Arbeitsgruppen NANO, QOM und AMO danke ich für die vielen unterhaltsamen Momente und Unterstützung.

Abschließend möchte ich sowohl meinen Eltern Frances und Udo als auch meiner Schwester Inka, Erik, und im Besonderen Anastasia und den vielen tollen Menschen in meinem Leben ganz herzlich danken und einen lieben Gruß übersenden.

Selbständigkeitserklärung

Ich erkläre, dass ich die vorliegende Arbeit selbständig und nur unter Verwendung der angegebenen Literatur und Hilfsmittel angefertigt habe.

Berlin, den 18.07.2012 Tim Schröder